



Dissertation  
Single Metal Adatoms at the Reconstructed  $\text{Fe}_3\text{O}_4(001)$   
Surface

ausgeführt zum Zwecke der Erlangung des akademischen Grades  
eines Doktors der technischen Wissenschaften unter der Leitung von

Univ.-Prof. Dipl.-Ing. Dr.techn. Ulrike Diebold  
Institut für Angewandte Physik (E134)

eingereicht an der Fakultät für Physik  
der technischen Universität Wien  
von

Roland Bliem  
0653668  
Siebenbrunnengasse 8/4, 1050 Wien

Wien, Juli 2016



## Acknowledgements

I would like to express my gratitude to my supervisor, Ulrike Diebold, for her support and guidance during my PhD studies and for always having an open door for discussions with her group members. She has given me the chance to bring in new ideas and interact with scientists in the field, and has provided important insights into different aspects of the world of scientific research. In the same way, I would like to thank Gareth Parkinson for being an inspiring and motivating co-supervisor, who was sometimes even more excited about my new results than me. He supported me during my PhD, starting from teaching me the basics of surface science up to giving me ideas about the everyday life of a young scientist. Moreover, I am grateful to Michael Schmid, who always has an open ear for questions concerning physics and chemistry, and a skillful helping hand for technical problems. I would like to say thank you to all members of the surface science group for the nice working atmosphere that I have enjoyed during the past three years and for all the fruitful scientific and non-scientific discussions. In addition, I would like to thank Peter Blaha for his guidance in the theory part of my PhD thesis, as well as all our other collaborators on the magnetite project. I acknowledge support from the Austrian Science Fund (FWF) doctoral school Solids4fun (Project W1243), the Austrian Science Fund START prize Y 847-N20 and Project No. P24925-N20 as well as the European Research Council (Advanced Grant "Oxide Surfaces").

Besides life in the research group, I would like to thank my friends at the TU Wien, in particular Bernhard Berger, Florian Laggner, and Anna Galler for the good times we had together.

Moreover, I would say thank you to my parents, Monika and Peter, and my sister Daniela for their loving support throughout my life. Finally, I would like to thank the most important person in my life, my wife Christina, for making the world a nicer place whenever she is with me.



## Abstract

Supported metal particles in the sub-nanometer regime frequently exhibit interesting functional properties such as catalytic activity, which can be highly size-dependent. In the emerging field of single-atom catalysis these effects are studied at the size limit, where the active phase is represented by isolated stable metal atoms on oxide supports or within surface alloys.

The present thesis is a surface-science study of metal adsorption at the magnetite  $\text{Fe}_3\text{O}_4(001)$  surface on synthetic and natural single-crystal specimens prepared in ultra-high vacuum (UHV). The properties of the  $\text{Fe}_3\text{O}_4(001)$  surface are investigated using scanning tunneling microscopy (STM), photoelectron spectroscopy (PES), low-energy electron diffraction (LEED), and density functional theory (DFT) calculations based on the WIEN2k program package. These experimental surface-science methods combined with DFT are also employed in the study of metal adsorption at this surface, performed in UHV as well as during exposure to low pressures of common reactant gases ( $2 \times 10^{-10}$  mbar to  $10^{-6}$  mbar of gases such as CO, O<sub>2</sub>, NO).

Magnetite ( $\text{Fe}_3\text{O}_4$ ) is a naturally abundant material, which finds application in energy technology as a catalyst or as a support material of active metal particles. The  $\text{Fe}_3\text{O}_4(001)$  surface stabilizes isolated metal adatoms up to a temperature of 700 K and is thus a highly promising model system for the study of single-atom properties. The present thesis provides an overview of the adsorption properties of selected metals (Ag, Co, Cu, Mn, Ni, Pt, Rh, Ti, and Zr) at this surface and their interaction with gas molecules. As a first step, the structure of the  $(\sqrt{2} \times \sqrt{2})\text{R}45^\circ$  reconstruction of the B-terminated (i.e.,  $\text{FeO}_2$ -terminated)  $\text{Fe}_3\text{O}_4(001)$  surface is resolved via quantitative low-energy electron diffraction and *ab initio* thermodynamics. The stable reconstructed surface structure is based on a rearrangement in the subsurface layers, involving two subsurface Fe vacancies and one interstitial Fe atom per unit cell. This reconstruction creates a twofold coordinated adsorption site in each unit cell, which is the preferential site for metal atoms. In this site the adatoms bind strongly to surface oxygen and assume a cationic charge state. However, the adatom configuration does not correspond to the thermodynamic equilibrium; thus the adatoms can be destabilized by annealing to high temperatures. In this case the deposited metal atoms follow one of two observed pathways: incorporation or clustering. Metals that form stable spinel compounds (e.g. Ni in  $\text{NiFe}_2\text{O}_4$ ) exhibit an energetic preference to enter the surface, filling the subsurface Fe vacancy and locally lifting the

reconstruction. The incorporation barrier varies for different chemical elements, leading to differences in the specific behavior. In most cases mild annealing is required to overcome the incorporation barrier (for Ni, Co, Mn, and Rh), whereas for example Ti and Zr are almost fully incorporated upon deposition at room temperature and Cu retains a partial coverage of adatoms even at 870 K. Noble metals (Au, Ag, Pt, and Pd), on the other hand, do not incorporate but form clusters once a critical number of interacting metal atoms is exceeded. The number of interacting metal atoms can be enhanced by high coverage or by increasing the mobility of the metal adatoms, for example thermally or chemically, via the formation of mobile metal-adsorbate complexes. The onset temperature of clustering for noble metals is found to be  $\approx 700$  K; close to the temperature where the surface reconstruction is lifted.

The combination of the experimental data with density functional theory calculations allows determining trends in the adsorption behavior. Thus, it is for example possible to ascribe a stronger metal-oxide bond to the  $3d$  metals compared to the  $4d$  and  $5d$  metals, which are characterized by an increased strength of the metal-metal bond. Moreover, the concept of stable metal adatoms at the reconstructed  $\text{Fe}_3\text{O}_4(001)$  offers the possibility to combine the specific chemical properties of different metals by co-deposition.

The prospective applications of single adatoms in catalysis encourage characterizing their interaction with reactive gas molecules such as CO,  $\text{O}_2$ , and NO. Strong adsorption is found to stimulate the mobility of adatoms in various metal-gas combinations, such as Pt-CO, Rh-NO, and Rh- $\text{O}_2$ . For example Pt adatoms exposed to CO form stable, mobile carbonyl species, driving the formation of Pt clusters. When heated in UHV to 520 K, the smallest Pt clusters are destabilized and decay back to adatoms. In contrast, annealing the surface with Pt clusters at 550 K in reactive atmosphere ( $10^{-7}$  mbar CO,  $\text{H}_2$ , or  $\text{O}_2$ ) causes the clusters to activate the interaction between gas molecules and support. Under these conditions the Pt clusters mediate the oxidation of CO and  $\text{H}_2$  via the extraction of lattice oxygen, and island growth via oxygen spillover in  $\text{O}_2$  atmosphere.

## Kurzfassung

Die funktionellen Eigenschaften von Metallpartikeln auf Oxidoberflächen sind häufig von der Teilchengröße abhängig. Ein bekanntes Beispiel dafür ist die erhöhte katalytische Aktivität vieler Metalle im Sub-Nanometer-Bereich. Im aktiven Forschungsgebiet der Einzelatom-Katalyse beruht diese Aktivität auf einzelnen Metallatomen, die an Oxidoberflächen gebunden sind oder als Bausteine von Oberflächenlegierungen stabilisiert werden.

In der vorliegenden Dissertation wird die Stabilität einzelner Metallatome auf der (001)-Oberfläche synthetischer und natürlicher Magnetit ( $\text{Fe}_3\text{O}_4$ )-Einkristalle mittels oberflächenphysikalischer Methoden untersucht. Die Experimente wurden in Ultrahochvakuum (UHV) durchgeführt und bedienten sich hauptsächlich der Methoden Rastertunnelmikroskopie (STM), Photoelektronenspektroskopie (PES) und der Beugung niederenergetischer Elektronen (low energy electron diffraction, LEED). Die Interpretation der experimentellen Ergebnisse wurde von Dichtefunktionaltheorie-Rechnungen basierend auf dem WIEN2k Programmpaket unterstützt. Dieselben Methoden wurden zur Untersuchung der Wechselwirkung von stabilen Metallatomen mit niedrigen Drücken reaktiver Gase wie CO,  $\text{O}_2$ , oder NO herangezogen ( $2 \times 10^{-10}$  mbar bis  $10^{-6}$  mbar).

Magnetit ist ein weit verbreitetes, natürlich vorkommendes Material, das zum Beispiel als Katalysator oder als Trägermaterial für aktive Teilchen Anwendung findet. Die  $\text{Fe}_3\text{O}_4(001)$  Oberfläche hat die einzigartige Eigenschaft, einzelne Metallatome bis zu einer Temperatur von 700 K zu stabilisieren, und ist daher ein vielversprechendes Modellsystem zur Untersuchung einzelner Adatome. Die vorliegende Arbeit bietet einen Überblick über die Eigenschaften verschiedener Metallatome (Ag, Co, Cu, Mn, Ni, Pt, Rh, Ti und Zr) auf der  $\text{Fe}_3\text{O}_4(001)$  Oberfläche und die Wechselwirkungen dieser Metalle mit reaktiven Gasen wie CO,  $\text{O}_2$  und NO. Die Struktur der  $(\sqrt{2} \times \sqrt{2})\text{R}45^\circ$ -rekonstruierten  $\text{Fe}_3\text{O}_4(001)$  Oberfläche bildet die Basis ihrer Adsorptionseigenschaften. Mittels quantitativer Elektronenbeugung und *Ab-initio*-Thermodynamik wird gezeigt, dass diese Rekonstruktion auf einer regelmäßigen Anordnung von Eisenfehlstellen in der  $\text{FeO}_2$ -Lage unmittelbar unter der Oberfläche sowie zusätzlichen Fe Atomen in der obersten Fe-Lage basiert. Metallatome adsorbieren bevorzugt in einer spezifischen Position in der rekonstruierten Einheitszelle, in der sie eine stabile Bindung mit zwei Sauerstoffatomen eingehen. Die Adatome sind zwar stabil, stellen aber nicht den thermodynamischen Gleichgewichtszustand dar.

Daher können sie durch hohe Temperaturen destabilisiert werden, was zu zwei unterschiedlichen Verhaltensweisen der Metallatome führt: Inkorporation oder Clusterbildung. Metalle, die stabile Spinell-Mischphasen mit Magnetit bilden (z.B. Ni in  $\text{NiFe}_2\text{O}_4$ ), werden vorzugsweise in die Oberfläche eingebaut und füllen dort die Eisenfehlstellen. Dies führt dazu, dass die Rekonstruktion lokal in der betroffenen Einheitszelle aufgehoben wird. Meist muss die Temperatur der Probe erhöht werden, damit die Metallatome die Inkorporationsbarriere überwinden können (für Ni, Co, Mn und Rh). Ti und Zr hingegen sind bereits bei Raumtemperatur fast vollständig in die Oberfläche eingebaut. Im Gegensatz dazu bilden die Edelmetalle Au, Ag, Pt und Pd Cluster, sobald eine überkritische Anzahl an wechselwirkenden Atomen erreicht wird. Die Anzahl wechselwirkender Atome kann auf verschiedene Weisen variiert werden, wie zum Beispiel durch die Menge an aufgebrachtem Metall oder über die Mobilität der Adatome, die von der Temperatur der Probe abhängt, aber auch durch Adsorption von Molekülen erhöht werden kann. Auf einer Oberfläche, auf der sich nur Edelmetall-Adatome befinden, beginnt die Entstehung von Clustern bei etwa 700 K. Dies entspricht in etwa der Temperatur, die auch zur Aufhebung der Rekonstruktion benötigt wird. Die hohe Stabilität der Metallatome ermöglicht es auch, zwei Metalle mit verschiedenen Eigenschaften auf der Oberfläche zu kombinieren.

Die potenzielle Anwendung einzelner Atome in Katalysatoren stellt eine starke Motivation dar, die Wechselwirkung der Adatome mit reaktiven Gasen wie CO, O<sub>2</sub> und NO zu untersuchen. Meist äußert sich eine starke Wechselwirkung mit Gasmolekülen durch starke Adsorption, die zu erhöhter Mobilität der Adatome führt. Für Pt und CO wird zum Beispiel die Bildung eines mobilen Pt-Carbonyls beobachtet, dessen Mobilität entscheidend zur Entstehung von Clustern beiträgt. Bei erhöhten Temperaturen aktivieren Pt Cluster die Wechselwirkung mit dem Trägermaterial Magnetit, was in CO oder H<sub>2</sub> Atmosphäre (bei  $10^{-7}$  mbar) zur Oxidation der Moleküle mittels Extraktion von Sauerstoff aus der Oberfläche führt. In O<sub>2</sub> Atmosphäre hingegen bewirkt Spillover von Sauerstoff das Wachstum von Magnetit-Inseln an der Oberfläche.

## List of Abbreviations

AAAS	American Association for the Advancement of Science
AES	Auger electron spectroscopy
AFM	Atomic force microscopy
APDB	Antiphase domain boundary
APW	Augmented plane wave
APW+lo	Augmented plane wave plus local orbital
ARPES	Angle-resolved photoelectron spectroscopy
DBT	Distorted bulk truncation
DFT	Density functional theory
DOS	Density of states
e.g.	exempli gratia (for example)
fcc	Face-centered cubic
HAXPES	Hard X-ray photoelectron spectroscopy
hcp	Hexagonal close-packed
i.e.	id est (that is)
ISS	Ion scattering spectroscopy
LAPW	Linearized augmented plane wave
LEED	Low-energy electron diffraction
(SP)LEEM	(Spin-polarized) Low-energy electron microscopy
LEIS	Low-energy ion scattering spectroscopy
ML	Monolayer
PES	Photoelectron spectroscopy
RT-STM	Room-temperature scanning tunneling microscopy chamber where most experiments were performed
SCV	Subsurface cation vacancy
STM	Scanning tunneling microscopy
STS	Scanning tunneling spectroscopy
(S)TEM	(Scanning) Transmission electron microscopy
UHV	Ultrahigh vacuum
UPS	Ultraviolet photoelectron spectroscopy
XAS	X-ray absorption spectroscopy
XPS	X-ray photoelectron spectroscopy



# Contents

<b>1</b>	<b>Introduction</b>	<b>1</b>
1.1	Surface science . . . . .	1
1.2	Single-atom catalysis . . . . .	3
<b>2</b>	<b>Methods</b>	<b>7</b>
2.1	Experimental methods . . . . .	7
2.1.1	Sample preparation . . . . .	8
2.1.2	Scanning tunneling microscopy (STM) . . . . .	8
2.1.3	Low-energy electron diffraction (LEED) . . . . .	11
2.1.4	Photoelectron spectroscopy (PES) . . . . .	12
2.1.5	Low-energy ion scattering (LEIS) . . . . .	12
2.2	Electronic structure calculations . . . . .	13
2.2.1	Hohenberg-Kohn and Kohn-Sham theorems . . . . .	14
2.2.2	The implementation in WIEN2k . . . . .	16
<b>3</b>	<b>Magnetite Fe<sub>3</sub>O<sub>4</sub></b>	<b>19</b>
3.1	Bulk properties . . . . .	19
3.2	Surface properties . . . . .	21
3.2.1	Fe <sub>3</sub> O <sub>4</sub> (001) . . . . .	21
<b>4</b>	<b>Results</b>	<b>25</b>
4.1	Surface structure of Fe <sub>3</sub> O <sub>4</sub> (001) . . . . .	25
4.1.1	Surface defects and dopants . . . . .	36
4.2	Metal adsorption . . . . .	38
4.2.1	Single metal adatoms and their stability . . . . .	38
4.2.2	Silver . . . . .	39

4.2.3	Nickel . . . . .	47
4.2.4	Incorporation of transition metals . . . . .	57
4.2.5	Platinum . . . . .	69
4.2.6	Rhodium . . . . .	81
4.2.7	Copper . . . . .	90
4.2.8	Co-deposition of metals . . . . .	95
4.3	Properties and applications of metal clusters . . . . .	97
4.4	Trends in metal adsorption . . . . .	103
<b>5</b>	<b>Summary and Outlook</b>	<b>107</b>
<b>A</b>	<b>List of Publications</b>	<b>124</b>
<b>B</b>	<b>Further experimental details</b>	<b>126</b>
B.1	Fe <sub>3</sub> O <sub>4</sub> (001) single crystals . . . . .	126
<b>C</b>	<b>Additional Figures</b>	<b>127</b>





# 1 Introduction

## 1.1 Surface science

Surfaces and interfaces are the contact points of solids and their environment, which have crucial influence on most interaction processes in everyday life. The characterization of solid surfaces is therefore essential to describe, understand, and utilize the functional properties of solids interacting with other phases. Bonds are broken at the surface of a solid-state body and thus the coordination of the surface atoms is changed. The initial state created by cleaving or cutting a solid to form a surface is usually balanced by relaxations of the atoms from their bulk equilibrium positions or by reconstructions of the structure in the surface and subsurface layers. As a result, the electronic structure of the surface as well as its properties can differ substantially from the bulk, demanding a systematic study of surface structure and properties to obtain a deep understanding of the interaction of different materials with their environment. There is a variety of techniques for research on surfaces, a selection of which will be explained in chapter 2.

Surface science, i.e., the study of surface properties of single crystals and thin films under idealized conditions (e.g. ultrahigh vacuum (UHV) environment), is a highly interdisciplinary field, combining surface-sensitive methods from physics and chemistry. Research on surfaces has received considerable attention since its results do not only describe the basic interaction processes at interfaces but are directly relevant to applications in many cases. Functional properties such as catalytic activity or different types of electronic conductivity often rely on the characteristics of the surfaces. Thus understanding and modifying the underlying surface processes can lead to significant improvements, for example in the performance of catalysts. The importance of the field found universal recognition with the 2007 Nobel Prize in Chemistry awarded for the surface-science study of chemical processes on solid surfaces<sup>1</sup>. While mostly technologically relevant metal surfaces were studied initially, the focus of attention has shifted increasingly to metal oxides<sup>2,3</sup>. This development is not only related to the propensity of most chemical ele-

ments to form compounds with oxygen, the most abundant element in the earth's crust<sup>4</sup>, making oxides important as the naturally occurring phase of most materials. It also reflects the increasing importance of metal oxides in technology<sup>3</sup>, ranging from all-oxide electronics to applications in heterogeneous catalysis.

In heterogeneous catalysis, oxides can find application as catalytically active phase<sup>5,6,7,8,9</sup> or as support material for active nanoparticles<sup>10,11,12,13</sup>. Oxide surfaces are particularly well-suited for reaction processes requiring sites of (Lewis) acidic and basic character, because the positively charged metal and the negatively charged oxygen ions facilitate dissociation processes. In addition to the acid-base character, which is closely related to the elemental composition of the oxide surface and the valence states of the constituent atoms, the catalytic activity of a specific material depends on surface properties such as the bonding geometry, the (under-)coordination of the surface species, and the nature and concentration of defects. For a single compound all these properties can vary significantly for different exposed facets and the respective stable terminations, resulting in a different catalytic activity. The intrinsic reactivity of a surface can be enhanced via doping or the deposition of active species, such as metal nanoparticles. Active, oxide-supported metal deposits are widely employed in technological applications<sup>14</sup>, ranging from industrial processes like Fischer-Tropsch synthesis to three-way catalytic converters in car exhaust systems. Nanoparticles exhibit a high surface-to-volume ratio compared to bulk crystals, which allows combining a large active area with an economical use of precious metals. While the properties of large particles usually closely resemble the characteristics of bulk metals, approaching the nanometer scale can lead to remarkable changes. One of the most prominent examples of unexpected effects in the nano-regime is the enhanced low-temperature CO oxidation activity of Au nanoparticles for cluster diameters below 5 nm discovered by Haruta *et al.*<sup>15,16</sup>. This observation has converted the image of gold from an inert metal to an important and widely studied nanocatalyst<sup>17,18</sup> and has motivated numerous studies of the nanoscale properties of different metals.

Typical nanoparticle catalysts consist of a heterogeneous distribution of particle sizes and shapes, rendering a well-defined study of size-dependent properties challenging. Furthermore, ensembles of nanoparticles with various different sizes are susceptible to ripening processes at elevated temperatures, also known as sintering. These growth processes can potentially change the properties of the metal particles during reactivity measurements. In addition to temperature, adsorbate species can play a decisive role in sintering processes<sup>19,20,21</sup> by inducing the mobility of a metal species, for example by weakening the metal-metal or metal-surface bonds. Depending on the nature of the diffusing species, two types of sintering processes can be distinguished: Ostwald ripening or particle

migration and coalescence<sup>22,23,24</sup>. In the latter case the adsorbed clusters are mobile and diffuse to meet and coalesce to larger particles, whereas in Ostwald ripening atoms or molecular species detach from clusters and diffuse at the surface leading to mass exchange between clusters. The lower surface free energy per atom for increased particle sizes results in a reduced rate of detachment from larger particles, which eventually leads to their growth at the expense of small clusters. Well-defined single-size cluster ensembles thus lead to the inhibition of Ostwald ripening, as Wettergren *et al.* demonstrated for Pt clusters<sup>25</sup> on an amorphous Si<sub>3</sub>N<sub>4</sub> support.

The development of sources of such size-selected clusters has raised metal cluster research to a new level by providing access to (sub-)nano particle ensembles with a narrow size distribution<sup>26,27,28,29</sup>. Studies on size-selected clusters have shown that changing the cluster size by a single atom<sup>30,31,32,33</sup> can result in dramatic changes to essential properties of the clusters such as catalytic activity and selectivity<sup>29</sup>. In particular for particles consisting of few atoms, it is possible to establish a direct connection between application-related characteristics such as adsorption energies of molecules and variations of the electronic structure<sup>32</sup> or the cluster geometry<sup>18</sup>. In addition to the size dependence, changes of surfactants or the support material<sup>12,34,35</sup> have been observed to modify the catalytic properties of the sub-nano metal species. The reactivity of the sub-nano clusters compared to larger particles or bulk metals is often assessed by measuring the adsorption strength of gas molecules, for example via temperature programmed desorption (TPD). In these model studies CO is a popular probe molecule since it is involved in many important reactions and extensive reference data is available on metal single crystals. The remarkable increase in activity observed for small metal clusters and the strong effect of the cluster size raise the question whether catalytic reactions are also possible at the ultimate size limit of sub-nano clusters – single atoms. Indeed single atoms have been reported as catalytically active species, giving rise to the emergence of a new branch in heterogeneous catalysis research: single-atom catalysis<sup>36,37</sup>.

## 1.2 Single-atom catalysis

The catalytic activity of isolated metal adatoms was discovered initially in size-selected cluster studies approaching the limit of single atoms. Pioneering studies include the observation of CO oxidation at 90 K over Pd atoms soft-landed onto an MgO(100) support<sup>38</sup>, where they are anchored at surface oxygen vacancies. Later, the water-gas shift activity of Pt and Au on a ceria support was shown to remain constant when all metallic particles

were removed by leaching, indicating that ionic noble metal species are responsible for the catalytic activity<sup>39</sup>. Based on temperature programmed reaction and infrared spectroscopy or X-ray photoelectron spectroscopy (XPS), respectively, these initial studies provide clear evidence that single atoms bound to an oxide support can efficiently catalyze reaction processes. More recently, technological advances in imaging methods such as aberration-corrected (scanning) transmission electron microscopy ((S)TEM) have opened new pathways for the atomic-scale characterization of supported single metal atoms. Successful examples specifically targeting the reactivity of isolated metal atoms include studies of Pt/FeO<sub>x</sub><sup>40</sup> for CO oxidation, Au on zeolite for CO oxidation<sup>41</sup>, Pt-(OH)<sub>x</sub> on alumina<sup>42</sup> catalyzing the water-gas shift reaction, or Pt-CeO<sub>2</sub> for fuel cell applications<sup>43</sup>. The combination of high-resolution imaging with advanced spectroscopic techniques such as X-ray absorption spectroscopy (XAS) has proven a powerful approach to establish the activity of mononuclear species and further characterize potential single-atom catalysts<sup>36,37,44</sup>. Based on this methodology studies of catalytically active single atoms have flourished and potential reaction pathways have been proposed in many studies, usually supported by *ab initio* calculations. However, providing the atomic-scale knowledge of the support surface and the exact geometry of the adsorption sites required by the calculations remains challenging for TEM and XAS experiments, in particular at a level that allows for accurate predictions of reaction mechanisms. Thus, while these studies substantially advance the field of single-atom catalysis by expanding the repertoire of metals and reactions, their contribution to a profound understanding of reaction processes over supported single atoms remains controversial. The required mechanistic insights can be provided by surface-science experiments on well-defined model systems, allowing for a combination of experiments and *ab initio* calculations based on established surface structures, which can be prepared reproducibly. The emerging field of single-atom catalysis represents a new frontier in catalysis research, which is accessible to application-oriented methodology as well as surface-science techniques, opening the opportunity to combine the results on activity with mechanistic understanding for well-defined catalysts at the ultimate size limit.

In recent years, the field of single-atom catalysis has been growing rapidly; the number of different reactions and their complexity are increasing as well as the range of potential single-atom catalysts. In the selection of new single-atom catalysts, the stability of the isolated atoms represents one of the major criteria. The agglomeration to larger particles originates to a large degree in the decreased surface-to-volume ratio of nanoparticles compared to single atoms, which usually results in a lower surface free energy per atom. Thus, on most surfaces deposited metal atoms lower their energy by agglomerating to clusters or islands, unless the atoms are prevented from assuming their equilibrium growth

mode<sup>10,45</sup>, for example by suppressed diffusion. Common methods to inhibit diffusion processes include trapping the mobile species by cryogenic temperatures or creating surface sites with high binding energies, such as defects. While low temperatures are not the appropriate approach for single-atom catalysis applications, there are effective strategies to stabilize atomically dispersed metal species at surfaces up to reaction temperatures<sup>36</sup>: In dilute “single-atom alloys”<sup>42,46</sup>, reactive single metal atoms are stabilized as part of the alloy’s surface lattice and catalyze reaction processes. For example Pt-Cu single-atom alloys with a surface coverage of 0.02 ML Pt have been shown to catalyze hydrogenation reactions<sup>47</sup>. The agglomeration of Pt is suppressed by strain and in this case additionally by the mixing enthalpy of Pt in Cu. In zeolites, nanoporous crystalline oxide materials, the stability of the mononuclear metal species is established in the form of metal complexes deposited from selected organic precursors<sup>36</sup> containing single metal atoms<sup>41,48</sup>. On similar non-reducible oxides, such as alumina or silica, stable single atoms can be achieved via the addition of alkali oxides to such complexes, which also contribute to the local activity of the support<sup>36</sup>. Reducible metal oxides such as ceria<sup>36,39</sup> or FeO<sub>x</sub><sup>37,40</sup> constitute another important class of supports, on which surface defects provide anchoring sites for metal adatoms and sub-nano clusters in a stable metal-oxygen-substrate configuration<sup>37</sup>. Surface defects are known to stabilize single atoms also on various other supports, which can be promising for single-atom catalysis applications, for example graphene<sup>49</sup>. The stability of metal adatoms in catalysts must be considered in the context of the operating temperature and environment. The operation conditions of an active and stable single-atom catalyst are therefore constrained to the regime where it is not affected by deactivation processes such as poisoning or sintering, which are commonly associated with the reactive atmosphere required for catalytic reactions<sup>50</sup>.

In most single-atom catalysts, the properties of the metal species are determined by their interaction with the support. Oxide-supported metal atoms are usually cationic<sup>39</sup>, resulting from coordination to surface oxygen, which can be regarded as a type of incorporation into the oxide<sup>44</sup> by filling continuation sites of the cation lattice<sup>37</sup>. Their ionic nature can modify the bond to molecules<sup>36</sup> and lead to enhanced reactivity for different metal-support combinations such as Pt and Ir on FeO<sub>x</sub><sup>40,51</sup>; Pd, Rh and Pt on Al<sub>2</sub>O<sub>3</sub><sup>52,53,54,55</sup>; and Au on various supports, described in a comprehensive review by Flytzani-Stephanopoulos<sup>44</sup>. The broad experience with Au has led to a promising observation<sup>44</sup>: The intrinsic activity of the single-atom Au species for the water-gas shift reaction is transferable to a large selection of supports. This selection of substrate materials for active Au atoms is even enhanced by the recent discovery that alkali metals stabilize active Au atoms on non-reducible supports such as zeolite or silica<sup>48</sup>. The transferability between

different support materials increases the importance of understanding the properties of single metal adatoms for the ambitious objectives of single-atom catalysis, such as designing optimized operating catalysts by combining the best-suited supported metals for specific tasks in the reaction process. Only the study of the interaction of metals with small and simple reactant molecules, such as CO, CO<sub>2</sub>, O<sub>2</sub>, and H<sub>2</sub>, can provide the required base of knowledge for these endeavors. In the next step of elucidating single-atom reaction mechanisms, the stability of the active metal phase can be tested under different operation conditions. One example of such a mechanistic study shows that the changes in selectivity with variations of the ratio of the reactant gases CO<sub>2</sub> and H<sub>2</sub> over Rh/TiO<sub>2</sub> originate from an increase in isolated Rh atoms under CO<sub>2</sub>-rich conditions<sup>56</sup>, rather than changes in the preferred reaction pathways. The trend towards *in situ* studies of single-atom catalysts is an important step bridging the pressure gap to application-relevant conditions. For Pd on La-doped alumina, for example, an *operando* X-ray absorption spectroscopy study provides important insights into the stabilization and reaction mechanisms<sup>57</sup> of CO oxidation and demonstrates redispersion of the active atoms achieved by high-temperature oxidation in air.

The development of advanced characterization methods and reliable single-atom supports is particularly important in the context of a recent article<sup>58</sup> showing the controversial nature of single-atom catalysts. Using infrared spectroscopy this study demonstrates that single Pt atoms are a spectator species in the water-gas shift reaction over sub-nano Pt particles, casting doubt over the general assumption that single atoms exhibit increased catalytic activity. The literature presented above includes several careful studies on single-atom catalysts which clearly establish their existence, but each newly proposed system should therefore be critically reviewed, also regarding the irreversible changes that can occur at reaction conditions. Well-defined model systems such as the ( $\sqrt{2} \times \sqrt{2}$ )R45°-reconstructed Fe<sub>3</sub>O<sub>4</sub>(001) surface, studied in the present thesis, gain particular importance in this context. This surface has been shown to stabilize single Au adatoms, which can clearly be distinguished from clusters, up to catalytically relevant temperatures of 700 K in one lattice site per reconstructed surface unit cell<sup>59</sup>. The surface structure is well known, exhibits a broad stability range, and can be reproducibly prepared. Recently Pd adatoms<sup>60</sup> at this surface have been reported to host adsorbed CO, mobilizing the adatoms and leading to adsorbate-induced sintering processes observable using scanning tunneling microscopy. The present thesis builds on the discovery of reactive single metal adatoms at the Fe<sub>3</sub>O<sub>4</sub>(001) surface and aims to provide a detailed description of the adsorption of metals using surface-science methodology.

## 2 Methods

The present thesis is based on a combination of experimental surface science and density functional theory (DFT). This comprehensive approach has proven an effective strategy to unravel the physical background of surface processes on complex materials. When new adsorption phenomena are discovered in experiments, DFT calculations provide the background information that is required to relate observations to the structural and electronic properties of the surface, such as adsorption energies, site preferences, energy barriers, electronic densities of states, and partial charge distributions. This chapter is intended to give a brief introduction to the most relevant experimental techniques and to density functional theory calculations.

### 2.1 Experimental methods

The majority of the single-atom experiments on  $\text{Fe}_3\text{O}_4(001)$  were performed at room temperature in an ultrahigh-vacuum chamber referred to as “room-temperature scanning tunneling microscopy chamber” (RT-STM). The RT-STM is a two-vessel ultrahigh-vacuum system consisting of a preparation chamber and an analysis chamber connected through a gate-valve via a magnetic manipulator rod. The preparation chamber is equipped with a VG Microtech EX05 scanning ion gun, retractable contacts for the integrated target heater on the manipulator rod (filament current, high voltage), a single-pocket and a triple-pocket electron-beam evaporator (Focus EFM 3, EFM 3T), a home-built Zr sputter source<sup>61</sup>, a quadrupole mass spectrometer, and four high-precision leak valves; one of the leak valves is combined with a gas doser to achieve higher local pressures at the sample surface. The experimental equipment on the analysis chamber comprises an Omicron  $\mu$ -STM, a VSI ErLEED low-energy electron diffraction (LEED) setup, a VG Microtech XR3E2 dual anode X-ray source, a SPECS EA 10 Plus analyzer, a SPECS IQE 12/38 scanning ion gun, a SPECS EQ 22/35 electron gun, a Perkin Elmer Model 3017 Auger electron spectroscopy system, and four high-precision leak valves. The base pressures in the analysis and pre-

preparation chambers are in the range of  $\approx 5 \times 10^{-11}$  mbar and  $< 10^{-10}$  mbar, respectively, as measured using a cold cathode Penning gauge in the preparation chamber and a Bayard-Alpert (hot filament) gauge in the analysis chamber.

### 2.1.1 Sample preparation

The experiments are performed on magnetite single crystals, which were cut in (001)-direction and polished by commercial suppliers (SurfaceNet, Mateck, Surface Preparation Labs). These companies are also the suppliers of the natural magnetite single crystals, whereas the synthetic crystals employed in the experiments were grown by Professor Zhiqiang Mao at Tulane University (New Orleans, USA) using the floating zone method. The natural crystals are square-shaped (from  $5 \times 5 \text{ mm}^2$  to  $10 \times 10 \text{ mm}^2$ ) with thicknesses ranging from 0.5 to 1.5 mm. A list of the different crystals used for the metal deposition experiments is given in the appendix B.1. The polished crystals are mounted onto Mo (or Ta) Omicron-type sample plates using two stripes of flat Ta wire that are shaped to clips which uniformly press the sample down and are fixed by spotwelding the ends to the Mo/Ta plate. Usually a thin Au foil is mounted between sample plate and crystal to improve the thermal contact. All parts (sample plate, Au foil, Ta clips) are cleaned via several cycles in acetone followed by isopropanol in an ultrasonic cleaner. Organic residues are blown off by pressurized  $\text{CO}_2$ .

Once a sample is in ultrahigh vacuum, it is slowly annealed to 870 K to desorb residual molecules from the surface and further cleaned using sputter-anneal cycles. The standard UHV sample preparation cycle consists of sputtering with 1 keV- $\text{Ar}^+$  ions and annealing to 870 K in UHV. After several UHV annealing cycles, the sample is usually heated to 870 K in a background pressure of  $10^{-6}$  mbar  $\text{O}_2$  before the experiment in order to avoid Fe-rich surface terminations.

If the previous experiment involved metal deposition, several cleaning cycles are necessary ( $\approx 10$ ) and often automated cycles in Ar atmosphere are performed over night. Without any oxidation step, this treatment is likely to cause Fe enrichment in the surface region.

### 2.1.2 Scanning tunneling microscopy (STM)

Scanning tunneling microscopy (STM) is the main experimental technique employed in the present work. This technique provides real-space imaging of flat, conductive surfaces with atomic resolution on the basis of the quantum-mechanical tunneling effect between the surface and an atomically sharp metallic tip. The theoretical basis for STM was laid

by Bardeen<sup>62</sup> in his description of the quantum-mechanical tunneling effect using time-dependent perturbation theory. Bardeen showed that the tunneling probability between two metals separated by an insulating layer can be described by the simple expression  $(2\pi/\hbar)|M|^2\rho_f$ , where  $M$  represents the tunneling matrix element and  $\rho_f$  the density of final states. Thus the tunneling current for a certain  $\rho_f$  can be used to analyze the overlap of the electronic wave functions of a sample and a well-defined probe at a certain tunneling barrier (contained in  $M$ ).

G. Binnig and H. Rohrer<sup>63</sup> recognized the potential of the tunneling effect for a device mapping the electronic structure of surfaces with high spatial resolution and developed the scanning tunneling microscope. This experimental device is based on measuring the tunneling current between a flat surface and an atomically sharp metal probe – the STM tip. In order to achieve an overlap of the wave functions sufficient for tunneling the STM tip is positioned very close to the surface (typical  $\Delta z \approx 0.5\text{--}1$  nm) using piezoelectric actuators. The tunneling matrix element depends exponentially on the tip-sample distance, which makes this technique highly sensitive to the electronic structure of the surface but also to vibrations. To establish measurable tunneling currents (typically in the range of a few pA to 10 nA), a bias voltage is applied between the sample, increasing the accessible final density of states  $\rho_f$ . The polarity of the bias voltage determines whether the measurement probes the filled or empty density of states of the sample.

The principle of operation is illustrated in Figure 2.1. The STM acquires images by scanning the tip over the surface line by line. The tunneling current at each point is amplified, recorded as output signal, and fed into a feedback loop, which controls the z-position of the tip. Similar to the positioning in z-direction, the scanning motion of the tip is realized using piezoelectric actuators, which respond to the application of voltage with small, accurate length changes. If the tip position perpendicular to the scanned area (z-direction) is not changed, the STM is operated in “constant height” mode. The acquired STM image represents a map of the tunneling current recorded in each pixel of the scanned area. In the more common “constant current” operation mode the distance to the sample is adjusted to achieve a tunneling current equal to the current setpoint, a user input parameter. The difference between measured current and setpoint amplified by a gain factor (set by the user) is used to adjust the tip position. Operation in constant current mode allows to scan rougher surfaces at a lower risk of touching the surface with the STM tip (tip crash).

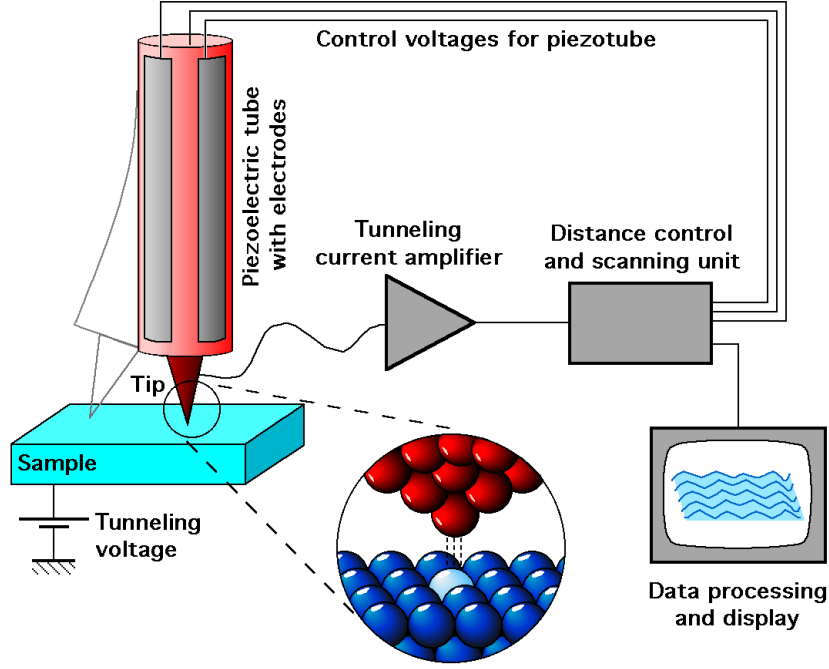


**Figure 2.1:** Illustration of the working principle of a scanning tunneling microscope (Figure by Michael Schmid, TU Wien)<sup>64</sup>. The STM tip is positioned close enough to a conductive sample to achieve tunneling current at an applied bias voltage. The current is amplified, recorded, and used as feedback signal to adjust the position of the tip using piezoelectric actuators, while the tip is scanning a small region of the surface.

### 2.1.2.1 Tersoff-Hamann approximation

Based on the perturbation theory by Bardeen<sup>62</sup>, it is clear that scanning tunneling microscopes provide information on a convolution of the electronic structure and the topography of surfaces. An approximate description of the tunneling process specifically for STM was introduced by Tersoff and Hamann<sup>65</sup>, starting from the tunneling current in first order perturbation theory.

$$I = (2\pi e/\hbar) \sum_{\mu\nu} f(E_\mu)[1 - f(E_\nu + eV)] |M_{\mu\nu}|^2 \delta(E_\mu - E_\nu) \quad (2.1)$$

Here,  $e$  is the electronic charge,  $f(E)$  the Fermi function,  $V$  the applied voltage,  $M_{\mu\nu}$  the tunneling matrix element containing the overlap integral of the wave functions and  $\delta(E_\mu - E_\nu)$  ensures elastic tunneling. The Fermi function is evaluated at the relevant energies for the electronic states of the tip  $f(E_\mu)$  and the sample including the applied bias voltage  $f(E_\nu + eV)$ , resulting in a factor for the occupation probability of all the tip and

sample states, denoted  $\mu$  and  $\nu$ , respectively. The matrix element is represented by an integral of the current operator in the region separating the tip and the surface.

$$M_{\mu\nu} = -(\hbar^2/2m) \int d\vec{S}(\psi_\mu^* \nabla \psi_\nu - \psi_\nu \nabla \psi_\mu^*) \quad (2.2)$$

In the Tersoff-Hamann approximation the tip is approximated using a fixed radius of curvature and a spherical wave function. In the approximation of low bias voltage and temperature (resulting in a sharp Fermi level) an expansion of the wave functions into in-plane Bloch waves decaying exponentially into the tunneling gap results in a tunneling current depending linearly on the tunneling voltage and the density of states at the Fermi energy and exponentially on the distance ( $I \propto e^{-2kd}$ ).

### 2.1.3 Low-energy electron diffraction (LEED)

Low-energy electron diffraction is a surface-sensitive diffraction technique providing reciprocal-space information about surface structures. LEED is a powerful tool, which is widely used in surface science, from assessing simple surface reconstructions and superstructures up to quantitatively determining surface structures via complex multiple-scattering simulations.

In a typical LEED setup, an electron source irradiates the surface with a beam of low-energy electrons (30–500 eV) (usually in perpendicular incidence to the sample surface, defined as z-direction). The electrons are diffracted from the (periodic) surface structure and accelerated onto a fluorescent screen after passing retarding grids which filter out the inelastically scattered electrons.

Unlike bulk diffraction techniques such as X-ray diffraction, LEED does not image sharp spots in the three-dimensional reciprocal space. Since the penetration depth perpendicular to the surface is limited, the diffraction spots only represent the periodicity of the surface plane (xy-plane) and a few bulk-like layers below. In z-direction, however, these spots extend to lines of varying intensity. The construction of an Ewald sphere and the lattice rods in reciprocal space illustrates that LEED spots are observed at any energy if the Ewald sphere intersects the lattice truncation rods. The spot intensity varies as one follows the rods in z-direction, corresponding to a change in the incident electron energy. These intensity variations can only be explained by dynamic scattering theory including multiple scattering events<sup>66</sup>, but they can serve as a fingerprint for unambiguously determining surface structures. If intensity curves for the LEED spots are recorded and simulated using dynamic scattering theory, the results can be compared quantitatively using the so-called Pendry  $R$ -factor ( $0 \leq R_P \leq 2$ ), a number assessing the agreement of the ex-

perimental and simulated sets of intensity curves<sup>67</sup>. This method (called LEED *IV*) can be used to unambiguously confirm or falsify a surface structure model.

### 2.1.4 Photoelectron spectroscopy (PES)

X-ray and ultraviolet photoelectron spectroscopy (XPS, UPS) are common methods to analyze the chemical composition of surfaces. Both methods are based on the photoelectric effect: When a material is irradiated with photons of sufficient energy, the energy of a photon can be transferred to an electron, which is released if it can overcome its binding energy  $E_B$  and (in the case of solids) the work function of the surface  $\Phi$ . The excess energy accounts for the kinetic energy of the photoemitted electron in vacuum:

$$E_{kin}^{e^-} = h\nu - E_B - \Phi \quad (2.3)$$

In photoemission spectra the electron intensity is recorded as a function of the kinetic energy. A peak at a certain kinetic energy thus provides information about the binding energy, which is characteristic for the chemical species that emitted the electron. In addition, the exact position and shape of the peaks contain information on the valence states of the atoms (peak shifts) and their bonding environment (peak shapes, satellites)<sup>68</sup>.

The surface sensitivity of electron spectroscopies originates in the short inelastic mean free path of electrons in solids owing to their high probability to undergo scattering processes. While (high-energy) photons can penetrate deep into the bulk of solids, the attenuation length of the electrons (few Å to nm) usually determines the probing depth of electron spectroscopies. In surface studies this fact is used for modifying the surface sensitivity of the measurement by varying the emission angle of the detected electrons or the energy of the exciting photons. At synchrotron photon sources a large continuous range of photon energies is available at high intensities whereas in laboratory-based experiments the photon energy can only be varied by switching between X-ray and UV sources or using different X-ray anode materials.

### 2.1.5 Low-energy ion scattering (LEIS)

Low-energy ion scattering (or ion scattering spectroscopy ISS) is a highly surface sensitive technique to analyze the composition of the surface via determining the masses of the surface atoms<sup>69</sup>. In LEIS the sample surface is bombarded by a low-current beam of light ions such as He<sup>+</sup> or Ne<sup>+</sup> with a well-defined energy between a few hundred eV and a few keV. The incident ions undergo elastic scattering processes with the surface

atoms in a fixed scattering geometry. In the elastic collisions the incident ions transfer a certain amount of energy to the surface atoms, which is determined by the masses of the scattering partners, the scattering angle, and the incident energy. The ions emitted from the sample at a fixed angle are detected as a function of their kinetic energy using a hemispherical analyzer. Since the neutralization probability of the ions is very high, low-energy ion scattering is a highly surface sensitive method for determining the surface composition. A LEIS measurement can however rapidly change the surface structure and composition since the ion bombardment is comparable to mild sputtering.

## 2.2 Electronic structure calculations

The electronic structure of a solid surface determines the majority of its experimentally accessible properties. The combination of experiments and electronic structure calculations is therefore a powerful approach to characterize surfaces of functional materials. A full quantum mechanical description of a physical system requires the solution of the Schrödinger equation. While the solution for a hydrogen atom is a textbook example, analytical solutions quickly become impossible once many-particle systems are considered. An example of a many-body Schrödinger equation with  $N$  electrons in Born-Oppenheimer approximation<sup>70</sup> is provided in equation 2.4. In the Born-Oppenheimer approximation the ionic and electronic energies of the system are separated, allowing to describe the interaction of the electrons with the lattice via the static potential  $v_{latt}(\mathbf{x}_i)$ . The constant energy contribution of the ionic-core lattice is not considered here.

$$\hat{H}\Psi(\mathbf{x}_1, \dots, \mathbf{x}_N) = E\Psi(\mathbf{x}_1, \dots, \mathbf{x}_N)$$

$$\hat{H} = \sum_{i=1}^N \left( -\frac{1}{2} \nabla_i^2 \right) + \sum_{i=1}^N v_{latt}(\mathbf{x}_i) + \sum_{i < j}^N \frac{1}{|\mathbf{x}_i - \mathbf{x}_j|} \quad (2.4)$$

Since the many-body problem of a solid can be solved neither analytically nor numerically, different strategies are required. The most common approach to calculate the electronic ground state of solids and surfaces is density functional theory (DFT). The many-body problem with a  $3N$ -dimensional wave function is mapped onto a single three-dimensional variable describing the system, the electron density.

## 2.2.1 Hohenberg-Kohn and Kohn-Sham theorems

The theoretical basis of this approach to calculate the electronic structure of many-electron systems is established in the Hohenberg-Kohn<sup>71</sup> and the Kohn-Sham<sup>72</sup> theorems. Hohenberg and Kohn proved that the many-particle ground state of a system described by the Schrödinger equation is a unique functional of the ground-state electron density. Thus, all observable ground-state properties are described by the respective electron density. According to the second Hohenberg-Kohn theorem<sup>71</sup> the ground state density can be determined using the variational principle to find an energy minimum. However, detailed knowledge of the so-called Hohenberg-Kohn functional  $F[n(\mathbf{r})]$  in analytical or numerical form is required to perform the minimization. In addition to the kinetic energy  $T_S[n]$  and the Coulomb repulsion of the electrons,  $F[n(\mathbf{r})]$  includes the exchange and correlation energy  $E_{xc}[n]$  of the interacting system. The complete energy functional  $E[n(\mathbf{r})]$  in the formulation of Kohn and Sham<sup>72</sup> also includes the external potential  $v(\mathbf{r})$  due to the nuclei:

$$\begin{aligned} E[n(\mathbf{r})] &= \int v(\mathbf{r})n(\mathbf{r})d\mathbf{r} + F[n(\mathbf{r})] \\ &= \int v(\mathbf{r})n(\mathbf{r})d\mathbf{r} + T_S[n] + \frac{1}{2} \int \int \frac{n(\mathbf{r})n(\mathbf{r}')}{|\mathbf{r} - \mathbf{r}'|} d\mathbf{r}d\mathbf{r}' + E_{xc}[n] \end{aligned} \quad (2.5)$$

Again using a variational approach, Kohn and Sham derived a set of single-particle Schrödinger equations of non-interacting electrons in an effective potential  $v_{\text{eff}}(\mathbf{r})$ :

$$\begin{aligned} \left( -\frac{1}{2}\nabla^2 + v_{\text{eff}}(\mathbf{r}) \right) \psi_i(\mathbf{r}) &= \epsilon_i \psi_i(\mathbf{r}), \\ v_{\text{eff}} &= v(\mathbf{r}) + \int \frac{n(\mathbf{r}')}{|\mathbf{r} - \mathbf{r}'|} d\mathbf{r}' + \frac{\delta E_{xc}[n]}{\delta n(\mathbf{r})}, \\ n(\mathbf{r}) &= \sum_{i=1}^N |\psi_i(\mathbf{r})|^2 \end{aligned} \quad (2.6)$$

This approach avoids the usage of approximations for  $T_S[n]$ , which are too crude and inaccurate to be of practical use. The effective potential contains the external potential  $v(\mathbf{r})$ , the Coulomb repulsion of the electrons, and an exchange-correlation potential described by  $\delta E_{xc}[n]/\delta n(\mathbf{r})$ . The respective wavefunctions  $\psi_i(\mathbf{r})$  are often called Kohn-Sham orbitals but they usually do not correspond exactly to physical electronic orbitals. Correspondingly, the orbital eigenvalues  $\epsilon_i$  are formally only Lagrange parameters and their use as excitation energies to compare to experimental results is not fully justified. However, the sum of the square absolute values of  $\psi_i(\mathbf{r})$  equals the correct electron density  $n(\mathbf{r})$  and is therefore a reliable descriptor.

At this stage, density functional theory is still exact and includes quantum mechanical exchange and correlation effects. The Kohn-Sham representation provides a set of equations which can be solved iteratively in order to obtain a self-consistent solution. A direct solution is not possible since the effective potential that determines the ground-state density is also a functional of exactly this density. The main impediment to an exact solution, however, is the exchange-correlation potential describing the quantum mechanical interactions of the electrons, which is generally not known. Thus, different approaches have been developed to approximate this term. In several types of approximations the exchange and correlation energy is derived from the properties of the uniform electron gas. In the simplest case, the so-called local density approximation<sup>71,72</sup> (LDA), the exchange-correlation functional is assumed to depend only on the local electron density of the system and the corresponding value of exchange and correlation energy in a homogeneous electron gas. In the next step of improving the accuracy, gradient terms of the electron density are taken into account. One of the most widely used functionals using this so-called generalized gradient approximation (GGA) was introduced by Perdew, Burke, and Ernzerhof (the PBE functional)<sup>73</sup>. For various applications the accuracy achieved using GGA functionals is sufficient. Hence GGA is employed in many studies, including complex systems such as transition metal oxides. However, there are a variety of methods beyond the GGA level, such as hybrid DFT, including a contribution of exact exchange energy calculated using Hartree-Fock methods. The accurate description of exchange and correlation remains one of the main limiting factors of DFT calculations and presents a particular challenge regarding highly correlated systems.

One possible way to treat the strong correlations of  $3d$  or  $4f$  electrons within DFT is to explicitly include the correlation energy<sup>74</sup> via an “on-site Hubbard term”, inspired by the Hubbard model describing correlations on the basis of the free electron gas<sup>75</sup>. In this approach called DFT+ $U$  (LDA+ $U$ , GGA+ $U$ ), the effective potential in the Kohn-Sham equations (equation 2.6) is modified by adding terms accounting for the Coulomb repulsion energy ( $U$ ) and exchange energy ( $J$ ) of certain localized electrons with spin  $\sigma$  occupying a certain type of orbital  $m$  (usually  $d$ - or  $f$ -type orbitals). Equation 2.7 states the total energy functional modified for the DFT+ $U$  self-interaction-correction (SIC) method according to Anisimov *et al.*<sup>74</sup>.

$$\begin{aligned}
E = E^{LDA} - & \left[ \frac{UN(N-1)}{2} - \frac{JN(N-2)}{4} \right] \\
& + \frac{1}{2} \sum_{m,m',\sigma} U_{mm'} n_{m\sigma} n_{m'-\sigma} \\
& + \frac{1}{2} \sum_{m,m',\sigma,(m \neq m')} (U_{mm'} - J_{mm'}) n_{m\sigma} n_{m'\sigma}
\end{aligned} \tag{2.7}$$

Here,  $n_{m',\sigma}$  represents the occupation of an orbital  $m'$  with electrons of spin  $\sigma$  in the LDA+ $U$  calculation. The Coulomb energy  $U$  accounts for the repulsion of two electrons in fully occupied orbitals; the term in brackets corrects for the LDA Coulomb energy of  $d$ - $d$  interactions for a total number of  $N$  correlated ( $d$ -)electrons. The matrices  $U_{mm'}$  and  $J_{mm'}$  represent the non-spherical Coulomb and exchange interactions, taking into account the dependence on the specific orbitals  $m, m'$ . In the calculations in the present thesis, an effective energy  $U_{eff}=U - J$  is employed instead of the two parameters  $U$  and  $J$  (in the calculation one sets  $J=0$ ), which considerably simplifies equation 2.7. The calculations on  $\text{Fe}_3\text{O}_4$  presented in the results section are based on PBE functionals including a Hubbard- $U$  term ( $U_{eff}=3.8$  eV) for the strongly correlated Fe  $3d$  electrons.

## 2.2.2 The implementation in WIEN2k

DFT is realized in a variety of computational packages using different basis sets for the representation of the wave functions and different approximations of the atomic potentials and electronic interaction. In the computational implementation the electronic wave functions are expanded into a set of basis functions (e.g. plane waves) up to a certain cut-off energy defined in the calculation. Simple plane waves, however, are not a good choice to describe rapid changes in the wave function that occur close to the nuclei. This problem can be overcome by employing pseudopotentials, effective potentials for all but the core electrons replacing the exact ionic potential. The pseudopotential method is successfully used in various code packages such as VASP<sup>76</sup>. Alternatively, a version of augmented plane wave basis sets is employed frequently in all-electron approaches, which include the full ionic potential and thus offer a more accurate description of the density close to the nucleus. In the original augmented plane wave (APW) approach developed by Slater<sup>77</sup> the potential is assumed to be spherically symmetric within a defined radius surrounding the nuclei of the constituent atoms and constant in the interstitial region. The solution is represented in the form of sums of two types of basis functions: atomic wave functions

(product of spherical harmonics and a radial function) inside the spheres and plane waves in the interstitial region. In the approach of Slater, a set of unperturbed basis functions is set up, each consisting of a single plane wave in the interstitial region (I) transitioning continuously to a function inside the muffin-tin-type spheres (MT), as shown in the formulation of Sjöstedt *et al*<sup>78</sup>:

$$\psi_{\mathbf{G}}^{APW}(\mathbf{r}, \mathbf{k}) = \begin{cases} e^{i\mathbf{k}_{\mathbf{G}} \cdot \mathbf{r}} & \mathbf{r} \in I \\ \sum_{\{l,m\}} a_{lm}^{\mathbf{k}_{\mathbf{G}}} u_l(r, E) Y_{\{l,m\}}(\hat{\mathbf{r}}) & \mathbf{r} \in \text{MT} \end{cases} \quad (2.8)$$

Here,  $\mathbf{G}$  is a reciprocal lattice vector,  $\mathbf{k}_{\mathbf{G}} = \mathbf{k} + \mathbf{G}$ ,  $u_l(r, E)$  the radial part of the wave function, and  $Y_{\{l,m\}}(\hat{\mathbf{r}})$  are spherical harmonics. The coefficients  $a_{lm}$  are determined by the condition of continuity between the basis functions at the boundary. Since  $u_l(r, E)$  is energy dependent, a new set of coefficients ( $a_{lm}$ ) must be calculated for each energy that is considered for the eigenvalue problem. The solution is represented as a series of the unperturbed wave functions  $\psi^{APW}$ ; the respective coefficients are determined using variational methods. Different types of basis sets have been developed starting from the APW scheme, for example linearized augmented plane wave (LAPW)<sup>79</sup> and the APW plus local orbital (APW+lo)<sup>78</sup> basis functions, which are the two basis sets of choice in WIEN2k<sup>80,81,82</sup>, the code package employed in the present thesis. In the LAPW method, energy independent linearized radial basis functions are constructed by forming a linear combination of a full radial function and its energy derivative  $\dot{u}_l$  evaluated at a fixed energy ( $a_{lm}u_l(r, E_1) + b_{lm}\dot{u}_l(r, E_1)$ ). The coefficients are again determined by the boundary conditions, which in the case of LAPW require that the basis functions should be continuously differentiable. The linearization in the LAPW method simplifies the problem since the radial functions are no longer energy dependent but still sufficient to describe the radial dependence in a range around  $E_1$ . However, a larger set of basis functions is required for the solution. In an attempt to combine the accuracy of the APW functions at a smaller basis set and the flexibility of the LAPW method Sjöstedt *et al.*<sup>78</sup> proposed adding complementary radial basis functions to the APW method, so-called local orbitals. These local orbitals are linearized functions describing selected single orbitals, which are physically relevant to the specific problem and are also used to describe extended core states<sup>83</sup>. They offer additional freedom to vary the wave function inside the ionic sphere, while not contributing to the solution in the interstitial region. The radial part inside the sphere is described by  $a_{\{l,m\}}^{\text{lo}}u_l(r, E_1) + b_{\{l,m\}}^{\text{lo}}\dot{u}_l(r, E_1)$ , similar to a single summand of an LAPW basis function (for single  $\{l, m\}$  values). The resulting APW+lo basis set offers higher flexibility than the APW method while retaining a smaller basis set than LAPW calculations. In WIEN2k,

atoms which require small spheres and orbitals that are difficult to converge (e.g. valence *f*-states) are calculated using the APW+lo basis, whereas in all other cases generally the LAPW method is used.

## 3 Magnetite $\text{Fe}_3\text{O}_4$

Iron oxides are widely abundant materials consisting of two of the most common chemical elements in the earth's crust. Under ambient conditions,  $\text{Fe}^{\text{III}}$ -oxides like  $\alpha\text{-Fe}_2\text{O}_3$  form preferentially, but also  $\text{Fe}_3\text{O}_4$ ,  $\text{FeO}$ , and various hydroxides are stable phases which are frequently found in rocks and soil<sup>84</sup>. Common iron oxides find application in science and technology at various levels, ranging from energy materials for photoelectrochemistry and energy storage to bio-nanomedicine<sup>85</sup> and source materials for iron and steel production<sup>84</sup>. A comprehensive review of the properties and applications of iron oxides and hydroxides is provided by Cornell and Schwertmann<sup>84</sup>. In addition to their interesting applications, these materials also present intriguing physical properties. Magnetite, for example, is a half-metallic mixed-valence oxide, which undergoes a metal-insulator transition involving charge order concomitant with a monoclinic lattice distortion at  $\approx 125\text{ K}$ , the so-called Verwey transition<sup>86,87</sup>.

### 3.1 Bulk properties

At room temperature magnetite ( $\text{Fe}_3\text{O}_4$ ) crystallizes in the inverse spinel structure, a face-centered cubic oxygen lattice with Fe cations filling interstitial sites in octahedral ( $\text{Fe}_{\text{oct}}$ ) and tetrahedral ( $\text{Fe}_{\text{tet}}$ ) coordination to oxygen<sup>84,88</sup>. The structure can be viewed as alternating stacking of  $\text{Fe}_{\text{tet}}$  layers (A layers) and  $\text{Fe}_{\text{oct}}\text{O}_2$  layers (B layers), rotated by  $90^\circ$  and shifted by a quarter of a lattice constant after each double-layer. One cubic unit cell with a lattice parameter of  $8.396\text{ \AA}$ , containing eight formula units of  $\text{Fe}_3\text{O}_4$ , is depicted in Figure 3.1. Magnetite contains Fe in two different valence states (one  $\text{Fe}^{2+}$ , two  $\text{Fe}^{3+}$  cations per formula unit), which occupy the cation sites in the characteristic order of the inverse spinel structure: the tetrahedral sites are exclusively occupied by  $\text{Fe}^{3+}$  cations, while  $\text{Fe}^{2+}$  and  $\text{Fe}^{3+}$  coexist on sites with octahedral coordination ( $\text{Fe}_{\text{oct}}^{2+}\text{Fe}_{\text{oct}}^{3+}\text{Fe}_{\text{tet}}^{3+}\text{O}_4$ ). This arrangement of the iron is energetically preferable regarding the crystal field energy of  $\text{Fe}^{2+}$ , which favors the octahedral coordination<sup>88</sup>. The valence states  $\text{Fe}^{2+}$  and  $\text{Fe}^{3+}$

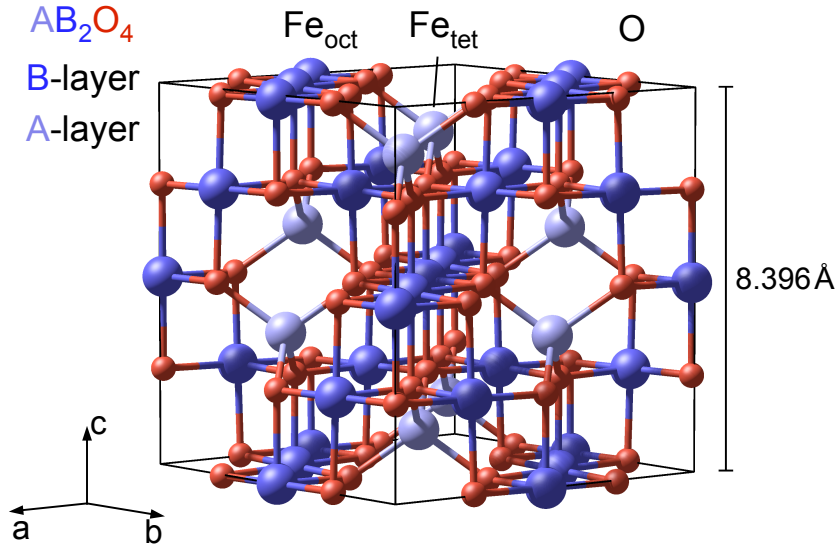


**Figure 3.1:** Bulk unit cell of  $\text{Fe}_3\text{O}_4$  in the cubic inverse spinel phase stable at room temperature. Red spheres represent oxygen, dark and light blue spheres the Fe cations in octahedral and tetrahedral coordination, respectively.

should be regarded as nominal values, used as simplifying terminology of an actually significantly smaller charge deproportionation<sup>89</sup>. In particular at elevated temperatures, the distinction between  $\text{Fe}^{2+}$  and  $\text{Fe}^{3+}$  sites breaks down as a consequence of the conductivity of magnetite along the rows of  $\text{Fe}_{\text{oct}}$ . The conduction behavior is described as a mixture of band conduction and small-polaron hopping, with increasing importance of polaron hopping at elevated temperatures<sup>90</sup>.

The iron cations in magnetite exhibit magnetic moments originating in the Fe 3d orbitals in high-spin configuration (nominally  $5 \mu_B$  and  $4 \mu_B$  for  $\text{Fe}^{3+}$  and  $\text{Fe}^{2+}$ , respectively), which couple ferromagnetically within the respective A or B layer. The exchange interaction between the layers is antiferromagnetic, leading to a net ferrimagnetic magnetization of  $4 \mu_B$  per formula unit. The Curie temperature at 850 K marks the transition from the ferrimagnetic to a paramagnetic phase<sup>84</sup>.

At low temperatures magnetite undergoes a structural and electronic phase transition at 125 K, the Verwey transition<sup>86,87</sup>. The lattice assumes a monoclinic structure, the electrical conductivity decreases by two orders of magnitude, and charge order ( $\text{Fe}^{2+}$  and  $\text{Fe}^{3+}$ ) emerges in the B layer. DFT calculations with an on-site Coulomb interaction  $U$  reproduced the charge order and in addition found  $t_{2g}$  orbital ordering of the  $\text{Fe}^{2+}$  cations<sup>91</sup>. A recent X-ray diffraction (XRD) and DFT study describes the charge order in magnetite below the Verwey transition as the formation of chains of three B cations sharing the addi-

tional electron in the  $\text{Fe}^{2+}$  site. The enhanced bonding of these three-atom entities leads to small lattice distortions which can be regarded as three-atom polaron-type quasiparticles, termed trimerons<sup>89</sup>. The magnetic structure of magnetite is also susceptible to temperature variations close to the Verwey transition. At room temperature, the magnetic easy axes align with the cube diagonals, the  $\langle 111 \rangle$  directions. When cooling through 130 K, the magnetic anisotropy undergoes a change of the easy axes to the cubic  $\langle 100 \rangle$  directions<sup>92</sup>. The reduced symmetry in the monoclinic phase causes the magnetic easy axis to align with the monoclinic c-axis<sup>92</sup>. At the surface, this change of the magnetic axis projected to the (001) plane has recently been observed in real space using spin-polarized low-energy electron microscopy (SPLEEM)<sup>93</sup>.

## 3.2 Surface properties

The low-index surfaces of  $\text{Fe}_3\text{O}_4$  have been intensively studied<sup>88</sup> due to their importance in technological applications, as well as for their interesting physical properties. A recent DFT study of the surface energies of  $\text{Fe}_3\text{O}_4$  constructing the Wulff-shape revealed that the {111}- and {001}-type surfaces correspond to the most stable low-index magnetite surfaces<sup>94</sup>. Although the stability trend agrees with experimental observations, it should be noted that the structural models in this study deviate from the experimentally observed structures. The (110) surface has also been prepared in experiments, which find a strong preference for faceting to expose {111} faces<sup>95</sup>. For the (111) surface, six different bulk-like terminations are possible, all of which correspond to so-called polar surfaces (type III in the classification by Tasker)<sup>96</sup>. Surfaces are referred to as polar if charge neutrality of the layers of the lattice is not fulfilled and the stacking sequence of the layers leads to the so-called “polar catastrophe”, i.e. the buildup of a dipole moment, increasing the electrostatic energy of the crystal with each additional layer. Therefore either reconstructed or partially occupied bulk-like terminations are expected for the  $\text{Fe}_3\text{O}_4(111)$  surface, in agreement with the observation of a strongly relaxed plane of  $\text{Fe}_{\text{tet}}$ , which is described as the regular termination in a review on iron oxide surfaces by Parkinson<sup>88</sup>.

### 3.2.1 $\text{Fe}_3\text{O}_4(001)$

The {001}-type surface planes correspond to the faces of the cube depicted in Figure 3.1; the (001) surface is the plane perpendicular to the c-axis, parallel to the top face of the cube. In a bulk-terminated scenario, two different surface terminations are possible: the B-layer ( $\text{Fe}_{\text{oct}}\text{O}_2$ ) or the A-layer termination, consisting only of  $\text{Fe}_{\text{tet}}$  atoms. If bulk-like oxi-

dation states are considered, both terminations result in polar surfaces (Tasker type III). The first atomically resolved STM images of the  $\text{Fe}_3\text{O}_4(001)$  showed undulating rows of Fe atoms along the  $\langle 110 \rangle$  directions, suggesting a B-layer termination<sup>97</sup>. The contrast obtained using a magnetic tip was interpreted as real-space observation of charge order in the surface<sup>98</sup>. Early structural models of the  $(\sqrt{2} \times \sqrt{2})\text{R}45^\circ$ -reconstructed B-layer surface were proposed on the basis of STM<sup>99</sup> or AFM<sup>100</sup> images and reconstructed LEED patterns. In these studies, polarity compensation was suggested to be achieved via ordered hydroxyl groups or oxygen vacancies. The idea of a charge-order-based B-layer termination was revisited by Mariotto *et al.* in a study using antiferromagnetic tips<sup>101</sup>. In 2005, Pentcheva *et al.* proposed a structural model for the B-layer termination based on a relaxed Jahn-Teller distortion of a bulk-terminated surface unit cell, depicted in Figure 3.2. This nominally polar surface structure was predicted to be stable by DFT-based *ab-initio* thermodynamics<sup>102</sup> and showed acceptable agreement in experimental quantitative structural analyses using surface X-ray diffraction<sup>102</sup> and LEED *IV*<sup>103</sup> (Pendry *R*-factor of 0.34). Thus it was broadly accepted as the correct surface structure, qualitatively explaining the experimental observations of the time. In the present thesis, this structural model is referred to as “distorted bulk truncation” (DBT). Łodziana refined the model by introducing DFT+*U* calculations<sup>104</sup>, leading to charge order in the subsurface rows of octahedrally coordinated Fe atoms, which form pairs of  $\text{Fe}^{2+}$  and  $\text{Fe}^{3+}$ . This so-called “surface Verwey transition” causes small undulations in the rows of surface Fe, which qualitatively agree with the undulating rows observed in STM images in the  $(\sqrt{2} \times \sqrt{2})\text{R}45^\circ$ -reconstructed unit cell. The surface reconstruction can be lifted thermally at 720 K, in an order-disorder transition to a  $(1 \times 1)$  structure, which has been observed using LEED<sup>105</sup>.

Under reducing conditions STM results show a different type of surface structure, which also presents the  $(\sqrt{2} \times \sqrt{2})\text{R}45^\circ$  symmetry but is typically associated with a polarity-compensated half-filled A-layer termination. Fe dimers and Fe(A) atoms are the dominant features on these surfaces, which are only created under very Fe-rich conditions, for example on magnetite thin films grown on an Fe buffer layer<sup>106</sup>. Recently, the thickness of the Fe buffer layer has been shown to critically influence the surface termination of  $\text{Fe}_3\text{O}_4(001)$  on Pt(100)<sup>107</sup>, leading to several metastable surface structures. A study on single crystals presents an improved structural model of this dimer-structure based on atomically resolved STM images of complete well-defined layers created by depositing Fe<sup>108</sup>.

The presented structural models provided a sufficient description of the  $\text{Fe}_3\text{O}_4(001)$  surface until, in 2012, the unique metal adsorption properties of this surface<sup>109</sup> were discovered. Au was found to adsorb in the form of isolated adatoms with the periodicity of the

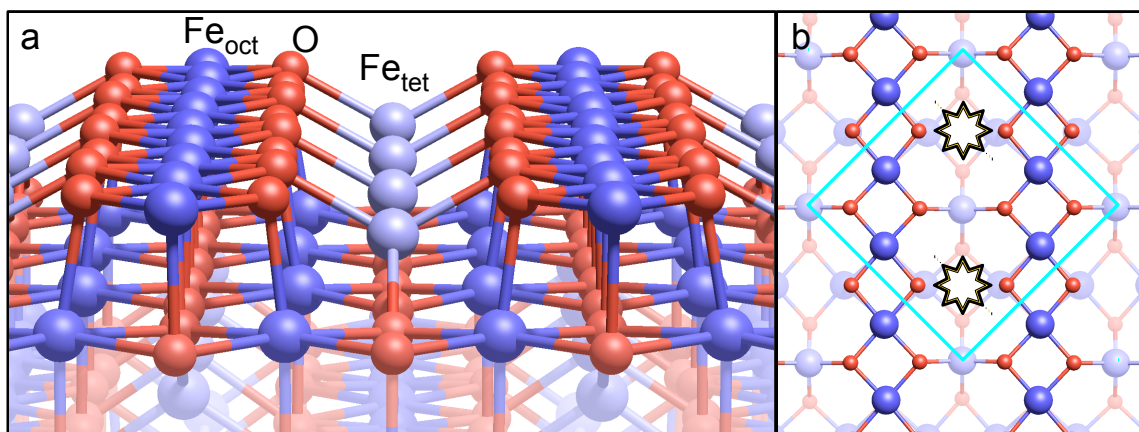


**Figure 3.2:** Distorted bulk truncation model of the  $\text{Fe}_3\text{O}_4(001)$  surface introduced by Pentcheva et al.<sup>102</sup> (a) Side view image along the  $[110]$  Fe row direction illustrating the different Fe sites of a force-relaxed structural model. (b) Top view: The cyan square indicates the reconstructed unit cell. The sites at the corners and in the center are blocked for metal adsorption by the subsurface  $\text{Fe}_{\text{tet}}$ , but the two oxygen bridging sites marked by the black stars are both available for the adsorption of two-fold coordinated metal adatoms.

$(\sqrt{2} \times \sqrt{2})\text{R}45^\circ$  reconstruction with a 100% preference for one of the two bulk continuation sites ( $\text{Fe}_{\text{tet}}$ ) of the reconstructed unit cell<sup>59</sup>, illustrated by the black stars in Figure 3.2(b). The adatoms assume a bridging configuration between two oxygen atoms at adjacent rows of  $\text{Fe}_{\text{oct}}$  in a site which is not blocked by a subsurface  $\text{Fe}_{\text{tet}}$ . Annealing experiments demonstrated the remarkable thermal stability of these Au adatoms<sup>59</sup>, which are resistant to agglomeration up to 700 K. Prior to the work presented in the present thesis, the room-temperature stability of metal adatoms was also demonstrated for deposited Pd and Fe<sup>60,108</sup>, which both also display the equivalent low-coverage site preference observed for Au. Pd shows high reactivity towards CO adsorption, which induces mobility and agglomeration at room temperature. Interestingly, Au was also found to adsorb in the form of adatoms under Fe-rich conditions on the Fe-dimer termination<sup>110</sup>. DFT+ $U$  calculations based on the distorted bulk truncation model successfully describe the strong adsorption of metal adatoms but fail to reproduce the preference for one adsorption site per unit cell. The adatoms show equivalent adsorption behavior in both available oxygen-bridging sites that are not blocked by a subsurface  $\text{Fe}_{\text{tet}}$ . This problem is resolved by the correct structural model for the surface<sup>111</sup>, the subsurface cation vacancy (SCV) structure, which is one of the central results of the present thesis. Using LEED IV, DFT (so-called *ab-initio* thermodynamics), and STM we determined the stable surface structure, which is based on an ordered array of cation vacancies and rearrangement of the subsurface Fe cations. An interstitial  $\text{Fe}_{\text{tet}}$  blocks one of the two favored adsorption sites in the distorted bulk trun-

cation model, explaining the observed adsorption behavior. The existence of Fe vacancies implies a more oxidized stoichiometry of the surface region, which is in good agreement with the formation of new surface area by O<sub>2</sub> dissociation and Fe diffusion upon exposure to O<sub>2</sub> at elevated temperatures ( $p_{O_2} \approx 10^{-6}$  Torr,  $T \approx 650^\circ\text{C}$ ) observed using LEEM<sup>112</sup>. The LEED IV, DFT (*ab-initio* thermodynamics), and STM results proving the subsurface cation vacancy model are described in full detail in section 4.1.

### 3.2.1.1 Spectroscopy

The more oxidized nature of the surface layer is also observed in PES experiments. In angle-resolved photoelectron spectroscopy (ARPES) a reduction in the intensity close to  $E_F$  is observed at strongly grazing emission angles<sup>113</sup>, indicating that the surface layer is depleted of Fe<sup>2+</sup> species which are commonly associated with this energy range<sup>114</sup>. The comparison of valence-band photoemission spectra acquired using ultraviolet light and soft X-rays (21.22 eV, 707.6 eV) for different surfaces also supports an Fe<sup>3+</sup>-rich surface region of the Fe<sub>3</sub>O<sub>4</sub>(001) surface<sup>115</sup>. A similar conclusion is drawn from a comparison of soft and hard X-ray photoelectron spectroscopy (HAXPES) in a recent study which highlights the different nature of Fe<sub>oct</sub> in the Fe<sub>3</sub>O<sub>4</sub>(001) surface region compared to the bulk<sup>116</sup>. The main focus of the HAXPES study, however, is the composition of the Fe 2*p* core levels for Fe<sub>oct</sub>, which are commonly assigned to Fe<sup>2+</sup> and Fe<sup>3+</sup> components<sup>117</sup>. The HAXPES results demonstrate that above the Verwey temperature all Fe<sub>oct</sub> can be modeled as one component of the spectrum, comprising Fe<sup>3+</sup> and considerable intensity of a charge transfer peak in bulk-sensitive spectra. The same study further provides information about the controversial nature of the Verwey transition regarding the existence of a gap in the electronic density of states, which is also discussed in many of the spectroscopic studies mentioned previously. The results at high probing depth indicate that magnetite is metallic rather than semiconducting above the transition temperature<sup>116</sup>, in contrast to the small gap suggested in previous studies<sup>115,118</sup> but in agreement with an early UPS study<sup>119</sup>. There are also several spectroscopic studies on adsorption on the Fe<sub>3</sub>O<sub>4</sub>(001) surface in the literature, which are discussed in the sections on related results.

## 4 Results

This chapter provides detailed information on metal adsorption at the reconstructed  $\text{Fe}_3\text{O}_4(001)$  surface and the interaction of the supported metals with gas molecules. Initially the subsurface cation vacancy structure of the  $\text{Fe}_3\text{O}_4(001)$  surface will be introduced. After a short overview over the observed types of adsorption behavior, the experimental results for each metal will be discussed in the context of the respective DFT calculations. Where possible, analogies will be drawn to metal adsorption and metal-gas interactions on different (reducible) substrates such as  $\text{CeO}_2$  or other iron oxide surfaces, in particular regarding single-atom catalysis results in the literature.

### 4.1 Surface structure of $\text{Fe}_3\text{O}_4(001)$

Prior to the work described in the present thesis, the accepted description of the  $(\sqrt{2} \times \sqrt{2})R45^\circ$ -reconstructed  $\text{Fe}_3\text{O}_4(001)$  surface was the polar distorted bulk truncation (DBT) model by Pentcheva *et al.*<sup>102</sup>, depicted in Figure 3.2. In the DBT model the surface reconstruction was based on subsurface charge order found in DFT+ $U$  calculations by Łodziana<sup>104</sup>. Here, the  $\text{Fe}_{\text{oct}}$  cations form alternating pairs of  $\text{Fe}^{2+}$  and  $\text{Fe}^{3+}$  in the subsurface  $\text{Fe}_{\text{oct}}\text{O}_2$  layers. The fair agreement of the structural model obtained using quantitative structural methods ( $R_p=0.34$  in LEED  $IV$ )<sup>102,103</sup> left room for improvement. The insufficient description of the  $\text{Fe}_3\text{O}_4(001)$  surface by this model became apparent when the strong site preference of highly stable Au adatoms<sup>59</sup> deposited onto this surface could not be reproduced in DFT calculations.

The search for the correct structural model was guided by the attempt to explain the preference for one of the two equivalent metal adsorption sites as well as the oxidized ( $\text{Fe}^{3+}$ -rich) nature of the  $\text{Fe}_3\text{O}_4(001)$  surface. Concerning the  $\text{Fe}^{3+}$ -rich surface region, it is important to note that the Fe oxides and hydroxides prefer to accommodate stoichiometry changes via the cation lattice<sup>84</sup>, in contrast to other oxides such as  $\text{TiO}_2$ , where the density of oxygen vacancies is varied to adjust to the environment for small degrees

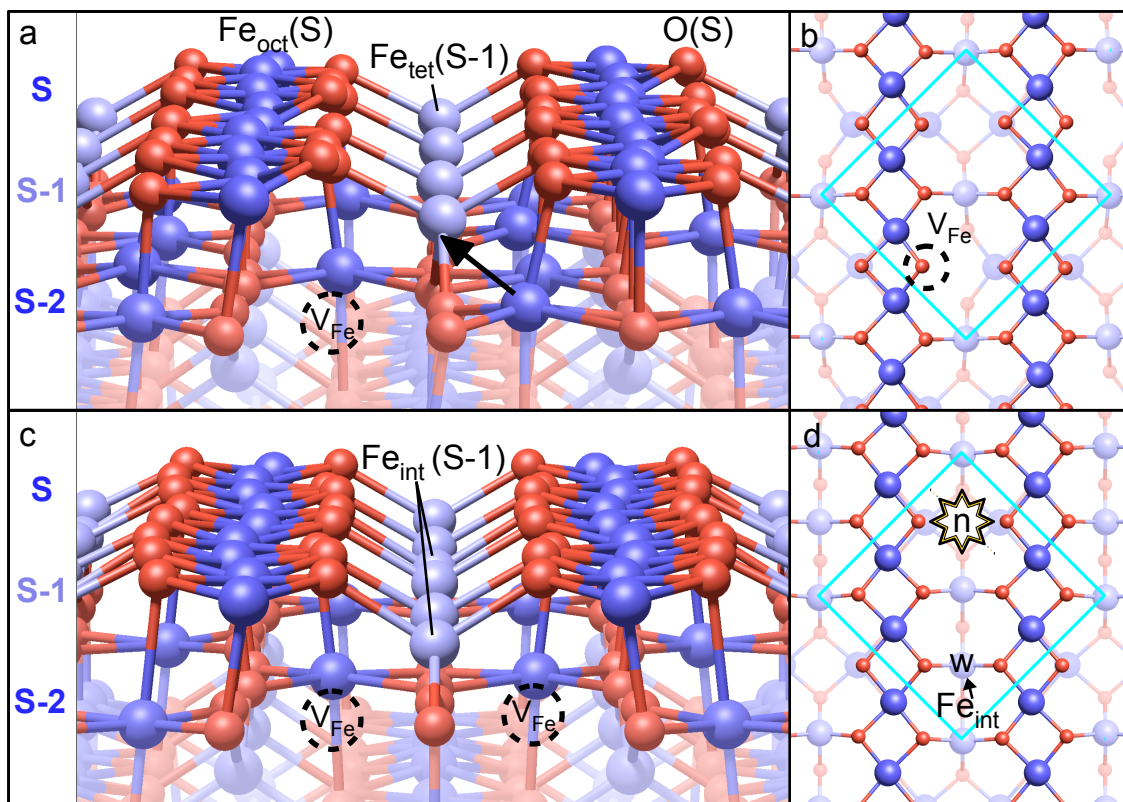


**Figure 4.1:** Structural models of the  $\text{Fe}_3\text{O}_4(001)$  surface. The layers are labeled  $(S-i, i \in \mathbf{N})$  starting at the surface  $\text{Fe}_{\text{oct}}\text{O}_2$  layer ( $S$ ).  $\text{Fe}_{\text{oct}}\text{O}_2$  and  $\text{Fe}_{\text{tet}}$  layers are considered as separate. (a,b) Force-relaxed model of a structure with one  $\text{Fe}_{\text{oct}}$  vacancy per unit cell (“maghemite-like” subsurface defect) in the subsurface B-layer ( $S-2$ ). The black arrow indicates the possibility of a neighboring  $\text{Fe}_{\text{oct}}$  to assume a tetrahedral coordination in the ( $S-1$ ) layer. (c,d) Subsurface cation vacancy structure<sup>111</sup>. The occupation of the tetrahedral site by  $\text{Fe}_{\text{int}}$  blocks metal adsorption in one of the two oxygen bridging sites of the bulk-terminated structure. The preferred adsorption site is marked by a black star and labeled “n” in the top view in panel (d).

of reduction<sup>8</sup>. The creation of Fe vacancies and interstitials in iron oxides is facilitated by the flexibility of the valence state of Fe ( $\text{Fe}^{2+}$ ,  $\text{Fe}^{3+}$ ). The oxygen-rich character of the  $\text{Fe}_3\text{O}_4(001)$  surface was established in the spectroscopy experiments described in section 3.2, and agrees with the fact that the typical surface preparation conditions partially extend into the stability range of  $\text{Fe}_2\text{O}_3$  in the iron-oxygen phase diagram<sup>120</sup>. The most stable iron oxide in oxidizing conditions is hematite ( $\alpha\text{-Fe}_2\text{O}_3$ ), which is based on a different type of oxygen sublattice structure (hcp instead of fcc stacking) than  $\text{Fe}_3\text{O}_4$ , hindering a facile transformation. While hematite is the thermodynamically more stable phase, maghemite ( $\gamma\text{-Fe}_2\text{O}_3$ ) maintains the spinel-type structure of magnetite, but vacancies are introduced into the  $\text{Fe}_{\text{oct}}$  lattice. Thus, upon initial oxidation, the formation of a maghemite

layer is a valid assumption, although the growth of hematite inclusions is known to occur in magnetite single crystals before measurable amounts of the crystal are transformed to maghemite<sup>112</sup>. Removing one  $\text{Fe}_{\text{oct}}^{2+}$  per unit cell from the first subsurface B-layer (the (S-2) layer) creates one “maghemite-like” defect, illustrated in Figure 4.1(a,b). This  $\text{Fe}^{3+}$ -rich configuration is stable in DFT+*U* calculations and keeps the periodicity of the reconstruction, but it creates one undercoordinated surface O atom per unit cell and causes an asymmetry between the two rows of surface Fe which is not observed in STM images. However, the oxide can attain an equal coordination number of all the surface oxygen atoms in a symmetrical configuration by a one-step rearrangement: The additional space created by the  $\text{Fe}_{\text{oct}}$  vacancy allows one neighboring  $\text{Fe}_{\text{oct}}$ (S-2) to migrate closer to the surface and assume a tetrahedral geometry as  $\text{Fe}^{3+}$  in the first subsurface  $\text{Fe}_{\text{tet}}$ (S-1)-layer (indicated by the arrow in Figure 4.1(a)), restoring a familiar bonding environment ( $\text{Fe}_{\text{oct}}$  or  $\text{Fe}_{\text{tet}}$ -like) for all atoms. The resulting structure depicted in Figure 4.1(c,d) is the stable, force-relaxed structural model of the correct surface structure, the so-called subsurface cation vacancy (SCV) structure<sup>111</sup>. The labels  $\text{Fe}_{\text{int}}$  in Figure 4.1(c,d) highlight the additional tetrahedral interstitial cation blocking adsorption in one oxygen-bridging site; the black star labeled “n” in the top view in panel (d) marks the preferred metal adsorption site. DFT+*U* calculations of a Au atom at the surface predict strong adsorption in the preferred site ( $E_B(\text{Au})=1.98$  eV, referenced to an isolated Au atom in vacuum,  $\Delta z_{\text{Au}-\text{FeB}}=0.70$  Å above the average surface  $\text{Fe}_{\text{oct}}$ , bond length  $d_{\text{Au}-\text{O}_S}=2.01/2.00$  Å), while the Au atom does not bond in the blocked site but moves away from the surface in *ab initio* force relaxations.

### DFT stability and *ab initio* thermodynamics

After initial DFT+*U* calculations had demonstrated the stability of the structure and the fact that it reproduces key experimental observations, such as the  $(\sqrt{2}\times\sqrt{2})\text{R}45^\circ$  reconstruction, the  $\text{Fe}^{3+}$ -rich stoichiometry, and the site preference in adsorption, further details of the structure were calculated. The presented DFT+*U* calculations of  $\text{Fe}_3\text{O}_4(001)$  were performed using WIEN2k<sup>80</sup> in a collaboration with Professor Peter Blaha. The  $\text{Fe}_3\text{O}_4(001)$  is modeled by a 17-layer symmetric slab of one  $(\sqrt{2}\times\sqrt{2})\text{R}45^\circ$ -reconstructed unit cell with a vacuum layer of  $\approx 13$  Å, using periodic boundary conditions. (A  $(2\times 2)$  slab corresponding to two reconstructed unit cells is used for most adatom calculations). The atomic radii of iron and oxygen were set to  $r_{\text{MT}}(\text{Fe})=1.86$  bohr ( $=0.98$  Å) and  $r_{\text{MT}}(\text{O})=1.5$  bohr ( $=0.79$  Å) in the adatom calculations and  $r_{\text{MT}}(\text{O})=1.15$  bohr ( $=0.61$  Å) in the *ab initio* thermodynamics comparing different structural models. The strong correlations of the Fe 3*d* electrons

are taken into account via GGA+ $U$  employing a Hubbard- $U$  of 3.8 eV for all Fe atoms. Owing to the large unit cell, a  $(3 \times 3 \times 1)$   $k$ -mesh represents a sufficient sampling of the reciprocal space. Basis functions up to a plane wave energy cut-off of  $\approx 23$  Ry ( $\approx 310$  eV) are included at the final level of convergence.

Since different structural models can have different stoichiometries, the stability of the models was compared via *ab initio* thermodynamics using the approach by Scheffler and Reuter<sup>121</sup>. *Ab initio* thermodynamics aims to provide a comparison of the surface energies of structural models with different stoichiometries (numbers of Fe and O atoms in the slab) at different temperatures and oxygen pressures. The approach describes the surface energy as a function of oxygen chemical potential and provides well-defined energies for the O<sub>2</sub>-rich and O<sub>2</sub>-poor limits (corresponding to the chemical potential of O in the O<sub>2</sub> molecule and at the point of decomposition of bulk Fe<sub>3</sub>O<sub>4</sub>, respectively). In the region of intermediate chemical potentials the energy curves of different terminations are approximated by lines connecting the respective values for high and low oxygen chemical potentials, since the exact solution is not accessible. This approach does not take into account phase changes to FeO or Fe<sub>2</sub>O<sub>3</sub>, which would occur under very reducing or oxidizing conditions, respectively. The surface energy diagram was originally calculated for the distorted bulk truncation and the subsurface cation vacancy model<sup>111</sup> together with Dr. Eamon McDermott, a PhD student in Professor Peter Blaha's group. In further calculations the surface energies of different terminations have also been assessed. Figure 4.2 shows a graph comparing the stability of a selection of different structural models as a function of the chemical potential of oxygen. In addition to the structures discussed above, the graph contains the surface energies of the following models: One Fe dimer per reconstructed unit cell on the SCV structure and on the DBT structure, one Fe adatom per unit cell on the SCV structure (labeled Fe(A)-terminated SCV structure), and a surface oxygen vacancy in the DBT structure. The oxygen vacancy was created in one of the oxygen sites, which are not coordinated to a subsurface Fe<sub>tet</sub>(S-1) atom, because removing this type of surface oxygen atom could also lead to a site preference in the metal adsorption behavior. However, all of these options are less favorable than the SCV structure under realistic conditions. The highly reducing conditions are accessible by deposition of Fe onto the surface, which can lead to Fe-terminated surfaces, which are thermodynamically not stable but stabilized by kinetic limitations in experiments<sup>108</sup>. The 0.5 ML-Fe<sub>tet</sub> termination has not been considered, since it was already discounted compared to the DBT model by Pentcheva *et al.*<sup>102</sup>.

One of the common initial considerations for proposed structural models is an analysis of the dipole moment created by the stacking of charged layers, i.e. the polarity of the

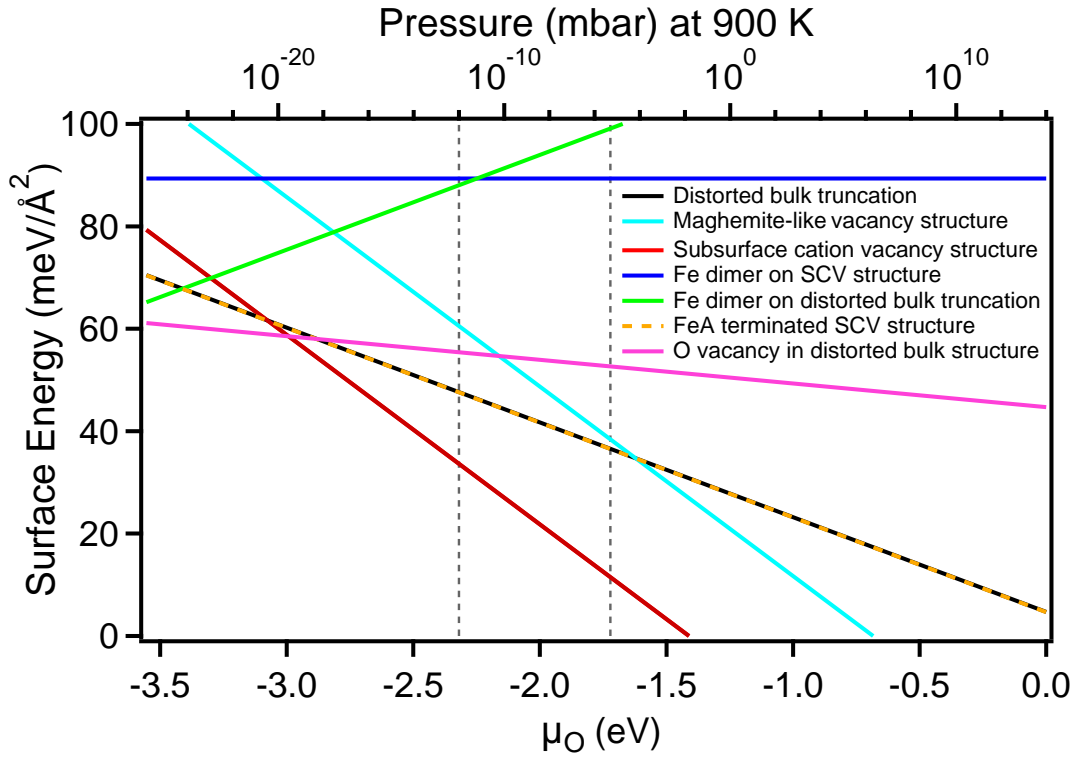


**Figure 4.2:** *Ab initio* surface phase diagram of different possible terminations of the  $\text{Fe}_3\text{O}_4(001)$  surface. The surface energy is plotted as a function of oxygen chemical potential, corresponding to the  $\text{O}_2$  pressures at 900 K on the top axis. The two vertical dashed lines indicate the range of UHV preparation conditions. Across the entire accessible pressure range, the subsurface cation vacancy model is the most favorable surface termination.

surface. Since polarity compensation was found to play an important role in the stability of many oxide surfaces<sup>96,122</sup>, it is interesting to assess the dipole moments in the SCV structure. The case of magnetite is particularly interesting, because its metallic nature at temperatures above the Verwey transition provides the opportunity to rearrange charges in the surface. Therefore the DFT-derived oxidation states rather than bulk-like ionic charges should be considered to determine the surface polarity. The comparison of the bulk-like and the DFT-derived charge states and the resulting stacking of charged layers are shown in Figure 4.3. The DFT+ $U$  calculations determine the Fe cations in the first three layers to be  $\text{Fe}^{3+}$ , which is in good agreement with the oxidized surface observed in spectroscopy studies. In addition, the two surface oxygen atoms adjacent to the preferred adsorption site exhibit a nonzero magnetic moment ( $0.35 \mu_B$ ), indicating that they assume the unusual charge state of  $\text{O}^{1-}$ . These modified charges sum to  $-2q$ ,  $+9q$ , and  $-10q$  per reconstructed unit cell for the surface and the first subsurface  $\text{Fe}_{\text{tet}}$  and  $\text{Fe}_{\text{oct}}\text{O}_2$  layers ( $q$  is one positive elementary charge unit), respectively, continued with the bulk-like  $+6q$  ( $2 \times \text{Fe}_{\text{tet}}^{3+}$ ) and

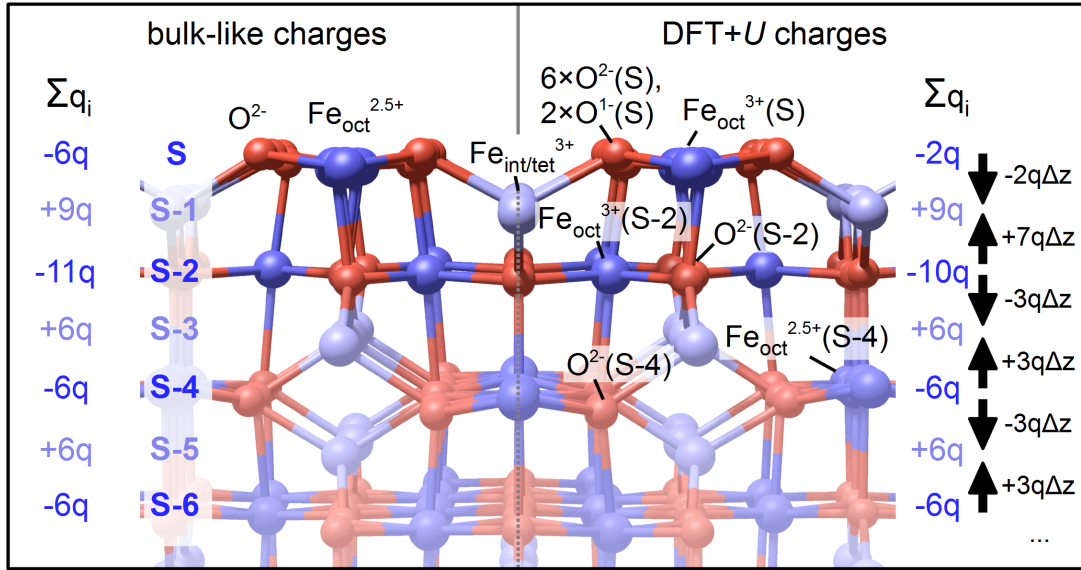


**Figure 4.3:** Illustration of the charged layer stacking of the SCV structure using bulk-like and DFT-derived charge states. The values of the bulk-like charge states are equivalent for all atoms in the slab, while the calculated charges show enrichment of  $\text{Fe}^{3+}$  in the surface region and two  $\text{O}^{1-}$  species per unit cell. The labeled arrows at the right end of the image illustrate the respective dipole moments, resulting in a polarity compensated stacking with a residual dipole moment at the surface. The bulk-like charges would result in a polar stacking of the charged layers.

$-6q$  ( $4 \times \text{Fe}_{\text{oct}}^{2.5+} + 8 \times \text{O}^{2-}$ ) stacking. In the simple model of equidistant charged planes, this leads to dipole moments of  $2q \times \Delta z$  (between surface and first  $\text{Fe}_{\text{tet}}$ -layer) and  $-7q \times \Delta z$  (between the remaining charge in  $\text{Fe}_{\text{tet}}$ -layer and the  $\text{Fe}_{\text{oct}}$ -layer with vacancies) per unit cell in the first two layers. In the subsurface layers below, a compensated (Tasker type II)<sup>96</sup> stacking is possible: Starting from the remaining charge of  $-3q$  ( $= -10q + 7q$ ) in the  $\text{Fe}_{\text{oct}}$ -layer with vacancies, the stacking of  $+6q$  and  $-6q$  is compensated, leaving only a finite dipole moment in the surface region. In a simplified alternative approach, the charges of the first three layers are considered as part of one single layer (summing to  $-3q$ ), which would again result in a polarity compensated stacking ( $-3q$ ,  $+6q$ ,  $-6q$ ,...). In this approximation, the different layer spacing close to the surface also gives rise to a finite dipole moment in the surface region. In the common approach to assume bulk-like ionic charges for all constituent atoms (in this case  $\text{Fe}_{\text{oct}}^{2.5+}$ ,  $\text{Fe}_{\text{tet}}^{3+}$ , and  $\text{O}^{2-}$ ), the result would be an uncompensated polar stacking ( $-6q$ ,  $+9q$ , and  $-11q$  in the surface and first two subsurface layers, respectively, followed by a sequence of  $+6q$ ,  $-6q$ ). This analysis emphasizes the importance of *ab initio* calculations for correct conclusions in the determination of surface structures.

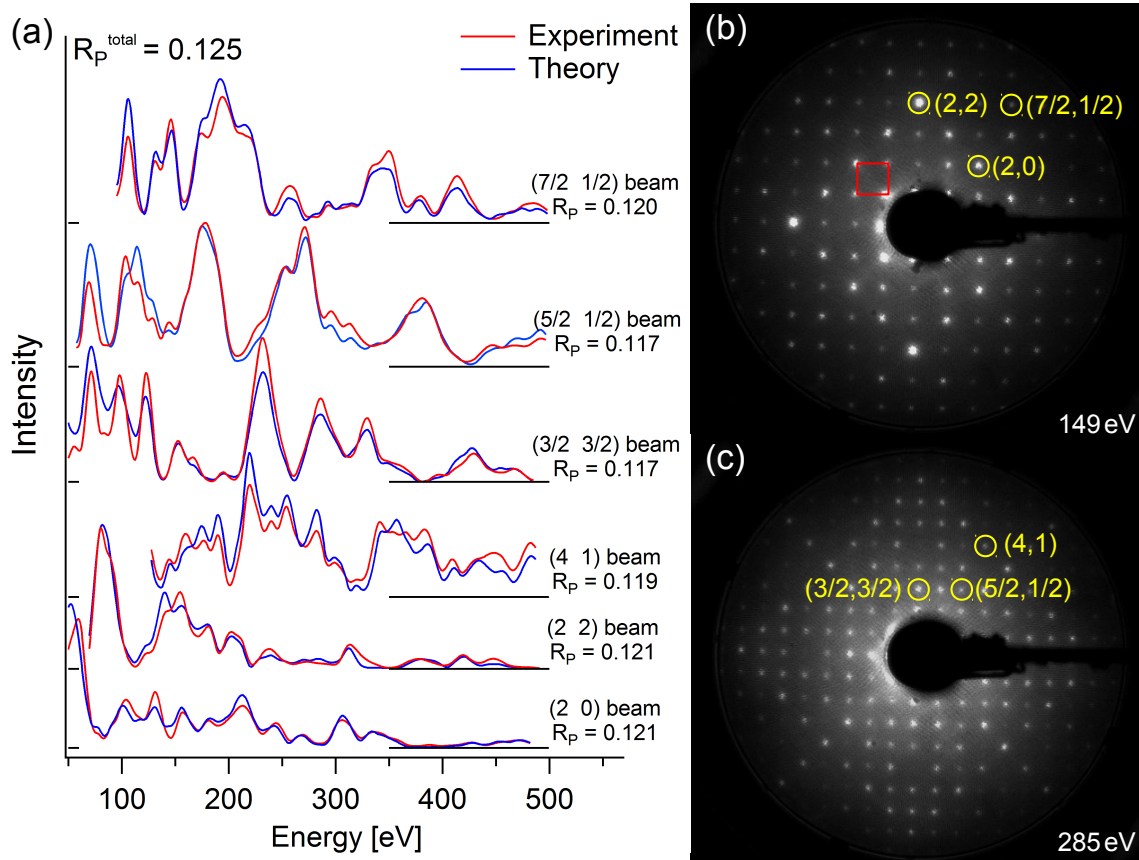


**Figure 4.4:** Results of the LEED IV study<sup>111</sup>. (a) Representative examples of LEED IV intensity curves with an  $R_p$  comparable to the total one. (b,c) Reconstructed LEED patterns at 149 eV and 285 eV. The red square indicates a reconstructed unit cell. The spots highlighted by yellow circles correspond to the intensity curves in (a). From *Science* 346, 1215 (2014)<sup>111</sup>. Reprinted with permission from AAAS.

### Experimental proof: LEED IV

The promising DFT results encouraged the attempt for quantitative experimental structure determination using LEED IV. In LEED IV the intensity of the diffraction spots is recorded as a function of the electron energy and simulated using dynamic scattering theory implemented in specialized code packages. The measurements were performed in collaboration with the LEED IV group at the University of Erlangen-Nürnberg in Erlangen with Dr. Lutz Hammer and Pascal Ferstl using a specialized UHV setup for LEED studies, equipped with standard preparation facilities and an STM. In LEED experiments, the quality of the diffraction patterns benefits from low temperature measurements, increasing the importance of fast data acquisition and low residual gas pressures. Several LEED datasets were acquired on a synthetic  $\text{Fe}_3\text{O}_4(001)$  single crystal (#357) above and

below the Verwey transition but no discernible difference was found. The data analysis was performed mainly in Vienna using the programs AIDA (Ee2010) to follow the individual LEED spots and record the intensity as a function of electron energy. IgorPro was employed to process the acquired intensity curves (smoothing, normalizing) and correct for variations in the beam intensity using curves recorded on background LEED movies. In total 40 independent LEED intensity curves were recorded, amounting to a total data set of 11 308 eV. The simulation and fitting procedures were performed by the collaboration partners in Erlangen using the TensErLEED program package<sup>123</sup>. Figure 4.4 shows examples of experimental and simulated LEED *IV* curves (a) and LEED patterns at 149 eV and 285 eV (b,c), in which the diffraction spots corresponding to the curves are highlighted. In the fitting of the structural models 59 geometrical and 5 vibrational parameters were employed, resulting in a redundancy factor of the data of 8.3, which excludes any overfitting. The fit quality in LEED *IV* is usually assessed via the Pendry reliability factor<sup>67</sup>  $R_P$  ( $0 \leq R_P \leq 2$ ), a number determining the correlation of the fit and the experimental data ( $R_P = 0$  corresponds to identical,  $R_P = 1$  to uncorrelated,  $R_P = 2$  to anticorrelated curves). The final *R*-factor of  $R_P = 0.125$  corresponds to very good agreement, providing a clear proof of the structural model. Furthermore, the absolute difference between LEED and DFT coordinates does not exceed 0.08 Å for any atom. A recent surface X-ray diffraction study shows very good agreement with the LEED and DFT coordinates of the SCV structure and thus provides additional confirmation for this structural model<sup>124</sup>.

## Electronic structure

The SCV surface reconstruction exhibits several interesting aspects regarding the electronic structure of the surface. Figure 4.5 shows plots of the spin-resolved electronic density of states of the entire 17-layer slab and the partial density of states for different components of the slab. In (a) the contributions of oxygen and iron to the total DOS are identified, while (b) shows the individual contributions of the surface and bulk-like layers of iron. The sketch in the bottom-right corner of (b) illustrates the labels for the different layers introduced in Figure 4.1. The DOS of the entire slab is fully spin-polarized (spin-down) in a broad energy range straddling the Fermi level ( $E_F \pm 1$  eV), where the electronic states are clearly dominated by Fe. The peak below  $E_F$  corresponds to Fe<sup>2+</sup>-like states<sup>114</sup>, which are not present in the outermost six layers ( $S$  to  $(S-5)$ ). The unoccupied spin-up Fe DOS consists entirely of Fe<sub>tet</sub> states, showing the ferrimagnetic order in the magnetite lattice. The states of the O<sup>1-</sup> atoms (not shown) contribute to the whole spectrum of oxygen DOS but their main intensity is located in the two first peaks in the occupied spin-up DOS (at

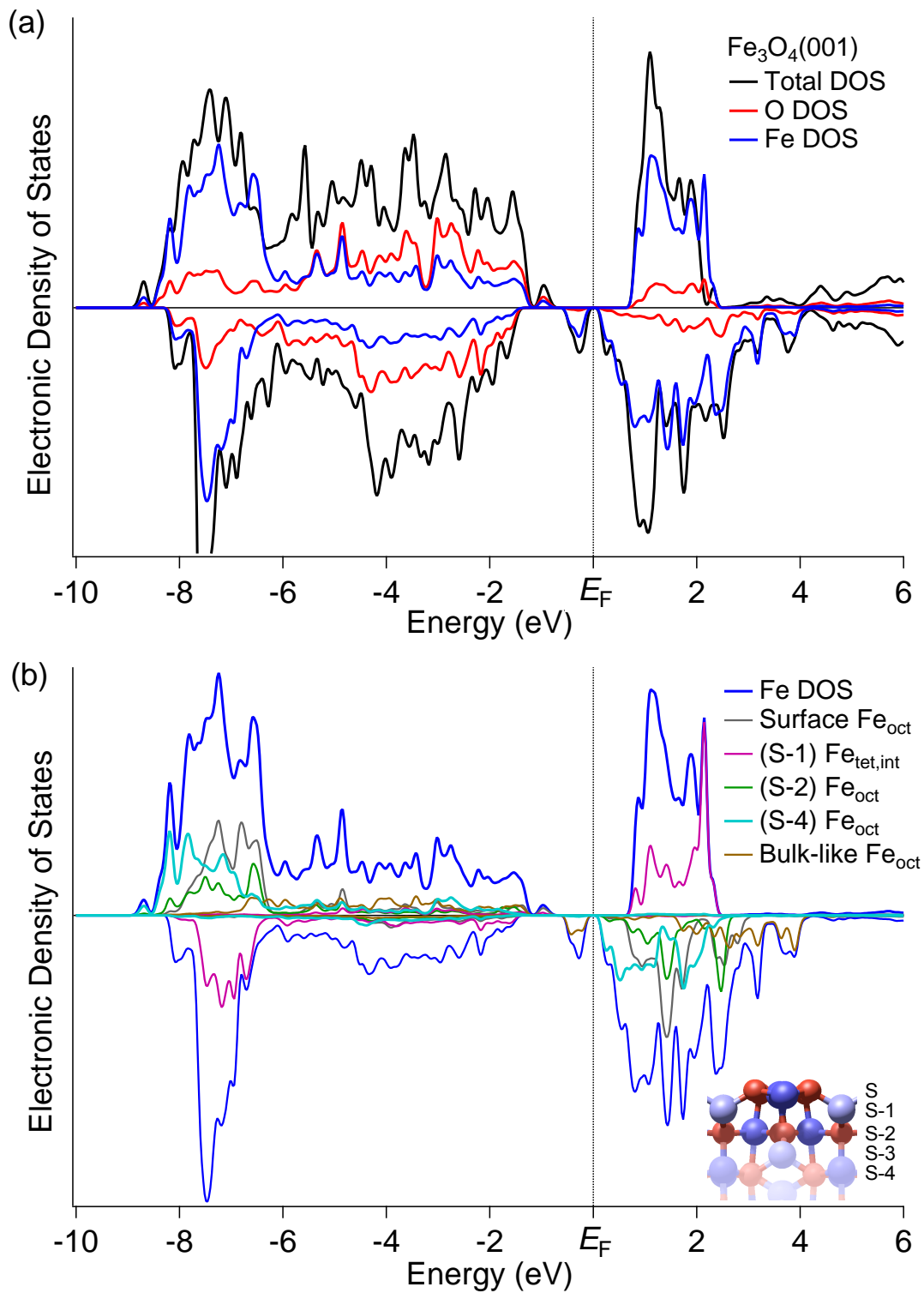


**Figure 4.5:** Density of states of the SCV reconstructed  $\text{Fe}_3\text{O}_4(001)$  surface. (a) Total, iron, and oxygen DOS. (b) Contributions to the Fe DOS from different layers. The inset in (b) explains the labeling of the layers.

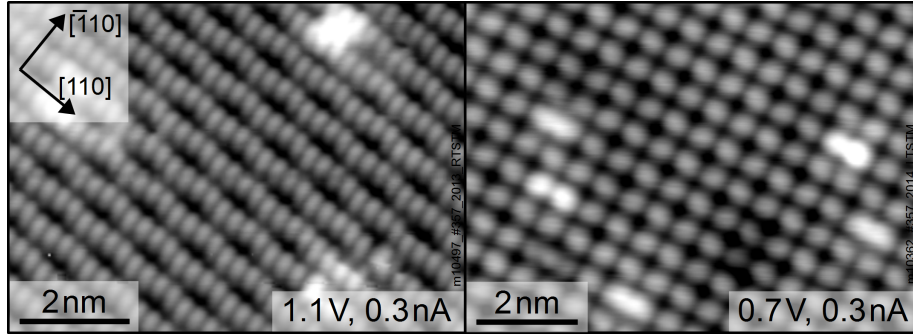


**Figure 4.6:** STM images of the  $\text{Fe}_3\text{O}_4(001)$  surface at common scanning conditions. (left) Atomically resolved surface layer, undulating rows of surface Fe. (right) Common contrast: One elongated protrusion corresponds to two Fe atoms. Here, the direction of the Fe rows is the  $[110]$  direction, parallel to the bright, elongated defect features.

$E_B \approx 1$  eV and 1.5 eV) and at 2.5 eV in the unoccupied spin-down DOS. The total DOS of the slab exhibits negligible but nonzero intensity at the Fermi energy. However, the electronic structure in this region is highly sensitive to changes of the Hubbard- $U$  parameter ( $U_{eff} = 3.8$  eV in the presented data): Increasing or decreasing the value of  $U_{eff}$  by 1 eV leads to an unambiguous gap ( $\Delta E \approx 140$  meV for  $U_{eff} = 4.8$  eV) or clear half-metallicity in the case of  $U_{eff} = 2.8$  eV, respectively.

### STM and electronic effects

The electronic structure of the surface has also been probed using STM. The broad range without any electronic states of oxygen around the Fermi level indicates that Fe atoms are imaged. This is in agreement with the first atomically resolved STM images of the  $\text{Fe}_3\text{O}_4(001)$  surface, which were acquired in 1992 and interpreted as rows of B-layer  $\text{Fe}_{\text{oct}}$  atoms<sup>98</sup>. Examples of STM images of the clean surface at two different common tip conditions are provided in Figure 4.6. Figure 4.6(a) shows an atomic-resolution image of the undulating rows of protrusions corresponding to individual surface  $\text{Fe}_{\text{oct}}$  atoms, whereas at the contrast in Figure 4.6(b) the protrusions correspond to pairs of surface  $\text{Fe}_{\text{oct}}$  atoms. In the latter case, the row direction is indicated by the direction of elongation of the defect features (bright protrusions on the rows of surface Fe, explained in section 4.1.1). Interestingly, the undulations observed at voltages near  $U_{\text{sample}} = +1$  V do not follow the surface topography of the reconstruction but are in fact exactly opposite: In the preferred adsorption site, where the spacing between two rows of surface Fe is larger in the structural model depicted in Figure 4.1, the Fe atoms appear to be closer to each other in STM images, equivalent with an apparent relaxation away from  $\text{Fe}_{\text{int}}$ . Since the voltage range

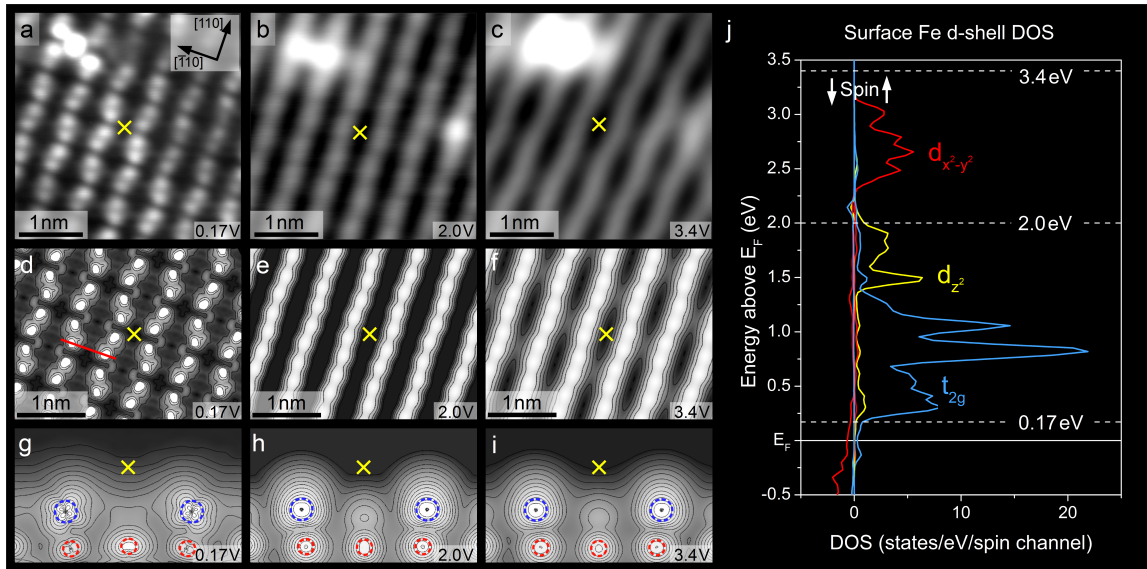


**Figure 4.7:** Electronic effects in empty-state STM images of the  $\text{Fe}_3\text{O}_4(001)$  surface: The undulations in the rows of surface Fe observed in experimental (a-c) and simulated (d-f) STM images are weakened and change phase when the sample bias is increased from +0.17 V in constant height mode (a) to +2 V and +3.4 V in constant current mode at 0.15 nA (b,c). The yellow  $\times$  marks one site in each experimental image, referenced to an Fe adatom in the top left corner, and the equivalent site in the simulated STM images (d-f). The red line in (d) indicates the position used for charge density contour plots (g-i) at energies corresponding to the bias voltages. These contour plots and the Fe 3d DOS (j) explain the observed behavior as a transition from a tilted, asymmetric configuration at low bias (g) to more spherically symmetric charge distributions when additional Fe 3d orbitals become available (h,i). From *Science* 346, 1215 (2014)<sup>111</sup>. Reprinted with permission from AAAS.

near  $U_{\text{sample}}=+1$  V corresponds to common stable scanning conditions the sites of maximum and minimum apparent distance between the surface Fe rows were called wide (“w”) and narrow (“n”) sites of the reconstruction. The specifications “narrow” and “wide” were established before the SCV structure was discovered, rendering them an inadequate description of the preferred metal adsorption site and the site blocked by  $\text{Fe}_{\text{int}}$ , respectively. In the present thesis the labels “n” and “w” will be retained in order to avoid confusion, but their interpretation will be changed to “no  $\text{Fe}_{\text{int}}$ ” and “with  $\text{Fe}_{\text{int}}$ ”. The observed reversal between topography and STM images is a good example of a strong effect of electronic structure in STM, summarized by Figure 4.7<sup>111</sup>(reprinted with permission from AAAS). A series of subsequent STM images at different bias voltages (a-c) was acquired in the same location at the surface, illustrated by the Fe adatom in the top left corner, which serves as a marker. The same preferred metal adsorption site is highlighted by a yellow “ $\times$ ” symbol in each image. A comparison of the images reveals a reproducible reversal

of the undulations of surface Fe atoms when varying the bias voltage: At low tunneling bias ( $U_{\text{sample}}=+0.17$  V, constant height mode) the Fe atoms appear closer to the yellow “×”, whereas straight rows are imaged at +2 V and a further shift away from the marker is observed for +3.4 V (both images at a constant current of 0.15 nA). The same behavior is observed in the corresponding simulated STM images in Figure 4.7 (d-f), in which an equivalent site is also marked by a yellow “×”. The Fe 3*d* states plotted in Figure 4.7 (j) (spin down) are the dominant electronic states contributing to the tunneling current in the energy range close to the Fermi energy and thus determine the structure observed in STM images. Up to  $\approx 1.5$  V, only the Fe  $t_{2g}$  states are imaged, while the  $e_g$ -type states become accessible only with increasing voltage. The surface  $\text{Fe}_{\text{oct}}^{3+}$  atoms occupy lattice sites in which the bonding environment is distorted by the relaxations in the surface layer. The consequence for STM images is illustrated in the charge density plot in Figure 4.7 (g), portraying a cut of the charge density at +0.17 eV in the plane indicated by the red line in (d): The orbitals are tilted and thus point away from  $\text{Fe}_{\text{int}}$  and towards each other in the preferred adsorption site. With increasing bias voltage, additional Fe 3*d* states contribute to the tunneling current and the sum of the surface Fe orbitals approaches a spherically symmetric distribution (4.7 (h,i)). This trend leads to a smaller amplitude of the undulations in STM images at +2 V (Figure 4.7 (b,e)). Finally, at  $U_{\text{sample}}=+3.4$  V (Figure 4.7 (c,f)), all orbitals contribute to the tunneling current and the rows of surface Fe observed in STM images follow the direction of the surface relaxation. Thus, the Fe positions in the STM images at higher bias voltages are closer to the surface topography. However, since the most stable scanning conditions and the best resolution can be achieved at lower bias voltages, the majority of STM images are acquired in the range of +0.7 V to +2 V.

#### 4.1.1 Surface defects and dopants

Surface defects can play an important role in the surface properties observed in experiments, such as providing nucleation sites or promoting reactivity. One of the most common defects on the  $\text{Fe}_3\text{O}_4(001)$  surface, a surface hydroxyl group ( $\text{O}_\text{S}\text{H}$ ), was identified by dosing atomic hydrogen<sup>125</sup>. On  $\text{Fe}_3\text{O}_4(001)$ , the adsorption of hydrogen modifies the density of states of the two adjacent surface  $\text{Fe}_{\text{oct}}$  atoms, giving them an  $\text{Fe}^{2+}$ -like character, as shown by UPS and XPS. This change in the local density of states is observed in STM images as a bright double protrusion on the adjacent row of surface Fe; an example is shown in Figure 4.8(a). At room temperature, the adsorbed hydrogen atoms are mobile, but their mobility is restricted to hopping between two surface Fe rows across the preferred metal adsorption site<sup>125</sup> created by the surface reconstruction (labeled “n” for “no  $\text{Fe}_{\text{int}}$ ”

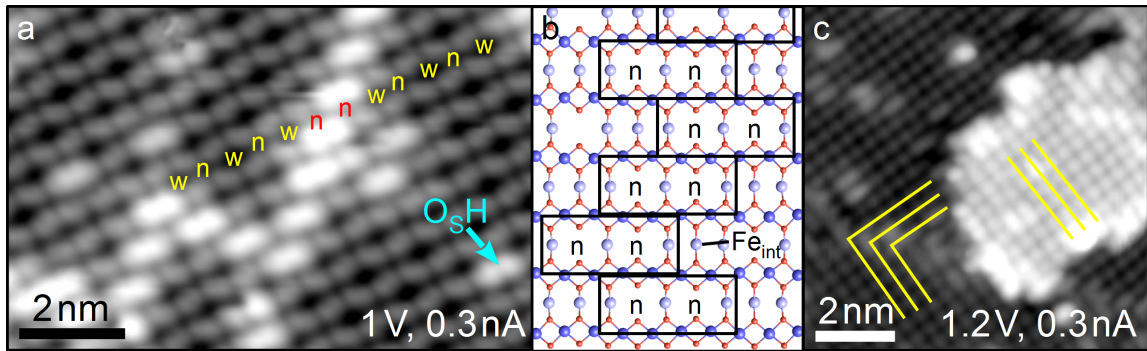


**Figure 4.8:** STM images of defects on the  $\text{Fe}_3\text{O}_4(001)$  surface. (a) Surface hydroxyl groups ( $\text{O}_\text{SH}$ ) appear as bright protrusions<sup>125</sup> on the rows of  $\text{Fe}_{\text{oct}}$ . An example is highlighted by the cyan arrow. A second type of defect, an antiphase domain boundary (APDB) in the reconstructed B-layer appears as chain of bright features on the surface Fe rows. The labels “n” and “w” denote the preferred adsorption site and the blocked site in the surface reconstruction, respectively (no  $\text{Fe}_{\text{int}}$  and with  $\text{Fe}_{\text{int}}$ ). The labeling indicates that the APDB creates two neighboring “n” sites<sup>126</sup>, which is also illustrated in the schematic top view in (b). The dark blue atoms represent surface  $\text{Fe}_{\text{oct}}$ , the light blue atoms  $\text{Fe}_{\text{tet}}(\text{S-1})$ , and the red atoms oxygen. (c) Screw dislocation at a single step: The yellow lines mark the row direction, which changes when crossing a domain boundary and remains parallel when ascending the step from the bottom part of the image.

in Figure 4.8). Therefore it can be used to distinguish these sites from the blocked sites (labeled “w” for “with  $\text{Fe}_{\text{int}}$ ”) in the case of an unfavorable tip condition.

Another common surface defect is related to the surface reconstruction: the antiphase domain boundary<sup>126</sup>. When the surface reconstruction nucleates during cooling through the high-temperature transition<sup>105</sup>, the surface reconstruction is formed. The undulations created by the reconstruction result in a different appearance of the sites with an interstitial  $\text{Fe}_{\text{int}}$  (“w”) and the sites with no  $\text{Fe}_{\text{int}}$  (“n”) (labelled in Figure 4.8(a), inspired by the figure by Parkinson *et al.*<sup>126</sup>). If the reconstruction nucleates and grows starting from two locations that are offset by one ( $1 \times 1$ ) surface unit cell, two adjacent sites of the same type will meet, forming a so-called antiphase domain boundary (APDB) of the reconstruction. In experiment, exclusively pairs of “n” sites are observed to meet<sup>126</sup>. The alternative case of two adjacent “w” sites, both blocked by an interstitial  $\text{Fe}_{\text{int}}$ , would lead to a patch of four Fe vacancies in the subsurface  $\text{Fe}_{\text{oct}}$  (S-2) layer, resulting in undercoordinated (two-fold) oxygen atoms, which is likely a highly unfavorable configuration. Figure 4.8(b) illustrates the surface configuration along an APDB in a top-view structural model, showing pairs of “n” sites.

Further defects include Fe adatoms, unit cells with incorporated Fe atoms, and impurities. Fe adatoms are not only created by Fe deposition but can also be intrinsic (usually at

very low coverage). Their apparent height of  $\approx 65\text{-}80$  pm (at 1 V, 0.3 nA)<sup>109</sup> is significantly lower compared to other metal adatoms such as Au ( $\approx 100$  pm)<sup>109</sup>, which makes Fe adatoms easy to distinguish from most deposited metals. Another type of defect is created by the incorporation of an Fe atom into one of the subsurface vacancies while the second vacancy is filled by Fe<sub>int</sub>, corresponding to a single unreconstructed surface unit cell. In STM images, this defect appears as two bright protrusions on neighboring Fe rows, resembling two adjacent surface hydroxyl groups. Further similar bright features on the rows of surface Fe are ascribed to impurity metal atoms in the surface or subsurface layer. For example, Ca and K contaminants have been reported to segregate to the surface and lead to restructuring to a  $p(1\times 4)$  missing-row reconstruction<sup>127</sup>. Similar effects were observed for Mg segregation<sup>128</sup> through Fe<sub>3</sub>O<sub>4</sub>(001) films on MgO(001). The last defect described here, the screw dislocation, is commonly observed on thin-film samples<sup>107</sup> and involves at minimum two Fe<sub>oct</sub>O<sub>2</sub> layers: Local errors in the layer stacking allow for single steps which connect a single inclined terrace to itself, marked by the lack of the typical 90° rotation of the Fe row direction when ascending a step. The balancing counterpart of this defect caused by a screw dislocation is a type of domain boundary involving the rotation of the row direction by 90° on a continuous terrace (both features illustrated in Figure 4.8(c)). The height of the dislocation steps can vary between different locations on the surface and often deviates from the correct step height of the Fe<sub>3</sub>O<sub>4</sub>(001) surface (2.1 Å). In room-temperature studies on bulk single crystals these defects are usually not observed. However, on a synthetic single crystal (#357), which was frequently used at room temperature over a period of years, a high density of screw dislocations ( $\geq \frac{1}{50\times 50\text{nm}^2}$ ) developed during a series of STM experiments at 78 K using equivalent preparation conditions to the room-temperature study. Thus, the formation of screw dislocations may be related to the lattice distortions involved in the Verwey transition<sup>86</sup> to a monoclinic structure.

## 4.2 Metal adsorption

### 4.2.1 Single metal adatoms and their stability

The study of metal adsorption at the Fe<sub>3</sub>O<sub>4</sub>(001) surface is mainly motivated by the property of the surface to stabilize isolated metal adatoms at elevated temperatures. At room temperature, most metals deposited onto this surface form stable adatoms, which adsorb in a two-fold coordination to oxygen in the preferential adsorption site created by the surface reconstruction (see Figure 4.1(d)). Nevertheless the adatom configuration does not represent the thermodynamic equilibrium for any metal. If sufficient additional energy is

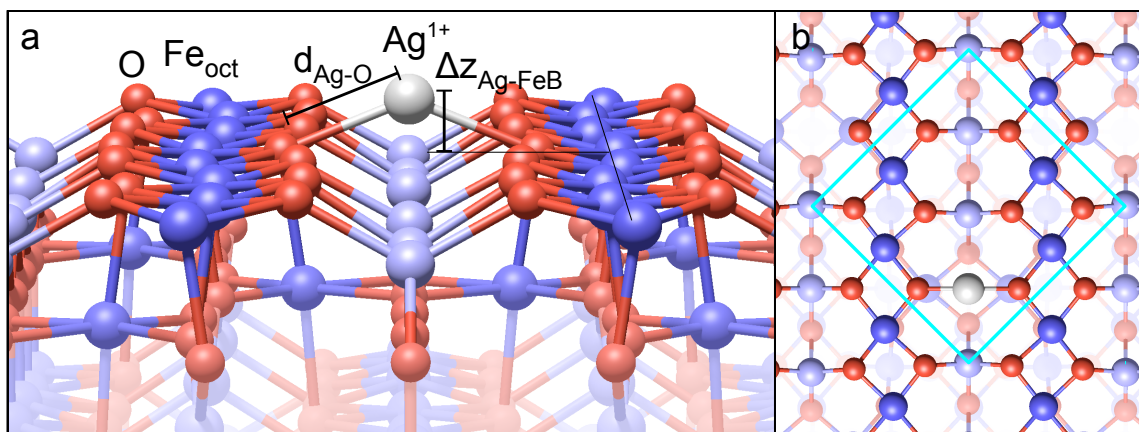


**Figure 4.9:** Adsorption geometry of a Ag adatom: (a) The cationic Ag adatom occupies the preferred adsorption site. The labeled length indicators correspond to the Ag-O bond length ( $d_{\text{Ag-O}}=2.08 \text{ \AA}$ ) and the height above the average surface  $\text{Fe}_{\text{oct}}$  ( $\Delta z_{\text{Ag-FeB}}=0.97 \text{ \AA}$ ). (b) The top view shows that no further equivalent adsorption site is available within the surface unit cell (cyan square).

provided (e.g. by annealing Au to temperatures exceeding 700 K) or a metal-specific critical local coverage is exceeded, the metals transition into an energetically more favorable configuration. Depending on the chemical element, the metals prefer one of two observed final states: They either form metal nanoparticles, which is common on many oxide materials<sup>10</sup>, or a solid solution with  $\text{Fe}_3\text{O}_4$  via incorporation into the surface region, forming a sub-stoichiometric spinel ferrite  $\text{M}_x\text{Fe}_{3-x}\text{O}_4$ . The surface reconstruction based on one Fe vacancy per reconstructed surface unit cell provides one site for the incorporation of metal atoms, either by directly filling the vacancy or by displacing a surface Fe atom. In both cases of incorporation, the second  $\text{Fe}_{\text{oct}}$  vacancy is filled by the interstitial tetrahedral iron atom  $\text{Fe}_{\text{int}}$ , locally lifting the surface reconstruction. In the case of a preference for nanoparticle formation, important parameters such as the critical cluster size, the bond strength of the metal adatom to the oxide, and the interaction strength with gas molecules depend on the specific chemical element considered. In order to describe these two different types of adsorption and stability in detail, the first two metals presented in this section will be Ag, a prototypical noble metal, which does not incorporate, and Ni, which forms adatoms at room temperature, but prefers to form solid solution with  $\text{Fe}_3\text{O}_4$ .

#### 4.2.2 Silver

Silver is a promising material for noble metal single-atom catalyst studies, since it has been reported to be active for different reactions, such as dehydrogenation<sup>129</sup> and ep-

oxidation reactions<sup>130</sup>. In particular the observation of size effects in the sub-nanometer regime in the epoxidation of propylene<sup>131</sup> catalyzed by silver motivates the study of the single-atom properties of Ag at the Fe<sub>3</sub>O<sub>4</sub>(001) surface.

#### 4.2.2.1 Silver adsorption

The deposition of silver onto the Fe<sub>3</sub>O<sub>4</sub>(001) surface at room temperature results in single Ag adatoms<sup>132</sup> occupying the preferred metal adsorption site in the reconstructed unit cell, similar to the previous observations for Au<sup>59</sup> and Pd<sup>60</sup>. Figure 4.9 illustrates the force-relaxed adsorption geometry of a Ag adatom. Since the bridging configuration two-fold coordinated to oxygen is common to all metal adatoms described in the present thesis, this image of Ag will serve as an example for all metals. The two length indicators labeled in Figure 4.9(a) correspond to the bond length of Ag to the surface oxygen atom ( $d_{Ag-O}=2.08 \text{ \AA}$ ) and the height above the average Fe<sub>oct</sub> in the surface layer ( $\Delta z_{Ag-FeB}=0.97 \text{ \AA}$ ) derived from DFT+*U* calculations. These two parameters are determined for each metal adatom considered in the DFT study of metal adsorption, allowing a quantitative comparison of the different metals. Further characteristic parameters include the adsorption energies ( $E_{ads}(Ag)=1.85 \text{ eV}$  (SCV model),  $E_{ads}(Ag)=1.44 \text{ eV}$  (DBT model<sup>132</sup>, for a  $(2 \times 2 \times 1)$  *k*-mesh, 163 eV plane-wave cutoff)) and the charge transfer to the substrate, described by the nominal valence state of the adatom (Ag<sup>1+</sup>, with a spherically symmetric electron distribution indicating a  $5s^0 4d^{10}$  configuration). The calculations of the Ag adatom on the SCV model were performed using an atomic radius of  $r_{Ag}=2.1 \text{ bohr}=1.11 \text{ \AA}$ , a  $(3 \times 3 \times 1)$  *k*-mesh, a plane-wave cut-off energy of  $\approx 183 \text{ eV}$ , and no Hubbard-*U* correction for Ag.

Ag is an ideal metal to demonstrate the concept of the Fe<sub>3</sub>O<sub>4</sub>(001) adsorption template, because the adatom coverage that can be obtained without creating clusters is substantially higher than for many other metals, including Au. Figure 4.10 illustrates that at an adatom coverage of 0.51 ML (1 ML =  $1.42 \times 10^{18} \text{ m}^{-2}$ , one “monolayer”, corresponding to one adatom per reconstructed unit cell) the density of Ag clusters is very low. Thus the onset of cluster formation is estimated to be close to 0.5 ML, whereas clustering starts<sup>59</sup> at approximately 0.17 ML for Au. The higher achievable adatom coverage indicates intrinsic differences in the growth behavior of Ag and Au, for example in the critical cluster size or the difference between metal-metal and metal-oxide bond strength. In order to determine the physical properties underlying the growth behavior, further experiments on the adsorption of Ag at this surface were performed.

STM image sequences of Ag/Fe<sub>3</sub>O<sub>4</sub>(001) demonstrate that Ag adatoms are mobile at an

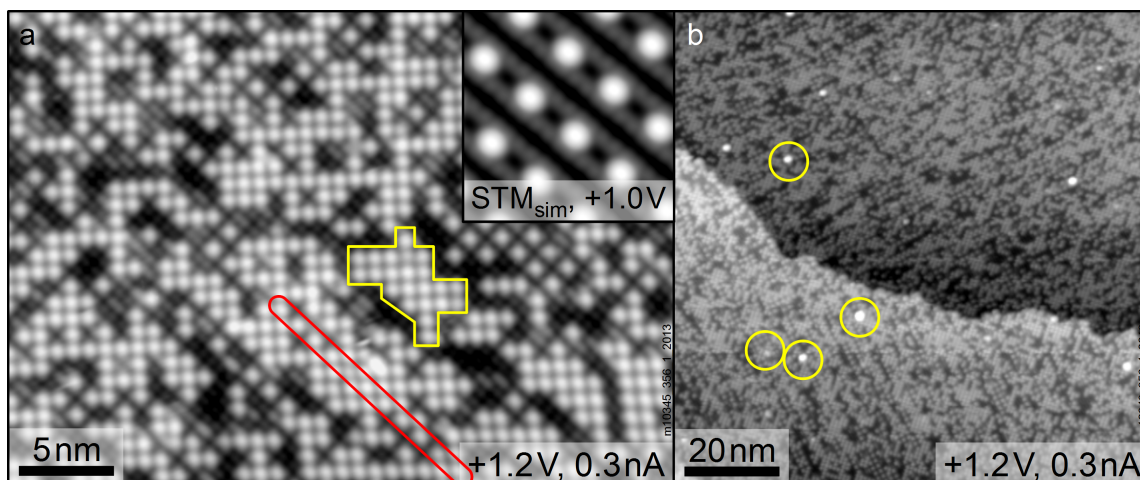


**Figure 4.10:** STM images of 0.51 ML Ag adatoms at the  $\text{Fe}_3\text{O}_4(001)$  surface, a coverage close to the onset of cluster formation: (a) Detailed image of Ag adatoms. Locally, full coverage of adatoms can be achieved in patches (yellow frame) and along the rows of surface Fe (red frame). (b) Few clusters are observed at this coverage ( $\approx 20$  in this  $100 \times 100 \text{ nm}^2$ -sized image). Four examples are highlighted by the yellow circles.

observable time scale at room temperature. This mobility usually presents as hopping of the adatoms between adjacent adsorption sites and is guided by the rows of surface Fe. Figure 4.11 provides examples of adatom hopping taken from a 67-frame STM movie of 0.29 ML Ag. The yellow arrows indicate the hopping direction of the adatoms in the solid circles. The dashed circles indicate the position of an adatom in the previous frame. In this movie, an average rate of three site changes per frame was observed on an area of  $\approx 30 \times 30 \text{ nm}^2$ , scanned at  $U_{\text{sample}} = +1.2 \text{ V}$  and  $I_t = 0.4 \text{ nA}$ . For site changes across one of the rows of surface Fe a strong preference ( $>90\%$ ) for the fast STM scanning direction is observed, indicating that the STM tip influences the mobility. The hopping parallel to the Fe rows is likely also enhanced by the STM tip, but it is assumed to be intrinsic, because it is observed independent of the scanning conditions.

The mobility of the adatoms provides information about the clustering behavior of Ag because it would allow two adatoms to meet when diffusing at the surface. The fact that no dimer formation is observed in STM movies indicates that two Ag atoms are not sufficient to form a stable cluster. This conclusion is confirmed by DFT calculations comparing the adsorption energy of two Ag adatoms ( $1.44 \text{ eV/Ag atom}$ ) to one Ag dimer ( $1.25 \text{ eV/atom}$ )<sup>132</sup>. (These DFT calculations were performed on the distorted bulk truncation model before the SCV model was established. The Ag dimer was not calculated on the SCV model.) In addition to the energetic preference for adatoms, the cationic nature of the  $\text{Ag}^{1+}$  potentially leads to an electrostatic barrier inhibiting the adatoms to hop onto

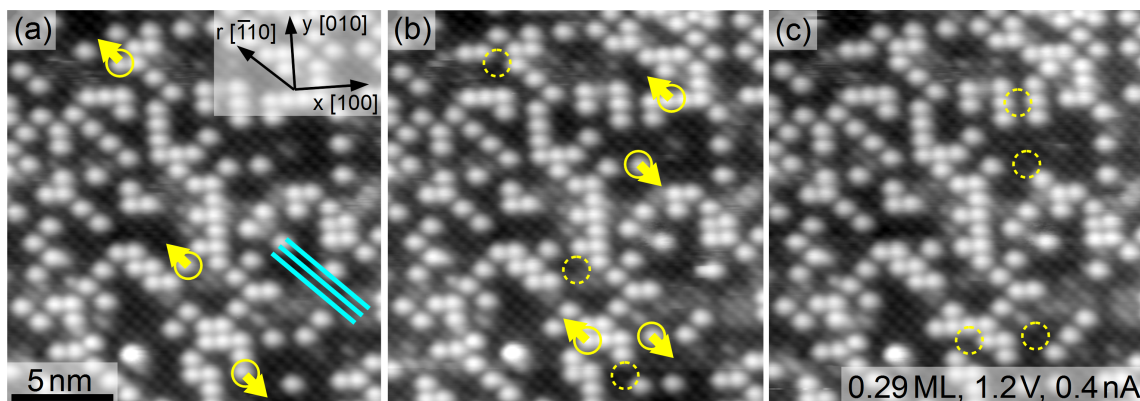


**Figure 4.11:** STM images demonstrating the mobility of 0.29 ML Ag adatoms. The cyan lines indicate the row direction (vector “r” in the inset). The yellow arrows and circles indicate the motion of Ag adatoms; the dashed circles in the subsequent image mark the original position of the respective atom.

an occupied site, thus preventing the formation of dimers. Since Ag adatoms are mobile and dimers are not stable, Ag atoms deposited onto a patch with fully occupied adsorption sites can temporarily share an adsorption site with an adatom and diffuse within the filled region, possibly forming and breaking metastable dimers. Unless two of these additional diffusing Ag atoms meet in one occupied site, no cluster formation will occur.

At high deposited Ag coverages, however, the majority of additional Ag atoms enter clusters. Increasing the adatom coverage beyond the 0.51 ML shown in Figure 4.10 mainly leads to the creation of new clusters and the growth of existing ones. Increasing the deposited Ag coverage to 0.65 ML, for example, results in an adatom coverage of 0.58 ML, whereas the cluster density increases by a factor of four compared to the coverage coexisting with 0.51 ML Ag adatoms. The adatom layer is filled slowly, but at a nominal deposited coverage of 1.45 ML (shown in Figure 4.12(b)) almost all sites are occupied. The adatoms are randomly distributed; no preference for vacancies in the adatom layer is observed. This observation indicates that incorporation of the mobile adatoms into the existing clusters is not a common growth process at room temperature. Moreover, it allows the conclusion that a newly formed Ag cluster remains bound to the adsorption site and cannot diffuse to capture additional atoms. In contrast, strong evidence for this type of mobility and growth was observed by Novotny *et al.* for Au clusters<sup>59</sup>: STM images showed trails devoid of adatoms adjacent to many Au clusters, indicating a diffusing species collecting and incorporating adatoms until the growing cluster size limits the diffusion.

A study of the thermal stability of Ag/Fe<sub>3</sub>O<sub>4</sub>(001) for different coverages provides insights into the influence of Ag clusters on the stability of the adatom phase. Figure 4.12(a)

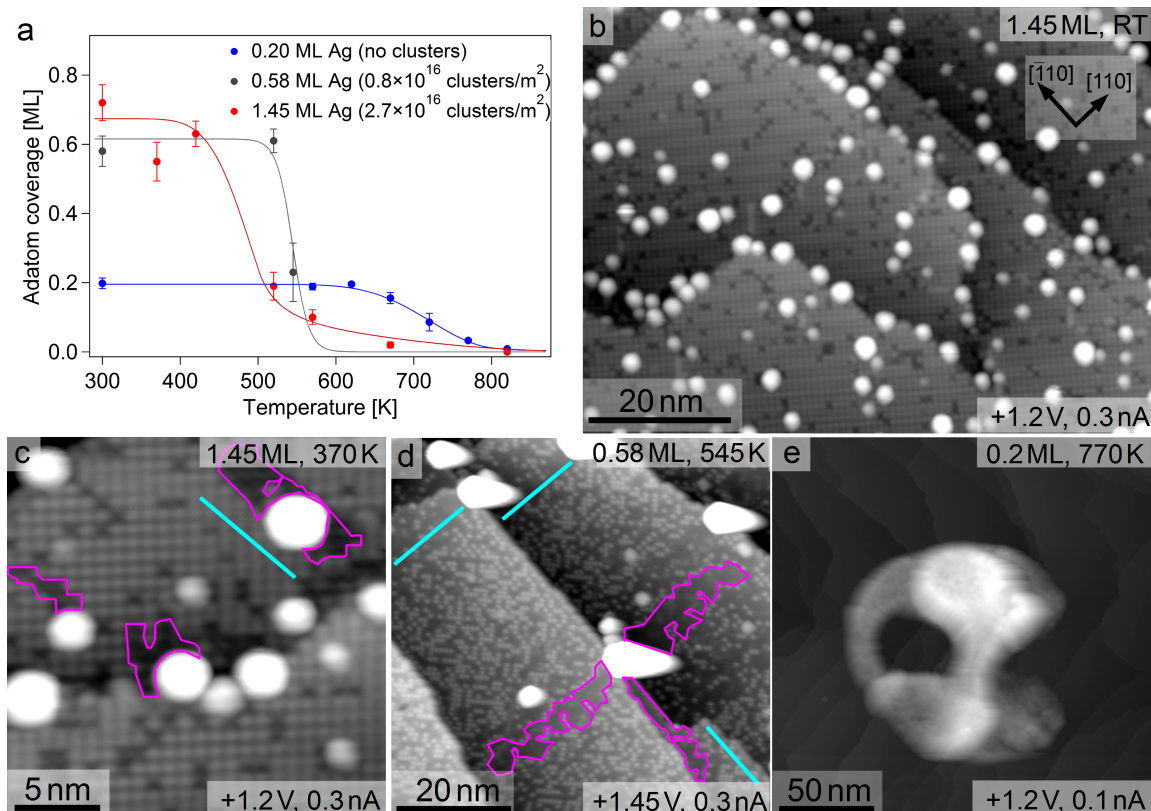


**Figure 4.12:** Thermal stability of different coverages of Ag/Fe<sub>3</sub>O<sub>4</sub>(001). (a) Ag adatom coverage as a function of annealing temperature: Without clusters Ag adatoms are highly stable, whereas a higher initial cluster coverage leads to a faster decrease of the adatom coverage during annealing. The solid lines are intended as guide to the eye only. (b) Image of 1.45 ML Ag/Fe<sub>3</sub>O<sub>4</sub>(001) deposited at room temperature. (c) Mild annealing (370 K) leads to patches devoid of atoms adjacent to clusters (surrounded by purple lines), interpreted as growth at the expense of the adatom phase. (d) 0.58 ML adatoms coexisting with clusters, flash-annealed to 545 K: The areas surrounded by purple lines extend across long distances aligned with the preferential direction of Ag adatom diffusion. (e) At temperatures beyond 720 K, all adatoms are destabilized and large clusters (>10 nm) can form. The cluster shown here is sharper than the STM tip, resulting in an image reflecting the tip shape.

illustrates the effect of different annealing temperatures on three coverages: 0.2 ML Ag adatoms without clusters and two coverages of adatoms coexisting with clusters (0.58 ML adatoms coexisting with clusters and a nominal deposited total coverage of 1.45 ML Ag). Each data point represents the average count of adatoms after flash-annealing to the respective temperature. The solid lines do not correspond to a functional dependence but are intended to serve as a guide to the eye. For low coverages of Ag, such as the 0.2 ML Ag represented by the blue data points, exclusively adatoms populate the surface. In the absence of clusters, the adatom phase remains highly stable up to ≈700 K, corresponding

to the temperature at which the surface reconstruction is lifted.

The red and gray curves in the stability graph in Figure 4.12(a) demonstrate that the presence of clusters at the surface decreases the thermal stability of the adatom phase. At a coverage of 0.58 ML of Ag adatoms (nominally deposited 0.65 ML Ag), an initial cluster density of  $\approx 0.8 \times 10^{16}$  clusters/m<sup>2</sup> is observed. Flash-annealing the sample to 520 K does not cause any discernible change to the adatom layer, whereas the coverage decreases rapidly when the temperature is increased further to 545 K. A similar behavior is observed for the deposition of 1.45 ML Ag, creating a very high adatom and cluster density ( $2.7 \times 10^{16}$  clusters/m<sup>2</sup>), which is depicted in the STM image in Figure 4.12(b). In the thermal stability study of 1.45 ML Ag, the decrease in the number of adatoms is shifted further to lower temperatures; it starts at 370 K.

In Figure 4.12(c-e) the results of the thermal stability study are illustrated by STM images at representative temperatures and coverages. After annealing 1.45 ML Ag to 370 K, patches devoid of adatoms are observed adjacent to many clusters (area surrounded by the purple line in Figure 4.12(c)). Figure 4.12(d) shows an equivalent but stronger effect after annealing 0.58 ML Ag adatoms coexisting with a low coverage of clusters to 545 K. On each terrace, trails devoid of Ag adatoms are formed, extending away from a cluster in straight lines. These trails are aligned with the direction of the surface Fe rows, which also guide the diffusion of the mobile Ag adatoms at room temperature. The direction of the rows is indicated by the cyan lines in (c,d). The elongated shape of the clusters in (d) is a result of a high scanning speed, which was set too fast for the STM tip to follow the topography of the cluster back to the surface in the scanning direction immediately after passing the highest point. After the 545 K annealing step, a large proportion of the clusters is located at step-edges, indicating that short trails leading to steps could be caused by the diffusion of a cluster collecting metal adatoms. The long trails at different terraces observed in (d), however, are more likely to originate in the thermally enhanced diffusion of the Ag adatoms, which are incorporated into the cluster when coming into contact. The very large cluster (apparent height 10.4 nm) in Figure 4.12(e) is the result of annealing 0.2 ML of Ag to 770 K. Its unusual and very broad shape is a good illustration of the limitations of STM with respect to imaging large clusters or rough surfaces. While the height of the cluster with respect to the terraces of Fe<sub>3</sub>O<sub>4</sub>(001) can be measured accurately, the width and the shape of the cluster are a result of the STM tip shape. For large clusters, the cluster is likely to be sharper than the front part of the STM tip if it is considered at a scale of several nanometers. Thus, the high cluster protruding from the otherwise flat surface scans the shape of the STM tip, resulting in an apparently irregularly shaped cluster in the image shown in Figure 4.12(e).

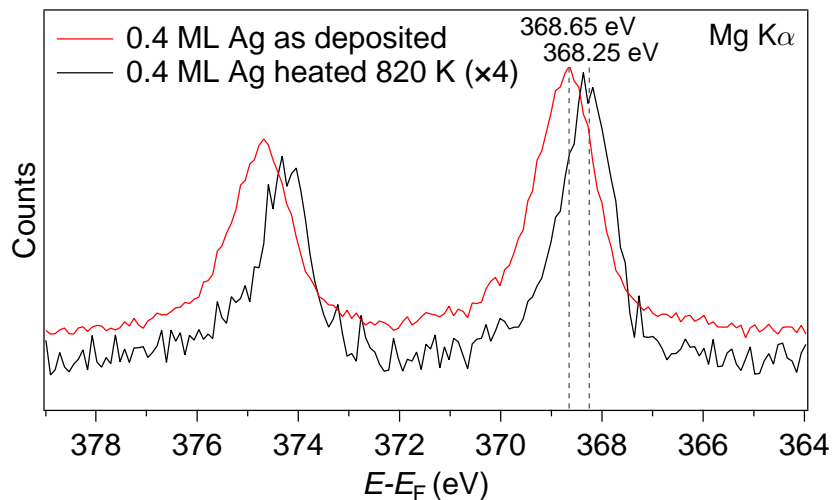


**Figure 4.13:** Comparison of Ag 3d XPS spectra of 0.4 ML Ag/Fe<sub>3</sub>O<sub>4</sub>(001) as deposited at room temperature (adatoms only) and after annealing to 820 K (large clusters). The spectra are aligned such that the respective O 1s binding energy corresponds to 530.1 eV.

The clear trend towards cluster formation at temperatures exceeding 670 K is also borne out in XPS measurements. Figure 4.13 shows XPS spectra of the Ag 3d peak of 0.4 ML Ag, comparing the as-deposited adatoms to the clusters after annealing to 820 K. The spectrometer is not calibrated accurately. Thus, both spectra are shifted by a constant energy offset of +0.4 eV, corresponding to the offset required to reproduce the correct O 1s peak position measured in the same experiments. The O 1s peak position is referenced to the binding energy of 530.1 eV in Fe<sub>3</sub>O<sub>4</sub>(001), in agreement with literature values<sup>108</sup> and reference measurements using a monochromatized X-ray source calibrated to the Fermi-edge and core-level peaks of metal samples (Au, Cu). This procedure is used for all XPS spectra acquired with the same spectrometer setup (all spectra acquired with Mg K $\alpha$  in the present thesis). The presented Ag spectra show a peak shift to higher binding energy for the as-deposited Ag adatoms, which is typical for an oxidized metal species. After annealing, the peak is located at a lower binding energy ( $\Delta E \approx -0.4$  eV), characteristic of the more metallic nature of Ag clusters. In the case of pure Ag samples, however, a peak shift towards lower binding energies is observed when oxidizing the metal<sup>133,134</sup>. This negative peak shift is qualitatively attributed to the negative Madelung potential at the cation site in an ionic lattice, which is enhanced for the small lattice constants observed in Ag oxides<sup>134</sup>. In the two-fold coordinated bonding geometry at the Fe<sub>3</sub>O<sub>4</sub>(001) surface, however, the Ag adatoms are not embedded in an oxidized lattice but protrude from the surface layer, providing a potential explanation for the shift to higher binding en-

ergies, which is not observed for  $\text{Ag}_x\text{O}$ . Hansen *et al.* also reported a shift towards higher binding energies compared to metallic Ag<sup>135</sup> in experiments on the adsorption of Ag nanoparticles on  $\text{TiO}_2(110)$  surfaces, indicating that sub-nano metal particles coordinated to an oxide surface differ substantially from  $\text{Ag}_x\text{O}$  samples. The large size of the Ag clusters on  $\text{Fe}_3\text{O}_4(001)$  after annealing is reflected in the strong decrease in the intensity of the Ag peak, resulting from a reduced number of Ag atoms and Ag surface area contributing to the photoemission intensity. The peak height of the Ag peak decreased by a factor of  $\approx 0.25$ , in contrast to a factor of  $\approx 0.77$  for the O 1s peak. (The small intensity drop of the O 1s peak is also observed for other peaks and the background in survey spectra and is thus attributed to a change in the sample position between the two XPS experiments.)

The results on the adsorption of Ag/ $\text{Fe}_3\text{O}_4(001)$  allow analyzing its behavior in the context of the standard growth modes in thermodynamic equilibrium. The increasing occupation of the adatom layer, coexisting with 3D particles at higher coverages, suggests Stranski-Krastanov-type growth of a wetting layer and 3D nanoparticles. Stranski-Krastanov growth is the predominant equilibrium growth mode if the deposited material exhibits a lower surface energy than the respective substrate, but generally cluster formation of the deposit is favorable. In the present case, however, the adatom layer does not correspond to a system in thermodynamic equilibrium, since annealing to lift the surface reconstruction destabilizes the adatoms and leads to agglomeration into large particles, in agreement with a study at high coverages of Ag on the  $\text{Fe}_3\text{O}_4(001)$  surface<sup>136</sup>. The experimental heat of adsorption of Ag atoms measured by adsorption calorimetry on different oxides is found to rapidly approach the value of the bulk heat of sublimation of Ag (285 kJ/mol) with increasing cluster size<sup>13</sup>. The corresponding experimental adsorption energy ( $\approx 2.9$  eV/atom) is substantially higher than the 1.44 eV (1.85 eV on the SCV structure) calculated in the present study<sup>132</sup>. Thus, the stability of the Ag adatom layer is due to kinetic limitations caused by the instability of the Ag dimer and the high stability of Ag single atoms at the temperatures studied.

#### 4.2.2.2 Silver adatom–gas interactions

The interaction of Ag adatoms with CO and  $\text{CO}_2$  was studied in STM image sequences. CO and  $\text{CO}_2$  were dosed subsequently within one experiment up to pressures of  $10^{-8}$  mbar while scanning ( $U_{\text{sample}}=+1.2$  V and  $I_t=0.4$  nA), but no effect was observed. The DFT+ $U$  calculations of the adsorption of CO find a relatively high adsorption energy of 1.38 eV compared to other 3d, 4d, and 5d transition metal adatoms, which were part of the DFT study. Ni and Cu, for example, exhibit a lower CO adsorption energy of 1.28 eV. The ab-

solute numbers include changes in the bonding environment of the adatoms and are referenced to free atoms and molecules in vacuum, which are usually not good reference values for absolute energies in DFT calculations. However, the comparability of energies between different adatom species as well as all other calculated properties such as adsorption geometries, charge states, and the electronic structure are not compromised. For CO adsorption on Ag, the adatom is found to be lifted up from its initial position, stretching the Ag-O bond length to  $d_{Ag-O}(Ag-CO)=2.28 \text{ \AA}$  ( $\Delta d=0.20 \text{ \AA}$ ) and the height above the average  $Fe_{oct}$  to  $\Delta z_{Ag-FeB}(Ag-CO)=1.60 \text{ \AA}$  ( $\Delta(\Delta z)=0.63 \text{ \AA}$ ). The Ag-C bond length is  $d_{Ag-C}=2.10 \text{ \AA}$ , the CO bond length  $d_{C-O}=1.151 \text{ \AA}$  (compared to  $d_{C-O}(free)=1.141 \text{ \AA}$ ). The charge state of  $Ag^{1+}$  and the spherically symmetric charge distribution of the Ag adatom are unaffected by the adsorption of CO.

## 4.2.3 Nickel

### 4.2.3.1 Nickel adsorption and incorporation

Many transition metals exhibit promoting effects when used as additives and dopants in catalytically active materials. Owing to their cationic nature and the undercoordinated bonding environment, metal adatoms at the  $Fe_3O_4(001)$  surface are expected to interact strongly with common reactant gases such as CO, NO, or  $O_2$ . A DFT study of CO oxidation over Ni adatoms on  $FeO_x$  confirms this expectation and predicts a high catalytic activity for this reaction at room temperature<sup>137</sup>. The water-gas shift activity of several ferrite ( $M_xFe_{3-x}O_4$ ) materials adds further interesting aspects to the study of Ni adsorption on  $Fe_3O_4(001)$ <sup>138,139</sup>. The results on the adsorption and stability of Ni/ $Fe_3O_4(001)$  presented in this section have been published in a recent article on the adsorption and incorporation of transition metals at this surface<sup>140</sup>. Here, the adsorption properties of Ni are discussed in three parts focusing on the results obtained using STM, photoelectron spectroscopy, and density functional theory calculations.

### STM of Ni adsorption

The coverage dependence of Ni adsorption on display in Figure 4.14 shows a type of behavior that can only be understood in the context of the subsurface cation vacancy surface structure. Upon deposition of 0.2 ML Ni, stable adatoms in the preferential adsorption site are the main species (Figure 4.14(a)). At room temperature Ni adatoms are immobile and do not show any adsorption from the residual gas ( $p < 10^{-10}$  mbar). The number of defects in Figure 4.14(a) is comparable to the clean surface defect density. However, at higher cov-

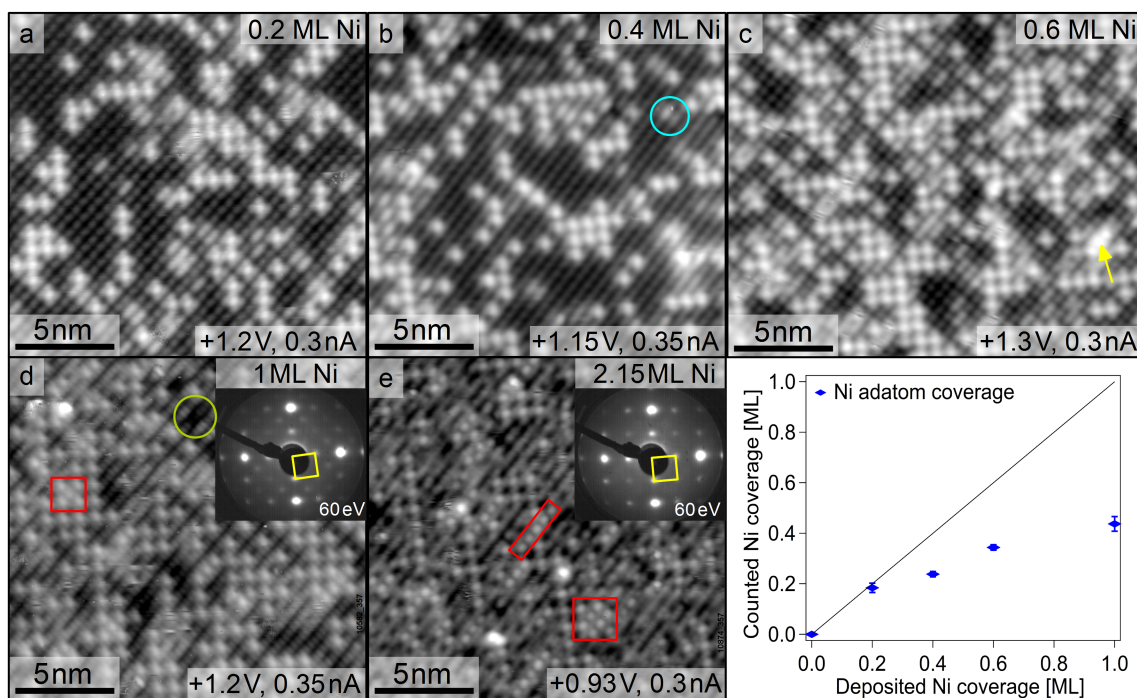


**Figure 4.14:** Coverage-dependent adsorption of Ni: (a) STM image of 0.2 ML Ni adatoms. (b) Deposited 0.4 ML Ni: Small increase in the adatom coverage and the density of bright “on-the-row” features corresponding to unit cells with filled subsurface vacancies (cyan circle). (c) Deposited 0.6 ML Ni: First adatoms occupy formerly blocked sites, where the reconstruction was lifted (yellow arrow). (d) Deposited 1 ML Ni: A large fraction of the Fe rows is brighter; reconstructed patches without adatoms appear as depressions in the rows (green circle). Fully occupied patches start to form (red square). The LEED pattern (inset) shows weak reconstruction spots; the yellow square indicates an unreconstructed unit cell. (e) Deposited 2.15 ML Ni: The filling of the adatom layer is still incomplete, but more and larger densely occupied patches have formed. Only few reconstructed patches remain. Very bright species are attributed to first small clusters. Inset: unreconstructed LEED pattern. (f) Graph showing the adatom coverage determined from STM images as a function of the deposited coverage.

erage (Figure 4.14(b,c)) an increasing number of defects imaged as bright features on the surface Fe rows is observed (cyan circle). These “on-the-row” defects resemble a surface hydroxyl group at similar scanning conditions but differ in apparent height and do not exhibit the characteristic hopping behavior of the adsorbed hydrogen<sup>125</sup>. The present thesis provides evidence for the interpretation of these defects as “incorporated metal defects”, corresponding to a unit cell, where the subsurface  $\text{Fe}_{\text{oct}}$  vacancies of the SCV structure are filled by two metal atoms,  $\text{Fe}_{\text{int}}$  and a deposited metal atom or a second  $\text{Fe}_{\text{oct}}$ . The metal incorporation locally lifts the reconstruction, reverting the cation rearrangement and rendering the adsorption site and the (formerly) blocked site equivalent. At coverages of 1 ML (Figure 4.14(d)) and beyond, the increasing density of “on-the-row” defects becomes

apparent in STM images: The fraction of bright Fe rows is increasing with the deposited Ni coverage and the remaining reconstructed patches are imaged as depressions in the rows (example highlighted by a green circle in Figure 4.14(d)). At 2.15 ML Ni (Figure 4.14(e)) the bright features are dominant. Moreover, at higher Ni coverages the formerly blocked sites are also available for Ni adsorption, resulting in densely occupied areas, such as the regions highlighted by red frames in Figures 4.14(d,e). Figure 4.14(f) shows a graph of the counted adatom coverage as a function of the deposited amount of Ni. At coverages exceeding 0.2 ML the blue markers deviate strongly from the black line corresponding to 100% adsorption as adatoms. This nonlinear behavior is also clearly visible in the high-coverage STM images: For example after the deposition of 1 ML Ni less than half ( $\approx 44\%$ ) of a layer of adatoms is observed. While a systematic error in the calibration of the deposited coverage is a possible explanation for a constant correction factor of the coverage, the increasing deviation from a linear behavior with growing coverage cannot be explained that way. The absence of a significant number of clusters from the images demonstrates that agglomeration to larger particles cannot be the underlying reason for the reduced number of adatoms either. Thus, the deviation from a linear increase in Ni adatom coverage is interpreted as the incorporation of Ni adatoms, resulting in filled subsurface Fe vacancies leading to bright “on-the-row” features, which correspond to “incorporated metal defects” here. This conclusion is strengthened by the local lifting of the reconstruction, which is demonstrated by the tendency to form Ni adatoms in those sites of the reconstruction, which should be blocked by  $\text{Fe}_{\text{int}}$  (yellow arrow in Figure 4.14(c), red frames in (d,e)). The weakening and disappearance of the reconstruction spots in LEED patterns (insets in Figures 4.14(d,e)) serve as proof that the lifting of the reconstruction is not limited to the areas scanned in STM images but occurs on the entire surface.

A study of the thermal stability of 0.2 ML Ni demonstrates that the incorporation is a transition to a more favorable state, which can be excited thermally. Figure 4.15 shows images of different areas of the  $\text{Fe}_3\text{O}_4(001)$  surface acquired (a) at room temperature and (b) after annealing for 10 min at 423 K and (c) 448 K. The room-temperature image shows almost exclusively Ni adatoms (example highlighted by a red circle in each image) and few bright features on the surface Fe rows. After annealing the surface at 423 K, a lower coverage of Ni adatoms coexists with bright “on-the-row” features (examples highlighted by yellow frames in (b,c)). Heating to 448 K results in an almost complete conversion of the remaining adatoms to bright “on-the-row” features. The features, created from adatoms by annealing, are equivalent to the “incorporated metal defects” observed in increasing numbers at augmented coverages of Ni. The observed behavior leads to the conclusion that Ni incorporation can be driven by high coverage as well as excited thermally. Annealing

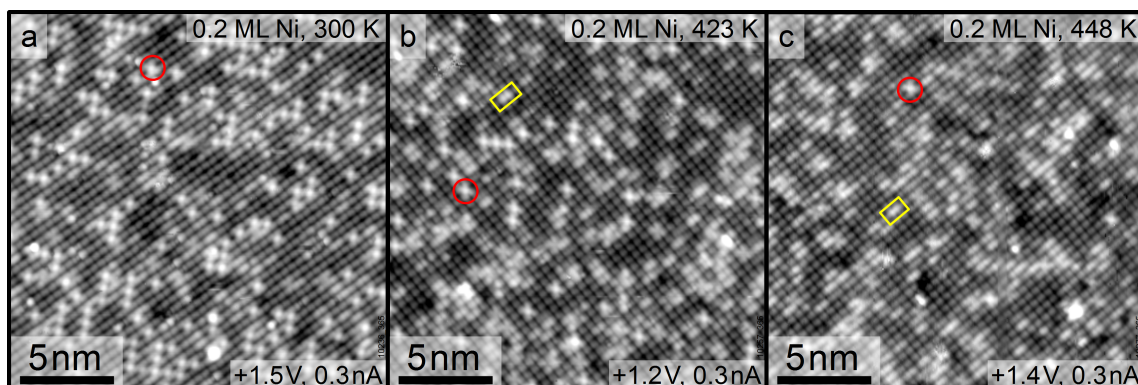


**Figure 4.15:** Thermal stability study of 0.2 ML Ni adatoms (different area in each image): (a) At room temperature almost exclusively adatoms are observed (example highlighted by a red circle). No discernible increase in the concentration of bright features on the surface Fe rows is found in comparison to the pristine surface. (b) Heating to 423 K (10 min) results in a decrease in the Ni adatom coverage and a higher number of bright “on-the-row” features (yellow frames). (c) After annealing at 448 K the adatom density is close to zero and the number of “on-the-row” features has increased significantly. (Figure from *Physical Review B* 92, 075440 (2015); reprinted with permission from APS.)<sup>140</sup>

at temperatures exceeding 448 K leads to the recovery of a clean surface in STM images, attributed to the diffusion of the incorporated Ni to deeper layers.

### Photoelectron spectroscopy of Ni adsorption

The conclusions of the STM study are supported by photoemission results. The experiments were performed on natural  $\text{Fe}_3\text{O}_4(001)$  single crystals, whose purity was evaluated using STM and XPS prior to these experiments. The Ni 2*p* spectra (Figure 4.16) were obtained in the surface chemistry UHV chamber of the surface science group at TU Wien using a monochromated Al  $K\alpha$  X-ray source and a SPECS Phoibos 150 analyzer. The Fe 2*p* and the valence band spectra (Figure 4.17) were acquired at grazing emission ( $55^\circ$  off normal) at the synchrotron beamline I311 of the MaxIV Laboratory in Lund, Sweden. The Ni 2*p* spectrum of 1 ML Ni, as-deposited at room temperature (Figure 4.16, red spectrum), exhibits a peak at  $\approx 855$  eV with a strong shoulder at lower binding energy ( $\approx 853.7$  eV). Compared to metallic Ni, both contributions are shifted to higher binding energies by  $>2$  eV and  $\approx 1$  eV, respectively. Temperature-dependent experiments indicate that the lower binding energy peak corresponds to Ni adatoms: Annealing to 465 K causes this peak to disappear (black spectrum), indicating that the high binding energy peak represents the bright surface features attributed to incorporated Ni. Deposition of Ni at 200 K, which is expected to enhance the adatom coverage compared to room-temperature

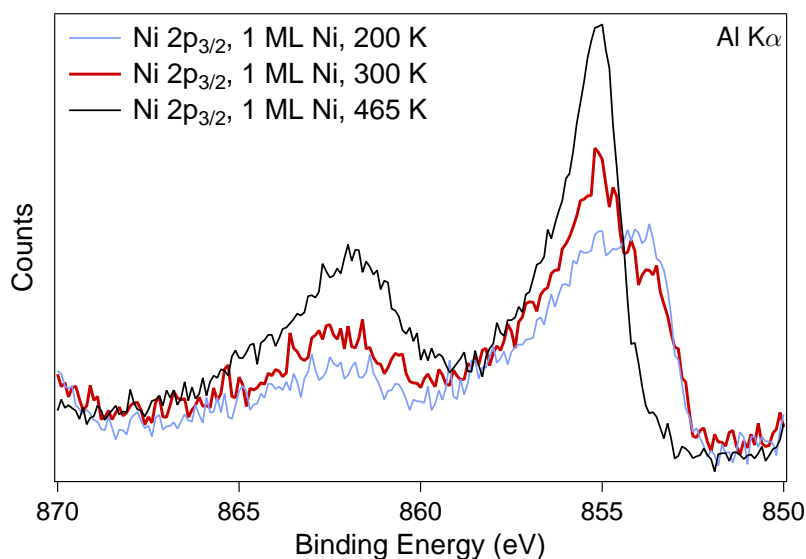


**Figure 4.16:** Ni 2p XPS spectra of different treatments of 1 ML Ni/Fe<sub>3</sub>O<sub>4</sub>(001). The red spectrum was acquired for as-deposited Ni at room temperature. It consists of two components with different oxidation states. The main Ni peak is shifted to higher binding energy by >2 eV with respect to metallic Ni. The low binding energy shoulder corresponds to Ni adatoms and disappears after annealing to 465 K (black curve), leading to full incorporation of all Ni adatoms. At low temperature (200 K, blue curve), less Ni is incorporated upon deposition.

deposition, leads to an almost equal ratio of the two contributions, resulting in one broad, flat peak.

The valence band (VB) and Fe 2p spectra presented in Figure 4.17 illustrate the influence of metal deposition on the electronic structure of the substrate in a comparison of the clean surface spectra (red) and the spectra after deposition of 1 ML Ni (black). The clean surface VB spectrum exhibits little intensity close to the Fermi energy, which is enhanced by the deposition of 1 ML Ni, causing the onset of the valence band maximum to shift closer to the Fermi level. The peak at  $E_B \approx 1$  eV is commonly attributed to an Fe<sup>2+</sup> state<sup>114</sup>. The Fe 2p spectra confirm the observation of a higher Fe<sup>2+</sup> content: Following the deposition of 1 ML Ni, a shoulder at lower binding energy is observed. The vertical lines indicate the positions which are attributed to Fe<sup>2+</sup> (708.3 eV) and Fe<sup>3+</sup> (710.6 eV) peaks<sup>141</sup>, in agreement with an increase of the Fe<sup>2+</sup> content in the surface region. Furthermore, the high-binding-energy satellite at  $\approx 719$  eV, attributed<sup>142</sup> to Fe<sup>3+</sup>, disappears with the deposition of 1 ML Ni. These enhanced contributions of Fe<sup>2+</sup> in the surface region agree with the oxidized Ni species observed in the Ni 2p spectra, which are expected to donate electrons to the Fe<sup>3+</sup>-rich layers. The spectroscopy results provide additional evidence for the incorporation of Ni adatoms at high coverages and elevated temperatures

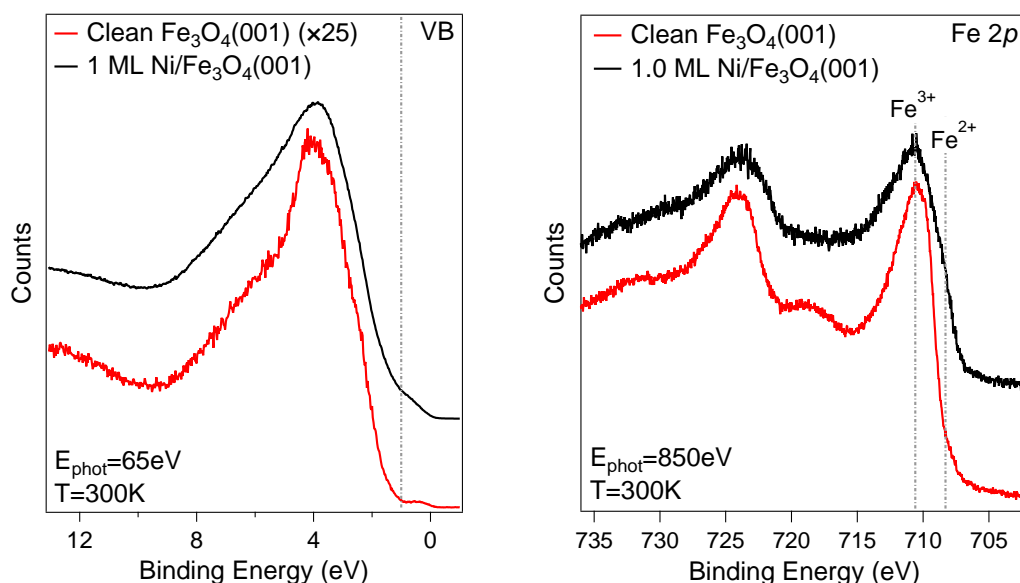


**Figure 4.17:** Valence band (VB) and Fe 2p spectra of 1 ML Ni/Fe<sub>3</sub>O<sub>4</sub>(001): Compared to the Fe<sup>3+</sup>-rich clean surface (red spectra), the deposition of 1 ML Ni (black spectra) causes the emergence of an Fe<sup>2+</sup>-like state. In the valence band, this is borne out by a peak at  $\approx 1$  eV, causing a shift of the onset of the valence band maximum closer to the Fermi level. In the Fe 2p spectrum, the shoulder at low binding energies is enhanced, and the satellite at high binding energy is suppressed.

and support the interpretation of the STM results. The presence of two oxidized species with different valence states reflects the coexistence of two-fold coordinated Ni adatoms at the surface with incorporated Ni within the full bonding environment of a spinel lattice.

### DFT+*U* calculations of Ni adsorption

In order to confirm the experimentally observed trends and study further details of the behavior of Ni, DFT+*U* calculations were performed. The atomic radius of the Ni atoms was set to 1.9 bohr ( $\approx 1.01$  Å) and a Hubbard-*U* of 3.8 eV was applied to the correlated Ni 3*d* electrons in all configurations. For the Ni adatom and the favored incorporated configuration, the calculation was also performed for  $U_{eff}(\text{Ni})=5$  eV but no significant difference was observed. The reciprocal space was mapped using a  $(3 \times 3 \times 1)$  *k*-mesh, and a plane-wave cut-off energy of  $\approx 297$  eV was used. The calculations were mainly focused on finding out which geometry is favored for Ni incorporation. The adatom configuration is determined by a force-relaxation of a Ni atom in the metal adsorption site of the SCV structure, whereas the structural models of incorporated Ni are based on a bulk-truncated structure, where one Fe atom is replaced by Ni, followed by a force relaxation. Figure 4.18 illustrates the four different configurations, which were considered for the Ni adsorption and

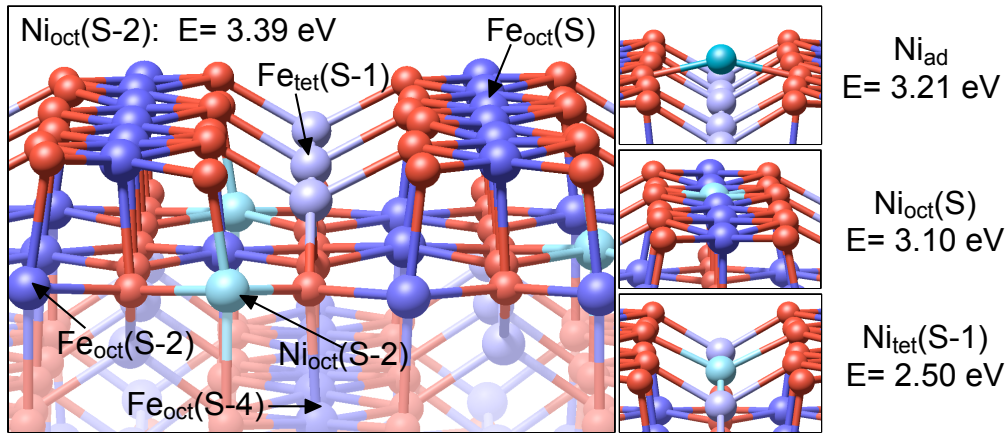


**Figure 4.18:** Configurations considered for the adsorption and incorporation of Ni. The large image shows the energetically favored configuration. Here, Ni is incorporated in the subsurface  $Fe_{oct}$  vacancy; the second vacancy is filled by diffusion of  $Fe_{int}$  to the  $Fe_{oct}(S-2)$  site, resulting in a relaxed, unreconstructed geometry. The small images illustrate a Ni adatom on the SCV structure, Ni incorporated in an octahedral site in the surface layer, and Ni in a tetrahedral site in the (S-1) layer. In the latter two cases the structure corresponds to a bulk-truncated, relaxed surface with one Ni replacing the Fe atoms labeled  $Fe_{oct}(S)$  and  $Fe_{tet}(S-1)$  instead of  $Ni_{oct}(S-2)$  in the large structural model.

incorporation study. The large image depicts the structural model of Ni incorporated in the (S-2) site. The Fe atoms labeled  $Fe_{oct}(S)$  and  $Fe_{tet}(S-1)$  are the ones which are replaced by  $Ni_{oct}(S)$  or  $Ni_{tet}(S-1)$  in the respective calculation. The small images display a selected area of the structural models of the adatom ( $Ni_{ad}$ ) and the two alternative incorporated configurations ( $Ni_{oct}(S)$  and  $Ni_{tet}(S-1)$ ) labeled with the respective energies, referenced to the initial state of a pristine SCV structure and a free Ni atom in vacuum. The calculated energies convey a clear preference for the incorporation in octahedral sites, in agreement with a recent X-ray absorption fine structure study of Ni-doped magnetite<sup>143</sup>. Moreover, the octahedral sites are known to be the characteristic sites<sup>144</sup> of Ni atoms in the inverse spinel ferrite  $NiFe_2O_4$ . Ni incorporated in the subsurface  $Fe_{oct}$  vacancy results in the lowest energy ( $Ni_{oct}(S-2)$ :  $\Delta E=3.39$  eV), while  $Ni_{tet}(S-1)$  is unlikely to form ( $\Delta E=2.50$  eV). However, the Ni adatom configuration ( $E_{ads}=3.21$  eV) is favored over incorporation into the surface octahedral layer ( $\Delta E=3.10$  eV). In analogy to Ag, the characteristic distances (illustrated in the image for Ag in Figure 4.9) of the force-relaxed Ni adatom geometry were also determined. The values of  $d_{Ni-O}=1.85$  Å and  $\Delta z_{Ni-FeB}=0.62$  Å are significantly lower than for Ag (2.08 Å, 0.97 Å), which is in agreement with the higher adsorption energy of Ni. The magnetic moments within the atomic sphere of the Ni atoms differ between the adatom ( $|\vec{\mu}_{Ni}|\approx 1 \mu_B$ ) and the incorporated Ni configurations ( $|\vec{\mu}_{Ni}|\approx 1.66 \mu_B$ ).

Moreover, they are found to be ferromagnetically aligned with the  $\text{Fe}_{\text{oct}}$  moments for the  $\text{Ni}_{\text{oct}}$  geometries and the Ni adatom, and antiferromagnetically for the  $\text{Ni}_{\text{tet}}(\text{S-1})$  site. The charge transfer to the substrate is analyzed by comparing the magnetic moments of the entire slab and of the atoms as well as the partial charges inside the atomic spheres. The total magnetic moment of the slab is unchanged by the adsorption of a Ni adatom with a moment of  $\approx 1 \mu_{\text{B}}$ . This is interpreted as a  $4s^0 3d^9$  electron configuration, corresponding to  $\text{Ni}^{1+}$ . In the case of the incorporation of Ni, the magnetic moments of the symmetric slab change drastically because of the rearrangements in the subsurface layers (for a symmetric slab with two surfaces:  $\Delta\mu_{\text{slab}} = +20 \mu_{\text{B}}$  for  $\text{Ni}_{\text{oct}}(\text{S})$  and (S-2),  $\Delta\mu_{\text{slab}} = +32 \mu_{\text{B}}$  for  $\text{Ni}_{\text{tet}}(\text{S-1})$ ). If each  $\text{Fe}^{3+}$  cation in the surface region is considered as a contribution of  $5 \mu_{\text{B}}$  (fully spin-polarized) and the incorporated Ni atom as totally contributing  $2 \mu_{\text{B}}$ , these results correspond to a residual difference of  $2 \mu_{\text{B}}$ . This difference can be explained by a Ni charge state of  $\text{Ni}^{2+}$ , donating two electrons to the slab, which convert  $\text{Fe}_{\text{oct}}^{3+}$  ( $5 \mu_{\text{B}}$ ) to  $\text{Fe}_{\text{oct}}^{2+}$  ( $4 \mu_{\text{B}}$ ).

Further analysis of the electronic structure of the Ni configurations allows correlating the calculated structures to the observations in STM. The density of states of the surface layer and the  $\text{Fe}_{\text{oct}}$  layers, together with simulated STM images, provide information about the nature of the bright features attributed to incorporated Ni atoms. Figure 4.19 (adapted from Physical Review B 92, 075440)<sup>140</sup> shows the layer-resolved Fe DOS and simulated STM images of the pristine SCV surface (a,d), the SCV surface with one Ni adatom per reconstructed unit cell (b,e), and the configuration of incorporated  $\text{Ni}_{\text{oct}}(\text{S-2})$  (c,f), which is depicted in the large structural model in Figure 4.18. The layer-resolved  $\text{Fe}_{\text{oct}}$  DOS of the pristine surface shows that there is little intensity close to the Fermi energy in the unoccupied states below  $\approx 0.6 \text{ eV}$ . Moreover, the  $\text{Fe}^{2+}$ -like states at a binding energy of  $\approx 1 \text{ eV}$ <sup>114</sup> are absent in the entire surface region. The deposition of a Ni adatom causes the emergence of states close to  $E_{\text{F}}$  in the  $\text{Fe}^{2+}$  region as well as in the unoccupied states. The Ni adatom exhibits little density in the unoccupied states, explaining its smaller appearance in STM images compared to Ag adatoms. The Ni DOS consists of localized Ni 3d peaks for the adatom, which broaden to resemble the  $\text{Fe}_{\text{oct}}$  atoms in the case of incorporated Ni. The incorporation of Ni in the  $\text{Ni}_{\text{oct}}(\text{S-2})$  site causes a significant  $\text{Fe}^{2+}$  peak in the (S-4) layer, in accord with the spectroscopy results presented above. Furthermore the emergence of a peak in the unoccupied DOS close to  $E_{\text{F}}$  is observed, which explains the brighter features on the surface Fe rows observed in STM images. The peak close to  $E_{\text{F}}$  results in bright protrusions on the surface Fe rows in simulated STM images (Figure 4.19 (f)). Both  $\text{Fe}_{\text{oct}}$  vacancies of the SCV structure are filled, resulting in straight surface Fe rows, which exhibit an enhanced brightness above both filled vacancies. The effect

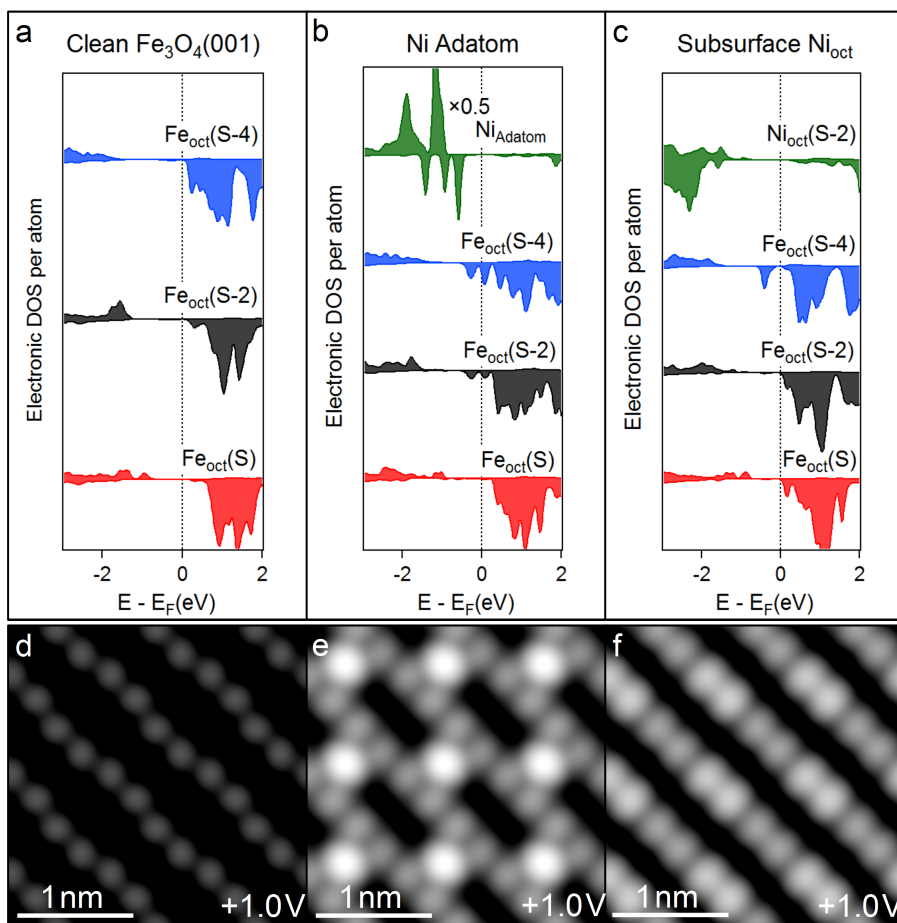


**Figure 4.19:** Electronic structure of adsorbed/incorporated Ni: DOS of the  $\text{Fe}_{\text{oct}}$  layers and Ni (if applicable) for (a) the pristine SCV surface, (b) the Ni adatom on the SCV surface, and (c) incorporated  $\text{Ni}_{\text{oct}}(\text{S-2})$ . (d-f) Simulated STM images ( $U_{\text{sample}} = +1$  V) of the respective structures: (d) pristine SCV, (e) Ni adatom, and (f)  $\text{Ni}_{\text{oct}}(\text{S-2})$ .

is substantially stronger for the surface Fe located above the  $\text{Fe}_{\text{oct}}(\text{S-2})$ . The study of Ni adsorption provides conclusive evidence that metal atoms can be incorporated into the subsurface Fe vacancies underlying the reconstruction.

#### 4.2.3.2 Nickel adatom–gas interactions

The adatom-molecule interactions of Ni adatoms were studied for CO and  $\text{O}_2$  using STM and DFT+ $U$  calculations. Additional STM experiments were performed for NO exposure. For CO, the adsorption energy on Ni ( $E_{\text{ads,CO}} = 1.27$  eV) is found to be lower than on Ag. This is in contrast to the experimental observations: STM image sequences indicated an interaction between CO and Ni, whereas Ag was found to be inert towards CO adsorption

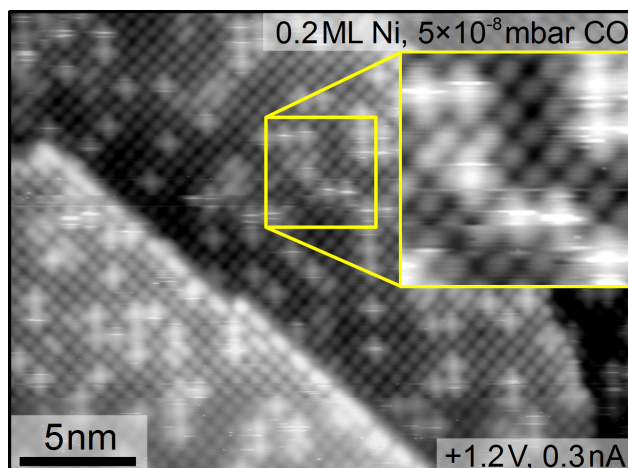


**Figure 4.20:** STM image demonstrating the interaction of Ni adatoms with CO molecules: The image was acquired in an atmosphere of  $5 \times 10^{-8}$  mbar CO. It shows scratchy features on the Ni adatoms; the scratchy lines are parallel to the fast STM scanning direction, indicating an interaction of the tip with CO adsorbed on the Ni adatoms.

at room temperature. In STM image sequences the adsorption of CO manifested itself in the form of scratchy features on the Ni adatoms, aligned with the fast STM scanning direction (see Figure 4.20). This interaction of adsorbed CO molecules with the STM tip was observed only at elevated CO pressures of  $5 \times 10^{-8}$  mbar and beyond. Closing the CO leak valve caused the scratchy features to disappear, indicating an adsorption energy corresponding to a slow desorption rate at room temperature. The differences in the characteristic distances are in agreement with a weak interaction of CO on Ni adatoms:  $d_{Ni-O}(Ni-CO)=1.99 \text{ \AA}$  ( $\Delta d=0.14 \text{ \AA}$ ) and  $\Delta z_{Ni-FeB}(Ni-CO)=1.13 \text{ \AA}$  ( $\Delta(\Delta z)=0.51 \text{ \AA}$ ). The Ni-C bond length corresponds to  $d_{Ni-C}=1.81 \text{ \AA}$ , the CO bond length to  $d_{C-O}=1.153 \text{ \AA}$ .

The DFT calculations of the Ni-O<sub>2</sub> interaction predict a flat adsorption geometry of O<sub>2</sub>, creating a bonding environment of Ni resembling a tetrahedral coordination to oxygen. The calculated adsorption energy  $E_{ads,O_2}=2.05 \text{ eV}$  is high but the lowest among the metals in the oxygen adsorption study (Ni, Co, Rh, and Pd). Similar to CO, the adsorption of O<sub>2</sub> increases the bond lengths to the surface oxygen atoms  $d_{Ni-O}(Ni-O_2)=1.98 \text{ \AA}$  ( $\Delta d=0.13 \text{ \AA}$ ) and the height above the average Fe<sub>oct</sub>(S)  $\Delta z_{Ni-FeB}=1.03 \text{ \AA}$  ( $\Delta(\Delta z)=0.41 \text{ \AA}$ ). The bond length between Ni and the oxygen molecule ( $d_{Ni-O(O_2)}=2.03 \text{ \AA}$ ) is comparable to the distance to the surface oxygen atoms. Experimentally, Ni adatoms were found to interact with O<sub>2</sub> molecules, but the interpretation of the observed surface processes is difficult. In an STM image sequence acquired while dosing  $5 \times 10^{-10}$  mbar O<sub>2</sub> the formation of bright features on several Ni adatoms was observed. However, the remaining Ni adatoms did not show any activity, even when increasing the O<sub>2</sub> pressure up to  $10^{-7}$  mbar.

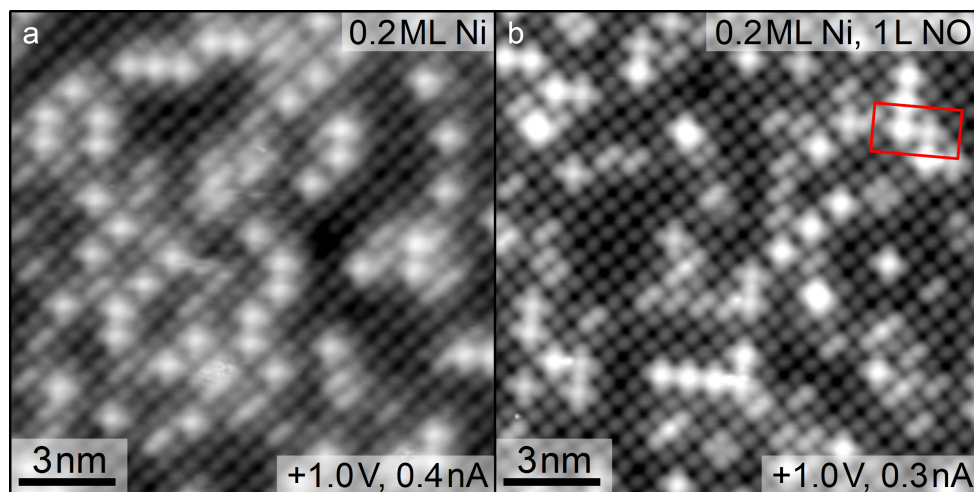


**Figure 4.21:** STM images of 0.2 ML Ni before and after dosing 1 L NO: (a) The as-deposited Ni adatoms all exhibit the same apparent height of  $\approx 100$  pm at 1 V, 0.3 nA. (b) Upon exposure to 1 L NO, an increase in apparent height ( $\Delta h \approx +40$  pm at 1 V, 0.3 nA) is observed for many Ni adatoms, which is attributed to NO adsorption. The red frame highlights a pair of adatoms with different apparent heights (with/without NO).

Experiments with NO showed strong, permanent adsorption at room temperature and adsorbate-induced mobility of the Ni adatoms. Figure 4.21 presents a comparison of Ni adatoms (a) before and (b) after dosing 1 L NO. A species with an increased apparent height compared to the Ni adatoms is observed ( $\Delta h \approx +40$  pm, at  $U_{\text{sample}} = 1$  V,  $I_t = 0.3$  nA). If a high sticking probability of the reactive gas molecule NO is assumed, 1 L of NO is sufficient for adsorption on a large fraction of Ni adatoms. Brighter Ni adatoms of this type were not observed without dosing NO, which is not a usual component of the residual gas. Thus, the observed feature is likely an NO molecule adsorbed on a Ni adatom.

At room temperature no evidence of the interaction of CO, O<sub>2</sub>, NO, H<sub>2</sub>, and H<sub>2</sub>O molecules with the “incorporated metal defects” was observed. This is most likely due to the preferential incorporation into the subsurface, excluding the incorporated Ni from direct interaction with molecules. However, the filling of the subsurface vacancies and the concomitant modification of the surface Fe<sub>oct</sub> DOS has been reported to enhance the reactivity of the surface Fe atoms for the adsorption of methanol<sup>145</sup>.

#### 4.2.4 Incorporation of transition metals

Ni is only one example of reactive 3d transition metals which can form solid solution with magnetite and incorporate into the Fe<sub>3</sub>O<sub>4</sub>(001) surface layer. A variety of transition metals

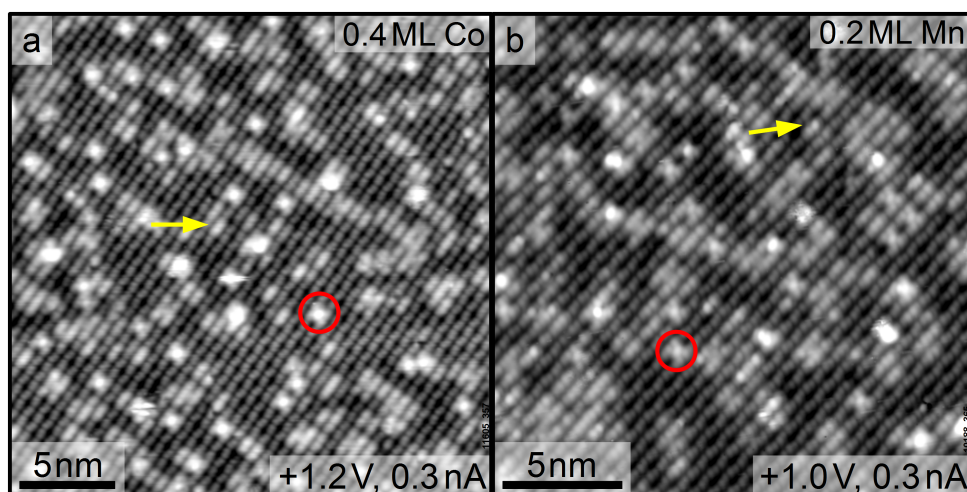


**Figure 4.22:** STM images of (a) Co and (b) Mn at the  $\text{Fe}_3\text{O}_4(001)$  surface. (a) After deposition of 0.4 ML Co, adatoms are the main species (example in the red circle) but they coexist with a large number of bright “on-the-row” features (example highlighted by the yellow arrow). The Co adatom coverage is significantly smaller than 0.4 ML. Several brighter adatom-like features are observed and attributed to adsorption from the residual gas. (b) Upon deposition of 0.2 ML Mn the observed surface features are similar. Reactive adatoms coexist with bright surface Fe row features.

is reported to be active for different reactions, such as the oxygen reduction reaction<sup>146</sup> over Mn ferrite or Co- and Mn-promoted  $\text{H}_2\text{O}_2$  production<sup>147</sup>. Regarding the adsorption behavior at the  $\text{Fe}_3\text{O}_4(001)$  surface, most  $3d$  transition metals follow the trend described for Ni, but the different characteristics of each chemical element determine the details of the surface processes.

#### 4.2.4.1 Adsorption of Cobalt and Manganese

The results on the deposition of cobalt and manganese are combined into one section since their behavior is similar in many respects, and Mn was only studied using STM. Both metals, Co and Mn, are observed to form single adatoms upon deposition. In contrast to Ni and Ag, however, the surface is rich in bright features on the  $\text{Fe}_{\text{oct}}$  rows already after the deposition of low coverages of Co and Mn. Figure 4.22 shows two STM images of the  $\text{Fe}_3\text{O}_4(001)$  surface, one with 0.4 ML Co (a), the second one with 0.2 ML Mn (b). In both cases the metal adatoms closely resemble Ni adatoms, but their coverage is substantially lower than the nominally deposited amount of metal. Moreover, a large number of “on-the-row” features is observed. For Ni, such a high density was only observed after depositing a significantly higher metal coverage. For Co and Mn, adatom-like features

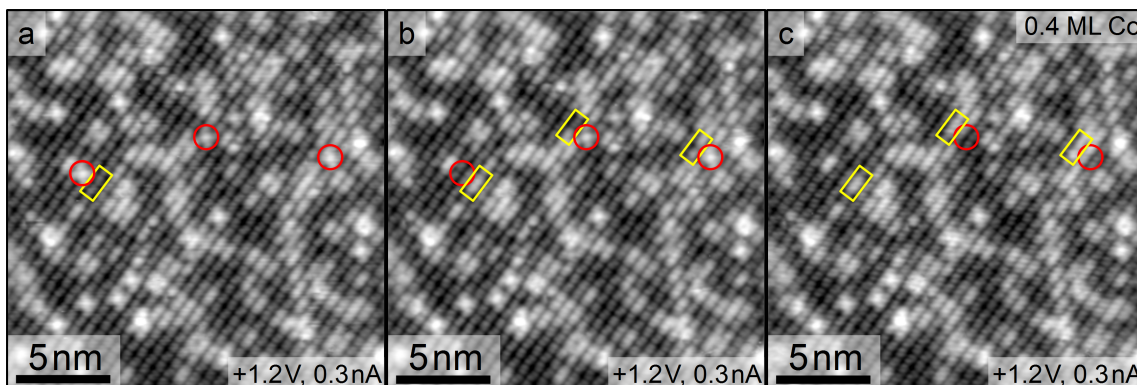


**Figure 4.23:** Incorporation of Co adatoms at room temperature. Subsequent STM images (same area) of 0.4 ML Co/Fe<sub>3</sub>O<sub>4</sub>(001) show the transition of the Co adatoms in the red circles to bright “on-the-row” features highlighted by the yellow frames.

with an increased apparent height are observed as well as further, unidentified bright species. These features form while the sample is kept in UHV and are therefore attributed to adsorption of molecules from the residual gas (analyzed in detail for Co below, see for example Figure 4.26).

Figure 4.23 shows an STM image sequence selected from a continuous 11-frame STM movie (in total 26 frames in two different areas) demonstrating the transition from Co adatoms to bright “on-the-row” features at room temperature. The adatoms in the red circles disappear, and bright protrusions are created on the adjacent surface Fe row sections, as highlighted by the yellow frames. This process is observed after each deposition of Co and at all stable scanning conditions. In accord with the Ni results, this process is attributed to Co incorporation into the surface region. This lifts the reconstruction locally, in agreement with the unreconstructed surface observed for Co-doped Fe<sub>3</sub>O<sub>4</sub> films<sup>113</sup> at doping levels  $\geq 18\%$ . A detailed study of the thermal stability of Co adatoms was not performed, but for 0.6 ML Co significant loss of Co-related features was found to occur upon annealing at 520 K for 5 min (not observed after a previous annealing step at 420 K). This is most likely related to Co diffusing from the surface region into the Fe<sub>3</sub>O<sub>4</sub> bulk. For Mn adatoms, similar incorporation processes are observed. However, Mn is found to be highly reactive for adsorption from the residual gas, rendering a detailed characterization challenging. The short sequence of two STM images in Figure 4.24 illustrates a selection of the processes occurring at the surface after the deposition of Mn. The red frame highlights the transition of a Mn adatom to a bright “on-the-row” feature. The yellow frame marks two adatoms, which undergo different processes attributed to adsorption from the residual gas and mobility. The upper adatom disappears, leaving an empty adsorption site, while the second

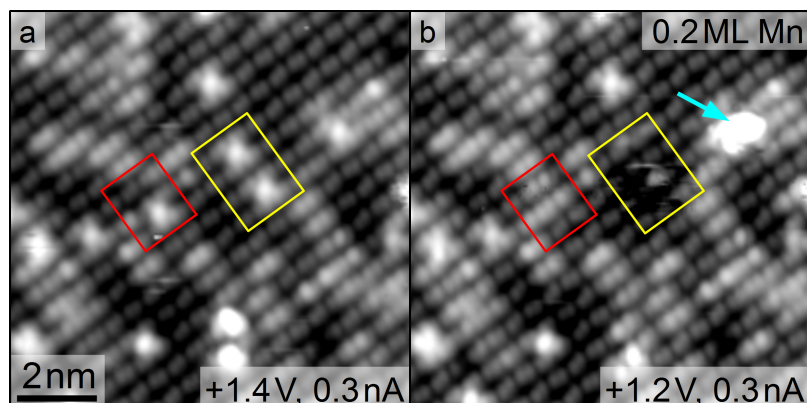


**Figure 4.24:** Incorporation, mobility, and reactivity of Mn adatoms. STM images of the same area of 0.2 ML Mn/Fe<sub>3</sub>O<sub>4</sub>(001) demonstrate the incorporation of a Mn adatom into the surface region (highlighted by the red frame). In parallel Mn adatoms in the yellow frame contribute to the formation of a dark surface feature (yellow frame in (b)) and the bright feature highlighted by the cyan arrow. Both processes are likely related to adsorption from the residual gas and are characteristic of the high activity of Mn adatoms.

one is replaced by a dark, scratchy feature. Adjacent to this area, another adatom is transformed to the bright feature highlighted by the cyan arrow. In addition to demonstrating the incorporation of Mn at room temperature, this experiment portrays Mn adatoms as highly reactive species since different adsorption events from the residual gas are observed at pressures  $<10^{-10}$  mbar.

The valence states of the Co species in the surface region were studied using XPS. The spectra were acquired in the surface chemistry chamber described in the previous section on Ni adatoms (section 4.2.3). Since the Co  $2p$  peak position coincides with a strong Fe Auger peak for the excitation energy of Al-K $\alpha$ , monochromated Ag-L $\alpha$  X-rays were used in this experiment. Figure 4.25(a) shows a photoemission spectrum of 2 ML Co acquired at room temperature. The peak positions of the Co  $2p_{3/2}$  peak and its satellite at high binding energy are in good agreement with literature values<sup>113,148</sup> for CoO, indicative of Co<sup>2+</sup> ions in an octahedral coordination to oxygen. The room temperature STM image of 1 ML Co/Fe<sub>3</sub>O<sub>4</sub>(001) in Figure 4.25(b) provides real-space information on the adsorption preference of Co at high coverages. Bright features on the surface Fe rows, assigned to incorporated Co atoms, are the main Co-related species in the image. They coexist with a low coverage of Co adatoms (examples are highlighted by the red circles). The high-coverage results indicate a low adatom saturation coverage and a strong tendency to incorporate. Several preferential metal adsorption sites are occupied by features that resemble Co adatoms but exceed their apparent height. In the low-coverage images these

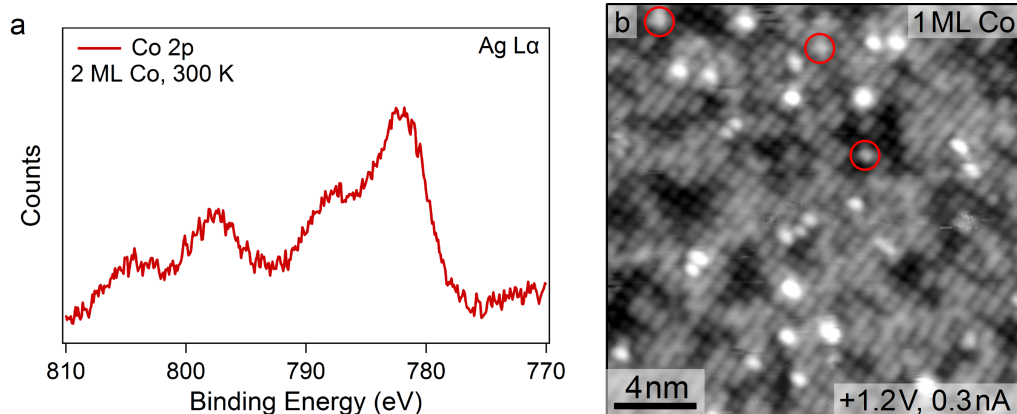


**Figure 4.25:** High coverage of Co/Fe<sub>3</sub>O<sub>4</sub>(001). (a) Co 2p XPS of 2 ML Co. The spectrum shows two components, which can be assigned as Co<sup>2+</sup> and a high-binding energy satellite, which is common in CoO. (b) STM image of 1 ML Co. The majority species are bright “on-the-row” features corresponding to incorporated Co atoms; the red circles highlight examples of Co adatoms.

species were attributed to adsorption from the residual gas on the basis of STM movies. However, here their formation is not observed and in particular the bright, oval features cannot be identified unambiguously. Their occurrence at high coverages suggests that they could be a dimer species, forming as a result of the lifting of the reconstruction and the concomitant reduction of the distance between two potential Co adsorption sites. This assignment is supported by the lack of two nearest-neighbor Co adatoms in the image, and the absence of the bright oval species in larger reconstructed patches (e.g. in the immediate surroundings of the highlighted adatoms).

The adsorption and incorporation of Co was also studied in DFT+*U* calculations on a single ( $\sqrt{2} \times \sqrt{2}$ )R45°-reconstructed unit cell. For Co, the atomic radius was set to 1.9 bohr (=1.01 Å) and a Hubbard-*U* of 3.8 eV was used to describe the correlated Co 3*d* electrons. The plane-wave cut-off energy was set to  $\approx 297$  eV and the reciprocal space was mapped using a (3×3×1) *k*-mesh. In the Co adsorption study the same configurations were calculated as for Ni: the Co adatom on the SCV structure and the incorporation of Co in three different sites (Co<sub>oct</sub>(S), Co<sub>tet</sub>(S-1), Co<sub>oct</sub>(S-2)). These configurations are illustrated for Ni in Figure 4.18. In the case of incorporated Co, the characteristic subsurface vacancies underlying the reconstruction are filled by Fe<sub>int</sub> and a Co atom (Co<sub>oct</sub>(S-2)) or a second Fe atom displaced by the incorporation of Co (Co<sub>oct</sub>(S), Co<sub>tet</sub>(S-1)). In addition, the incorporation in a deeper FeO<sub>2</sub> layer (Co<sub>oct</sub>(S-6)) was calculated to determine if the preference for diffusion to the bulk is predicted correctly by the DFT calculations. The incorporation in the bulk-like layer is indeed the most favorable configuration with an energy

of  $\Delta E=5.75$  eV. The trends in the incorporation behavior of Co are similar to Ni, but the energy differences are smaller. In the surface region,  $\text{Co}_{\text{oct}}(\text{S-2})$  is the favored geometry ( $\Delta E=5.59$  eV) followed by the Co adatom ( $E_{\text{ads}}=5.46$  eV) and the incorporation into the surface layer ( $\Delta E=5.41$  eV). The tetrahedrally coordinated  $\text{Co}_{\text{tet}}(\text{S-1})$  is the least favorable site ( $\Delta E=5.27$  eV). The smaller energy differences compared to Ni agree with the weaker preference of  $\text{CoFe}_2\text{O}_4$  for the inverse spinel arrangement<sup>144</sup>. The Co atoms assume a  $\text{Co}^{2+}$ -like charge state and a high-spin magnetic configuration ( $|\vec{\mu}_{\text{Co}}|\approx 3 \mu_{\text{B}}$ ). This is the case for all geometries including the Co adatom, which shows a slightly reduced magnetic moment. The magnetic moments all follow the ferrimagnetic arrangement of the octahedral and tetrahedral sublattices in magnetite; in contrast to most metals including Ni, the Co adatom couples antiferromagnetically to the  $\text{Fe}_{\text{oct}}$  cations. As in the case of Ni, the Co charge states were determined from a comparison of the magnetic moments of the entire slab before and after deposition. In combination with the changes of the moments and the charge distribution inside the atomic spheres, this analysis allows conclusions on the electronic configuration of the atoms and the electron transfer to the substrate. Both, the adsorbed and incorporated Co atoms, are found to donate the two Co 4s electrons to the  $\text{Fe}_{\text{oct}}(\text{S-4})$  cations, inducing a  $\text{Fe}^{2+}$ -like character in two atoms in the (S-4) layer. This is interesting in the context of a valence band ARPES study on Co-doped  $\text{Fe}_3\text{O}_4(001)$  thin films, which reports the suppression of the  $\text{Fe}^{2+}$ -like peak for Co doping levels in excess of 18%. The authors attribute this effect to the preferential formation of  $\text{Co}^{2+}$  replacing the  $\text{Fe}^{2+}$  in the spinel lattice. This explanation is in accord with the present DFT results, since the doping level corresponding to the incorporation of a single adatom is substantially lower, leading to the donation of electrons to  $\text{Fe}_{\text{oct}}$  atoms to form  $\text{Fe}_{\text{oct}}^{2+}$ .

The characteristic distances introduced in Figure 4.9 were also determined for the Co adatom: The bond length to the surface oxygen atoms is  $d_{\text{Co-O}}=1.86$  Å and the height above the average surface  $\text{Fe}_{\text{oct}}$  ( $\Delta z_{\text{Co-FeB}}=0.55$  Å). The presented results on Co and Mn adsorption provide additional evidence for the incorporation of transition metals. The transition observed in STM at room temperature illustrates the fact that each metal is subject to a different barrier for incorporation. Considering the manifold of processes occurring in parallel while scanning a small area of the sample in UHV ( $<10^{-10}$  mbar) at low adatom coverages, Co and Mn should be well-suited for reactivity studies. The interactions with the residual gas portray Co and Mn ferrite ( $\text{M}_x\text{Fe}_{3-x}\text{O}_4$ ,  $\text{M} = \text{Mn}, \text{Co}$ ) as promising materials for adsorption studies. For example, both materials have been reported to exhibit a high activity for the oxygen reduction reaction<sup>146</sup>.

## Cobalt adatom–gas interaction

For cobalt the interaction with CO and O<sub>2</sub> was studied using STM image sequences and DFT+*U* calculations. In a 30-frame STM movie the interaction of Co with up to 5×10<sup>-8</sup> mbar CO was investigated. No discernible effects of CO compared to STM in UHV could be observed in the movie or in different regions on the surface scanned after exposure (not shown). These images in different areas were acquired to check for potential effects of the STM tip. The DFT+*U* calculations of CO adsorption on Co adatoms predict a weaker interaction than for example for Ni. The CO adsorption energy of  $E_{ads,CO}=1.16$  eV is the lowest among all adatoms considered in the CO adsorption study. The metal-surface bond is stretched to  $d_{Co-O}=1.99$  Å ( $\Delta d_{Co-O}=0.13$  Å), whereas the height above the average surface  $Fe_{oct}$   $\Delta z_{Co-FeB}=1.13$  Å changes significantly (by  $\Delta(\Delta z)=0.58$  Å), showing that the surface O atoms are also pulled upwards by the CO adsorption on the Co adatom. The charge state of the Co remains unchanged but its spin-polarization is slightly reduced.

The adsorption of O<sub>2</sub> was calculated for a flat O<sub>2</sub> geometry, resulting in a higher adsorption energy than on Ni ( $E_{ads,O_2}(Co-O_2)=2.26$  eV). The characteristic bond lengths are stretched to similar values to the ones after CO adsorption ( $d_{Co-O}(Co-O_2)=1.99$  Å and  $\Delta z_{Co-FeB}=1.15$  Å). This prediction of a strong interaction between Co and O<sub>2</sub> is supported by experimental findings. Figure 4.26 shows representative images from an STM movie of 0.4 ML Co exposed to different pressures of O<sub>2</sub>, resulting in adsorption processes and the creation of different bright surface species. The surface before O<sub>2</sub> exposure contains Co adatoms (examples highlighted by red circles) and bright “on-the-row” features, corresponding to filled subsurface vacancies due to incorporated Co. The image in Figure 4.26(b) was acquired after ≈15 min exposure to 10<sup>-9</sup> mbar O<sub>2</sub>. The significantly increased apparent height of the adatoms in the cyan circles is attributed to adsorption of O<sub>2</sub>. The yellow frame indicates an area with an adatom and incorporated Co atoms, which rearrange to become a bright, scratchy feature in (c). The observations in this movie offer an explanation for the bright surface features, which are present on the as-prepared sample after the deposition of Co. The metals are deposited in the preparation chamber after preparing the sample via sputtering and annealing. For annealing, background pressures of O<sub>2</sub> up to 5×10<sup>-6</sup> mbar are used, which can lead to O<sub>2</sub> in the residual gas during deposition, potentially creating a low density of adsorption-induced Co species at the surface.

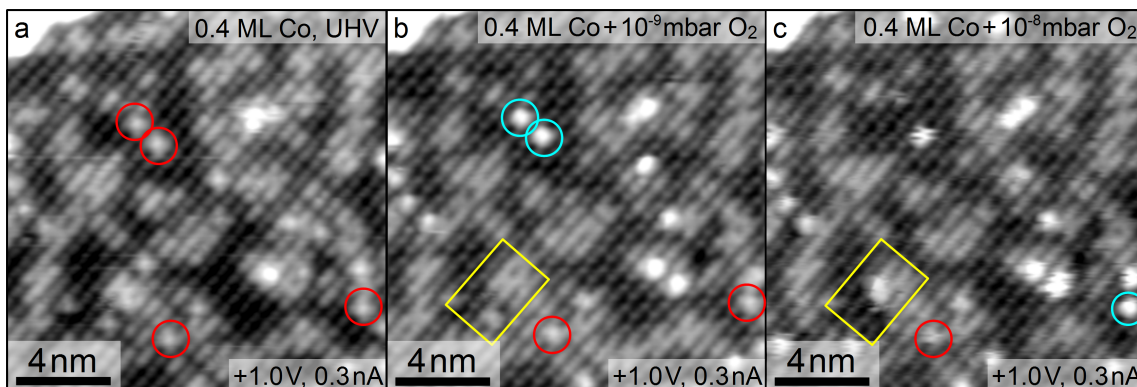


**Figure 4.26:** STM image sequence of  $\text{Co}/\text{Fe}_3\text{O}_4(001)$  exposed to  $\text{O}_2$ : (a) 0.4 ML Co before  $\text{O}_2$  exposure. The red circles highlight Co adatoms. Many bright “on-the-row” features (incorporated Co) are observed. (b) Exposure to  $10^{-9}$  mbar  $\text{O}_2$  for 15 min results in bright,  $\text{O}_2$ -related features on the Co adatoms (cyan circles). The yellow frame highlights an area where rearrangement occurs between (b) and (c). (c) Subsequent image after increasing the  $\text{O}_2$  pressure to  $10^{-8}$  mbar. The adatom in the yellow frame in (b) joins an “on-the-row” feature to form a bright, scratchy species.

#### 4.2.4.2 Adsorption of Titanium and Zirconium

The study of transition metals at the  $\text{Fe}_3\text{O}_4(001)$  surface also includes metals that preferentially assume a 4+ charge state in the respective binary oxides. The two examples described in the present thesis are titanium and zirconium; both elements form binary oxides with a broad range of potential applications<sup>8,149,150</sup>. These two elements are discussed in one section since they exhibit similar behavior when deposited onto the  $\text{Fe}_3\text{O}_4(001)$  surface. Parts of the presented data have been published in an article on the adsorption and incorporation of transition metals<sup>140</sup>.

Figure 4.27 shows STM images of the  $\text{Fe}_3\text{O}_4(001)$  surface after the deposition of (a) 0.4 ML Ti and (b) 0.4 ML Zr onto a synthetic magnetite crystal (#356\_1). For both metals, only few adatoms are observed; examples are highlighted by red circles. The bright “on-the-row” features are the majority species observed in STM images. Considering the results presented in the previous chapters, these features are assigned to the incorporation of metal atoms. The features exceeding the adatoms in brightness are attributed to adsorption from the background gas on adatoms or at reactive sections of the surface Fe rows.

LEED experiments of high metal coverages provide additional evidence for the incorporation of Zr and Ti into the  $\text{Fe}_3\text{O}_4(001)$  surface. Figure 4.28(a) shows a diffraction pattern of the pristine surface. The red and yellow frames indicate the  $(\sqrt{2} \times \sqrt{2})\text{R}45^\circ$ -

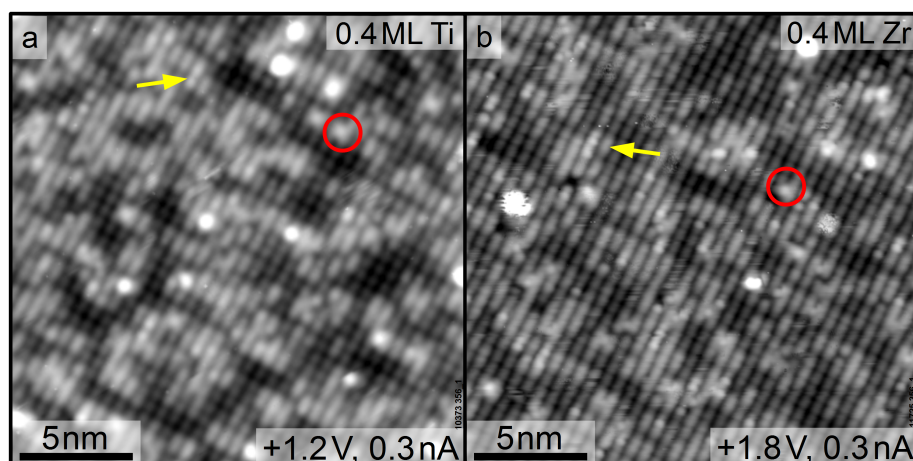


**Figure 4.27:** STM images of (a) 0.4 ML Ti and (b) 0.4 ML Zr deposited onto the  $\text{Fe}_3\text{O}_4(001)$  surface. Few single metal adatoms are observed (examples in the red circles). The bright features on the surface Fe rows are the majority species (examples indicated by yellow arrows). The different, very bright species on the surface Fe rows and in the preferential adsorption sites are assigned to adsorption from the residual gas.

reconstructed and the  $(1 \times 1)$  unit cells, respectively. The labels  $(1,0)$  and  $(0,1)$  highlight the first-order diffraction spots. For both experiments, the deposition of 1 ML Zr (b) and 2 ML Ti (c), the half-integer order diffraction spots vanish, demonstrating the lifting of the  $(\sqrt{2} \times \sqrt{2})\text{R}45^\circ$  reconstruction. The weaker relative intensity of the  $(-2,0)$  diffraction spot (compared for example to the  $(-1,1)$  spot) indicates that the surface structure has undergone a significant change, in agreement with the incorporation of a metal atom causing rearrangement in the subsurface layers.

Photoelectron spectroscopy of the adsorption of Ti and Zr shows large peak shifts, indicative of highly oxidized admetal species. The symmetric shape, the binding energy ( $\approx 458.4$  eV) and the peak separation ( $\Delta \approx 5.8$  eV) of the Ti  $2p$  peaks resemble spectra<sup>151</sup> of  $\text{TiO}_2$  (usually higher binding energy) and Ti ferrite<sup>152</sup> ( $\text{TiFe}_2\text{O}_4$ ), while the Zr  $3d$  peak at  $\approx 181.4$  eV is significantly lower in binding energy than  $\text{ZrO}_2$  but corresponds to Zr in mixed oxides<sup>153</sup>. Thus, the results for both deposited metals are interpreted as them being present in 4+ oxidation states. In analogy to Ni, Fe  $2p$  and valence band spectra for Ti were acquired at grazing emission ( $55^\circ$  off normal) at the synchrotron beamline I311 of the MaxIV Laboratory in Lund, Sweden. Figure 4.30 shows a comparison of spectra before (red lines) and after deposition of 0.4 ML Ti (blue lines). In the valence band region close to the Fermi energy the deposition of Ti causes the emergence of a strong shoulder at  $\approx 1$  eV (dashed vertical line), shifting the onset of the valence band maximum closer to the Fermi level. In the Fe core level region the  $2p_{3/2}$  peak is found to broaden towards lower

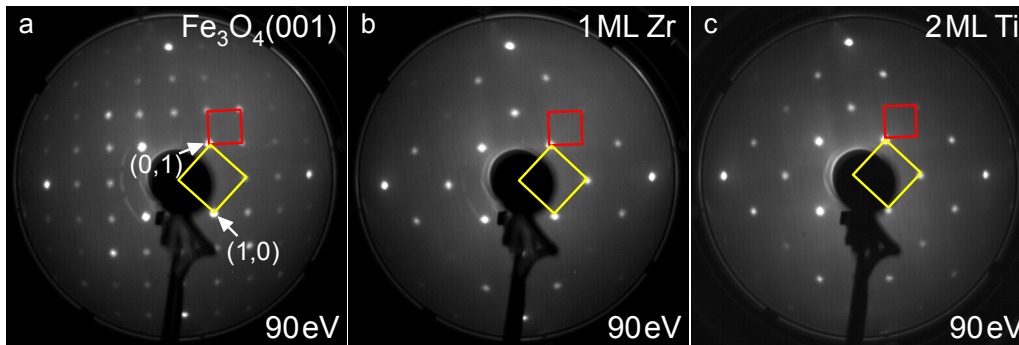


**Figure 4.28:** LEED patterns of (a) the pristine  $\text{Fe}_3\text{O}_4(001)$  surface and after deposition of (b) 1 ML Zr and (c) 2 ML Ti at room temperature. The yellow and red squares indicate the unreconstructed and the  $(\sqrt{2} \times \sqrt{2})R45^\circ$ -reconstructed unit cells, respectively. After deposition of a high coverage of Zr or Ti the reconstruction is lifted.

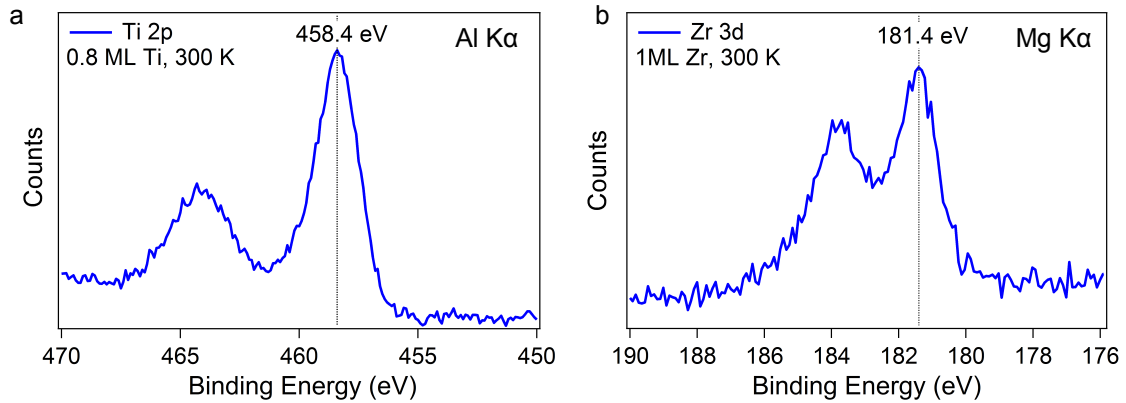


**Figure 4.29:** Photoemission spectra of (a) Ti and (b) Zr deposited onto the  $\text{Fe}_3\text{O}_4(001)$  surface at room temperature. The Ti 2p and Zr 3d peak positions both indicate highly oxidized species,  $\text{Ti}^{4+}$  and  $\text{Zr}^{4+}$ , suggesting a high degree of incorporation.

binding energies, which is a signature for a higher content of  $\text{Fe}^{2+}$  in the surface region. This indicates that the intensity in the valence band is related to an  $\text{Fe}^{2+}$  state<sup>114</sup> at  $\approx 1$  eV rather than to a Ti photoemission peak. These observations are qualitatively equivalent to the photoemission results after Ni deposition presented in section 4.2.3 (Figure 4.17) but the effects are significantly stronger for Ti, even though the nominally deposited coverage is significantly lower. This is in agreement with an almost complete incorporation of all deposited Ti atoms, which are expected to assume a  $\text{Ti}^{4+}$  state according to the Ti 2p spectra. The large number of electrons donated to the  $\text{Fe}^{3+}$  cations in the surface region results in the observed increase of the  $\text{Fe}^{2+}$  content close to the surface.

The strong effects observed in the VB photoemission and STM studies motivated DFT

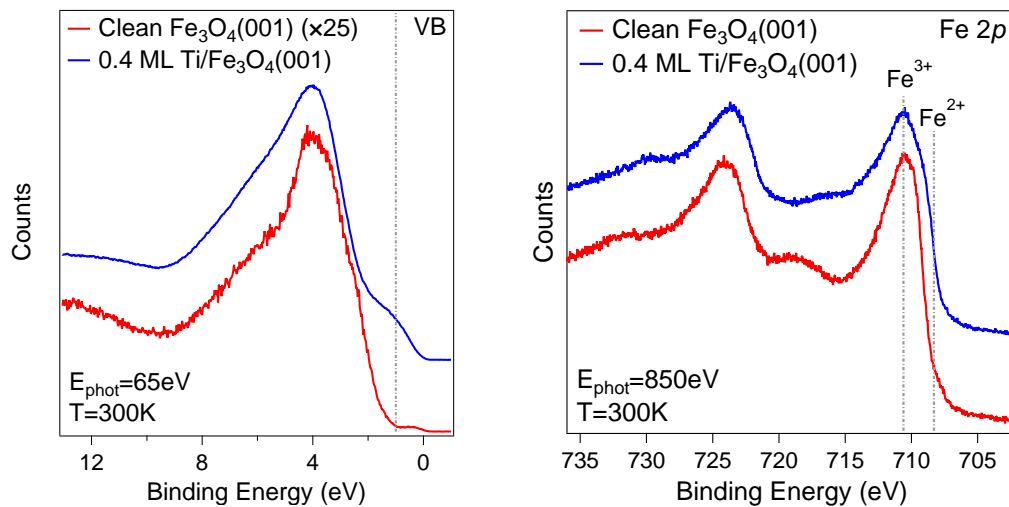


**Figure 4.30:** Valence band (VB) and Fe 2p spectra of 0.4 ML Ti/Fe<sub>3</sub>O<sub>4</sub>(001): Compared to the Fe<sup>3+</sup>-rich clean surface (red spectra), a strong Fe<sup>2+</sup>-like state emerges in the valence band region after the deposition of 0.4 ML Ti (blue spectrum). The presence of Ti causes a peak at a binding energy of  $\approx 1$  eV, corresponding to a shift of the onset of the valence band maximum closer to the Fermi energy. In the Fe 2p spectrum, the deposition of Ti enhances the shoulder at low binding energies and suppresses the Fe<sup>3+</sup> satellite peak.

calculations modeling the adsorption of Ti. The DFT calculations were performed on a slab consisting of one  $(\sqrt{2} \times \sqrt{2})R45^\circ$ -reconstructed unit cell, using an atomic sphere radius of 1.9 bohr for Ti ( $=1.01 \text{ \AA}$ ) and an effective Hubbard- $U$  of 3.8 eV to treat the correlated Ti 3d electrons. Increasing the value to  $U_{eff}=5$  eV for a relaxed structure did not lead to any significant changes in the electronic properties. The reciprocal space was sampled using a  $(3 \times 3 \times 1)$   $k$ -mesh and the plane-wave cutoff energy was set to  $\approx 297$  eV. For the adsorption of Ti, the same configurations as for Ni were considered (see Figure 4.18): a Ti adatom on the SCV structure and the incorporation of Ti creating a bulk-terminated configuration with one Ti atom per unit cell replacing an Fe atom as  $Ti_{oct}(S)$ ,  $Ti_{tet}(S-1)$ , or  $Ti_{oct}(S-2)$ . Ti was found to prefer the incorporation into one of the two octahedral sites with a small preference for the subsurface layer ( $\Delta E(Ti_{oct}(S-2))=8.28$  eV compared to  $\Delta E(Ti_{oct}(S-2))=8.22$  eV). The  $Ti_{tet}(S-1)$  configuration resulted in an energy of  $\Delta E=7.83$  eV, while the adatom was found to be unstable in the usual two-fold coordinated geometry. In the DFT force relaxation the Ti adatom entered the surface layer and distorted the first subsurface layer by displacing an  $Fe_{tet}(S-1)$  atom. Thus, the energy of  $E_{ads}=6.80$  eV does not fully correspond to an adatom geometry and the characteristic lengths  $d_{Ti-O}$  and  $\Delta z_{Ti-FeB}$  are not representative in a comparison to other metals. The instability of the Ti adatom on the SCV structure indicates that the few adatoms observed in experiments may be stabilized by unreconstructed unit cells due to incorporated Ti or other types of defects.

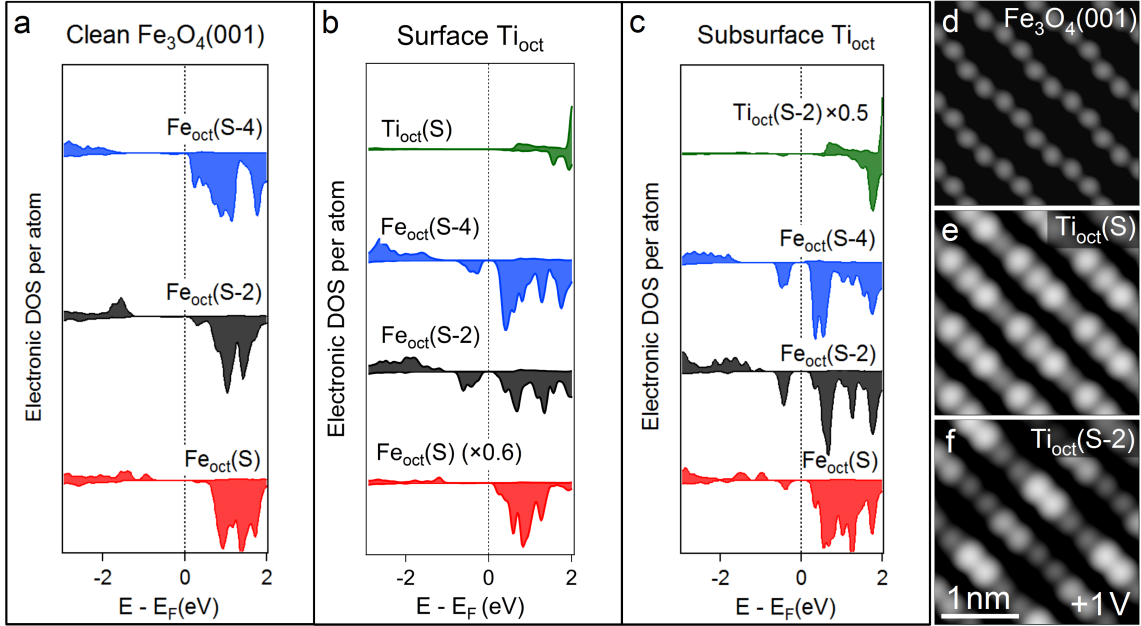


**Figure 4.31:** Density of states and STM simulations of incorporated Ti. (a) DOS of three  $\text{Fe}_{\text{oct}}$  layers showing no intensity in the occupied states close to  $E_{\text{F}}$ . (b) DOS after Ti incorporation in the surface layer. No Ti states are observed close to  $E_{\text{F}}$ , but the unoccupied surface Fe states shift closer to  $E_{\text{F}}$  and an  $\text{Fe}^{2+}$  state<sup>114</sup> emerges at  $\approx 1\text{ eV}$  below  $E_{\text{F}}$ . (c) DOS of the  $\text{Ti}_{\text{oct}}(\text{S}-2)$  configuration. Similar to (b), a shift towards  $E_{\text{F}}$  is observed in the unoccupied states, while an  $\text{Fe}^{2+}$  state emerges in the occupied DOS. (d-f) Simulated STM image of the pristine  $\text{Fe}_3\text{O}_4(001)$  surface and the  $\text{Ti}_{\text{oct}}(\text{S})$  (on a  $(\sqrt{2}\times\sqrt{2})R45^\circ$  reconstructed cell) and  $\text{Ti}_{\text{oct}}(\text{S}-2)$  (on a  $(2\times 2)$  supercell) configurations.

The very high energies for all configurations of Ti show that Ti gains a substantial amount of energy by binding to oxygen compared to the highly unfavorable state of a free atom. The Ti atoms do not exhibit a magnetic moment in any configuration, in agreement with the experimentally observed  $\text{Ti}^{4+}$  charge state. Moreover, the calculations reproduce the charge transfer to Fe atoms, which was concluded from the photoemission experiments. In all configurations of incorporated Ti the magnetic moments of Fe indicate the formation of  $\text{Fe}^{2+}$  in the  $\text{Fe}_{\text{oct}}(\text{S}-4)$  and  $\text{Fe}_{\text{oct}}(\text{S}-2)$  layers. The trend to reduce the Fe atoms in the surface region upon the incorporation of Ti is also discernible in the density of states of the  $\text{Fe}_{\text{oct}}$  layers after the incorporation of Ti in one of the two favorable sites ( $\text{Ti}_{\text{oct}}(\text{S})$  and  $\text{Ti}_{\text{oct}}(\text{S}-2)$ ) plotted in Figure 4.31(b, c). Compared to the  $\text{Fe}_{\text{oct}}$  DOS of the pristine surface in (a), a significant peak in the occupied states at  $\approx 1\text{ eV}$  below  $E_{\text{F}}$  emerges for both types of incorporation. In the unoccupied region, the Fe states shift closer to  $E_{\text{F}}$ , explaining the enhanced brightness of the incorporation-related features observed in STM images at low sample bias voltages. The simulated STM images in Figure 4.31(d-f) reflect the effects

observed in the DOS plots of the surface layer (red spectra). The image of Ti incorporated in the surface layer (e) shows a simulation of one reconstructed unit cell with periodic boundary conditions. Since the Ti DOS does not exhibit any states close to  $E_F$ , the features of enhanced brightness are attributed to the surface Fe atoms; the two atoms adjacent to the  $Ti^{4+}$  exhibit the largest apparent height. The STM simulation of the  $Ti_{oct}(S-2)$  configuration (f) is based on a  $(2 \times 2)$  slab (corresponding to a surface area of the size of two reconstructed unit cells), thus enabling a direct comparison of the unaffected, dark gray Fe atoms and the ones above a filled subsurface vacancy. In contrast to the incorporation of Ni, the brighter pair of surface Fe atoms corresponds to the site directly above the  $Ti^{4+}$ , indicating that for Ti even incorporation in the subsurface causes substantial changes in the electronic structure of the surrounding Fe atoms up to the surface layer. These modifications of the electronic structure provide promising prospects for tuning the properties of magnetite via the incorporation of Ti or Zr.

The present study of the adsorption of 3d transition metals at the  $Fe_3O_4(001)$  surface illustrates the potential of this surface to serve as a template for different ultrathin spinel ferrite layers created by the incorporation of metals into the magnetite lattice. The formation of these nonstoichiometric ferrite phases provides access to ultrathin layers with modified physical properties by varying the deposited metal or even the amount of the dopant. Since the onset of diffusion to the bulk is likely determined by the activation energy for Fe mobility within the magnetite lattice, also mixed metal phases localized to the surface should be possible. In the context of model catalysis, the facile modification of the surface properties offers a fast and simple way to test a broad selection of potentially active ferrite materials. However, the application is limited to low temperature reactions by the thermal stability of the metal species in the surface region.

#### 4.2.5 Platinum

Platinum is widely used in nanoparticle catalysis and is regarded one of the prototypical single-atom catalyst materials<sup>36,37</sup>. In pioneering single-atom catalysis studies, the essential role of Pt as an active metal was confirmed at the single particle level<sup>39</sup>, showing for example that Pt adatoms catalyze CO oxidation<sup>40</sup> when supported on  $FeO_x$ . Furthermore, Pt adatoms were reported active for a variety of further reactions, such as water-gas shift<sup>39</sup>, NO oxidation<sup>154</sup>, NO reduction<sup>155</sup>, or selective hydrogenation reactions<sup>47</sup>. Thus, Pt is also a highly promising metal for a reactivity study at the  $Fe_3O_4(001)$  surface. In a recent article on strong metal-support interactions of Pt clusters on  $Fe_3O_4(001)$  thin films, Zhang *et al.* present STM images of Pt adatoms and clusters<sup>156</sup>. The adsorption proper-

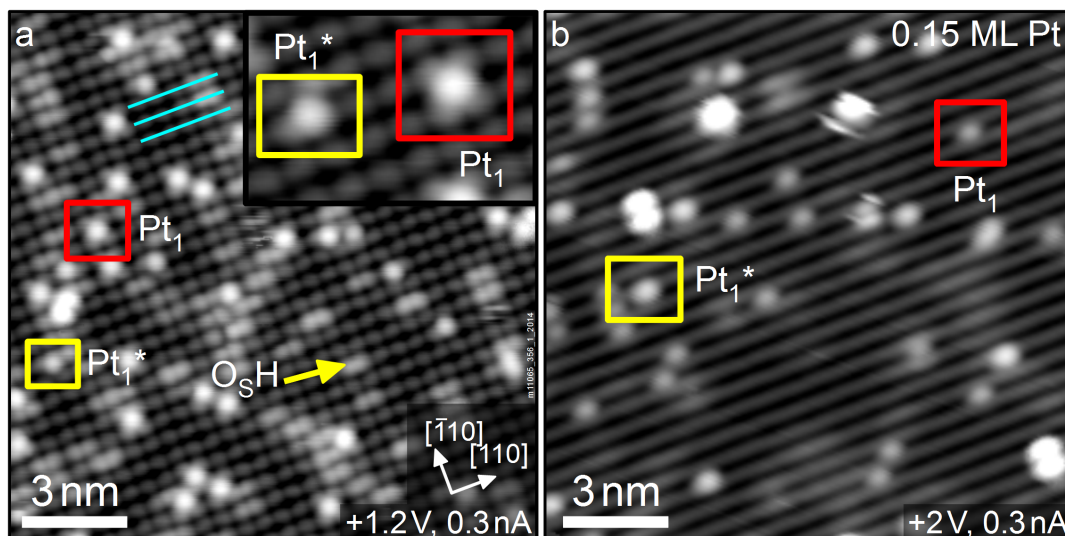


**Figure 4.32:** STM images of the as-deposited Pt/Fe<sub>3</sub>O<sub>4</sub>(001) acquired at two different scanning voltages (1.2 V (a), 2 V (b)). Two different species of Pt atoms are observed at the surface. Examples are highlighted by the red and yellow frames and labeled Pt<sub>1</sub> and Pt<sub>1</sub>\*. Pt<sub>1</sub> is located in the preferred adsorption site, whereas Pt<sub>1</sub>\* occupies a site offset to the side from Fe<sub>int</sub> and shifted by half an Fe-Fe distance along the surface rows. The cyan lines in (a) indicate the Fe row direction. The features with significantly larger apparent height than the adatoms in (b) are attributed to adsorption from the residual gas, which is analyzed in detail in section 4.2.5.2.

ties on Fe<sub>3</sub>O<sub>4</sub>(001) single crystals and the results on Pt-gas interactions described in the present section were published recently by Bliem *et al.*<sup>157</sup>.

#### 4.2.5.1 Pt adsorption

At room temperature platinum adsorbs mainly in the form of stable, immobile metal adatoms in the preferred metal adsorption site of the Fe<sub>3</sub>O<sub>4</sub>(001) surface reconstruction. Examples of Pt adatoms are highlighted by red frames labeled Pt<sub>1</sub> in Figure 4.32. However, the STM images in Figure 4.32 also exhibit a number of different features. The bright features offset to the side from the Fe<sub>int</sub> site (examples highlighted by yellow frames labeled Pt<sub>1</sub>\*) are observed in high density after deposition whereas they do not occur on the pristine surface or for any of the metals discussed above. Figure 4.33 demonstrates that these features correspond to an atomic Pt species. In the STM image in (a) three examples of Pt<sub>1</sub>\* species are highlighted by yellow frames. The subsequent STM image of the same area in (b) demonstrates that the highlighted features have diffused to a preferential adsorption site to become Pt<sub>1</sub> adatoms. This site change from Pt<sub>1</sub> to Pt<sub>1</sub>\* is observed regularly in STM image sequences. The opposite process does not occur, indicating a clear

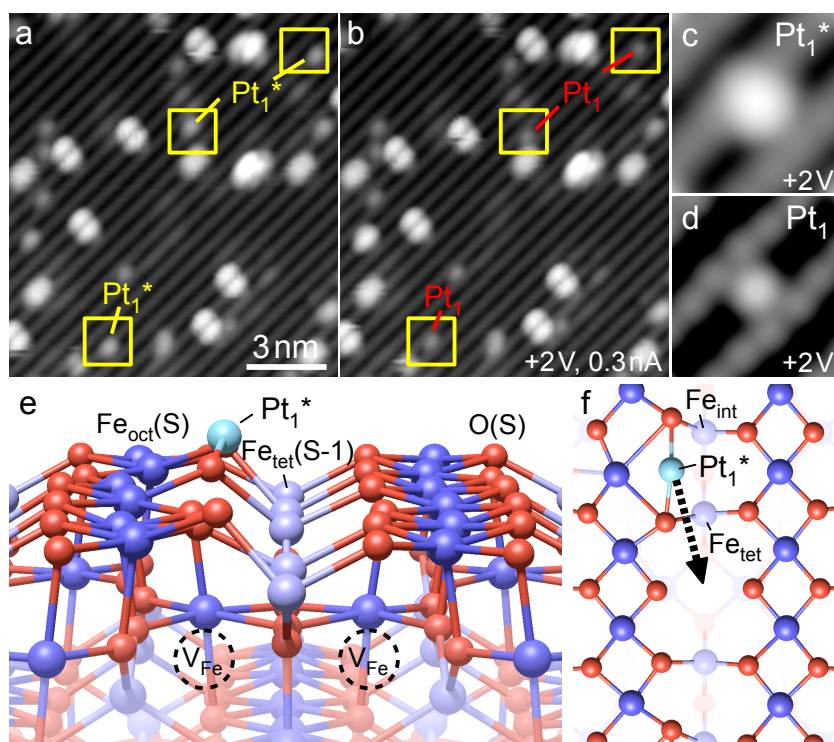


**Figure 4.33:** Pt adatoms in two adsorption sites. (a) STM image of 0.2 ML Pt/Fe<sub>3</sub>O<sub>4</sub>(001) with examples of Pt<sub>1</sub>\* species highlighted by the yellow frames. (b) Subsequent image (same area): The Pt<sub>1</sub>\* features labeled in (a) have switched to the preferred site and have become regular Pt<sub>1</sub> adatoms. (c, d) Simulated STM images of DFT force-relaxed Pt<sub>1</sub> and Pt<sub>1</sub>\* geometries. (e, f) Side and top view of the force-relaxed structure of Pt<sub>1</sub>\* / Fe<sub>3</sub>O<sub>4</sub>(001). The Pt atom cannot occupy the site blocked by Fe<sub>int</sub> but adsorption in a two-fold coordination to oxygen parallel to the surface Fe rows is possible. The black dashed arrow in (f) indicates the direct path connecting the Pt<sub>1</sub> and Pt<sub>1</sub>\* sites. The initial sites of Pt for the DFT-based calculation of the diffusion barrier are located at equidistant positions along this path.

energetic preference for adsorption in the bridging site between two surface FeO<sub>2</sub> rows, in analogy to the other metal adatom species presented above. The force-relaxed adsorption geometries for both sites were determined in DFT+*U* calculations (on a 2×2 unit cell,  $r_{Pt}=2.1$  bohr=1.11 Å, no Hubbard-*U* for the Pt because testing  $U(Pt)=3.8$  eV did not yield any significant effect). A plane-wave cut-off energy of ≈297 eV and a (3×3×1) *k*-mesh were employed. The simulated STM images of the respective equilibrium configurations of Pt<sub>1</sub>\* and Pt<sub>1</sub> shown in Figure 4.33 are in good agreement with the features in experimental images. The stable structure of the Pt<sub>1</sub> adatom resembles the structures shown previously for other metals, while the Pt<sub>1</sub>\* atom binds in a bridging geometry between two surface oxygen atoms at the same Fe<sub>oct</sub>O<sub>2</sub> row. A side view and a top view of the Pt<sub>1</sub>\* configuration are shown in Figures 4.33(e, f).

In agreement with the hopping preference observed experimentally, the DFT calculations predict a clear energy difference favoring the Pt<sub>1</sub> geometry ( $E_{ads}=3.89$  eV for Pt<sub>1</sub> compared to  $E_{ads}=3.01$  eV for Pt<sub>1</sub>\*). This result raises the question why any atoms are found to occupy the Pt<sub>1</sub>\* adsorption site at room temperature. The stability must result from a energy barrier, which is high enough to kinetically limit diffusion between the two sites. In DFT+*U* calculations, different geometries located in between the two favored adsorption sites were considered in order to confirm the existence of a diffusion barrier, which is sufficient to explain the experimentally observed behavior. For this purpose the calculations were started initially at six equidistant positions along the dashed arrow connecting the Pt<sub>1</sub>\* and the Pt<sub>1</sub> positions in the top-view structural model in Figure 4.33(f). Starting from each of the six positions, constrained force-relaxations were performed, in which the motion parallel to the surface Fe row direction was suppressed. Using this approach, the Pt atom relaxes to the local force minimum within a plane perpendicular to the surface Fe rows, constrained not to move towards one of the adsorption sites. Thus, the relaxation provides energy values at the specified intervals along the minimum energy path. The highest energy along this path corresponds to a good approximation of the diffusion barrier. This is true under the assumption that the approximation by discrete steps does not lead to sections of lower-energy paths which are not accessible to an atom undergoing a continuous diffusion process (e.g. strong relaxations in opposite directions). Close to the highest calculated energies, the density of the grid of starting positions was increased in order to find a close approximation to the full height of the barrier. The highest barrier was found for a position  $\approx 0.95$  Å from the Pt<sub>1</sub>\* site ( $\Delta E=0.913$  eV compared to  $E_{ads}(Pt_1^*)$ ). In order to ensure that the final value does not correspond to a local minimum, the calculation was restarted from two different positions in the plane perpendicular to the surface Fe rows, but both times the atom relaxed back to the same position. Assuming an Arrhenius-type behavior and a rate prefactor of  $10^{13} \text{ s}^{-1}$ , the calculated activation barrier corresponds to a thermally activated diffusion rate of  $<5 \times 10^{-3} \text{ s}^{-1}$  at 300 K. This value agrees with the timescale of the observed hopping process, indicating that it is thermally activated at room temperature; however, an influence of the STM tip cannot be excluded. The calculated barrier is in good accord with the experimental observation that annealing at 550 K for 10 min leads to a substantial decrease in the Pt<sub>1</sub>\*:Pt<sub>1</sub> ratio from 1:2.7 in room-temperature experiments to 1:14. The small number of remaining Pt<sub>1</sub>\* features is likely due to a higher kinetic barrier hindering diffusion, for example caused by surface defects.

While no clusters are created during the deposition of 0.2 ML Pt, STM images at different coverages demonstrate that the deposition of higher amounts of Pt increases the tendency towards cluster formation. Figure 4.34 provides a comparison of STM images

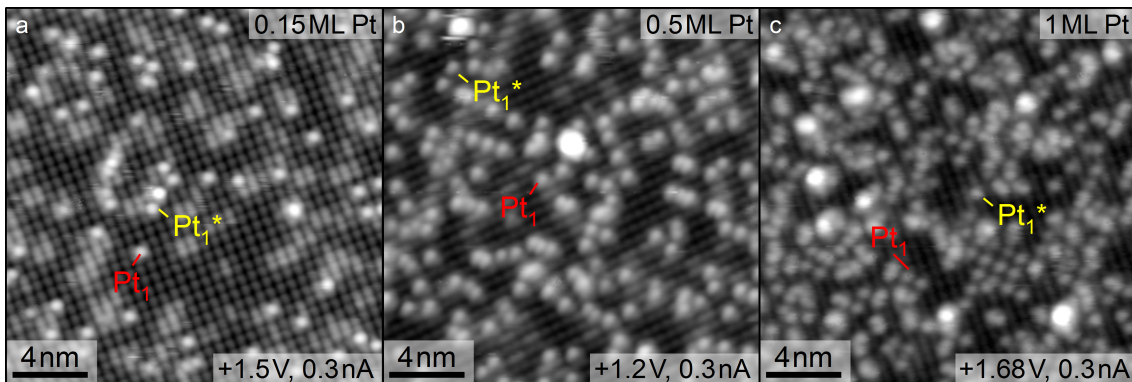


**Figure 4.34:** Increasing coverage of Pt/Fe<sub>3</sub>O<sub>4</sub>(001) (not the same area). (a) After the deposition of 0.15 ML only adatoms populate the surface; Pt atoms are observed in both adsorption sites. In all images examples of Pt<sub>1</sub> and Pt<sub>1</sub>\* are highlighted by red and yellow labels, respectively. (b) At 0.5 ML Pt a low coverage of clusters starts forming. (c) Further increases in the coverage lead to slow filling of the adatom layer and a growing tendency to form clusters. For 1 ML Pt more than ten clusters are observed in an area of 20×20 nm<sup>2</sup>.

at different (nominal) coverages to determine the approximate onset of cluster formation; a descriptor of the adatom stability. Examples of the two different adatom species are labeled in each panel. Similar to the Ag experiments, no clusters are observed at coverages  $\leq 0.2$  ML (see Figure 4.34(a)). Increasing the nominal deposited amount of Pt to 0.5 ML (b) results in a low coverage of clusters at the surface, see, e.g. the tall bright feature in the center of panel (b). This feature exhibits an apparent height in excess of 300 pm, compared to 130-150 pm for Pt<sub>1</sub> adatoms at the respective scanning conditions (1.2 V, 0.3 nA). Increasing the coverage to 1 ML (c) results in the creation of more clusters coexisting with adatoms at the surface. More than ten clusters are observed on a representative area of 20×20 nm<sup>2</sup> upon deposition, whereas the filling of the adatom layer proceeds more slowly. In analogy to Ag, the absence of clusters at intermediate adatom coverages is interpreted as an indication for a critical cluster size which is larger than a Pt dimer. One important difference, however, could be the mobility of Ag adatoms, which indicates a low barrier for site changes at room temperature. In contrast, the switching from the energetically less favorable Pt<sub>1</sub>\* site is the only observed mobility for pristine Pt adatoms. DFT+*U* calculations of a Pt dimer confirm the hypothesis that it is unstable with respect to decay into two adatoms. The energy of a Pt dimer  $E_{ads}(Pt_2)=6.35$  eV is substantially lower than two times the energy of a Pt adatom ( $E_{ads}(Pt_1)=3.89$  eV). However, a decay into two Pt<sub>1</sub>\* species ( $E_{ads}(Pt_1^*)=3.01$  eV) would be unfavorable. The force-relaxed Pt dimer assumes a configuration with one Pt atom in an adatom-like geometry while the second Pt atom is pointing upwards but is tilted parallel to the surface Fe rows, possibly

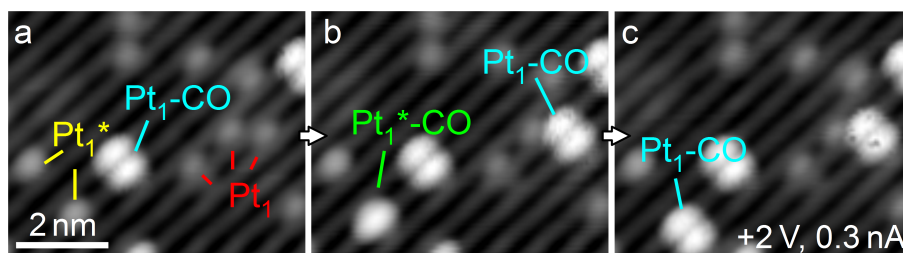


**Figure 4.35:** STM image sequence of Pt adatoms during exposure to  $2 \times 10^{-10}$  mbar CO. (a) Adatoms in both sites (highlighted in red and yellow) coexist with bright, two-lobed  $Pt_1$ -CO species (cyan). (b) CO adsorbs on a  $Pt_1^*$  (labeled in green) and on a  $Pt_1$  species (cyan). (c) The  $Pt_1^*$ -CO feature switches sites to become a  $Pt_1$ -CO.

forming a weak bond to one of the next surface O atoms. The dimer species is, however, not stable without the influence of adsorption, as is described in section 4.2.5.2.

The characteristic properties of the adatoms such as charge transfer, bond length, and height above the surface plane were also determined for the different Pt species. The Pt atoms exhibit only very weak spin-polarization in all configurations; the maximum magnetic moment inside the atomic sphere of Pt is  $0.3 \mu_B$  for the  $Pt_1$  adatom. The total magnetic moment of the slab is unchanged for both Pt adatom geometries. For the  $Pt_1$  adatom some charge is transferred to the substrate, borne out in a small reduction of the magnetic moments of the subsurface  $Fe_{oct}$  and the surface  $O^{1-}$  atoms. Since this is not the case for  $Pt_1^*$ , a neutral charge state is assigned to it, whereas for the Pt adatom in the preferential adsorption site the partial charges and magnetic moments indicate a weakly cationic character of  $Pt_1^{\delta+}$ . The two atoms comprising the Pt dimer exhibit different properties: The first atom's similarity to the adatom configuration is also expressed in the charge transfer ( $Pt^{\delta+}$ ) while the second Pt shows the characteristics of a neutral atom.

The two Pt adsorption sites differ also regarding the characteristic distances: The bond lengths to the surface oxygen atoms for  $Pt_1$  and  $Pt_1^*$  are  $d_{Pt-O} = 1.98 \text{ \AA}$  and  $d_{Pt^*-O} = 2.03 \text{ \AA}$ , ( $d_{Pt^*-O} = 2.05 \text{ \AA}$  for the second  $O_S$ ), respectively. The different bonding site is the origin of the large difference in the height above the surface:  $\Delta z(Pt_1) = 0.47 \text{ \AA}$  and  $\Delta z(Pt_1^*) = 1.01 \text{ \AA}$ . The formation of a dimer leaves the Pt adatom bonding geometry almost unchanged:  $d_{Pt-O} = 1.99 \text{ \AA}$  and  $\Delta z(Pt_{2,1}) = 0.48 \text{ \AA}$  ( $\Delta z(Pt_{2,2}) = 1.80 \text{ \AA}$ ).

#### 4.2.5.2 Platinum adatom–gas interactions

In the STM images of Pt presented above (see, e.g. Figure 4.33), the large and bright surface features were attributed to adsorption from the residual gas. In order to determine

the reactive molecule adsorbing on Pt, STM image sequences were acquired while dosing different gases to the UHV background (in separate experiments). No significant effects associated with any specific gas could be identified except for CO, which was found to accelerate the formation of the bright, two-lobed features from Pt<sub>1</sub> adatoms. A significant effect was already observed when dosing very low CO pressures ( $p_{CO}=2\times 10^{-10}$  mbar) in an STM image sequence of 41 frames, a selection of which is on display in Figure 4.35. (In total 55 frames were acquired; some of them at elevated pressures up to  $10^{-9}$  mbar.) At this low pressure, a dose of 1 Langmuir corresponds to  $\approx 6.6\times 10^3$  s, but more than half of the Pt adatoms undergo adsorption in less than 1 h. This observation demonstrates the very strong interaction between Pt and CO and suggests the presence of weakly adsorbed CO at the Fe<sub>3</sub>O<sub>4</sub>(001) surface at room temperature, increasing the probability for CO molecules to interact with Pt. The high adsorption rate observed in this experiment strongly indicates that the features formed during the STM movie correspond to the adsorption of a single CO molecule on a Pt adatom. Potential alternative adsorbates such as impurities in the CO or two CO molecules at the same Pt adatom are highly improbable to form at a comparable rate. Thus, the bright, two-lobed features created by adsorption on Pt<sub>1</sub> adatoms are attributed to Pt<sub>1</sub>-CO species (Pt carbonyls). Figure 4.35(b) demonstrates an example of CO adsorption on Pt<sub>1</sub>\* forming a brighter and larger feature, which resembles one half of the Pt<sub>1</sub>-CO species. The identification of the feature as Pt<sub>1</sub>\*-CO is supported by its conversion into a Pt<sub>1</sub>-CO species in the next frame (Figure 4.35(c)).

The unusual shape of the Pt<sub>1</sub>-CO species in STM images motivated DFT+*U* calculations of the adsorption geometry of CO on Pt. Figure 4.36(a) displays a force-relaxed structural model of Pt<sub>1</sub>-CO. The adsorption of CO stretches the bonds between the adatom and the surface oxygen atoms and pulls the Pt towards one of the surface Fe<sub>oct</sub>O<sub>2</sub> rows. Thus, the characteristic bond lengths are significantly elongated:  $d_{Pt-O_{S,1}}(\text{Pt}_1\text{-CO})=2.03$  Å and  $d_{Pt-O_{S,2}}(\text{Pt}_1\text{-CO})=2.98$  Å; as well as the height above the average Fe<sub>oct</sub>(S),  $\Delta z=1.74$  Å, compared to neat Pt adatoms ( $d_{Pt-O}(\text{Pt}_1)=1.98$  Å and  $\Delta z(\text{Pt}_1)=0.47$  Å). The same relaxation in the opposite direction (towards the other surface row) is equivalent in energy; the central position is unfavorable by  $\Delta E\approx 0.25$  eV. A similar weakening of one bond to surface oxygen is observed for the Pt<sub>1</sub>\* species, which remains offset to the side from the site blocked by Fe<sub>int</sub> but is also lifted up, strongly stretching the bond to one surface oxygen atom:  $d_{Pt^*-O_{S,1}}(\text{Pt}_1^*\text{-CO})=2.03$  Å,  $d_{Pt^*-O_{S,2}}(\text{Pt}_1^*\text{-CO})=3.25$  Å, and  $\Delta z_{Pt^*-FeB}=2.14$  Å. The simulated STM image in the inset in Figure 4.36(a) resembles one half of the Pt-CO observed in the room-temperature STM study. In STM images acquired at low temperature (78 K) also only one of the two lobes comprising the bright Pt-carbonyl feature at room temperature was observed in the Pt<sub>1</sub> adsorption site at tunneling condi-

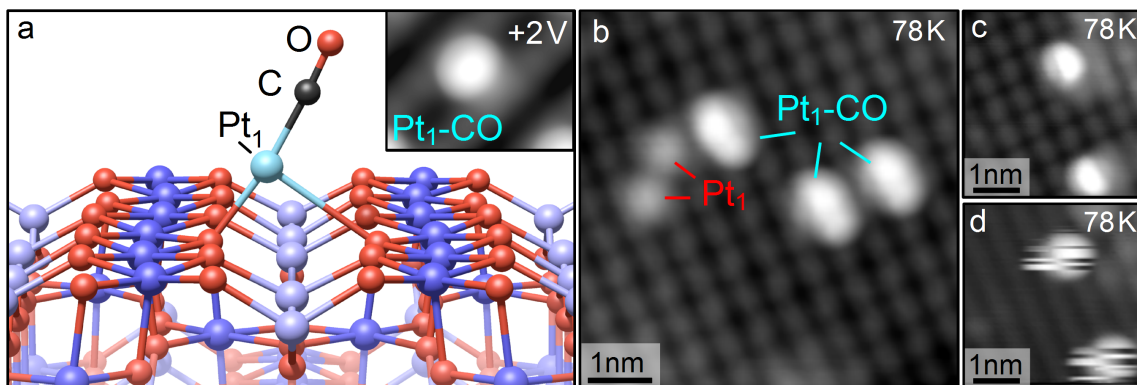


**Figure 4.36:** Adsorption geometry of  $Pt_1$ -CO. (a) Structural model of the force-relaxed DFT structure of  $Pt_1$ -CO on  $Fe_3O_4(001)$ . CO adsorption results in an asymmetric configuration; the Pt atom is pulled upwards and shifted closer to one of the Fe rows (both directions energetically equivalent). This asymmetry is also borne out in the simulated STM image in the inset. (b-d) Low-temperature STM images (78 K). The low temperature freezes the mobility between the two equivalent Fe row positions; one half of the two-lobed room-temperature feature is imaged in (b) at 1 V, 0.2 nA and (c) at 0.65 V, 0.3 nA. (d) Increasing the bias voltage (2 V, 0.3 nA) induces switching between the two equivalent sites, which are imaged as single lobes in (c).

tions of +1 V, 0.2 nA (b) and +0.65 V, 0.3 nA (c). The features observed at 2 V and 0.3 nA (d) are created by the influence of the STM tip, which shifts the Pt-CO between the two equivalent positions at the side of the adsorption site, demonstrating that the activation of this switching process is possible. The images of Pt-CO at room temperature are therefore interpreted as a time average of the fast, thermally activated hopping between the two equivalent sites offset from the center of the adsorption site of the neat adatom.

Figure 4.35 shows that the adsorption of CO, and the switching from  $Pt_1^*$ -CO to  $Pt_1$ -CO, can be observed step by step. The room-temperature STM image sequence in Figure 4.37 demonstrates that  $Pt_1$ -CO species are mobile at the surface and exhibit a tendency to agglomerate to small clusters. Initially adatoms are the main species at the surface and only few Pt-CO features or small clusters are observed (a). The image sequence in (b-g) focuses on the area highlighted by the yellow frame in (a). Starting from four adatoms in the two different adsorption geometries (two  $Pt_1$ , two  $Pt_1^*$  atoms) in (b), the sequence shows the adsorption of CO on one of each species in (c). In Figure 4.37(d) the first agglomeration step is observed and a Pt dimer is formed. In the following images, the  $Pt_1^*$ -CO becomes mobile to form a trimer species (e) and after the remaining Pt adatom adsorbs CO (f), a Pt tetramer is formed (g). The overview image in (h) demonstrates that agglomeration can be followed for all clusters in the scanned area. Images in different regions of the sample do not show any discernible difference, indicating that the STM tip

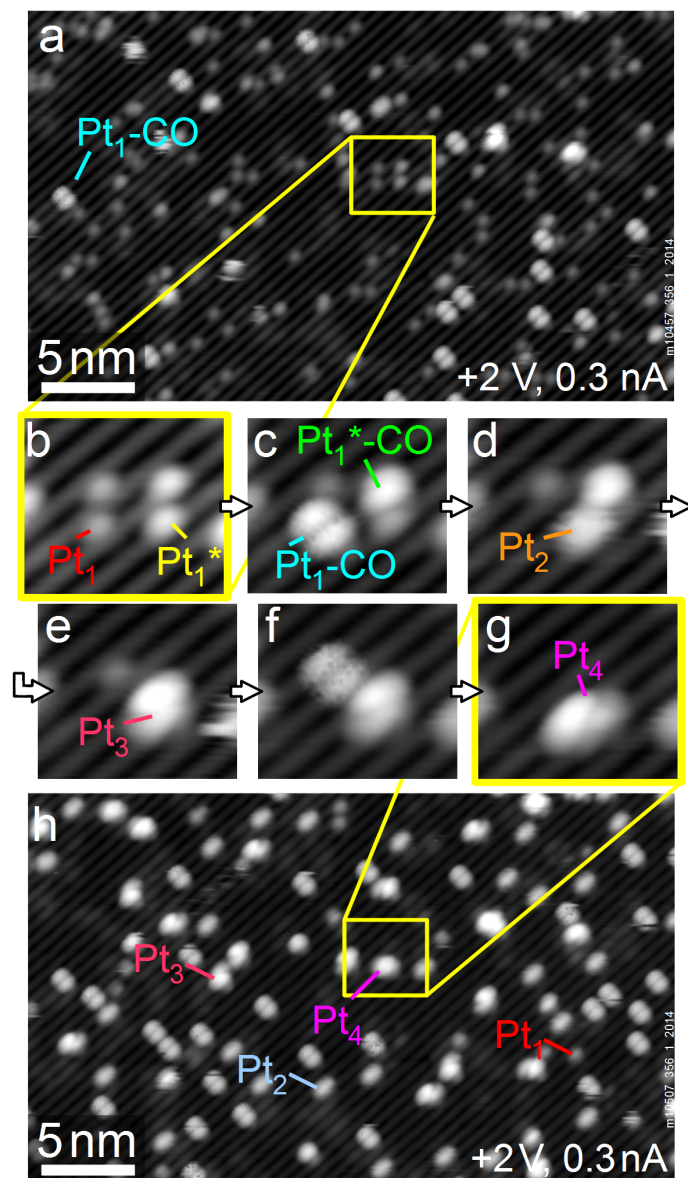


**Figure 4.37:** CO-induced mobility and coalescence of Pt/Fe<sub>3</sub>O<sub>4</sub>(001)<sup>157</sup>. (a) Initial state after 10 min CO exposure ( $2 \times 10^{-10}$  mbar, after  $\approx 5$  h in UHV): Mainly Pt adatoms are observed; few Pt-CO features and clusters are present. (b-g) STM image sequence on a selected area with four Pt adatoms in the two different adsorption configurations. CO exposure induces adsorption, mobility, and growth, which can be watched step by step. (h) After exposure only few adatoms remain; Pt<sub>2</sub>(CO)<sub>x</sub> are the main species.

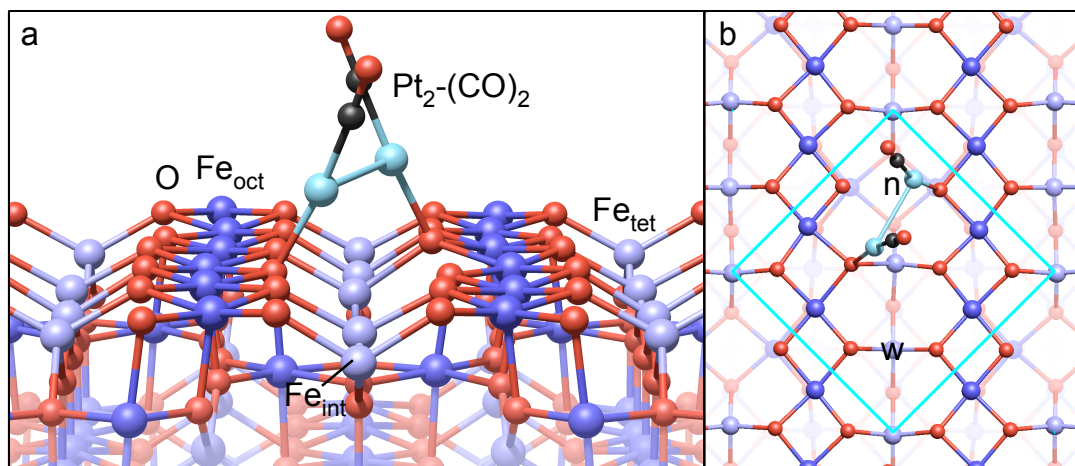


**Figure 4.38:** DFT+*U* force-relaxed geometry of the Pt<sub>2</sub>-(CO)<sub>2</sub> dimer in side-view (a) and top view (b). Both Pt atoms are coordinated to one surface oxygen atom, one in a comparable geometry to the Pt<sub>1</sub>-CO feature next to the preferred metal adsorption site (labeled “n”). Each CO molecule is adsorbed on top of one Pt atom, not directly coordinated to the surface.

plays a negligible role in the mobility and coalescence of Pt-CO species. A similar mobilizing effect of CO was observed for Pd adatoms on the Fe<sub>3</sub>O<sub>4</sub>(001) surface<sup>60</sup>. CO adsorption enhances the mobility of Pd adatoms and clusters, leading to the agglomeration to sub-nano particles. In contrast to the behavior reported for Pd, several STM movies at different scanning conditions and pressures of CO (up to 10<sup>-6</sup> mbar) show that the Pt<sub>1</sub>(\*)-CO features are the only mobile species driving agglomeration at room temperature. The immobile nature of all Pt clusters and the stability of the Pt<sub>1</sub>(\*)-CO species, which often remain in their initial site for several frames, allow following the coarsening process atom by atom and thus permit assigning the exact number of Pt atoms to each cluster. Moreover, the constrained mobility is a decisive factor in the size of the clusters, leading to a high density of small clusters; for example Pt dimers are the majority species in Figure 4.37(h). No decomposition of Pt clusters is observed in the STM image sequences at room temperature.

The agglomeration illustrated in Figure 4.37 is particularly interesting in the context of the Pt dimer DFT+*U* results, since the calculations predicted a dimer species, which is unstable against decay into two Pt adatoms. In order to test the stability of the Pt dimer in experiments, dimer species with one and two adsorbed CO molecules were modeled in DFT+*U* force relaxations. Indeed the addition of CO improves the stability of the Pt dimer. However, a Pt<sub>2</sub>-(CO) species is also unstable compared to one Pt adatom and a Pt-CO ( $E_{ads}(Pt_2-(CO))=8.44 \text{ eV} < E_{ads}(Pt_1-(CO))+ E_{ads}(Pt_1) = 5.53 \text{ eV} + 3.89 \text{ eV}$ ), whereas

adding a second CO molecule results in an energetically preferable  $\text{Pt}_2\text{-(CO)}_2$  dimer ( $E_{ads}(\text{Pt}_2\text{-(CO)}_2)=11.15 \text{ eV} > 2 \times E_{ads}(\text{Pt}_1\text{-(CO)}) = 2 \times 5.53 \text{ eV}$ ). Hence the adsorption of CO does not only mobilize the  $\text{Pt}_1^*$  adatom species but it is also crucial for stabilizing the smallest clusters. The small energy difference to two  $\text{Pt}_1\text{-CO}$  features motivated the study of different geometries of the  $\text{Pt}_2\text{-(CO)}_2$  dimer by starting DFT force-relaxations from different initial positions, but so far, no configuration with an energy  $E_{ads}(\text{Pt}_2\text{-(CO)}_2) > 11.15 \text{ eV}$  was found. In the most favorable configuration shown in Figure 4.38 the Pt-Pt bond in the  $\text{Pt}_2\text{-(CO)}_2$  dimer species is relatively flat (close to parallel to the surface plane, in contrast to the pristine  $\text{Pt}_2$  dimer) with each CO molecule adsorbed on top of one Pt atom. The dimer is not parallel to the surface Fe rows but slightly rotated, leading to two different bond lengths to the nearest two surface oxygen atoms:  $d_{\text{Pt}_{2,1}\text{-O}}=2.04 \text{ \AA}$  ( $3.21 \text{ \AA}$ ) for the atom closer to the adatom position and  $d_{\text{Pt}_{2,2}\text{-O}}=2.10 \text{ \AA}$  ( $3.25 \text{ \AA}$ ) for the second Pt atom. The distance above the average surface  $\text{Fe}_{\text{oct}}$  is smaller for the Pt atom closer to the preferred metal adsorption site:  $\Delta z_{\text{Pt}_{2,1}\text{-FeB}}(\text{Pt}_2\text{-(CO)}_2)=1.89 \text{ \AA}$  and  $\Delta z_{\text{Pt}_{2,2}\text{-FeB}}(\text{Pt}_2\text{-(CO)}_2)=2.21 \text{ \AA}$  for the second atom.

The stabilizing effect of CO on small Pt clusters was also assessed in experiments. The surface with clusters was created by exposure to CO pressures up to  $10^{-6}$  mbar, either inside the STM while scanning or with the sample in the preparation chamber. No difference between the two preparation methods is discernible. Once a surface with the Pt species almost fully sintered to clusters was achieved, the stability of the clusters was tested by annealing them to 520 K in UHV to desorb the CO. The initial state after exposure to  $10^{-6}$  mbar CO during scanning is shown in Figure 4.39(a)<sup>157</sup>. Most of the Pt-related features are small clusters; the sizes range up to 5 atoms, but Pt dimers are the majority species. The bar graph shows the relative number of clusters and adatoms referenced to the total number of Pt-related features (blue:  $71.5 \pm 4.7\%$ ,  $5.7 \times 10^{16} \text{ m}^{-2}$  clusters, and yellow:  $2.3 \times 10^{16} \text{ m}^{-2}$  adatoms). Annealing at 520 K leads to the recovery of Pt adatoms (coverage increased by 130%) and a reduction in the number of clusters by more than 60%. As a result, Pt adatoms ( $71.2 \pm 8.9\%$  of all Pt related features) are the dominant species after annealing, as illustrated by the bar graph in Figure 4.39(b). The cluster size after annealing cannot be determined by the shape, but comparing the initial adatom coverage after deposition with the number of atoms after the experiment allows to provide a rough estimate of the average cluster size:  $\approx 7.6$  atoms after annealing, compared to  $\approx 3.3$  atoms before (excluding single atoms and assuming the nominally deposited total coverage of 0.15 ML to be exact).

The recovery of a large number of adatoms with a simultaneous decrease of the number of clusters is interpreted as a break-up of the smallest Pt clusters following the

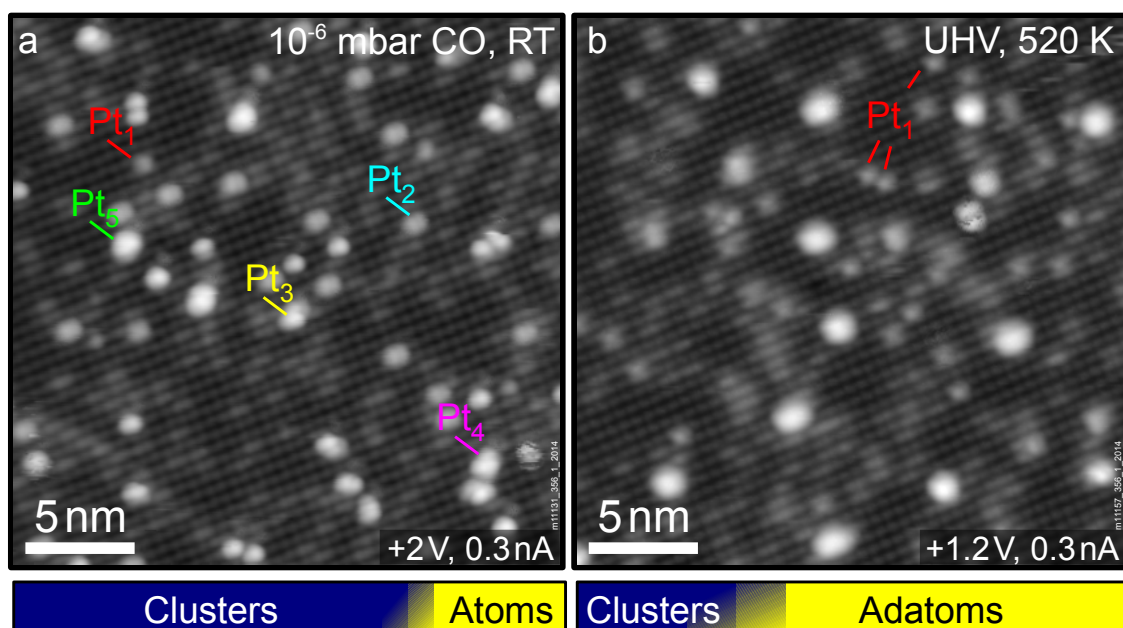


**Figure 4.39:** Redisperison of the smallest Pt clusters into adatoms<sup>157</sup>. (a) After sintering in  $10^{-6}$  mbar CO at room temperature, almost no Pt adatoms remain. The number of atoms in each Pt cluster is known. Pt dimers are the majority species at the surface. (b) Annealing in UHV at 520 K causes the desorption of CO, resulting in redisperison of Pt into the adatom phase via the break-up of the smallest Pt clusters. A large number of recovered adatoms coexists with a small number of large clusters. The bar graphs indicate the relative numbers of clusters and adatoms in the total number of surface features.

thermally activated desorption of CO. Thus, the instability of Pt dimers without adsorbed CO leads to redisperison of Pt into the adatom phase, in line with the large energy difference predicted by the DFT calculations. However, since the energetic preference for  $\text{Pt}_2\text{-(CO)}_2$  is very small, the experimentally observed stability at room temperature indicates the presence of a large energetic barrier hindering the breakup of this dimer species. An alternative explanation would be the existence of a more stable dimer  $\text{Pt}_2\text{-(CO)}_2$  configuration, which remains to be discovered in DFT calculations. While the behavior of Pt trimers cannot be determined with certainty, the stability of larger clusters is interpreted as a critical cluster size smaller than four Pt atoms also in the absence of CO. The larger average cluster size after annealing is attributed to the incorporation of adatoms as a result of thermally activated diffusion.

The reported findings draw a complete picture of the mobility, growth, and stability of Pt/ $\text{Fe}_3\text{O}_4(001)$ . In the surface processes occurring on a timescale observable using STM, the CO molecules are found to play a decisive role in mobilizing the Pt adatoms

and stabilizing the smallest cluster species. This stabilizing effect of CO is one of the crucial aspects enabling the formation of larger clusters, since the mobility of Pt is slow, reducing the probability of the simultaneous interaction of several Pt atoms. The slow time-scale of the coarsening process allows following its evolution resulting in a well-defined array of “size-distinguished” clusters<sup>157</sup>, which may prove valuable as initial state in further experiments focusing on the properties of the clusters. Moreover, the redispersion of small clusters to isolated adatoms provides insights into a potential pathway of recovering the active adatom phase after the onset of deactivation, which is a topic of broad interest in single-atom catalysis research.

## 4.2.6 Rhodium

### 4.2.6.1 Rhodium Adatoms

Rhodium is a versatile, catalytically active metal, which is widely studied in catalysis research<sup>1,36</sup>, for example for its relevance in the automotive three-way catalyst<sup>158,159</sup>. However, rhodium is also an expensive metal and could be used more broadly if the required amount of Rh in catalysts could be reduced without loss of active area. Thus, Rh is one of the typical candidate materials for single-atom catalysis research. Regarding its activity, Rh on different supports has been shown to catalyze various reactions, such as the CO oxidation reaction over Rh/ceria, or the hydrogenation of ethylene over site-isolated Rh complexes on MgO<sup>36</sup>. Further examples include the trimerization of acetylene to form benzene over Rh atoms stabilized by oxygen vacancies in MgO<sup>160</sup>. DFT calculations of Rh/ceria report an important role of the respective facet of the ceria support in the CO oxidation activity of the single Rh adatom species<sup>161</sup>. Further reports of active oxidized Rh species<sup>162</sup> draw attention to Rh/Fe<sub>3</sub>O<sub>4</sub>(001) as a promising system for single-atom reactivity.

Following the deposition of low coverages of Rh onto the Fe<sub>3</sub>O<sub>4</sub>(001) surface, Rh adatoms occupying the preferred metal adsorption site within the ( $\sqrt{2} \times \sqrt{2}$ )R45° reconstruction are the dominant species. Figure 4.40 displays STM images of 0.2 ML Rh/Fe<sub>3</sub>O<sub>4</sub>(001) and a comparison to STM simulations of a Rh adatom and a dimer species. The large-scale image in (a) demonstrates that mostly adatoms populate the surface and no large clusters are present at this low coverage. The small number of brighter surface features in the image is related to adsorption of molecules from the residual gas, which is discussed in detail in section 4.2.6.2. The small-scale image in Figure 4.40(b) shows the surface features in detail. In addition to the Rh adatoms (examples highlighted by the

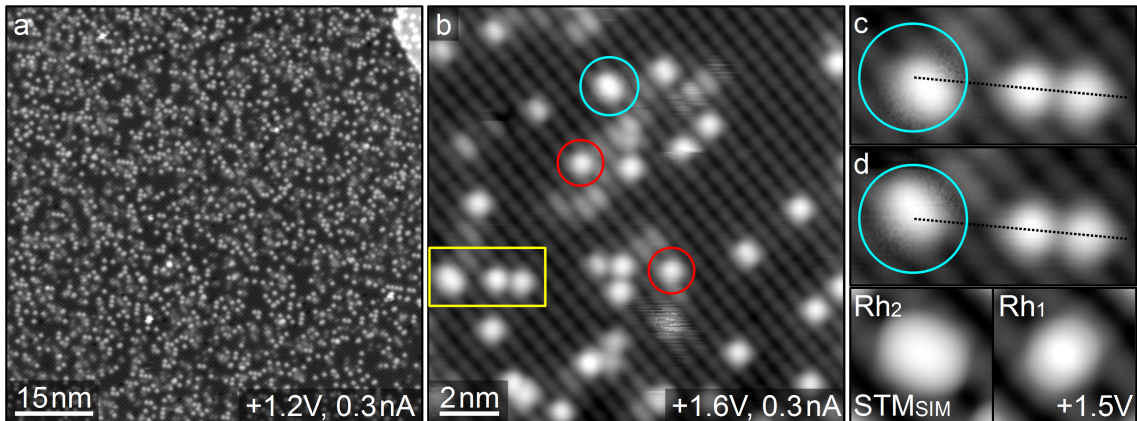


**Figure 4.40:** STM images of 0.2 ML Rh adsorbed at the  $\text{Fe}_3\text{O}_4(001)$  surface. (a) Overview image showing the random distribution of Rh adatoms and the absence of large clusters. The few brighter features at the surface are related to gas adsorption (see section 4.2.6.2). (b) Detailed image: Upon deposition two Rh-related species are observed: The Rh adatom (examples highlighted by red circles) and the Rh dimer (cyan circle). The area highlighted by the yellow frame is shown in the small-scale image sequence in (c,d). The black line highlights that the Rh dimer occupies the preferred metal adsorption site, offset from the center of the site. The dimer feature appears elongated and moves between the two equivalent asymmetric sites within the unit cell during STM image sequences. The simulated STM images (+1.5V) of the Rh adatom and dimer species in the panels below (d) are in good agreement with the experimental observations.

red circles) the preferred metal adsorption sites can also be occupied by a larger Rh-related feature, elongated parallel to the surface Fe row direction (example highlighted by the cyan circle). A low coverage of this species is present after each deposition in UHV, and no formation via adsorption from the residual gas is observed. The two sequential images in (c,d) show an enlarged view of the selected area in (b) (yellow frame). The black line in this short sequence connects the centers of the metal adsorption sites of the Rh adatoms and the elongated feature. This feature assumes an asymmetric geometry, off-centered from the metal adsorption site in the unit cell. Its elongated shape and the switching behavior between two equivalent geometries observed in STM image sequences, illustrated by the comparison of (c) and (d), are indicative of a Rh dimer, where one of the Rh atoms binds to the adsorption site more strongly than the other one. The adsorption geometries of the Rh adatom and a dimer species were calculated using density functional theory (with  $r_{\text{Rh}}=1.9 \text{ bohr}=1.01 \text{ \AA}$ , a  $(3 \times 3 \times 1)$   $k$ -mesh and a cut-off energy of the basis set of  $\approx 183 \text{ eV}$  ( $Rk_{\text{max}}=5.5$ )). The force-relaxed adatom geometry ( $E_{\text{ads}}(\text{Rh}_1)=3.67 \text{ eV}$ ) resembles the metal adatoms described above. For the Rh dimer a flat adsorption geometry is found to be favorable ( $E_{\text{ads}}(\text{Rh}_2)=8.40 \text{ eV} > 2 \times E_{\text{ads}}(\text{Rh}_1)=2 \times 3.67 \text{ eV}=7.34 \text{ eV}$ ). This dimer is rotated in the adsorption site compared

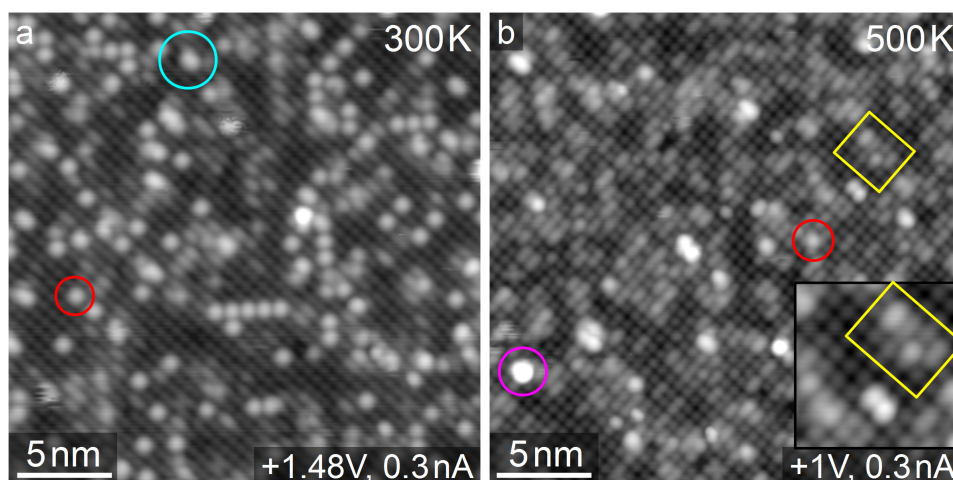


**Figure 4.41:** Thermal stability of Rh adatoms. (a) Room-temperature STM image of 0.4 ML Rh showing almost exclusively adatoms and dimers. (b) After annealing to 500 K bright surface row features are the dominant species; almost no adatoms remain (example in red circle). The yellow frame in the enlarged inset highlights different bright species on the surface Fe rows, which have formed during annealing. The different appearance of the bright on-the-row features is attributed to incorporation of Rh in different sites. The features larger and brighter than dimers are attributed to clusters (example in purple circle).

to the surface Fe row direction. The simulated STM images of the Rh adatom and of the dimer, depicted below panel (d) are in good agreement with the features observed in the experiment. The characteristic bond lengths of the Rh adsorption geometry were also determined in the DFT calculations:  $d_{Rh-O}(Rh_1)=1.94 \text{ \AA}$ ,  $\Delta z_{Rh-FeB}(Rh_1)=0.70 \text{ \AA}$ ; for the Rh adatoms and  $d_{Rh-O}(Rh_2)=1.98 \text{ \AA}$  for both Rh atoms of the dimer and  $\Delta z_{Rh-FeB}(Rh_2)=1.16/1.17 \text{ \AA}$ .

Following the deposition of a low coverage of Rh, the only Rh-related features observed are Rh adatoms and dimers (Figures 4.40(b), 4.41(a)). However, if the surface with 0.4 ML as-deposited Rh is heated to 500 K (Figure 4.41(b)), the Rh adatoms and dimers disappear and large parts of the surface are covered by bright features on the surface Fe rows. These “on-the-row” features coexist with different, larger species, which are attributed to Rh clusters. The yellow frame in Figure 4.41(b) enlarged in the inset highlights different examples of such bright “on-the-row” features, which resemble the signature of incorporation of Ni. Thus, the propensity of Rh for oxidation results in the incorporation of these noble metal atoms at elevated temperatures. The different sizes of the incorporation-related features in the yellow frame in Figure 4.41(b) are attributed to incorporation in different sites (e.g., surface or subsurface  $Fe_{oct}$ ).

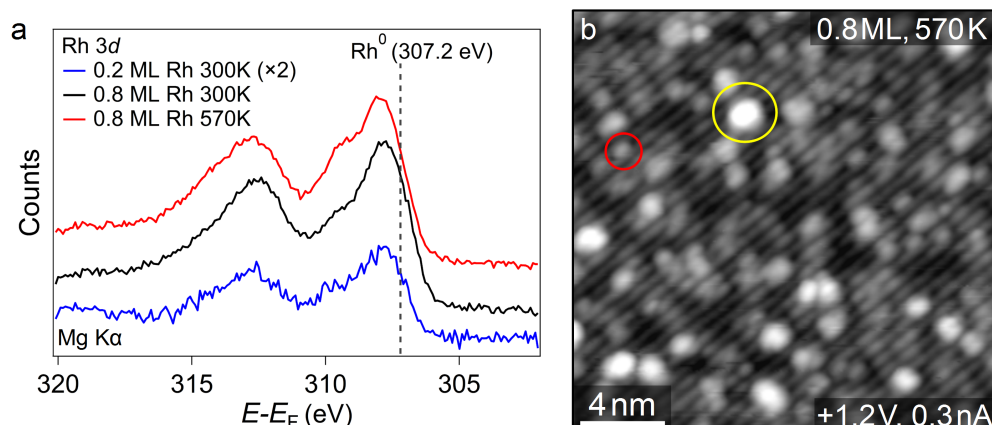


**Figure 4.42:** Thermal stability of 0.8 ML Rh/Fe<sub>3</sub>O<sub>4</sub>(001). (a) XPS spectra (Mg K $\alpha$ ) of 0.2 ML Rh (blue) and 0.8 ML Rh at room temperature (black) and after annealing at 570 K (red) for 10 min. All Rh states have a higher binding energy than metallic Rh (dashed vertical line). Annealing at 570 K causes a strong shoulder at high binding energies. (b) STM image of 0.8 ML Rh/Fe<sub>3</sub>O<sub>4</sub>(001) after annealing to 570 K, showing significantly more clusters and adatoms and less incorporated Rh than Figure 4.41(b).

The thermal stability of Rh was also studied using x-ray photoelectron spectroscopy (XPS). Figure 4.42 depicts Rh 3d XPS spectra acquired with Mg K $\alpha$  radiation and an STM image of 0.8 ML Rh/Fe<sub>3</sub>O<sub>4</sub>(001). At room temperature (blue and black spectra) the main component of the Rh 3d peak is oxidized compared to metallic Rh (dashed gray vertical line), in agreement with the strong bond to surface oxygen predicted by the DFT calculations. Annealing at 570 K results in the emergence of a high-binding energy shoulder, but the main component of the peak undergoes little change. (Only a small shift by <0.2 eV is observed). The STM image acquired after annealing (Figure 4.42(b)) provides additional insights into the behavior of the surface species: Compared to the images of 0.4 ML Rh (Figure 4.41), the surface with 0.8 ML Rh exhibits a much higher cluster coverage and the coverage of bright “on-the-row” features after annealing is lower than for 0.4 ML Rh. This STM image demonstrates that even though the blue XPS spectrum for 0.2 ML Rh is compatible with the high coverage spectrum, annealing experiments performed for the two coverages can yield different results. The STM image in Figure 4.42(b) shows the presence of a substantially higher coverage of clusters than for 0.4 ML Rh (Figure 4.41). Thus, the thermal energy provided by the annealing offers two competing pathways for the Rh adatoms: incorporation into the surface or into clusters. The XPS spectrum in Figure 4.42(a) shows the creation of an oxidized Rh species (comparable to Rh<sub>2</sub>O<sub>3</sub> according to Sleigh *et al.*<sup>163</sup>). However, for an unambiguous interpretation if this can be attributed to incorporated Rh, the experiment should be repeated at a coverage  $\leq 0.4$  ML.

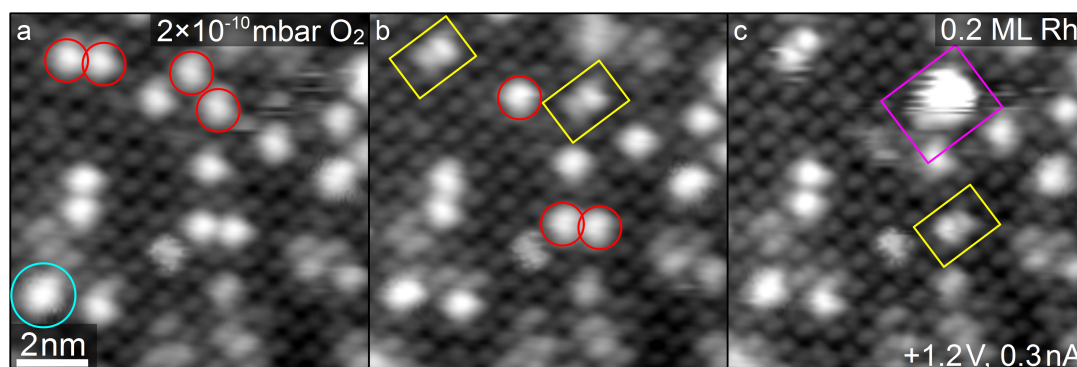


**Figure 4.43:** STM image sequence of Rh/Fe<sub>3</sub>O<sub>4</sub>(001) during exposure to  $2 \times 10^{-10}$  mbar O<sub>2</sub>. (a) Rh adatoms (examples in red circles) and dimers (example in cyan circle) populate the surface. (b) The adatoms highlighted by the red circles in (a) become mobile and combine to form new surface species (yellow frames). Their different appearance compared to the as-deposited dimer highlighted in (a) indicates that these features contain oxygen (Rh<sub>2</sub>O<sub>x</sub>). (c) Another Rh adatom is mobilized and joins a Rh<sub>2</sub>O<sub>x</sub> species, forming a Rh<sub>3</sub>O<sub>y</sub> species (purple frame). No adsorption on neat Rh<sub>2</sub> dimers is observed.

#### 4.2.6.2 Rhodium adatom–gas interactions

In the UHV study, adsorption of residual gas molecules on the Rh adatoms was observed as a slow but continuous process at pressures below  $10^{-10}$  mbar. These observations, in combination with reports of active Rh atoms on different supports, such as MgO<sup>36,164</sup> or ceria<sup>161</sup>, encourage a detailed study of the interaction of Rh adatoms and dimers with common reactant gases. The interaction of Rh with O<sub>2</sub>, CO, and NO is particularly interesting, since these are among the relevant reactant gases in some fields of application of Rh, such as automotive exhaust gas catalysis<sup>158,159</sup>.

Figure 4.43 illustrates the interaction of 0.2 ML Rh adatoms with oxygen, observed in an STM image sequence acquired with a background pressure of  $2 \times 10^{-10}$  mbar O<sub>2</sub>. Initially, Rh adatoms and dimers coexist at the surface (examples highlighted by red and cyan circles, respectively). Without the direct observation of an intermediate species of the adsorption of O<sub>2</sub>, the two pairs of Rh adatoms highlighted in (a) are mobilized and form a new surface species. The different appearance compared to the neat Rh<sub>2</sub> dimer indicates that the newly formed dimer species contains oxygen (Rh<sub>2</sub>O<sub>x</sub>). In (c) the adatoms highlighted by the red circles in (b) have again become mobile, driving growth processes at the surface. In addition to the formation of an additional Rh<sub>2</sub>O<sub>x</sub> species (yellow frame), one atom has joined the existing Rh oxide dimer, creating a trimer species, which is also likely to contain oxygen. The low oxygen dosage required to cause these effects suggests a high reactivity of Rh adatoms towards oxygen and excludes contaminants in the gas at

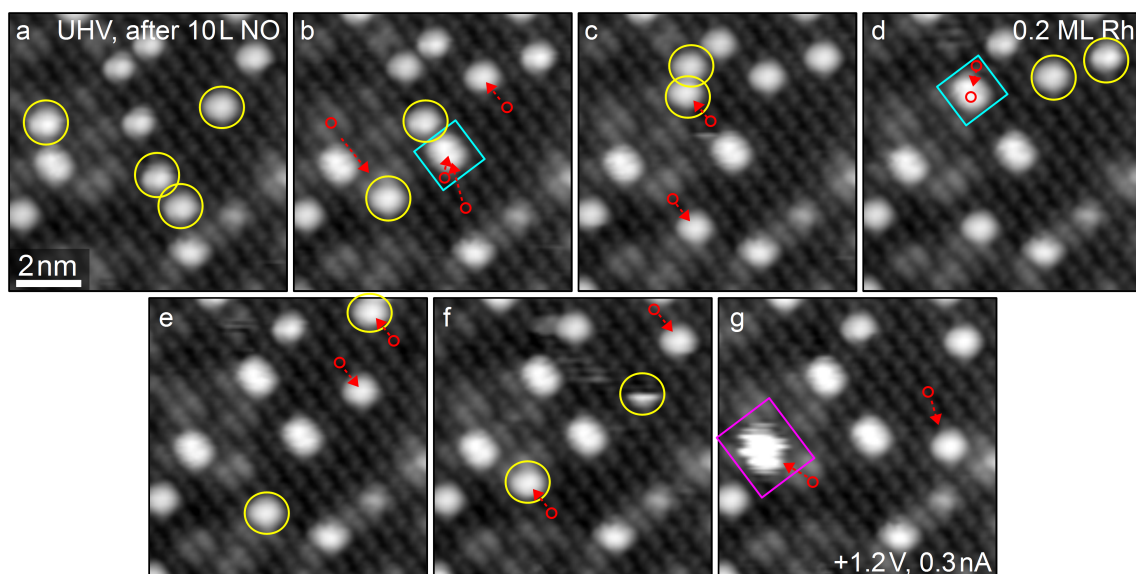


**Figure 4.44:** STM movie of 0.2 ML Rh/Fe<sub>3</sub>O<sub>4</sub>(001) in UHV after exposure to 10 L NO, demonstrating permanent adsorption of NO on Rh adatoms and its mobilizing effect. (a) After NO adsorption, Rh<sub>1</sub>-NO species populate the surface. These have an apparent height of 230-250 pm at  $U_{sample}=1.2$  V (yellow circles); no coexisting neat Rh<sub>1</sub> adatoms are observed. (a-g) The Rh<sub>1</sub>-NO features highlighted by yellow circles hop between preferred metal adsorption sites. Small red circles in the subsequent frame mark their respective prior locations; red arrows indicate the most likely hopping direction. The cyan frames in (b) and (d) highlight dimer features created from two mobile Rh<sub>1</sub>-NO species. In (g) a third Rh<sub>1</sub>-NO joins a dimer, forming the trimer feature highlighted by the purple frame.

the root of the coarsening behavior. This conclusion is further strengthened by the fact that similar processes are not observed in STM image sequences in UHV. After deposition in the preparation chamber, where residual oxygen from sample preparation can be present, a few adsorption-related features and a low density of clusters are usually discerned in large-scale images.

The high activity of Rh adatoms towards oxygen stimulated further studies of exposure to reactant gases such as NO. Figure 4.44 shows an STM image sequence of 0.2 ML Rh after exposure to 10 L NO. Acquiring an STM movie while dosing NO did not yield any images of adsorption processes. Since images acquired subsequently in other areas of the sample show a clear signature of NO adsorption, this was most likely due to tip shadowing effects. The images in Figure 4.44 were acquired at a different location after a total dose of 10 L NO. The density of features in the preferred metal adsorption sites remains initially unchanged by the exposure to NO, but the adatoms in Figure 4.44 are mobile and characterized by a significantly larger apparent height. This difference between

$h(\text{Rh}_1)=165\text{-}190\text{ pm}$  and  $h(\text{Rh}_1\text{-NO})=230\text{-}250\text{ pm}$  (at 1.2 V, 0.3 nA) is attributed to the adsorption of NO on the Rh adatoms and allows to clearly distinguish  $\text{Rh}_1\text{-NO}$  species from Rh adatoms in STM images. The mobility of the  $\text{Rh}_1\text{-NO}$  species is illustrated in Figure 4.44. In each STM image, all Rh atoms that occupy a different site in the subsequent frame are highlighted by yellow circles. The small, red circles mark the sites occupied in the respective previous image; the dashed red arrows indicate the most likely hopping direction, showing that the distance usually does not exceed two to three unit cells. Site changes are found to occur preferentially in parallel to the surface Fe row direction. Rh-NO features can also hop in the proximity of the STM tip, resulting in images of atoms “cut in half”, such as the upper atom in a yellow circle in (f). This mobility provides the opportunity for  $\text{Rh}_1\text{-NO}$  species to meet at the surface, giving rise to agglomeration processes. The cyan frames in Figure 4.44(b) and (d) highlight dimer species formed from two mobile  $\text{Rh}_1\text{-NO}$  features. In (g) the formation of a Rh trimer species is observed. The strong bond of NO to the Rh adatom and the different appearance of the neat Rh dimer indicate that the Rh dimers formed via NO-induced mobility contain at minimum one NO-related species. Similar features are also observed outside of the scanned area but an influence of the STM tip on the observed mobility and agglomeration cannot be fully excluded. At high bias voltages (3 V, 0.3 nA) the desorption of NO molecules from some Rh adatoms as well as the transfer of NO between adatoms have been observed (not shown).

A high activity of Rh adatoms for the adsorption of gas molecules is also observed with CO. Figure 4.45 displays an STM image sequence acquired while filling the STM chamber with a low pressure of CO. Already in the initial image, before intentional exposure to CO, two different types of adatoms are observed: A regular Rh adatom ( $\approx 180\text{ pm}$  at 1.2 V, 0.2 nA) and a Rh species with a smaller apparent height ( $\approx 95\text{-}125\text{ pm}$  at 1.2 V, 0.2 nA) highlighted by the red and the yellow circles, respectively. The selection in the blue frame in (a) shows four  $\text{Rh}_1$  adatoms. During exposure to  $5 \times 10^{-9}$  mbar CO, these adatoms are converted to the smaller Rh adatom type. This happens one by one over the course of 20 min, indicating that these “small” Rh adatoms are related to CO adsorption. Figure 4.45(e) shows an image of the surface after a total dose of  $\approx 12\text{ L}$ . The  $\text{Rh}_1\text{-CO}$  features correspond to the majority species at the surface, only a few  $\text{Rh}_1$  adatoms remain unaffected by the CO exposure (one example marked by a red circle). In a follow-up experiment, after additional CO exposure to saturate all Rh adatoms, oxygen was dosed to the surface. In an STM movie acquired while dosing up to  $10^{-8}$  mbar  $\text{O}_2$  no discernible effects were observed (not shown), even though on the as-deposited Rh adatoms  $\text{O}_2$  exposure was found to induce mobility and cluster formation already at very low pressures ( $2 \times 10^{-10}$  mbar, see Figure 4.43). Thus, the stable Rh carbonyl created by CO exposure is

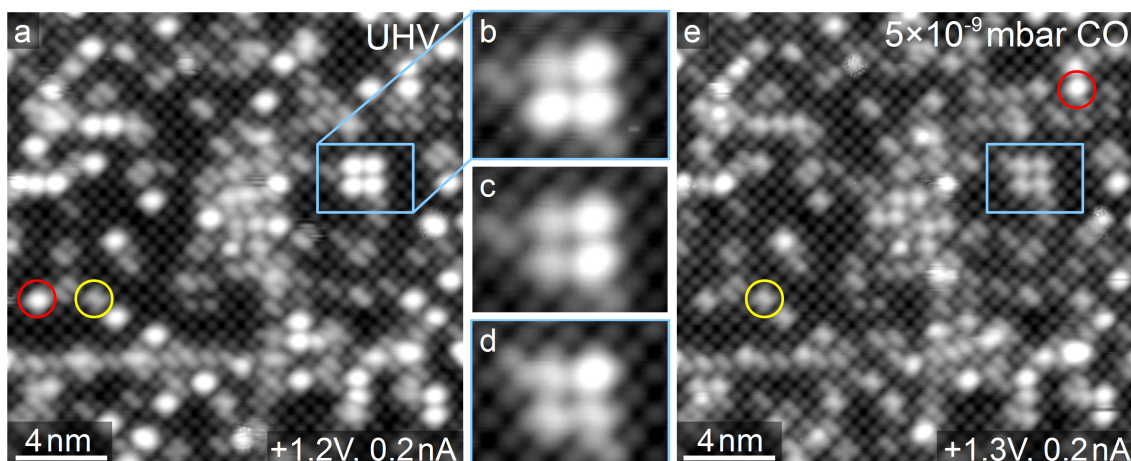


**Figure 4.45:** STM images of Rh/Fe<sub>3</sub>O<sub>4</sub>(001) acquired during exposure to increasing pressures of CO. (a) Initial state in UHV: Rh adatoms are the majority species (example highlighted by red circle), coexisting with a few adatom species with a lower apparent height (yellow circle). The blue frame emphasizes a selected area with four Rh<sub>1</sub> adatoms, which is shown in detail in (b-d). (b-d) Small-scale STM image sequence acquired in  $5 \times 10^{-9}$  mbar CO over  $\approx 20$  min. The Rh adatoms adsorb CO sequentially, becoming smaller in apparent height by the adsorption. (e) Final state after dosing  $\approx 12$  L CO. The Rh<sub>1</sub>-CO features are the majority species. No mobility is observed.

inactive for interactions with oxygen; CO adsorption poisons the reactivity of Rh adatoms at room temperature. However, the strong interaction with both, CO and O<sub>2</sub>, observed in the experiments holds potential for reactivity studies at elevated temperatures.

The strong interactions between Rh adatoms and oxygen or CO are in excellent agreement with the results of DFT+*U* calculations of adsorption on Rh adatoms. The calculations predict Rh to exhibit the strongest interaction with CO in the block of *d*-electron transition metals from Co to Au (groups 9, 10, and 11 in the periodic table):  $E_{ads}(\text{Rh-CO})=6.38$  eV ( $\Delta E(\text{CO})=2.71$  eV). The interaction of Rh with O<sub>2</sub> is also the strongest among the metals, for which O<sub>2</sub> adsorption was calculated (Co, Ni, Rh, Pd):  $E_{ads}(\text{Rh-O}_2)=6.62$  eV ( $\Delta E(\text{O}_2)=2.95$  eV), see section 4.4. However, it should be emphasized that these energies are referenced to free metal atoms and gas molecules in vacuum. Thus, they reflect the nature of the metal-molecule bond and depend on the tendency of the metals to oxidize. While they are good indicators for relative differences in binding strengths for similar metals, the absolute values should not be compared to experimental gas adsorption energies derived from methods such as temperature programmed desorption.

In the context of the electronic structure, the STM study of CO adsorption on Rh adatoms showed an interesting effect: The apparent height of the Rh adatom decreases

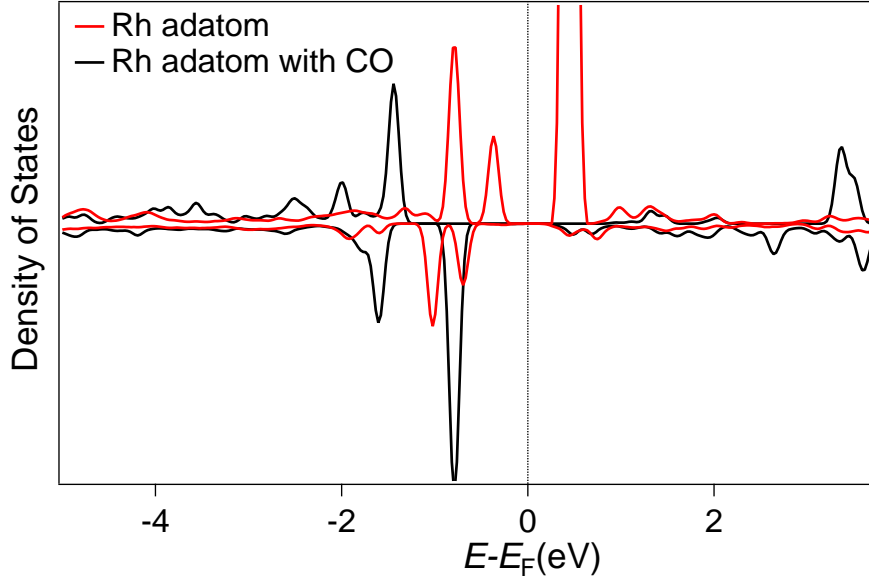


**Figure 4.46:** Electronic DOS of the Rh adatom at the  $\text{Fe}_3\text{O}_4(001)$  surface before (red) and after adsorption of CO (black curve). The very tall and bright Rh adatoms in empty-state STM images are partly due to the strong peak in the unoccupied DOS close to  $E_F$ . With the adsorption of CO, the intensity in the unoccupied states shifts away from the Fermi energy, explaining the smaller apparent height in STM images.

substantially with the adsorption of a CO molecule. According to the DFT results, this observation is based on a twofold effect of the CO adsorption: an electronic and a topographic effect. The decreased brightness in the STM images at positive sample bias originates partially in an intensity shift in the unoccupied density of states, shown in Figure 4.46 for a Rh adatom without (red spectrum) and with (black spectrum) an adsorbed CO molecule. The large peak close to  $E_F$  (spin-up) in the unoccupied DOS of the Rh adatom contributes strongly to the original apparent height. With the formation of the bond to the CO molecule, this peak is redistributed to unoccupied states at higher energies. After this redistribution, only little intensity close to  $E_F$  remains, resulting in a substantially lower apparent height of the  $\text{Rh}_1\text{-CO}$  in STM. In addition to this electronic effect, the distance of the Rh adatom to the surface layer also changes with the adsorption of CO. While the bond distance to the surface oxygen atoms remains similar ( $d_{\text{Rh-O}}(\text{Rh}_1\text{-CO})=1.99 \text{ \AA}$ ) the height above the surface layer decreases ( $\Delta z_{\text{Rh-FeB}}(\text{Rh}_1\text{-CO})=0.53 \text{ \AA}$ , a change of  $-0.17 \text{ \AA}$  compared to the neat Rh adatom). Thus, in contrast to most other metal adatoms, the Rh adatom sinks deeper into the adsorption site upon adsorption of CO, reducing the apparent height further in addition to the electronic effect. Following the adsorption of

oxygen, on the other hand, the bond lengths are stretched. This is indicative of a weakening of the bond to the surface and agrees well with the observed mobility and agglomeration:  $d_{Rh-O_S}(Rh_1-O_2)=2.02 \text{ \AA}$  and  $\Delta z_{Rh-FeB}(Rh_1-O_2)=1.08 \text{ \AA}$ , lifted up by  $0.38 \text{ \AA}$ .

While the high activity observed at 300 K suggests potential for reactivity studies at elevated temperatures, these could be limited by the thermal stability of the Rh adatoms. Determining characteristic parameters such as the desorption temperature of CO and NO will allow conclusions whether the stability range of Rh adatoms is sufficient to overcome, for example, the poisoning effect of CO adsorption. Regarding the activity, isolated Rh adatoms certainly meet the requirements for catalytic processes at low temperatures.

## 4.2.7 Copper

### 4.2.7.1 Copper adatoms

Copper is an interesting material for an adsorption study at the  $Fe_3O_4(001)$  surface. For example, Cu is a known promoter of the water-gas shift activity of the magnetite catalyst<sup>165,166</sup>. In contrast to many other catalytically active metals, Cu is a relatively inexpensive material, which is also widely available. Moreover, Cu is known to form stable solid solution with magnetite and should therefore also extend the selection of metals forming thin-film ferrites at the  $Fe_3O_4(001)$  surface.

Figure 4.47 illustrates the coverage-dependent adsorption properties of Cu observed in STM images. For Cu, a very high coverage of adatoms can be achieved before the onset of cluster formation. Following the deposition of 0.2 ML Cu (a), two different types of Cu-related features are observed at the surface: Cu adatoms in the preferred adsorption site are the dominant species. They coexist with triangular features appearing bright on one side of the site blocked by  $Fe_{int}$ . Examples of Cu adatoms and triangular features are highlighted by red and cyan circles, respectively. These triangular features, which also change the local DOS of the surface Fe rows, are only observed after Cu deposition. Moreover, they occur as isolated features already at low Cu coverages and at higher Cu density they coexist with Cu adatoms in fully occupied patches, without forming clusters. The consecutive STM images in the inset in Figure 4.47(a) demonstrate the mobility of a triangular feature, hopping across the blocked site to the opposite surface Fe row, constrained to one unit cell. These changes between two equivalent sites are interpreted as the mobility of a single Cu adatom across the site blocked by  $Fe_{int}$ . Thus, the triangular features are termed  $Cu_1^*$  and interpreted as single Cu atoms binding to the oxygen atoms adjacent to the blocked site, bonding more strongly at one side of the  $Fe_{int}$ . This

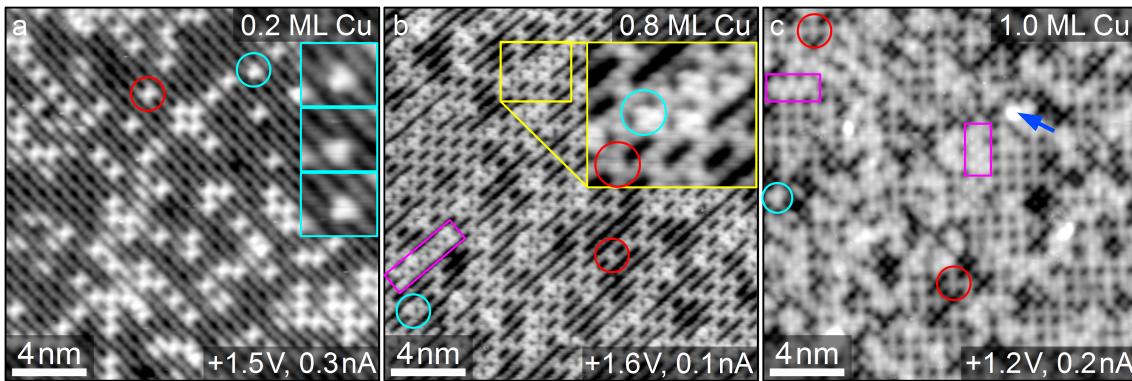


**Figure 4.47:** STM images of different coverages of Cu/Fe<sub>3</sub>O<sub>4</sub>(001). (a) 0.2 ML Cu: Cu adatoms are the dominant species at the surface (example in red circle). The cyan circle highlights a second type of Cu adatom (Cu<sub>1</sub>\*), an asymmetric feature occupying a site blocked by the subsurface Fe<sub>int</sub>. The Cu<sub>1</sub>\* can change to a symmetrically equivalent site (inset, consecutive images on the same area). (b) 0.8 ML Cu: Atomically resolved image of Cu adatoms and Cu<sub>1</sub>\* features. Fully occupied patches start to form (Cu<sub>1</sub> and Cu<sub>1</sub>\* sites filled, example highlighted by the purple frame). No clusters are observed. (c) 1 ML Cu: The fully occupied patches (purple frames) are growing in number and size compared to (b). First clusters start forming (example highlighted by the blue arrow).

asymmetric bond causes the triangular appearance, offset towards one surface Fe row from the center of the Fe<sub>int</sub> site. Alternatively, a Cu adatom binding strongly in the blocked site could push the Fe<sub>int</sub> down towards one of the Fe<sub>oct</sub> vacancies in the subsurface. This filled vacancy would also result in a local change of the DOS in the surface Fe row above, potentially resulting in a bright feature on one side of the blocked site. Both interpretations can offer an explanation for the triangular appearance and the mobility of the Cu<sub>1</sub>\* features, which is constrained to remain within one unit cell. A third alternative, a bond to two surface oxygen atoms parallel to the surface Fe rows (illustrated for the Pt<sub>1</sub>\* configuration in Figure 4.33(e,f)) cannot be excluded either. However, the expected offset of half an Fe-Fe distance along the surface Fe rows from the center of the blocked site is not observed in the STM images of the Cu<sub>1</sub>\* feature.

Increasing the Cu coverage to 0.8 ML results in a higher density of both Cu-related features, leading to fully occupied patches such as the one highlighted by the purple frame in Figure 4.47(b). The enlarged image in the inset (yellow frame) shows an area with a high Cu density, showing the two Cu species with atomic resolution. At a nominal deposited coverage of 1 ML (c) the densely occupied patches have grown in number and size. The blue arrow indicates a bright, tall species which is attributed to a Cu cluster. Such a cluster is most likely formed if a sufficient number of additional atoms is deposited

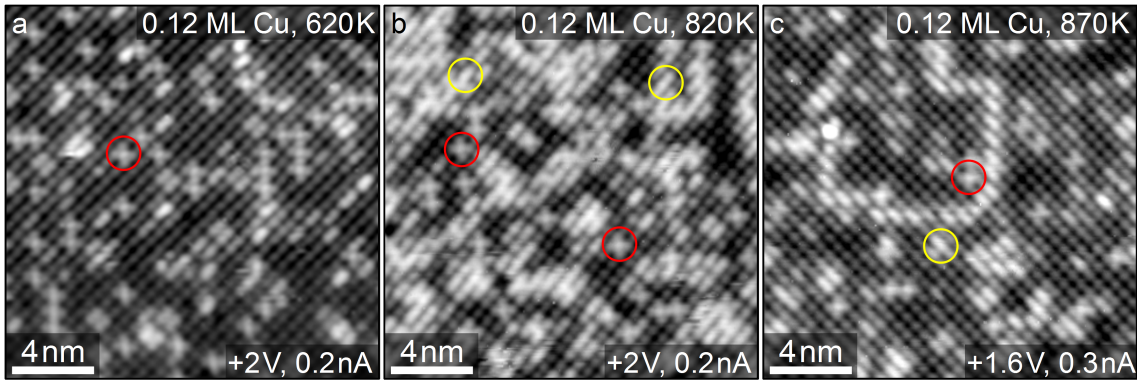


**Figure 4.48:** STM-based thermal stability study of 0.12 ML Cu/Fe<sub>3</sub>O<sub>4</sub>(001) (counted room-temperature coverage). (a) After annealing to 620 K for 10 min Cu adatoms (highlighted by red circles) are still the majority species. No Cu<sub>1</sub>\* features are observed. (b) After annealing to 820 K, ≈50% of the room-temperature coverage of Cu adatoms coexists with bright “on-the-row” features (yellow circles). These features are interpreted as a mixture of incorporated Cu features and unreconstructed unit cell defects, caused by thermally lifting the reconstruction at 820 K and incomplete re-nucleation during cooling. (c) Subsequent annealing to 870 K for 10 min results in a substantial decrease of the adatom coverage and the complete re-nucleation of the surface reconstruction. The density of the remaining “on-the-row” features can be attributed to the incorporation of Cu atoms. The coexistence of Cu adatoms indicates the presence of a high incorporation barrier.

onto an area where Cu<sub>1</sub> and Cu<sub>1</sub>\* occupy all available sites. The high adatom coverage coexisting with only few clusters in Figure 4.47(c) demonstrates that the Cu adatom layer is almost completely filled before first clusters are created. This trend indicates a strong bond of the Cu adatom in the preferred metal adsorption site, which is also borne out in DFT+*U* calculations predicting a much stronger bond for Cu than for example for Ag ( $E_{ads}(\text{Cu})=3.41$  eV). In these calculations the following parameters are used for Cu:  $r_{\text{Cu}}=1.9$  bohr (1.01 Å), no Hubbard-*U* on Cu, a (3×3×1) *k*-point grid in reciprocal space, and  $Rk_{max}=5.5$ , corresponding to an energy cut-off of the basis set of ≈183 eV. An analysis of the magnetic moments and partial charges indicates a Cu<sup>1+</sup> charge state in a 3d<sup>10</sup>4s<sup>0</sup> electron configuration. The adsorption geometry of Cu is flat with characteristic distances of  $d_{\text{Cu-O}}=1.84$  Å and  $\Delta z_{\text{Cu-FeB}}=0.53$  Å.

The thermal stability of the Cu adatoms was studied by annealing the surface with 0.12 ML Cu (counted coverage at room temperature) step by step to increasing temperatures. Figure 4.48 shows STM images of 0.12 ML Cu/Fe<sub>3</sub>O<sub>4</sub>(001) after annealing to (a) 620 K, (b) 820 K, and (c) 870 K (annealing for 10 min at each temperature). After annealing at 620 K, the Cu adatom coverage shows no measurable change compared to room temperature, but the Cu<sub>1</sub>\* features are entirely absent. This lack of Cu<sub>1</sub>\* is interpreted

as thermally induced transition of Cu atoms occupying the blocked site to adatoms in the preferred metal adsorption site. Subsequent annealing to 820 K (b) results in a high coverage of bright features on the surface Fe rows, while a residual adatom density of  $\approx 50\%$  of the original coverage is retained at the surface. The “on-the-row” species resemble incorporated transition metal atoms (see sections 4.2.3-4.2.4.2), but can also be attributed to defects such as unreconstructed unit cells or a high density of antiphase domain boundaries (APDB, see section 4.1.1). The combined coverage of both, Cu adatoms and “on-the-row” features, exceeds the original Cu coverage and thus also the possible number of Cu-related features. Hence, a significant number of the “on-the-row” features in Figure 4.47 is attributed to defects in the surface reconstruction, rendering the identification of incorporated-Cu features difficult. The high density of newly created defects most likely originates in annealing to a temperature high enough to lift the surface reconstruction (observed at 720 K<sup>105</sup>). If the temperature is close to the transition point, the reconstruction can nucleate simultaneously in many locations at the surface, avoiding the formation of large, uniform reconstructed patches. The coexistence of these defects with metal-related features has only been observed for Cu, owing to the high thermal stability of Cu adatoms, which exceeds the onset of bulk diffusion or clustering of all other metal species. The interpretation of Figure 4.48(b) as intrinsic defects in the reconstruction coexisting with incorporated Cu is supported by the STM image in (c) acquired after annealing at 870 K. Even though the adatom coverage has decreased substantially, the defect density at the surface is reduced. The chain of bright features in the top half of the image corresponds to an APDB, but all other bright “on-the-row” features are interpreted as incorporated Cu atoms (yellow circle) or intrinsic defects, which were already present after annealing to 620 K. The low coverage of incorporation-related features coexisting with residual Cu adatoms at high temperatures indicates that Cu shows only a very weak inclination to incorporate into the subsurface  $V_{\text{Fe}}$  of the SCV structure and potentially even prefers to diffuse directly to bulk-like layers. This speculation is based on the results on other 3d transition metals, which demonstrate that bulk diffusion is already possible at 500 K (see for example section 4.2.3 for the results on Ni incorporation). Thus, the high Cu adatom coverage at 620 K suggests the existence of a higher incorporation barrier than for other metals, or an energetic preference for the adatom configuration compared to incorporation in the near-surface region. In order to fully resolve the site preference of Cu at elevated temperatures and the geometry of  $\text{Cu}_1^*$ , additional DFT calculations of Cu in different sites would be required.

Figure 4.49 depicts an XPS spectrum of the Cu 2p region acquired after deposition of 0.8 ML Cu (STM image in Figure 4.47(b)). The gray, dashed lines indicate the Cu  $2p_{3/2}$

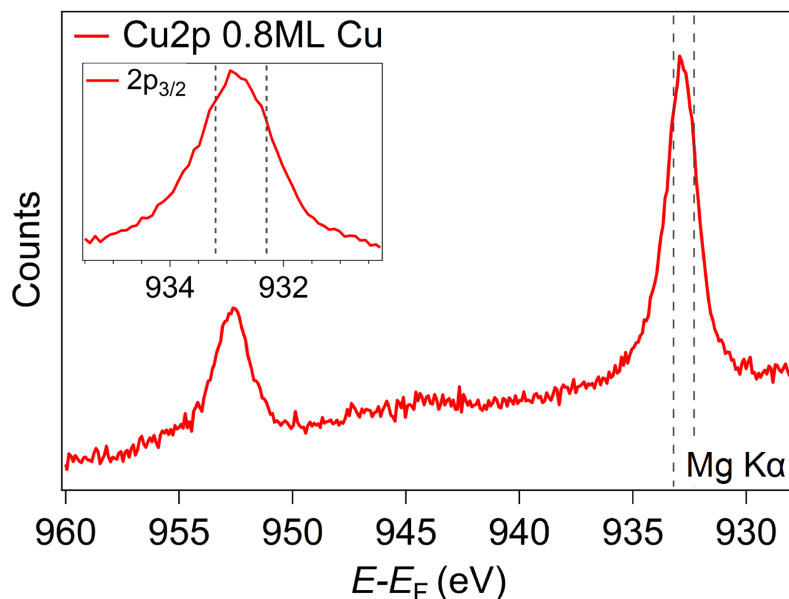


**Figure 4.49:** Cu 2p XPS spectrum of 0.8 ML Cu/Fe<sub>3</sub>O<sub>4</sub>(001). The inset shows the Cu 2p<sub>3/2</sub> peak, which is located between the two gray dashed lines illustrating the Cu 2p positions of metallic Cu (932.3 eV) and CuO (933.2 eV)<sup>167</sup>. The peak position at ≈932.9 eV indicates an oxidized Cu species.

binding energies in metallic Cu (932.3 eV) and CuO (933.2 eV)<sup>167</sup>. The inset provides a more detailed view of the Cu 2p<sub>3/2</sub> region, showing that the maximum of the approximately symmetrical peak is located at a binding energy of ≈932.9 eV. (It should be noted that the spectrometer used for these measurements is not calibrated for high-precision measurements, rendering an exact assignment of the charge state challenging for such a narrow range of binding energies. The peak positions were shifted by a constant value, determined by the offset of an oxygen spectrum acquired in the same experiment compared to the correct O 1s binding energy (530.1 eV) for Fe<sub>3</sub>O<sub>4</sub>(001).) The peak shape and position are indicative of a single partially oxidized component, which is in good agreement with the DFT+*U* prediction of a Cu<sup>1+</sup> adatom.

In gas adsorption experiments at room temperature, Cu was found to be inert to low pressures of CO, O<sub>2</sub>, H<sub>2</sub>O, and NO. In STM images no changes compared to the as-deposited Cu adatoms are discernible (data not shown). The adsorption of Cu is found to follow the trend of its group in the periodic table, i.e., Cu forms highly stable adatoms, which are inert to UHV-compatible pressures of reactant gases at room temperature. Regarding the metal adsorption behavior of the Cu group elements, another trend becomes apparent: An increasing tendency to form stable adatoms rather than clusters at augment-

ed deposited coverage is observed when comparing the adsorption of Au to Ag and Cu. This indicates that in the steps from Au to Ag and further to Cu the metal-oxide interaction strength is increasing compared to the metal-metal bond in the size regime close to single atoms. The high stability of Cu over a broad range of coverages and temperatures under UHV conditions portrays it as one of the most promising candidates for testing single-atom reactivity and promoting effects at elevated temperatures and pressures.

## 4.2.8 Co-deposition of metals

The deposition of two or more metals coexisting at the surface can provide interesting conclusions about the interactions of supported metal adatoms. Moreover the combination of two metal adatoms with complementary properties represents a promising approach towards custom-made functional materials, for example “catalysts by design” created by selecting metals specifically for a certain reaction. The results presented here can be considered proof-of-principle experiments demonstrating the possibility to co-deposit and distinguish different metals at the  $\text{Fe}_3\text{O}_4(001)$  surface.

Figure 4.50 shows a compilation of the co-deposition of selected metals. The co-deposition of Ag and Pt (Ag deposited first) in (a) results in the coexistence of Ag and Pt adatoms at the surface. At the scanning conditions of  $U_{\text{sample}}=+2.0$  V and  $I_t=0.3$  nA the Ag and Pt adatoms can be clearly distinguished by their apparent heights ( $h(\text{Pt}_1)=80$ -95 pm,  $h(\text{Ag}_1)=120$ -140 pm compared to the surface Fe rows). The yellow and cyan arrows highlight examples of Ag and Pt adatoms, respectively. While Ag adatoms represent the majority species at the surface, Pt is present in different configurations. The feature in the red circle corresponds to a  $\text{Pt}_1^*$  atom and the features that are larger and brighter than all adatoms are attributed to Pt clusters (example in cyan circle), created by CO-induced mobility.

Co-deposition of 1 ML Cu and 0.2 ML Pt (Pt deposited first) in (b) also results in the coexistence of Pt and Cu adatoms, highlighted by cyan and purple arrows, respectively. Again, the apparent heights allow discriminating between the two metal species ( $h(\text{Pt}_1)=85$ -105 pm,  $h(\text{Cu}_1)=45$ -60 pm compared to the surface Fe rows). For both metals, also the respective second single-atom adsorption sites, offset to the side from the site blocked by  $\text{Fe}_{\text{int}}$ , are found to be occupied. The co-deposition of Cu and Pt was an attempt to trap Pt adatoms in sites fully surrounded by Cu adatoms in order to suppress the CO-induced mobility and clustering. However, STM image sequences (not shown) demonstrate that the presence of Cu adatoms does not significantly influence the surface diffusion of the  $\text{Pt}_1$ -CO species.

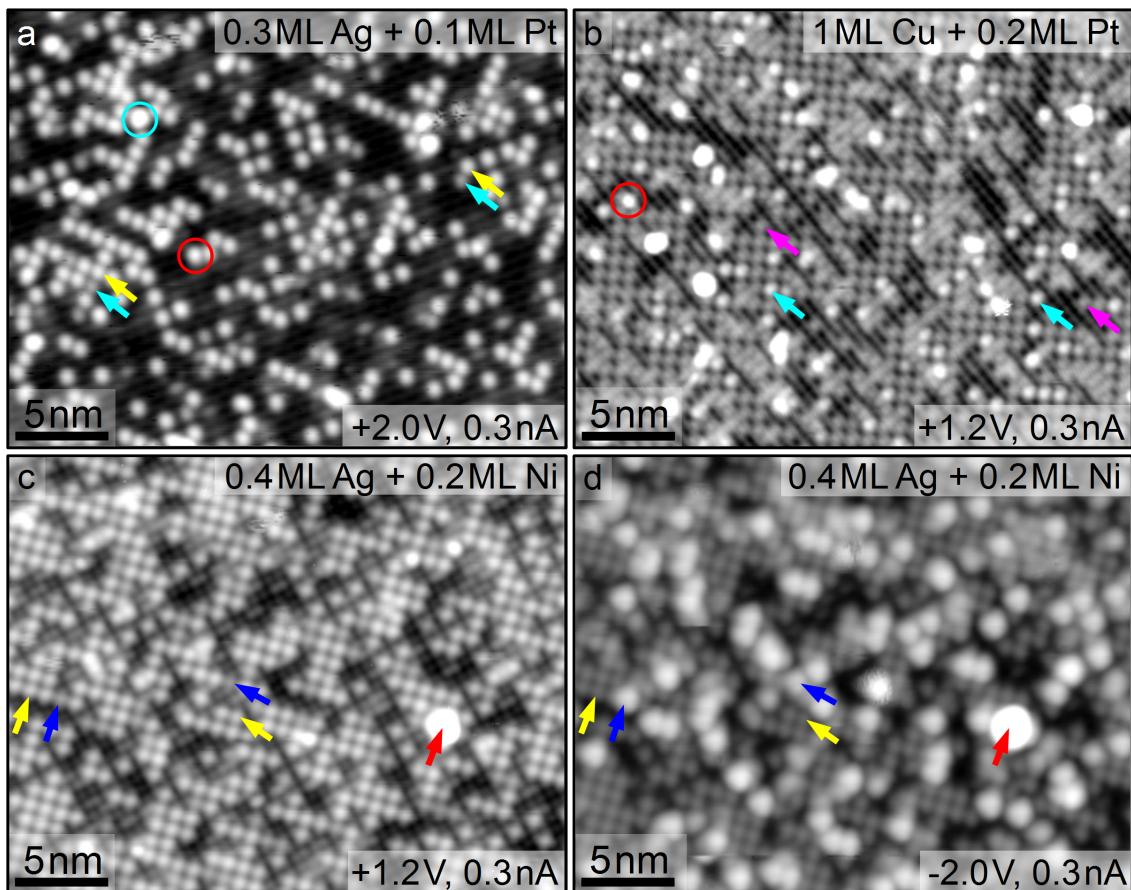


**Figure 4.50:** Co-deposition of different metals at the  $\text{Fe}_3\text{O}_4(001)$  surface. (a) 0.3 ML Ag + 0.1 ML Pt: Each metal preserves its individual adsorption properties. The Ag adatoms (example highlighted by yellow arrow) exceed Pt in apparent height (cyan arrow) when scanning at  $U_{\text{sample}} = +2.0 \text{ V}$  ( $I_t = 0.3 \text{ nA}$ ). An example of a  $\text{Pt}_1^*$  is highlighted by the red circle, an example of a cluster species by the cyan circle. (b) 1 ML Cu + 0.2 ML Pt: The brighter adatoms are Pt, while Cu adatoms are the majority species (examples highlighted by cyan and purple arrows, respectively). In large patches both types of Cu adatoms fully occupy the surface. The large, bright species are attributed to Pt clusters. Bimetallic clusters are possible in the case of Cu adatoms landing on Pt clusters or fully occupied patches. (c) 0.4 ML Ag + 0.2 ML Ni at  $U_{\text{sample}} = +1.2 \text{ V}$  ( $I_t = 0.3 \text{ nA}$ ): Ag adatoms appear brighter than Ni adatoms (yellow and blue arrows, respectively), but the difference is very subtle. (d) Changing the tunneling conditions to  $U_{\text{sample}} = -2.0 \text{ V}$  ( $I_t = 0.3 \text{ nA}$ ) results in very bright Ni adatoms, which can be clearly distinguished from Ag (the same Ag and Ni atoms as in (c) are highlighted by the yellow and blue arrows, respectively, the red arrow highlights a cluster as reference point).

The comparison of Figures 4.50(c) and (d) illustrates the importance of selecting a suitable tunneling bias voltage for distinguishing two metal species. While at  $U_{sample}=+1.2$  V ( $I_t=0.3$  nA) Ag and Ni adatoms (highlighted by the yellow and blue arrows, respectively) are difficult to distinguish, the same area imaged at  $U_{sample}=-2.0$  V ( $I_t=0.3$  nA) gives a very different impression. When imaging filled states, the Ni adatoms clearly exceed Ag in apparent height, although topographically, the DFT calculations predict the Ag to be significantly higher ( $\Delta z_{Ag-FeB}=0.97$  Å,  $\Delta z_{Ni-FeB}=0.62$  eV). This is a good example of an electronic effect in STM, indicating that the occupied DOS of the Ni adatom close to the Fermi level is significantly higher than that of the Ag adatom. Since imaging the surface at negative sample bias strongly changes the appearance in STM images, the cluster highlighted by the red arrow is used as a reference point to illustrate that the same area is imaged. A similarly strong effect is also observed for Ag and Pt when switching to negative sample bias voltage (not shown).

In summary, the co-deposition of adatoms has been demonstrated by three examples. The metals coexist as adatoms at the surface and all observations indicate a largely independent behavior of the metal species, each maintaining its characteristic properties. No specific interactions between different metallic species were observed. However, the formation of bimetallic clusters upon deposition of high coverages cannot be excluded. The images of the co-deposition of Ag and Ni indicate that finding suitable scanning conditions to distinguish the metal species is essential for experiments combining different metals at the surface. Nevertheless, the observations indicate high potential for attempts to combine two or more metals for the detailed study of a “model catalyst by design” based on single adatoms.

### 4.3 Properties and applications of metal clusters

The strong interaction of active metal species such as Pt and Rh with gas molecules was described to induce mobility and cluster formation (see sections 4.2.5.2 and 4.2.6.2). These systems are therefore only of limited use for single-atom catalysis applications but they offer a well-defined initial state for the study of cluster properties and activity, similar to size-selected clusters. While single atoms represent the ultimate limit of the size-effect of active particles in heterogeneous catalysis, the size-dependent activity of sub-nano metal clusters is equally promising for catalysis research<sup>12,16</sup>. In some cases, single-site catalysts exhibit further differences in the catalytic properties besides reactivity, such as selectivity for different products, shown for example for zeolite-supported Rh<sup>168</sup>. A recent

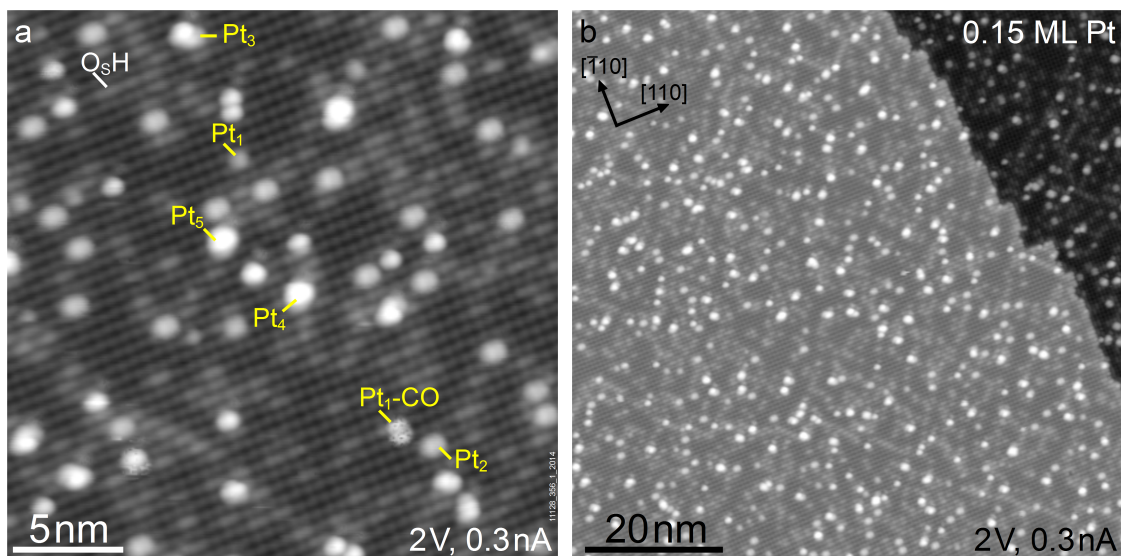
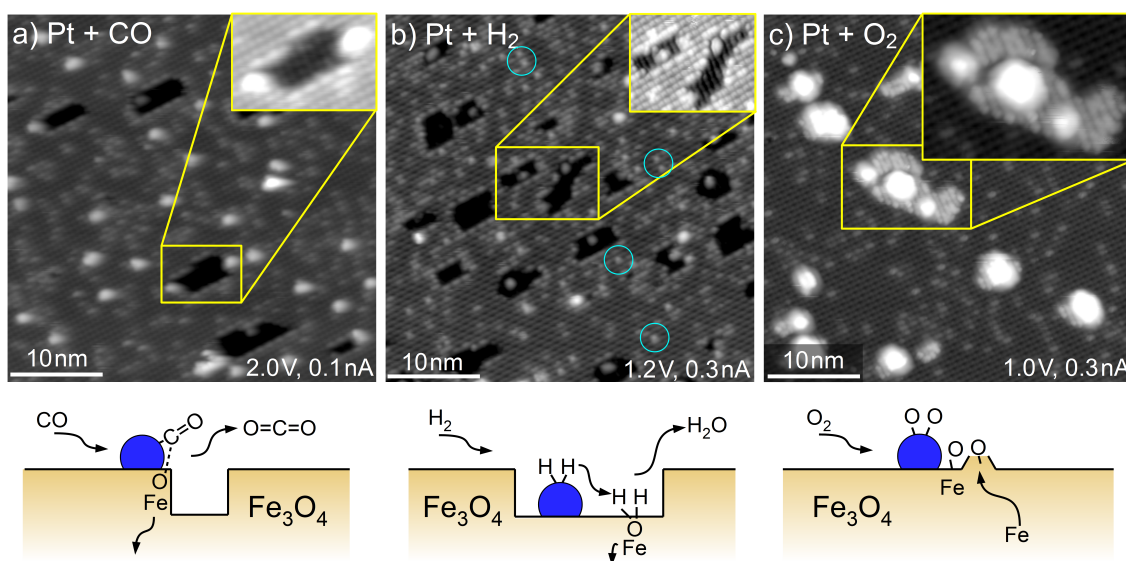


**Figure 4.51:** Initial state of the reactivity study of Pt sub-nano clusters<sup>169</sup> created by sintering 0.15 ML Pt adatoms in  $10^{-7}$  mbar CO. The STM images show the distribution of clusters on an ordered surface with large, flat terraces. Different cluster sizes are labeled, up to Pt<sub>5</sub>, the largest cluster formed in the scanned region. (b) Large-scale image showing clusters distributed homogeneously across a large terrace with a typical step-edge in the right part of the image.

article on the CO oxidation over Pt adatoms and clusters on a zeolite support<sup>58</sup> even raises the question whether single atoms contribute to the activity at all in this system. Here, the role of the reducible substrate Fe<sub>3</sub>O<sub>4</sub>(001) in the oxidation of CO and H<sub>2</sub> over Pt sub-nano particles is studied using STM. The figures in the present section are adapted from a recent article describing the support effects in this system<sup>169</sup>.

The initial state for the cluster study shown in Figure 4.51 is created by deposition of Pt adatoms onto the as-prepared Fe<sub>3</sub>O<sub>4</sub>(001) single crystal, and subsequent exposure to CO causing agglomeration to clusters, which contain only few atoms (described in detail in section 4.2.5.2). This process creates a distribution of small clusters with a preference for dimer species. Figure 4.51 displays STM images of Pt/Fe<sub>3</sub>O<sub>4</sub>(001) after CO exposure with Pt cluster sizes up to Pt<sub>5</sub> labeled in (a). The large-scale overview image in (b) shows a typical flat, continuous terrace with a step-edge. According to the results presented in section 4.2.5.2 all these clusters contain CO and the dimers decay if the CO molecules are desorbed thermally by annealing in UHV.

In the present section, the catalytic activity of these Pt sub-nano clusters is assessed by annealing the system in low pressures of reactant gases in order to obtain insights into the atomic-scale mechanisms of reaction processes and the influence of the support.



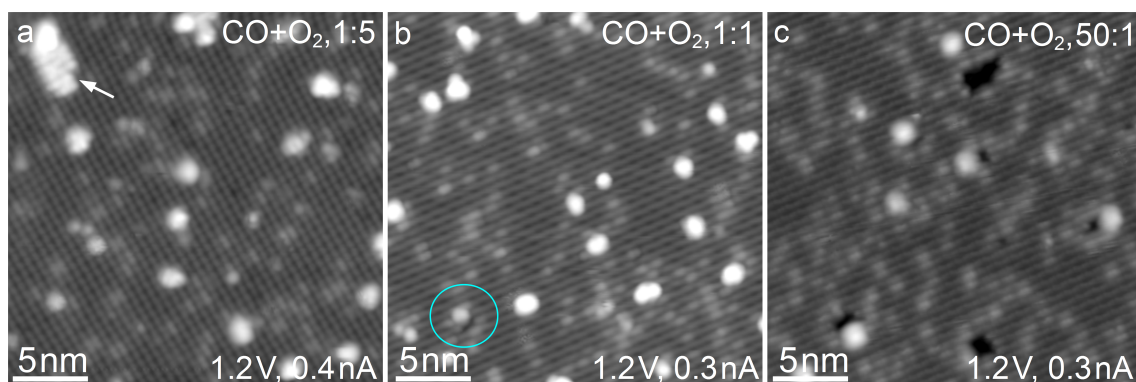
**Figure 4.52:** STM images after annealing in reactive atmosphere in three independent experiments, illustrating the atomic-scale mechanisms of the reactivity of Pt sub-nano clusters (reprinted with permission from Wiley and Sons<sup>169</sup>). (a) STM image after annealing at 550 K in  $10^{-7}$  mbar CO for 60 min. Monolayer-deep holes in the surface are observed adjacent to Pt clusters. The holes are attributed to the extraction of lattice oxygen and Fe diffusion to the bulk as sketched in the drawing below. The large fraction of inactive clusters indicates an autocatalytic process. (b) After annealing in  $10^{-7}$  mbar H<sub>2</sub> for 20 min Pt clusters coexist with adatoms. Adjacent to virtually all clusters the surface exhibits holes, resembling the ones created by CO. (c) Annealing in  $10^{-7}$  mbar O<sub>2</sub> for 20 min leads to regrowth of surface material adjacent to all Pt clusters. The insets in each STM image show monolayer-deep holes/monolayer-high islands with the rotation of the surface Fe rows expected in the spinel structure.

Figure 4.52 illustrates the effect of heating the Pt clusters to 550 K in  $10^{-7}$  mbar CO, H<sub>2</sub>, and O<sub>2</sub> in separate experiments. (For each result presented here, control experiments without Pt were performed under the same conditions but did not show any effects related to catalytic processes.) After annealing in CO for 60 min no Pt adatoms are observed, and the Pt species have agglomerated further to a small number of larger clusters compared to the initial state in Figure 4.51. The interaction of the clusters and the support with CO results in the creation of 2.1 Å deep holes (one full double layer consisting of Fe<sub>oct</sub>O<sub>2</sub> and Fe<sub>tet</sub>) in the surface adjacent to a fraction of the Pt clusters. The inset in (a) shows the selection highlighted by the yellow frame at an enhanced contrast, illustrating that the surface Fe rows are rotated by 90° inside the holes. The observation of monolayer-deep holes in the surface is interpreted as Pt-mediated extraction of surface oxygen atoms as part of a Mars-van Krevelen CO oxidation process, illustrated in the schematic drawing below the STM image. The Mars-van Krevelen mechanism is a common pathway for CO

oxidation over oxide-supported active particles<sup>170</sup> that proceeds via the extraction of lattice oxygen, which is replenished from O<sub>2</sub> in the gas phase. The energetic barrier usually involved in the removal of lattice oxygen is the main reason why this process preferentially occurs at elevated temperatures. In the STM images the Pt clusters are either located adjacent to relatively large holes, or not associated with any hole in the surface. This lack of small holes adjacent to clusters indicates that the extraction process is autocatalytic, i.e., the removal of the first oxygen atoms from the surface layer involves the largest energetic barrier and the subsequent removal of O<sub>s</sub> from the resulting step-edge is easier. The observation of the SCV surface structure inside the holes in the surface confirms the results presented in section 4.1, i.e., it is the energetically most favorable termination across a wide pressure range. Since Fe oxide surfaces are known to react to stoichiometry changes preferentially via the cation lattice<sup>88,171</sup>, the SCV structure can form at the surface if the temperature is sufficiently high for the excess Fe created by the CO oxidation process to diffuse to the bulk. (Bulk diffusion of deposited Fe was observed at ≈470 K.)

A similar result is obtained when the surface with Pt/Fe<sub>3</sub>O<sub>4</sub>(001) (sintered in 10<sup>-7</sup> mbar CO for 10 min) is annealed during exposure to 10<sup>-7</sup> mbar H<sub>2</sub> at 550 K for 20 min. The STM image in Figure 4.52(b) shows a high density of monolayer-deep holes adjacent to a large fraction of Pt clusters. The total area of holes is larger than in the images acquired after the CO oxidation experiment, although they were obtained within a shorter period of time, indicating a more efficient oxygen extraction process in the case of H<sub>2</sub> oxidation. The process catalyzed by the clusters during H<sub>2</sub> exposure is likely the adsorption, splitting, and spillover of hydrogen, followed by the extraction of surface oxygen to form H<sub>2</sub>O (see sketch below the STM image in Figure 4.52(b)). In the absence of metal adspecies the desorption of water from a strongly hydroxylated Fe<sub>3</sub>O<sub>4</sub>(001) surface was observed<sup>172</sup> at comparable temperatures, suggesting that the extraction of surface oxygen is not the limiting step of the catalytic reaction. In contrast to the CO oxidation experiment, the clusters are found coexist with a nonzero coverage of Pt adatoms after annealing in H<sub>2</sub>, suggesting that the redispersion process discussed for UHV conditions in section 4.2.5.2 is also active in H<sub>2</sub> atmosphere. The cyan circles in Figure 4.52(b) highlight a few examples of Pt adatoms. However, in this set of experiments no activity of single atoms was discernible, potentially because the catalyzed process is expected to require more than one active site for splitting the H<sub>2</sub> molecule.

Figure 4.52(c) provides an STM image of Pt clusters after exposure to 10<sup>-7</sup> mbar O<sub>2</sub> at 550 K for 20 min (after sintering the Pt in up to 10<sup>-7</sup> mbar CO). At these conditions no Pt adatoms are observed, indicating that also O<sub>2</sub> can play a role in the coarsening processes, albeit this was not observed at room temperature. The clusters decorating the



**Figure 4.53:** STM images after annealing in mixed CO:O<sub>2</sub> gas atmospheres (constant CO pressure ( $10^{-7}$  mbar)) illustrating the reactivity of Pt sub-nano clusters<sup>169</sup>. (a) Slow island growth is observed for annealing in excess oxygen at a CO:O<sub>2</sub> ratio 1:5 (60 min, 590 K). (b) For equal CO and O<sub>2</sub> pressures (1:1, each  $10^{-7}$  mbar, 550 K, 20 min) the effects involving the substrate are small: One small hole is observed adjacent to a cluster (cyan circle). (c) After prior exposure to CO:O<sub>2</sub> 1:1 and 5:1 (each at 550 K, 20 min) showed very weak effects, small holes adjacent to the Pt clusters were observed for heating in a 50:1 ratio (excess CO, 550 K, 20 min), showing that the presence of small amounts of O<sub>2</sub> does not block the extraction of lattice oxygen.

surface in this image are larger than the ones in the CO or H<sub>2</sub> experiments and all of them are surrounded by, or adjacent to, island-like features of a single magnetite step height. The island enlarged in the inset exhibits a row-like structure rotated by 90° compared to the main terrace and a step height of  $\approx 2$  Å, both of which are typical properties for a next layer of the Fe<sub>3</sub>O<sub>4</sub>(001) SCV surface. Thus, the results for the high-temperature exposure to O<sub>2</sub> are interpreted as oxygen spillover from the Pt clusters onto the substrate. At a temperature of 550 K, Fe can diffuse from the bulk to the surface as a response to the oxidizing conditions, leading to the growth of an additional layer of surface material adjacent to the Pt clusters. Since strong metal support interaction (SMSI) has been reported for Pt clusters on an Fe<sub>3</sub>O<sub>4</sub> support at elevated temperatures<sup>156</sup>, the surface with Pt clusters annealed at temperatures up to  $\approx 600$  K in UHV and in O<sub>2</sub> was tested for encapsulation (overgrowth by an oxide layer) using low-energy ion scattering (see Figure C.1 in Appendix C). However, in both cases strong Pt peaks were observed, excluding any encapsulation effect.

The presented results give insights into the role of a reducible substrate in elementary reaction processes of CO oxidation or other reactions involving CO, H<sub>2</sub>, or O<sub>2</sub>. Similar experiments in mixtures of CO and O<sub>2</sub> resulted in significantly smaller changes to the substrate (see Figure 4.53). Here, the CO pressure was kept constant ( $p_{CO}=10^{-7}$  mbar)

and the oxygen pressure was adjusted to test the behavior at different CO:O<sub>2</sub> ratios. Figure 4.53(a) shows an STM image after an experiment of annealing at 590 K in excess oxygen (CO:O<sub>2</sub>=1:5) for 20 min, demonstrating that the formation of islands is possible even in the presence of CO. STM images acquired after annealing in a 1:1 mixture show only very weak indications of support interactions, such as the small hole highlighted by the cyan circle in (b). A considerable number of holes started to form when dosing excess CO at a ratio of 50:1 for 20 min at 550 K (Figure 4.53(c)) after prior exposure to CO:O<sub>2</sub> ratios of 1:1 and 5:1 (each for 20 min at 550 K) showed very weak effects. The smaller changes that reactions cause to the support when annealing in gas mixtures can be interpreted in different ways: The simultaneous presence of CO and O<sub>2</sub> may lead to a change in the reaction pathway to perform the CO oxidation reaction largely on the cluster (i.e. in a Langmuir-Hinshelwood-type mechanism). On the other hand the effects observed in pure CO or O<sub>2</sub> atmospheres could occur in parallel. The slow reaction speeds in the pure gases combined with the high activity of small islands or holes offer a plausible explanation for the large range of pressures, at which no effects are observed. Further options such as poisoning of the catalytic process of the respective other species cannot be excluded either.

The presented observations provide insights into oxidation catalysis over active sub-nano Pt particles on an iron oxide support. The activity of the Pt clusters described here occurs at temperatures, which leave the surface unaffected by effects such as the encapsulation of Pt clusters observed on the Fe<sub>3</sub>O<sub>4</sub>(001) and (111) surfaces via strong metal-support interaction<sup>156</sup>. The study of H<sub>2</sub> and CO is particularly interesting in the context of a reactivity study for the preferential oxidation of CO (PROX) over Pt sub-nano clusters on an iron oxide support, showing high activity and stability for this reaction is available in a broad temperature window<sup>173</sup>. Under the realistic conditions in the reactivity study by Qiao *et al.*<sup>173</sup> the involvement of the substrate was clearly discernible, since different iron oxide phases were formed in temperature programmed reaction experiments using H<sub>2</sub>. The differences in the support material or temperature-dependent variations in the selectivity may be the reason for the reported suitability for PROX, which not fully in agreement with the higher activity for H<sub>2</sub> presented in Figure 4.52. The Mars-van Krevelen mechanism catalyzed by metal nanoparticles has been studied as well on a variety of reducible substrates, including for example Pt-doped ceria<sup>174</sup>, Au on ceria<sup>175</sup>, and TiO<sub>2</sub><sup>170</sup>. The results presented above provide atomic-scale insights into reaction processes over oxide-supported metal nanoparticles and shed light on the potential role of reducible oxide supports in oxidation reactions.

## 4.4 Trends in metal adsorption

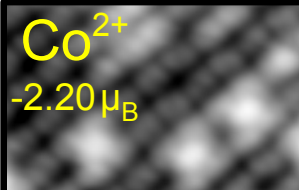
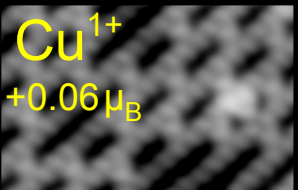
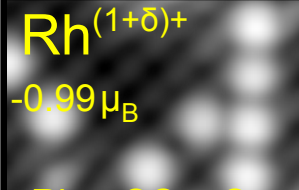
The experimental data and calculations for a broad selection of metals allow conclusions on general trends of metal adsorption at the  $\text{Fe}_3\text{O}_4(001)$  surface to be drawn. Regarding the variety of characteristic properties of the adatoms and their different interaction with the surface, a short summary of the calculations on metal adatoms is of interest. Figure 4.54 provides an overview of important metal adsorption properties and the interaction of the adatoms with CO and  $\text{O}_2$ , which shall be discussed in the context of the experimental results presented above. For this discussion, the nine metals of the Co, Ni, and Cu groups (groups 9, 10, and 11) of the periodic table of elements have been selected. All calculations were performed on 17-layer slabs of two  $(\sqrt{2} \times \sqrt{2})$ -reconstructed surface unit cells with a  $(3 \times 3 \times 1)$   $k$ -mesh to map the reciprocal space (except for Ir, which was described by a  $(2 \times 2 \times 1)$   $k$ -mesh). (The Ni and Co calculations were performed on a smaller 17-layer slab consisting of a single reconstructed cell.) A value of  $Rk_{max} \geq 5.5$  was used in all the adatom calculations (corresponding to an energy cut-off of the basis set of  $\approx 183$  eV, equivalent to  $Rk_{max} = 3.67$  in the presence of gas molecules with smaller atomic radii  $r_C(\text{CO}) = r_O(\text{CO}, \text{O}_2) = 1$  bohr (0.53 Å)). To describe the correlations of the Fe 3d electrons, an effective Hubbard- $U$  correction of 3.8 eV was employed. The same value for  $U$  was applied to the Ni 3d and Co 3d electrons, whereas no  $U$  was used to describe the Ag, Au, Cu, Ir, Pd, Pt, and Rh adatoms.

Figure 4.54 gives a brief account of the calculated metal adsorption properties, providing the data for each adatom in a separate panel according to the following scheme: On the background of a corresponding (experimental) STM image of adatoms, each panel is labeled with the respective element symbol with the approximate charge state of the neat adatom ( $\delta$  represents a small non-integer number,  $0 < \delta < 1$ ). The number below the label corresponds to the magnetic moment of the adatom within the atomic sphere (radii of 1 Å (Ni, Co, Cu, Rh, Pd, Ir) or 1.1 Å (Ag, Pt, Au) set in the calculations). The table below each image provides the adsorption energies (in eV) in the first line, the metal bond lengths to the surface oxygen atoms in the second line and the vertical distance above the average surface  $\text{Fe}_{\text{oct}}$  (both in Å) in the last line. The same two characteristic distances are also discussed for each metal in the respective sections and their geometry is illustrated in the structural model for Ag in Figure 4.9 (section 4.2.2). The three columns correspond to three different configurations described by the yellow labels in each panel: the metal adatom, the adatom with an adsorbed CO molecule, and the adatom with an adsorbed  $\text{O}_2$  species, which was only calculated for Co, Ni, Rh, and Pd. In the case of Pt and Pd, the adsorption of CO lifts the adatom out of the adsorption site closer to one of the two

neighboring surface Fe rows. Thus, for Pt and Pd the bonding geometry to oxygen is characterized by two different adatom-oxygen bond lengths, both of which are listed in Figure 4.54. Concerning the adsorption of oxygen, it should be noted that the magnetic moments and the oxygen-oxygen bond lengths of the adsorbed oxygen atoms indicate that oxygen may not be adsorbed molecularly as neutral O<sub>2</sub>. While the effect is relatively weak for Rh and Pd adatoms ( $d_{O-O}(\text{Rh-O}_2)=1.26 \text{ \AA}$ ,  $|\vec{\mu}_O(\text{Rh-O}_2)|=0.19 \mu_B$  and  $d_{O-O}(\text{Pd-O}_2)=1.24 \text{ \AA}$ ,  $|\vec{\mu}_O(\text{Pd-O}_2)|=0.17 \mu_B$ ), the values calculated for Co and Ni adatoms clearly suggest a charged nature of the adsorbed oxygen ( $d_{O-O}(\text{Ni-O}_2)=1.36 \text{ \AA}$ ,  $|\vec{\mu}_O(\text{Ni-O}_2)|=0.34 \mu_B$  and  $d_{O-O}(\text{Pd-O}_2)=1.38 \text{ \AA}$ ,  $|\vec{\mu}_O(\text{Pd-O}_2)|=0.31 \mu_B$ ).

A comparison of the charge states shows that all metal adatoms are cationic, typically donating their charge to the subsurface Fe<sub>oct</sub>(S-4) atoms. The additional electrons give these Fe<sub>oct</sub> atoms an Fe<sup>2+</sup>-like character, and thus modify the total magnetic moment of the slab, allowing conclusions on the approximate charge state of the metal adatoms. A fraction of the charge donated by the adatoms partially reduces the two O<sup>1-</sup> atoms, whose unsaturated character is expected to play an important role in the metal adsorption preference. While the reducing effect is weak for most adatoms, the magnetic moment indicative of the O<sup>1-</sup> state is almost fully suppressed for the Co-group metals, coinciding with their high oxidation states and adsorption energies. The presented charge states are in good agreement with the XPS results presented in the respective chapters or in the literature<sup>59,140,157</sup>. Regarding the magnetic moments of the adatoms, it is interesting to note the different orientation for the Co and the Ni groups, indicating a strong difference in the exchange interaction at comparable bond distances. With the adsorption of CO, the spin polarization of the 3d metal adatoms remains intact, whereas for the 4d and 5d metals it decreases to insignificant values ( $|\vec{\mu}| < 0.1 \mu_B$ , not shown), indicative of a stronger metal-substrate interaction of the 3d metals.

In the context of the experimental observations, the adsorption energies of the adatoms can be interpreted as descriptors of two competing bond strengths: the metal-metal and the metal-oxide bond. The balance of these two interactions is a decisive factor for a metal's ultimate preference for incorporation or agglomeration to metal clusters. Here, the 4d and 5d metals are found to present a higher tendency to form clusters, while the 3d metals prefer incorporation, indicated by the comparably high energy gain when adsorbing at the oxide surface. The strong interaction of Rh with oxygen, both in the O<sub>2</sub> molecule and in the surface (highest adsorption energy among the 4d metals), also suggests an energy gain by increasing the coordination to oxygen. In contrast, Ag and Au are examples for a relatively low energy gain by bonding to the surface. However, the relatively weak interaction of these metals with CO compared to Rh, Pd, or Pt inhibits destabilizing effects

			
	$\text{Co}^{2+}$ $-2.20\mu_B$	$\text{Ni}^{1+}$ $+0.99\mu_B$	$\text{Cu}^{1+}$ $+0.06\mu_B$
	Co +CO +O <sub>2</sub>	Ni +CO +O <sub>2</sub>	Cu +CO
$E_{ads} =$	5.46, 6.62, 7.72 eV	3.21, 4.48, 5.26 eV	3.41, 4.69 eV -
$d_{M-O} =$	1.86, 1.99, 1.99 Å	1.85, 1.99, 1.98 Å	1.84, 2.01 Å -
$\Delta z_{M-Fe} =$	0.55, 1.13, 1.15 Å	0.62, 1.13, 1.03 Å	0.53, 1.23 Å -
			
	$\text{Rh}^{(1+\delta)+}$ $-0.99\mu_B$	$\text{Pd}^{\delta+}$ $+0.25\mu_B$	$\text{Ag}^{1+}$ $+0.03\mu_B$
	Rh +CO +O <sub>2</sub>	Pd +CO +O <sub>2</sub>	Ag +CO
$E_{ads} =$	3.67, 6.38, 6.62 eV	2.59, 4.20, 4.92 eV	1.85, 3.23 eV -
$d_{M-O} =$	1.94, 1.99, 2.02 Å	1.99, $\frac{2.07}{3.03}$ , 2.10 Å	2.08, 2.28 Å -
$\Delta z_{M-Fe} =$	0.70, 0.53, 1.08 Å	0.46, 1.83, 1.24 Å	0.97, 1.60 Å -
			
	$\text{Ir}^{2+}$ $-0.96\mu_B$	$\text{Pt}^{\delta+}$ $+0.31\mu_B$	$\text{Au}^{1+}$ $+0.04\mu_B$
	Ir +CO	Pt +CO Pt <sub>1</sub> *	Au +CO
$E_{ads} =$	4.58, 7.27 eV -	3.89, 5.53, 3.01 eV	1.98, 3.48 eV -
$d_{M-O} =$	1.89, 1.99 Å -	1.98, $\frac{2.03}{2.98}$ , 2.03 Å	2.00, 2.22 Å -
$\Delta z_{M-Fe} =$	0.67, 0.47 Å -	0.47, 1.74, 1.02 Å	0.70, 1.49 Å -

**Figure 4.54:** Summary of the DFT+U results on nine metal adatoms at the  $\text{Fe}_3\text{O}_4(001)$  surface and their interaction with CO and  $\text{O}_2$ . For each metal, an STM image ( $5.2 \times 4.2 \text{ nm}^2$ ) of adatoms and a set of calculated properties are provided in the respective panel. The numbers adjacent to the element symbols correspond to the approximate charge state (with:  $0 < \delta < 1$  for small, non-integer numbers) of the respective adatom and its magnetic moment inside the atomic sphere. In the table below the STM image, the first line lists the total adsorption energies of the adatom, the adatom with adsorbed CO, and the adatom with adsorbed oxygen (only calculated for Co, Ni, Rh, Pd). (For Pt, the values in the last column correspond to the  $\text{Pt}_1^*$  configuration instead.) In the second and third lines, the bond length to surface oxygen and the height above the average surface  $\text{Fe}_{\text{oct}}$  are provided for the same configurations.

such as adsorbate-induced mobility. While the absolute adsorption energies of gas molecules are not quantitatively comparable with experimentally measured values due to the difficulty of good reference values for isolated atoms and molecules in DFT, the values are well suited for comparing the adsorption of probe molecules on different metal species. Overall, a qualitative comparison of the differences in adsorption strengths of CO and O<sub>2</sub> on metal adatoms gives good agreement with the experimental results. This includes the strong interactions of Rh with O<sub>2</sub> and CO or the effect of CO lifting the Pt adatom out of its adsorption site. In a more general view, the interaction strength between adatoms and gas molecules is observed to increase when moving to the left on the periodic table, towards more electropositive elements with a more open *d*-shell. The higher reactivity of these metals is also borne out in their stronger tendency to incorporate. The trends derived from this study present Ir as a highly promising reactive metal for future studies, provided it follows the tendency of the 5*d* metals not to incorporate.

Similar calculations assessing the stability of cationic metal adatoms were reported for a large selection of metals on the (100) facet of a CeO<sub>2</sub> nanoparticle<sup>176</sup> in the site which showed the strongest adsorption of Pt adatoms. The overall behavior is similar; adatoms are stabilized by bonding to surface oxygen and assume a cationic charge state. The ceria surface can be reduced more easily; thus, metals tend to be more strongly oxidized than on Fe<sub>3</sub>O<sub>4</sub>(001) (e.g. Ag<sup>3+</sup>, Co<sup>3+</sup>), donating electrons which reduce the Ce<sup>4+</sup>. The differences in oxidation states give rise to interesting phenomena such as support-related variations in the activity or selectivity for gas adsorption on the adatoms. Further analogies between ceria and the findings presented in Figure 4.54 include for example that the 4*d* metals also form the weakest bond to the oxide<sup>176</sup>. This range of similarities to ceria suggests that also other reducible oxide surface may be suitable supports for stable cationic metal adatoms, holding undiscovered potential for future single-atom catalysts.

## 5 Summary and Outlook

The properties of the magnetite  $\text{Fe}_3\text{O}_4(001)$  surface offer a variety of fascinating phenomena, which are ideal for an in-depth experimental surface science study complemented by density functional theory calculations. In the present thesis the  $\text{Fe}_3\text{O}_4(001)$  surface structure and different aspects of metal adsorption at this surface have been studied using a combined approach of experimental surface science methods (STM, PES, LEED, LEIS) and density functional theory. The adsorption of metals and their interaction with common reactant gas molecules is investigated, building on the discovery of thermally stable isolated metal adatoms at this surface<sup>59,60,109</sup> prior to this work.

As a first step in this study, the  $\text{Fe}_3\text{O}_4(001)$  surface structure was revisited and a new structural model based on an ordered array of subsurface Fe vacancies (the SCV structure) was introduced. Using quantitative low-energy electron diffraction and *ab-initio* thermodynamics, the SCV structure was established as the correct description of the most stable surface termination<sup>111</sup>; this proved to be crucial for understanding the surface properties. The characteristic cation rearrangement of the SCV structure creates a strong preference for metal adsorption in one specific site per unit cell. In this site the metal adatom is two-fold coordinated to surface oxygen and adsorption is not blocked by the presence of a tetrahedrally coordinated subsurface  $\text{Fe}_{\text{int}}$  (or  $\text{Fe}_{\text{tet}}$ ) atom. All metals studied in the present thesis form isolated metal adatoms in this site following deposition at room temperature. Although these adatoms are found to be thermally highly stable for many metals (up to an annealing temperature of  $\approx 700$  K for noble metals) the adatom configuration does not represent the thermodynamic equilibrium state for any of the deposited metals. If the stability of the adatoms is broken the metals follow one of two observed pathways: incorporation into the oxide lattice in the surface region or agglomeration to clusters. While most noble metals (Ag, Au, Pt, Pd) are found to favor cluster formation, metals exhibiting a strong tendency to form oxides prefer incorporation. The incorporation of metal cations results in the filling of the subsurface vacancies underlying the reconstruction, which is consequently lifted for high coverages of the incorporated metal. As a result of the incorporation, a thin film of a nonstoichiometric spinel ferrite ( $\text{M}_x\text{Fe}_{3-x}\text{O}_4$ , with  $\text{M} = \text{Ni}, \text{Co}$ ,

Ti, Mn) is formed. However, also reactive metals that are not naturally abundant in solid solution with  $\text{Fe}_3\text{O}_4$  are found to enter the  $\text{Fe}_3\text{O}_4(001)$  surface, for example Zr and Rh. In DFT+ $U$  calculations for Ni, Ti, and Co, the energetically favored incorporation site in the surface region was determined, showing a unanimous preference for the subsurface  $\text{Fe}_{\text{oct}}$  vacancy site. At elevated temperatures, however, the metal cations start diffusing into the bulk, a process which requires enhanced mobility of Fe in the lattice compared to the filling of vacancies in the surface region.

The high thermal stability of many metal adatoms encourages the study of their interaction with common reactant gases such as CO,  $\text{O}_2$ , and NO. The observed interaction strength at room temperature varies significantly; it extends from no discernible adsorption up to strong adsorption that induces mobility of the adatoms. In agreement with DFT predictions, the strongest interactions were observed for the combinations Pt-CO, Rh- $\text{O}_2$ , and Rh-CO, but also NO was found to adsorb on various metal adatoms (shown for Ni and Rh). In the case of Rh,  $\text{O}_2$  and CO both adsorbed strongly but led to contrasting effects: Oxygen adsorption mobilized the Rh adatoms and led to agglomeration, whereas CO adsorption strengthened the bond to the surface and poisoned any activity of the Rh adatom for gas adsorption (including  $\text{O}_2$ ). In the study of Pt, the adsorption of CO was found to play two essential roles in the formation of clusters: It weakens the bond to the substrate, mobilizing the Pt adatoms, and stabilizes Pt dimers, which are only energetically favorable if two CO molecules are adsorbed. The DFT+ $U$ -derived energetic preferences are borne out in experiments by the redispersion of Pt dimers into adatoms upon heating in UHV to desorb the stabilizing CO. Heating the Pt clusters to 550 K in reactive atmosphere ( $\text{CO}$ ,  $\text{H}_2$ , or  $\text{O}_2$ ), on the other hand, provides proof of the catalytic activity of Pt sub-nano clusters at this surface. In these experiments the reducible substrate  $\text{Fe}_3\text{O}_4(001)$  becomes involved in the reaction processes, leaving a signature in STM images: CO and  $\text{H}_2$  oxidation processes create holes in the surface layer adjacent to Pt clusters, whereas island growth next to the clusters is observed after annealing in  $\text{O}_2$ . Hence the study of active small clusters of archetypal catalytic metals such as Pt or Rh at the  $\text{Fe}_3\text{O}_4(001)$  surface presents an interesting alternative pathway to single-atom catalysis research at this surface.

The detailed understanding of the metal adsorption properties at this surface provides a good basis for testing the trends predicted in the DFT+ $U$  adsorption study of CO and  $\text{O}_2$  using for example temperature programmed desorption (TPD) or XPS at variable temperatures. An extensive TPD study would also enhance the knowledge of the effects of the different incorporated metals, as well as provide information about potential reactivity involving the  $\text{Fe}_3\text{O}_4(001)$  substrate by monitoring additional molecular masses. Regard-

ing the pathway to single-atom catalysis at the  $\text{Fe}_3\text{O}_4(001)$  surface, the research could be raised to the next level by targeting specific reaction processes, which are known to occur on sub-nano particles of selected metals. In particular the highly stable adatom species such as Ag and Cu are ideal for studies in surface chemistry setups, where *in-situ* imaging techniques are not available. Moreover, the study of single atoms in realistic environments will present another essential step from a model system to a potential single-atom catalyst. There are several promising reaction processes, which carry potential for the activity of single atoms. In the case of Cu, for example, water-gas-shift activity is reported at temperatures above 620 K over  $\text{CuFe}_2\text{O}_4$  and  $\text{Cu}/\text{Fe}_3\text{O}_4$ <sup>165</sup>. A study on single Ag adatoms could for example investigate if the high propylene epoxidation activity reported over size-selected  $\text{Ag}_3$  clusters<sup>131</sup> is transferable to single atoms. In particular in the context of the support effects observed in the oxidation reactions with Pt, the study of propylene adsorption using temperature programmed desorption, XPS, and STM appears to be a promising pathway. Via the deposition of different coverages and subsequent annealing, the size distribution of the Ag particles can be adjusted, ranging from a low coverage of single-phase Ag adatoms to mixed phases with adatoms and small clusters up to large clusters created when annealing to temperatures in excess of 700 K. For proof-of-principle experiments, the selection of metals for specific reactions guided by catalytic processes in the literature is a promising approach, which is also likely to improve the metal efficiency via minimizing the particle size in the active phase. Finally, the even more exciting future perspective of a single-atom catalyst model system such as  $\text{Fe}_3\text{O}_4(001)$  is the potential to combine two types of metal adatoms, each one excellent at performing its specific task, to create a customized catalyst for a certain reaction pathway based on spillover to enable interaction of the reaction intermediates.

## Bibliography

- [1] Gerhard Ertl. Reactions at surfaces: From atoms to complexity (Nobel lecture). *Angewandte Chemie International Edition*, 47(19):3524–3535, 2008.
- [2] Dawn A. Bonnell. Scanning tunneling microscopy and spectroscopy of oxide surfaces. *Progress in Surface Science*, 57(3):187 – 252, 1998.
- [3] Victor E. Henrich and P.A. Cox. *The Surface Science of Metal Oxides*. Cambridge University Press, 1996.
- [4] Frederick K. Lutgens and Edward J. Tarbuck. *Essentials of geology*. Upper Saddle River, NJ : Prentice Hall, 7th ed edition, 2000.
- [5] Mark A. Barteau. Organic reactions at well-defined oxide surfaces. *Chemical Reviews*, 96(4):1413–1430, 1996.
- [6] Hans-Joachim Freund. Adsorption of gases on complex solid surfaces. *Angewandte Chemie International Edition*, 36(5):452–475, 1997.
- [7] Werner Weiss and Wolfgang Ranke. Surface chemistry and catalysis on well-defined epitaxial iron-oxide layers. *Progress in Surface Science*, 70(1-3):1 – 151, 2002.
- [8] Ulrike Diebold. The surface science of titanium dioxide. *Surface Science Reports*, 48(5-8):53–229, 2003.
- [9] Helmut Kuhlenbeck, Shamil Shaikhutdinov, and Hans-Joachim Freund. Well-ordered transition metal oxide layers in model catalysis - a series of case studies. *Chemical Reviews*, 113(6):3986–4034, 2013.
- [10] Marcus Bäumer and Hans-Joachim Freund. Metal deposits on well-ordered oxide films. *Progress in Surface Science*, 61(7-8):127–198, 1999.
- [11] Charles T. Campbell. Ultrathin metal films and particles on oxide surfaces: Structural, electronic and chemisorptive properties. *Surface Science Reports*, 27(1-3):1–111, 1997.
- [12] Bokwon Yoon, Hannu Häkkinen, Uzi Landman, Anke S. Wörz, Jean-Marie Antonietti, Stéphane Abbet, Ken Judai, and Ueli Heiz. Charging effects on bonding and catalyzed oxidation of CO on Au<sub>8</sub> clusters on MgO. *Science*, 307(5708):403–407, 2005.

- [13] Charles T. Campbell. The energetics of supported metal nanoparticles: Relationships to sintering rates and catalytic activity. *Accounts of Chemical Research*, 46(8):1712–1719, 2013.
- [14] Alexis T. Bell. The impact of nanoscience on heterogeneous catalysis. *Science*, 299(5613):1688–1691, 2003.
- [15] Masatake Haruta, Tetsuhiko Kobayashi, Hiroshi Sano, and Nobumasa Yamada. Novel gold catalysts for the oxidation of carbon monoxide at a temperature far below 0°C. *Chemistry Letters*, 16(2):405 – 408, 1987.
- [16] Masatake Haruta. Size- and support-dependency in the catalysis of gold. *Catalysis Today*, 36(1):153 – 166, 1997.
- [17] Randall Meyer, Celine Lemire, Shamil K. Shaikhutdinov, and Hans-Joachim Freund. Surface chemistry of catalysis by gold. *Gold Bulletin*, 37(1):72–124, 2004.
- [18] Britt Hvolbæk, Ton V.W. Janssens, Bjerne S. Clausen, Hanne Falsig, Claus H. Christensen, and Jens K. Nørskov. Catalytic activity of Au nanoparticles. *Nano Today*, 2(4):14 – 18, 2007.
- [19] Patricia A. Thiel, Mingmin Shen, Da-Jiang Liu, and James W. Evans. Adsorbate-enhanced transport of metals on metal surfaces: Oxygen and sulfur on coinage metals. *Journal of Vacuum Science & Technology A*, 28(6):1285–1298, 2010.
- [20] Runhai Ouyang, Jin-Xun Liu, and Wei-Xue Li. Atomistic theory of Ostwald ripening and disintegration of supported metal particles under reaction conditions. *Journal of the American Chemical Society*, 135(5):1760–1771, 2013.
- [21] Nihed Chaâbane, Rémi Lazzari, Jacques Jupille, Gilles Renaud, and Edmar Avellar Soares. CO-induced scavenging of supported Pt nanoclusters: A GISAXS study. *The Journal of Physical Chemistry C*, 116(44):23362–23370, 2012.
- [22] Thomas W. Hansen, Andrew T. DeLaRiva, Sivakumar R. Challa, and Abhaya K. Datye. Sintering of catalytic nanoparticles: Particle migration or Ostwald ripening? *Accounts of Chemical Research*, 46(8):1720–1730, 2013.
- [23] Yves Fukamori, Michael König, Bokwon Yoon, Bo Wang, Friedrich Esch, Ueli Heiz, and Uzi Landman. Fundamental insight into the substrate-dependent ripening of monodisperse clusters. *ChemCatChem*, 5(11):3330–3341, 2013.
- [24] Stephen C. Parker and Charles T. Campbell. Kinetic model for sintering of supported metal particles with improved size-dependent energetics and applications to Au on TiO<sub>2</sub>(110). *Physical Review B*, 75:035430, 2007.
- [25] Kristina Wettergren, Florian F. Schweinberger, Davide Deiana, Claron J. Ridge, Andrew S. Crampton, Marian D. Rötzer, Thomas W. Hansen, Vladimir P. Zhdanov, Ueli Heiz, and Christoph Langhammer. High sintering resistance of size-selected platinum cluster catalysts by suppressed Ostwald ripening. *Nano Letters*, 14(10):5803–5809, 2014.

- [26] Pierre Fayet, Michael J. McGlinchey, and Ludger H. Woeste. Bonding capabilities of nickel cluster ions: Synthetic chemistry in a molecular beam. *Journal of the American Chemical Society*, 109(6):1733–1738, 1987.
- [27] Ueli Heiz, Fabrice Vanolli, Antonio Sanchez, and Wolf-Dieter Schneider. Size-dependent molecular dissociation on mass-selected, supported metal clusters. *Journal of the American Chemical Society*, 120(37):9668–9671, 1998.
- [28] Stefan Vajda, Sebastian Wolf, Thomas Leisner, Ulrike Busolt, Ludger H. Wöste, and David J. Wales. Reactions of size-selected positively charged nickel clusters with carbon monoxide in molecular beams. *The Journal of Chemical Physics*, 107(9):3492–3497, 1997.
- [29] Eric C. Tyo and Stefan Vajda. Catalysis by clusters with precise numbers of atoms. *Nature Nanotechnology*, 10(7):577–588, 2015.
- [30] Ueli Heiz, Antonio Sanchez, Stéphane Abbet, and Wolf-Dieter Schneider. Catalytic oxidation of carbon monoxide on monodispersed platinum clusters: Each atom counts. *Journal of the American Chemical Society*, 121(13):3214–3217, 1999.
- [31] Dong C. Lim, Rainer Dietsche, Moritz Bubek, Gerd Ganteför, and Young D. Kim. Oxidation and reduction of mass-selected Au clusters on SiO<sub>2</sub>/Si. *ChemPhysChem*, 7(9):1909–1911, 2006.
- [32] William E. Kaden, Tianpin Wu, William A. Kunkel, and Scott L. Anderson. Electronic structure controls reactivity of size-selected Pd clusters adsorbed on TiO<sub>2</sub> surfaces. *Science*, 326(5954):826–829, 2009.
- [33] Yoshihide Watanabe, Xingyang Wu, Hirohito Hirata, and Noritake Isomura. Size-dependent catalytic activity and geometries of size-selected Pt clusters on TiO<sub>2</sub>(110) surfaces. *Catalysis Science & Technology*, 1:1490–1495, 2011.
- [34] Z. Xu, F. S. Xiao, S. K. Purnell, O. Alexeev, S. Kawi, S. E. Deutsch, and B. C. Gates. Size-dependent catalytic activity of supported metal clusters. *Nature*, 372(6504):346–348, 1994.
- [35] Markus M Schubert, Stefan Hackenberg, Andre C van Veen, Martin Muhler, Vojtech Plizak, and R. Jürgen Behm. CO oxidation over supported gold catalysts—“inert” and “active” support materials and their role for the oxygen supply during reaction. *Journal of Catalysis*, 197(1):113 – 122, 2001.
- [36] Maria Flytzani-Stephanopoulos and Bruce C. Gates. Atomically dispersed supported metal catalysts. *Annual Review of Chemical and Biomolecular Engineering*, 3(1):545–574, 2012.
- [37] Xiao-Feng Yang, Aiqin Wang, Botao Qiao, Jun Li, Jingyue Liu, and Tao Zhang. Single-atom catalysts: A new frontier in heterogeneous catalysis. *Accounts of Chemical Research*, 46(8):1740–1748, 2013.
- [38] Stéphane Abbet, Ueli Heiz, Hannu Häkkinen, and Uzi Landman. CO oxidation on a single Pd atom supported on magnesia. *Physical Review Letters*, 86:5950–5953, 2001.

- [39] Qi Fu, Howard Saltsburg, and Maria Flytzani-Stephanopoulos. Active non-metallic Au and Pt species on ceria-based water-gas shift catalysts. *Science*, 301(5635):935–938, 2003.
- [40] Botao Qiao, Aiqin Wang, Xiaofeng Yang, Lawrence F. Allard, Zheng Jiang, Yitao Cui, Jingyue Liu, Jun Li, and Tao Zhang. Single-atom catalysis of CO oxidation using Pt<sub>1</sub>/FeO<sub>x</sub>. *Nature Chemistry*, 3(8):634–641, 2011.
- [41] Jing Lu, Ceren Aydin, Nigel D. Browning, and Bruce C. Gates. Imaging isolated gold atom catalytic sites in zeolite NaY. *Angewandte Chemie International Edition*, 51(24):5842–5846, 2012.
- [42] Haijun Zhang, Tatsuya Watanabe, Mitsutaka Okumura, Masatake Haruta, and Naoki Toshima. Catalytically highly active top gold atom on palladium nanocluster. *Nature Materials*, 11(1):49–52, 2012.
- [43] Yaroslava Lykhach, Alberto Figueroba, Matteo Farnesi Camellone, Armin Neitzel, Tomas Skala, Fabio R. Negreiros, Mykhailo Vorokhta, Nataliya Tsud, Kevin C. Prince, Stefano Fabris, Konstantin M. Neyman, Vladimir Matolin, and Jörg Libuda. Reactivity of atomically dispersed Pt<sup>2+</sup> species towards H<sub>2</sub>: model Pt-CeO<sub>2</sub> fuel cell catalyst. *Physical Chemistry Chemical Physics*, 18:7672–7679, 2016.
- [44] Maria Flytzani-Stephanopoulos. Gold atoms stabilized on various supports catalyze the water-gas shift reaction. *Accounts of Chemical Research*, 47(3):783–792, 2014.
- [45] Niklas Nilius. Properties of oxide thin films and their adsorption behavior studied by scanning tunneling microscopy and conductance spectroscopy. *Surface Science Reports*, 64(12):595 – 659, 2009.
- [46] Georgios Kyriakou, Matthew B. Boucher, April D. Jewell, Emily A. Lewis, Timothy J. Lawton, Ashleigh E. Baber, Heather L. Tierney, Maria Flytzani-Stephanopoulos, and E. Charles H. Sykes. Isolated metal atom geometries as a strategy for selective heterogeneous hydrogenations. *Science*, 335(6073):1209–1212, 2012.
- [47] Felicia R. Lucci, Jilei Liu, Matthew D. Marcinkowski, Ming Yang, Lawrence F. Allard, Maria Flytzani-Stephanopoulos, and E. Charles H. Sykes. Selective hydrogenation of 1,3-butadiene on platinum-copper alloys at the single-atom limit. *Nature Communications*, 6:8550, 2015.
- [48] Ming Yang, Sha Li, Yuan Wang, Jeffrey A. Herron, Ye Xu, Lawrence F. Allard, Sung-sik Lee, Jun Huang, Manos Mavrikakis, and Maria Flytzani-Stephanopoulos. Catalytically active Au-O(OH)<sub>x</sub>- species stabilized by alkali ions on zeolites and mesoporous oxides. *Science*, 346(6216):1498–1501, 2014.
- [49] Shuhui Sun, Gaixia Zhang, Nicolas Gauquelin, Ning Chen, Jigang Zhou, Songlan Yang, Weifeng Chen, Xiangbo Meng, Dongsheng Geng, Mohammad N Banis, Ruying Li, Siyu Ye, Shanna Knights, Gianluigi A. Botton, Tsun-Kong Sham, and Xueliang Sun. Single-atom catalysis using Pt/graphene achieved through atomic layer deposition. *Scientific Reports*, 3:1775, 2013.

- [50] J.A. Moulijn, A.E. van Diepen, and F. Kapteijn. Catalyst deactivation: Is it predictable?: What to do? *Applied Catalysis A: General*, 212(1-2):3–16, 2001.
- [51] Jian Lin, Ai Qin Wang, Botao Qiao, Xiaoyan Liu, Xiaofeng Yang, Xiaodong Wang, Jinxia Liang, Jun Li, Jingyue Liu, and Tao Zhang. Remarkable performance of Ir<sub>1</sub>/FeO<sub>x</sub> single-atom catalyst in water gas shift reaction. *Journal of the American Chemical Society*, 135(41):15314–15317, 2013.
- [52] Simon F. J. Hackett, Rik M. Brydson, Mhairi H. Gass, Ian Harvey, Andrew D. Newman, Karen Wilson, and Adam F. Lee. High-activity, single-site mesoporous Pd/Al<sub>2</sub>O<sub>3</sub> catalysts for selective aerobic oxidation of allylic alcohols. *Angewandte Chemie International Edition*, 46(45):8593–8596, 2007.
- [53] Tushar K. Ghosh and Nisanth N. Nair. Rh<sub>1</sub>/γ-Al<sub>2</sub>O<sub>3</sub> single-atom catalysis of O<sub>2</sub> activation and CO oxidation: Mechanism, effects of hydration, oxidation state, and cluster size. *ChemCatChem*, 5(7):1811–1821, 2013.
- [54] Ja Hun Kwak, Jianzhi Hu, Donghai Mei, Cheol-Woo Yi, Do Heui Kim, Charles H. F. Peden, Lawrence F. Allard, and Janos Szanyi. Coordinatively unsaturated Al<sup>3+</sup> centers as binding sites for active catalyst phases of platinum on γ-Al<sub>2</sub>O<sub>3</sub>. *Science*, 325(5948):1670–1673, 2009.
- [55] Melanie Moses-DeBusk, Mina Yoon, Lawrence F. Allard, David R. Mullins, Zili Wu, Xiaofan Yang, Gabriel Veith, G. Malcolm Stocks, and Chaitanya K. Narula. CO oxidation on supported single Pt atoms: Experimental and ab initio density functional studies of CO interaction with Pt atom on θ-Al<sub>2</sub>O<sub>3</sub>(010) surface. *Journal of the American Chemical Society*, 135(34):12634–12645, 2013.
- [56] John C. Matsubu, Vanessa N. Yang, and Phillip Christopher. Isolated metal active site concentration and stability control catalytic CO<sub>2</sub> reduction selectivity. *Journal of the American Chemical Society*, 137(8):3076–3084, 2015.
- [57] Eric J. Peterson, Andrew T. DeLaRiva, Sen Lin, Ryan S. Johnson, Hua Guo, Jeffrey T. Miller, Ja Hun Kwak, Charles H. F. Peden, Boris Kiefer, Lawrence F. Allard, Fabio H. Ribeiro, and Abhaya K. Datye. Low-temperature carbon monoxide oxidation catalysed by regenerable atomically dispersed palladium on alumina. *Nature Communications*, 5, 2014.
- [58] Kunlun Ding, Ahmet Gulec, Alexis M. Johnson, Neil M. Schweitzer, Galen D. Stucky, Laurence D. Marks, and Peter C. Stair. Identification of active sites in CO oxidation and water-gas shift over supported Pt catalysts. *Science*, 350(6257):189–192, 2015.
- [59] Zbynek Novotny, Giacomo Argentero, Zhiming Wang, Michael Schmid, Ulrike Diebold, and Gareth S. Parkinson. Ordered array of single adatoms with remarkable thermal stability: Au/Fe<sub>3</sub>O<sub>4</sub>(001). *Physical Review Letters*, 108(21):216103, 2012.
- [60] Gareth S. Parkinson, Zbynek Novotny, Giacomo Argentero, Michael Schmid, Jiri Pavelec, Rukan Kosak, Peter Blaha, and Ulrike Diebold. Carbon monoxide-induced adatom sintering in a Pd-Fe<sub>3</sub>O<sub>4</sub> model catalyst. *Nature Materials*, 12(8):724–728, 2013.

- [61] Lukas Mayr, Norbert Köpfle, Andrea Auer, Bernhard Klötzer, and Simon Penner. An (ultra) high-vacuum compatible sputter source for oxide thin film growth. *Review of Scientific Instruments*, 84(9):094103, 2013.
- [62] J. Bardeen. Tunnelling from a many-particle point of view. *Physical Review Letters*, 6:57–59, 1961.
- [63] G. Binnig, H. Rohrer, Ch. Gerber, and E. Weibel. Tunneling through a controllable vacuum gap. *Applied Physics Letters*, 40(2), 1982.
- [64] Michael Schmid. STM Gallery: STM Schematic. [http://www.iap.tuwien.ac.at/www/surface/stm\\_gallery/stm\\_schematic](http://www.iap.tuwien.ac.at/www/surface/stm_gallery/stm_schematic). Accessed: 2016-05-29.
- [65] J. Tersoff and D. R. Hamann. Theory and application for the scanning tunneling microscope. *Physical Review Letters*, 50(25):1998–2001, 1983.
- [66] Georg Held. Low-energy electron diffraction crystallography of surfaces and interfaces. *Bunsen-Magazin*, 12(12):124–131, 2010.
- [67] J. B. Pendry. Reliability factors for LEED calculations. *Journal of Physics C: Solid State Physics*, 13(5):937, 1980.
- [68] Paul S. Bagus, Eugene S. Ilton, and Connie J. Nelin. The interpretation of XPS spectra: Insights into materials properties. *Surface Science Reports*, 68(2):273–304, 2013.
- [69] H.H. Brongersma, M. Draxler, M. de Ridder, and P. Bauer. Surface composition analysis by low-energy ion scattering. *Surface Science Reports*, 62(3):63–109, 2007.
- [70] M. Born and R. Oppenheimer. Zur Quantentheorie der Molekeln. *Annalen der Physik*, 389(20):457–484, 1927.
- [71] P. Hohenberg and W. Kohn. Inhomogeneous electron gas. *Physical Review*, 136:B864–B871, 1964.
- [72] W. Kohn and L. J. Sham. Self-consistent equations including exchange and correlation effects. *Physical Review*, 140:A1133–A1138, 1965.
- [73] John P. Perdew, Kieron Burke, and Matthias Ernzerhof. Generalized gradient approximation made simple. *Physical Review Letters*, 77:3865–3868, 1996.
- [74] V. I. Anisimov, I. V. Solovyev, M. A. Korotin, M. T. Czyżyk, and G. A. Sawatzky. Density-functional theory and NiO photoemission spectra. *Physical Review B*, 48:16929–16934, 1993.
- [75] J. Hubbard. The description of collective motions in terms of many-body perturbation theory. II. The correlation energy of a free-electron gas. *Proceedings of the Royal Society of London A: Mathematical, Physical and Engineering Sciences*, 243(1234):336–352, 1958.
- [76] G. Kresse and J. Furthmüller. Efficiency of ab-initio total energy calculations for metals and semiconductors using a plane-wave basis set. *Computational Materials Science*, 6(1):15 – 50, 1996.

- [77] J. C. Slater. Wave functions in a periodic potential. *Physical Review*, 51:846–851, 1937.
- [78] E. Sjöstedt, L. Nordström, and D. J. Singh. An alternative way of linearizing the augmented plane-wave method. *Solid State Communications*, 114(1):15–20, 2000.
- [79] O. Krogh Andersen. Linear methods in band theory. *Physical Review B*, 12:3060–3083, 1975.
- [80] P. Blaha, K. Schwarz, G. K. H. Madsen, D. Kvasnicka, and J. Luitz. *WIEN2K, An Augmented Plane Wave + Local Orbitals Program for Calculating Crystal Properties*. Karlheinz Schwarz, Techn. Universität Wien, Austria, Wien, Austria, 2001.
- [81] K. Schwarz, P. Blaha, and G.K.H. Madsen. Electronic structure calculations of solids using the WIEN2k package for material sciences. *Computer Physics Communications*, 147(1-2):71–76, 2002.
- [82] Karlheinz Schwarz and Peter Blaha. Solid state calculations using WIEN2k. *Computational Materials Science*, 28(2):259 – 273, 2003.
- [83] David Singh. Ground-state properties of lanthanum: Treatment of extended-core states. *Physical Review B*, 43:6388–6392, 1991.
- [84] R. M. Cornell and U. Schwertmann. *The Iron Oxides: Structure, Properties, Reactions, Occurrences and Uses*. Wiley-VCH, 2003.
- [85] Pedro Tartaj, Maria P. Morales, Teresita Gonzalez-Carreño, Sabino Veintemillas-Verdaguer, and Carlos J. Serna. The iron oxides strike back: From biomedical applications to energy storage devices and photoelectrochemical water splitting. *Advanced Materials*, 23(44):5243–5249, 2011.
- [86] E. J. W. Verwey. Electronic conduction of magnetite ( $\text{Fe}_3\text{O}_4$ ) and its transition point at low temperatures. *Nature*, 144:327–328, 1939.
- [87] Friedrich Walz. The Verwey transition - a topical review. *Journal of Physics: Condensed Matter*, 14(12):R285, 2002.
- [88] Gareth S. Parkinson. Iron oxide surfaces. *Surface Science Reports*, 71(1):272 – 365, 2016.
- [89] Mark S. Senn, Jon P. Wright, and J. Paul Attfield. Charge order and three-site distortions in the Verwey structure of magnetite. *Nature*, 481(7380):173–176, 2012.
- [90] D. Ihle and B. Lorenz. Small-polaron conduction and short-range order in  $\text{Fe}_3\text{O}_4$ . *Journal of Physics C: Solid State Physics*, 19(26):5239, 1986.
- [91] Horng-Tay Jeng, G. Y. Guo, and D. J. Huang. Charge-orbital ordering and Verwey transition in magnetite. *Physical Review Letters*, 93:156403, 2004.
- [92] A. R. Muxworthy and E. McClelland. Review of the low-temperature magnetic properties of magnetite from a rock magnetic perspective. *Geophysical Journal International*, 140(1):101–114, 2000.

- [93] Laura Martín-García, Arantzazu Mascaraque, Beatriz M. Pabón, Roland Bliem, Gareth S. Parkinson, Gong Chen, Andreas K. Schmid, and Juan de la Figuera. Spin reorientation transition of magnetite (001). *Physical Review B*, 93:134419, 2016.
- [94] David Santos-Carballal, Alberto Roldan, Ricardo Grau-Crespo, and Nora H. de Leeuw. A DFT study of the structures, stabilities and redox behaviour of the major surfaces of magnetite  $\text{Fe}_3\text{O}_4$ . *Physical Chemistry Chemical Physics*, 16:21082–21097, 2014.
- [95] Gareth S. Parkinson, Peter Lackner, Oscar Gamba, Sebastian Maaß, Stefan Gerhold, Michele Riva, Roland Bliem, Ulrike Diebold, and Michael Schmid.  $\text{Fe}_3\text{O}_4(110)$ - $(1 \times 3)$  revisited: Periodic (111) nanofacets. *Surface Science*, 649:120 – 123, 2016.
- [96] P. W. Tasker. The stability of ionic crystal surfaces. *Journal of Physics C: Solid State Physics*, 12(22):4977, 1979.
- [97] R. Wiesendanger, I. V. Shvets, D. Bürgler, G. Tarrach, H.-J. Güntherodt, and J. M. D. Coey. Evidence for selective imaging of different magnetic ions on the atomic scale by using a scanning tunnelling microscope with a ferromagnetic probe tip. *Europhysics Letters*, 19(2):141, 1992.
- [98] R. Wiesendanger, I. V. Shvets, D. Bürgler, G. Tarrach, H. J. Güntherodt, J. M. D. Coey, and S. Gräser. Topographic and magnetic-sensitive scanning tunneling microscope study of magnetite. *Science*, 255(5044):583–586, 1992.
- [99] B. Stanka, W. Hebenstreit, U. Diebold, and S.A. Chambers. Surface reconstruction of  $\text{Fe}_3\text{O}_4(001)$ . *Surface Science*, 448(1):49 – 63, 2000.
- [100] F. C. Voogt, T. Fujii, P. J. M. Smulders, L. Niesen, M. A. James, and T. Hibma.  $\text{NO}_2$ -assisted molecular-beam epitaxy of  $\text{Fe}_3\text{O}_4$ ,  $\text{Fe}_{3-\delta}\text{O}_4$  and  $\gamma\text{-Fe}_2\text{O}_3$  thin films on  $\text{MgO}(100)$ . *Physical Review B*, 60:11193–11206, 1999.
- [101] G. Mariotto, S. Murphy, and I. V. Shvets. Charge ordering on the surface of  $\text{Fe}_3\text{O}_4(001)$ . *Physical Review B*, 66:245426, 2002.
- [102] R. Pentcheva, F. Wendler, H. L. Meyerheim, W. Moritz, N. Jedrecy, and M. Scheffler. Jahn-Teller stabilization of a “polar” metal oxide surface:  $\text{Fe}_3\text{O}_4(001)$ . *Physical Review Letters*, 94:126101, 2005.
- [103] R. Pentcheva, W. Moritz, J. Rundgren, S. Frank, D. Schrupp, and M. Scheffler. A combined DFT/LEED-approach for complex oxide surface structure determination:  $\text{Fe}_3\text{O}_4(001)$ . *Surface Science*, 602(7):1299 – 1305, 2008.
- [104] Zbigniew Łodziana. Surface Verwey transition in magnetite. *Physical Review Letters*, 99:206402, 2007.
- [105] Norman C. Bartelt, Shu Nie, Elena Starodub, Ivan Bernal-Villamil, Silvia Gallego, Lucia Vergara, Kevin F. McCarty, and Juan de la Figuera. Order-disorder phase transition on the (100) surface of magnetite. *Physical Review B*, 88(23):235436, 2013.

- [106] N. Spiridis, J. Barbasz, Z. Łodziana, and J. Korecki.  $\text{Fe}_3\text{O}_4(001)$  films on  $\text{Fe}(001)$ : Termination and reconstruction of iron-rich surfaces. *Physical Review B*, 74(15):155423, 2006.
- [107] Earl M. Davis, Ke Zhang, Yi Cui, Helmut Kuhlbeck, Shamil Shaikhutdinov, and Hans-Joachim Freund. Growth of  $\text{Fe}_3\text{O}_4(001)$  thin films on  $\text{Pt}(100)$ : Tuning surface termination with an Fe buffer layer. *Surface Science*, 636:42–46, 2015.
- [108] Zbynek Novotny, Narasimham Mulakaluri, Zoltan Edes, Michael Schmid, Rossitza Pentcheva, Ulrike Diebold, and Gareth S. Parkinson. Probing the surface phase diagram of  $\text{Fe}_3\text{O}_4(001)$  towards the Fe-rich limit: Evidence for progressive reduction of the surface. *Physical Review B*, 87(19):195410, 2013.
- [109] Zbynek Novotny. *The Reconstructed  $\text{Fe}_3\text{O}_4(001)$  Surface as Adsorption Template*. PhD thesis, Vienna University of Technology, 2013.
- [110] Nika Spiridis, Ewa Madej, and Józef Korecki. Adsorption of gold on an iron-rich  $\text{Fe}_3\text{O}_4(001)$  surface. *The Journal of Physical Chemistry C*, 118(4):2011–2017, 2014.
- [111] R. Bliem, E. McDermott, P. Ferstl, M. Setvin, O. Gamba, J. Pavelec, M. A. Schneider, M. Schmid, U. Diebold, P. Blaha, L. Hammer, and G. S. Parkinson. Subsurface cation vacancy stabilization of the magnetite (001) surface. *Science*, 346(6214):1215–1218, 2014.
- [112] Shu Nie, Elena Starodub, Matteo Monti, David A. Siegel, Lucía Vergara, Farid El Gabaly, Norman C. Bartelt, Juan de la Figuera, and Kevin F. McCarty. Insight into magnetite’s redox catalysis from observing surface morphology during oxidation. *Journal of the American Chemical Society*, 135(27):10091–10098, 2013.
- [113] F. Y. Ran, Y. Tsunemaru, T. Hasegawa, Y. Takeichi, A. Harasawa, K. Yaji, S. Kim, and A. Kakizaki. Valence band structure and magnetic properties of Co-doped  $\text{Fe}_3\text{O}_4(100)$  films. *Journal of Applied Physics*, 109(12), 2011.
- [114] V. I. Anisimov, I. S. Elfimov, N. Hamada, and K. Terakura. Charge-ordered insulating state of  $\text{Fe}_3\text{O}_4$  from first-principles electronic structure calculations. *Physical Review B*, 54(7):4387–4390, 1996.
- [115] D. Schrupp, M. Sing, M. Tsunekawa, H. Fujiwara, S. Kasai, A. Sekiyama, S. Suga, T. Muro, V. A. M. Brabers, and R. Claessen. High-energy photoemission on  $\text{Fe}_3\text{O}_4$ : Small polaron physics and the Verwey transition. *Europhysics Letters*, 70(6):789, 2005.
- [116] M. Taguchi, A. Chainani, S. Ueda, M. Matsunami, Y. Ishida, R. Eguchi, S. Tsuda, Y. Takata, M. Yabashi, K. Tamasaku, Y. Nishino, T. Ishikawa, H. Daimon, S. Todo, H. Tanaka, M. Oura, Y. Senba, H. Ohashi, and S. Shin. Temperature dependence of magnetically active charge excitations in magnetite across the Verwey transition. *Physical Review Letters*, 115:256405, 2015.
- [117] S.A Chambers and S.A Joyce. Surface termination, composition and reconstruction of  $\text{Fe}_3\text{O}_4(001)$  and  $\gamma\text{-Fe}_2\text{O}_3(001)$ . *Surface Science*, 420(2-3):111–122, 1999.

- [118] J.-H. Park, L. H. Tjeng, J. W. Allen, P. Metcalf, and C. T. Chen. Single-particle gap above the Verwey transition in  $\text{Fe}_3\text{O}_4$ . *Physical Review B*, 55:12813–12817, 1997.
- [119] A. Chainani, T. Yokoya, T. Morimoto, T. Takahashi, and S. Todo. High-resolution photoemission spectroscopy of the Verwey transition in  $\text{Fe}_3\text{O}_4$ . *Physical Review B*, 51:17976–17979, 1995.
- [120] Guido Ketteler, Werner Weiss, Wolfgang Ranke, and Robert Schlögl. Bulk and surface phases of iron oxides in an oxygen and water atmosphere at low pressure. *Physical Chemistry Chemical Physics*, 3:1114–1122, 2001.
- [121] Karsten Reuter and Matthias Scheffler. Composition, structure, and stability of  $\text{RuO}_2(110)$  as a function of oxygen pressure. *Physical Review B*, 65:035406, 2001.
- [122] Claudine Noguera. Polar oxide surfaces. *Journal of Physics: Condensed Matter*, 12(31):R367, 2000.
- [123] V. Blum and K. Heinz. Fast LEED intensity calculations for surface crystallography using Tensor LEED. *Computer Physics Communications*, 134(3):392–425, 2001.
- [124] Björn Arndt, Roland Bliem, Oscar Gamba, Jessi E. S. van der Hoeven, Heshmat Noei, Ulrike Diebold, Gareth S. Parkinson, and Andreas Stierle. Atomic structure and stability of magnetite  $\text{Fe}_3\text{O}_4(001)$ : An x-ray view. *Surface Science*, 653:76–81, 2016.
- [125] Gareth S. Parkinson, Narasimham Mulakaluri, Yaroslav Losovyj, Peter Jacobson, Rossitza Pentcheva, and Ulrike Diebold. Semiconductor-half metal transition at the  $\text{Fe}_3\text{O}_4(001)$  surface upon hydrogen adsorption. *Physical Review B*, 82(12):125413, 2010.
- [126] Gareth S. Parkinson, Thomas A. Manz, Zbynek Novotný, Phillip T. Springer, Richard L. Kurtz, Michael Schmid, David S. Sholl, and Ulrike Diebold. Antiphase domain boundaries at the  $\text{Fe}_3\text{O}_4(001)$  surface. *Physical Review B*, 85:195450, 2012.
- [127] G. Mariotto, S. Murphy, N. Berdunov, S. F. Ceballos, and I. V. Shvets. Influence of Ca and K on the reconstruction of the  $\text{Fe}_3\text{O}_4(001)$  surface. *Surface Science*, 564(1-3):79–86, 2004.
- [128] J. F. Anderson, Markus Kuhn, Ulrike Diebold, K. Shaw, P. Stoyanov, and D. Lind. Surface structure and morphology of Mg-segregated epitaxial  $\text{Fe}_3\text{O}_4(001)$  thin films on  $\text{MgO}(001)$ . *Physical Review B*, 56:9902–9909, 1997.
- [129] Takato Mitsudome, Yusuke Mikami, Hisashi Funai, Tomoo Mizugaki, Koichiro Jitsukawa, and Kiyotomi Kaneda. Oxidant-free alcohol dehydrogenation using a reusable hydrotalcite-supported silver nanoparticle catalyst. *Angewandte Chemie*, 120(1):144–147, 2008.
- [130] J.G Serafin, A.C Liu, and S.R Seyedmonir. Surface science and the silver-catalyzed epoxidation of ethylene: an industrial perspective. *Journal of Molecular Catalysis A: Chemical*, 131(1-3):157 – 168, 1998.

- [131] Y. Lei, F. Mehmood, S. Lee, J. Greeley, B. Lee, S. Seifert, R. E. Winans, J. W. Elam, R. J. Meyer, P. C. Redfern, D. Teschner, R. Schlögl, M. J. Pellin, L. A. Curtiss, and S. Vajda. Increased silver activity for direct propylene epoxidation via subnanometer size effects. *Science*, 328(5975):224–228, 2010.
- [132] Roland Bliem, Rukan Kosak, Lukas Perneczky, Zbynek Novotny, Oscar Gamba, David Fobes, Zhiqiang Mao, Michael Schmid, Peter Blaha, Ulrike Diebold, and Gareth S. Parkinson. Cluster nucleation and growth from a highly supersaturated adatom phase: Silver on magnetite. *ACS Nano*, 8(7):7531–7537, 2014.
- [133] Gunnar Schön. ESCA studies of Ag, Ag<sub>2</sub>O and AgO. *Acta Chemica Scandinavica*, 27:2623–2633, 1973.
- [134] Tiffany C. Kaspar, Tim Droubay, Scott A. Chambers, and Paul S. Bagus. Spectroscopic evidence for Ag(III) in highly oxidized silver films by x-ray photoelectron spectroscopy. *The Journal of Physical Chemistry C*, 114(49):21562–21571, 2010.
- [135] Jonas Ø Hansen, Estephania Lira, Patrick Galliker, Jian-Guo Wang, Phillip T. Sprunger, Zheshen Li, Erik Laegsgaard, Stefan Wendt, Bjørk Hammer, and Flemming Besenbacher. Enhanced bonding of silver nanoparticles on oxidized TiO<sub>2</sub>(110). *The Journal of Physical Chemistry C*, 114(40):16964–16972, 2010.
- [136] C. Gatel and E. Snoeck. Comparative study of Pt, Au and Ag growth on Fe<sub>3</sub>O<sub>4</sub>(001) surface. *Surface Science*, 600(13):2650 – 2662, 2006.
- [137] Jin-Xia Liang, Xiaofeng Yang, Ai-Qin Wang, Tao Zhang, and Jun Li. Theoretical investigations on non-noble metal single-atom catalysis: Ni<sub>1</sub>/FeO<sub>x</sub> for CO oxidation. *Catalysis Science & Technology*, 2016. (DOI:10.1039/C6CY00672H).
- [138] Priyank V. Kumar, Michael P. Short, Sidney Yip, Bilge Yildiz, and Jeffrey C. Grossman. High surface reactivity and water adsorption on NiFe<sub>2</sub>O<sub>4</sub> (111) surfaces. *The Journal of Physical Chemistry C*, 117(11):5678–5683, 2013.
- [139] Xiao Shi, Ye-Fei Li, Steve L. Bernasek, and Annabella Selloni. Structure of the NiFe<sub>2</sub>O<sub>4</sub>(001) surface in contact with gaseous O<sub>2</sub> and water vapor. *Surface Science*, 640:73 – 79, 2015.
- [140] Roland Bliem, Jiri Pavelec, Oscar Gamba, Eamon McDermott, Zhiming Wang, Stefan Gerhold, Margareta Wagner, Jacek Osiecki, Karina Schulte, Michael Schmid, Peter Blaha, Ulrike Diebold, and Gareth S. Parkinson. Adsorption and incorporation of transition metals at the magnetite Fe<sub>3</sub>O<sub>4</sub>(001) surface. *Physical Review B*, 92:075440, 2015.
- [141] Sarp Kaya, Hirohito Ogasawara, and Anders Nilsson. Determination of the surface electronic structure of Fe<sub>3</sub>O<sub>4</sub>(111) by soft x-ray spectroscopy. *Catalysis Today*, 240, Part B(0):184–189, 2015.
- [142] A. P. Grosvenor, B. A. Kobe, M. C. Biesinger, and N. S. McIntyre. Investigation of multiplet splitting of Fe 2p XPS spectra and bonding in iron compounds. *Surface and Interface Analysis*, 36(12):1564–1574, 2004.

- [143] Xiaoliang Liang, Zisen He, Wei Tan, Peng Liu, Jianxi Zhu, Jing Zhang, and Hongping He. The oxidation state and microstructural environment of transition metals (V, Co, and Ni) in magnetite: an XAFS study. *Physics and Chemistry of Minerals*, 42(5):373–383, 2015.
- [144] Hugh St. C. O'Neill and Alexandra Navrotsky. Simple spinels: Crystallographic parameters, cation radii, lattice energies, and cation distribution. *American Mineralogist*, 68:181–194, 1983.
- [145] O. Gamba, J. Hulva, J. Pavelec, R. Bliem, M. Schmid, U. Diebold, and G.S. Parkinson. The role of surface defects in the adsorption of methanol on  $\text{Fe}_3\text{O}_4(001)$ . *ArXiv e-prints*, 2016. (eprint: 1605.09137).
- [146] Huiyuan Zhu, Sen Zhang, Yu-Xi Huang, Liheng Wu, and Shouheng Sun. Monodisperse  $\text{M}_x\text{Fe}_{3-x}\text{O}_4$  (M = Fe, Cu, Co, Mn) nanoparticles and their electrocatalysis for oxygen reduction reaction. *Nano Letters*, 13(6):2947–2951, 2013.
- [147] Regina C.C. Costa, M.F.F. Lelis, L.C.A. Oliveira, J.D. Fabris, J.D. Ardisson, R.R.V.A. Rios, C.N. Silva, and R.M. Lago. Novel active heterogeneous fenton system based on  $\text{Fe}_{3-x}\text{M}_x\text{O}_4$  (Fe, Co, Mn, Ni): The role of  $\text{M}^{2+}$  species on the reactivity towards  $\text{H}_2\text{O}_2$  reactions. *Journal of Hazardous Materials*, 129(1-3):171–178, 2006.
- [148] Mark C. Biesinger, Brad P. Payne, Andrew P. Grosvenor, Leo W. M. Lau, Andrea R. Gerson, and Roger St C. Smart. Resolving surface chemical states in XPS analysis of first row transition metals, oxides and hydroxides: Cr, Mn, Fe, Co and Ni. *Applied Surface Science*, 257(7):2717–2730, 2011.
- [149] Ill Stephen A. Steiner, Theodore F. Baumann, Bernhard C. Bayer, Raoul Blume, Marcus A. Worsley, Warren J. MoberlyChan, Elisabeth L. Shaw, Robert Schlögl, A. John Hart, Stephan Hofmann, and Brian L. Wardle. Nanoscale zirconia as a non-metallic catalyst for graphitization of carbon and growth of single- and multiwall carbon nanotubes. *Journal of the American Chemical Society*, 131(34):12144–12154, 2009.
- [150] Brian C. H. Steele and Angelika Heinzl. Materials for fuel-cell technologies. *Nature*, 414(6861):345–352, 2001.
- [151] J. T. Mayer, U. Diebold, T. E. Madey, and E. Garfunkel. Titanium and reduced titania overlayers on titanium dioxide(110). *Journal of Electron Spectroscopy and Related Phenomena*, 73(1):1–11, 1995.
- [152] T. C. Droubay, C. I. Pearce, E. S. Ilton, M. H. Engelhard, W. Jiang, S. M. Heald, E. Arenholz, V. Shutthanandan, and K. M. Rosso. Epitaxial  $\text{Fe}_{3-x}\text{Ti}_x\text{O}_4$  films from magnetite to ulvöspinel by pulsed laser deposition. *Physical Review B*, 84:125443, 2011.
- [153] A. Galtayries, R. Sporcken, J. Riga, G. Blanchard, and R. Caudano. XPS comparative study of ceria/zirconia mixed oxides: powders and thin film characterisation. *Journal of Electron Spectroscopy and Related Phenomena*, 88-91(0):951–956, 1998.

- [154] Chaitanya K. Narula, Lawrence F. Allard, G. M. Stocks, and Melanie Moses-DeBusk. Remarkable NO oxidation on single supported platinum atoms. *Scientific Reports*, 4:7238, 2014.
- [155] Jian Lin, Botao Qiao, Ning Li, Lin Li, Xiucheng Sun, Jingyue Liu, Xiaodong Wang, and Tao Zhang. Little do more: a highly effective Pt<sub>1</sub>/FeO<sub>x</sub> single-atom catalyst for the reduction of NO by H<sub>2</sub>. *Chemical Communications*, 51:7911–7914, 2015.
- [156] Ke Zhang, Shamil Shaikhutdinov, and Hans-Joachim Freund. Does the surface structure of oxide affect the strong metal-support interaction with platinum? Platinum on Fe<sub>3</sub>O<sub>4</sub>(001) versus Fe<sub>3</sub>O<sub>4</sub>(111). *ChemCatChem*, 7(22):3725–3730, 2015.
- [157] R. Bliem, J. E. S. van der Hoeven, J. Hulva, J. Pavelec, O. Gamba, P. E. de Jongh, M. Schmid, P. Blaha, U. Diebold, and G. S. Parkinson. The dual role of CO in the stability of sub-nano Pt clusters at the Fe<sub>3</sub>O<sub>4</sub>(001) surface. *Proceedings of the National Academy of Sciences of the United States of America*, (accepted for publication), 2016.
- [158] Se H. Oh, Galen B. Fisher, Joyce E. Carpenter, and D. Wayne Goodman. Comparative kinetic studies of CO-O<sub>2</sub> and CO-NO reactions over single crystal and supported rhodium catalysts. *Journal of Catalysis*, 100(2):360 – 376, 1986.
- [159] M. Shelef and R. W. McCabe. Twenty-five years after introduction of automotive catalysts: What next? *Catalysis Today*, 62(1):35–50, 2000.
- [160] Ken Judai, Anke S. Worz, Stéphane Abbet, Jean-Marie Antonietti, Ueli Heiz, Annalisa Del Vitto, Livia Giordano, and Gianfranco Pacchioni. Acetylene trimerization on Ag, Pd and Rh atoms deposited on MgO thin films. *Physical Chemistry Chemical Physics*, 7:955–962, 2005.
- [161] Weiyu Song, Antonius P. J. Jansen, and Emiel J. M. Hensen. A computational study of the influence of the ceria surface termination on the mechanism of CO oxidation of isolated Rh atoms. *Faraday Discussions*, 162:281–292, 2013.
- [162] D. A. J. Michel Ligthart, Rutger A. van Santen, and Emiel J. M. Hensen. Supported rhodium oxide nanoparticles as highly active CO oxidation catalysts. *Angewandte Chemie International Edition*, 50(23):5306–5310, 2011.
- [163] Christopher Sleight, A.P. Pijpers, Alex Jaspers, Betty Coussens, and Robert J. Meier. On the determination of atomic charge via ESCA including application to organometallics. *Journal of Electron Spectroscopy and Related Phenomena*, 77(1):41 – 57, 1996.
- [164] Ken Judai, Stéphane Abbet, Anke S. Wörz, Ulrich Heiz, Livia Giordano, and Gianfranco Pacchioni. Interaction of Ag, Rh, and Pd atoms with MgO thin films studied by the CO probe molecule. *The Journal of Physical Chemistry B*, 107(35):9377–9387, 2003.
- [165] Michael Estrella, Laura Barrio, Gong Zhou, Xianqin Wang, Qi Wang, Wen Wen, Jonathan C. Hanson, Anatoly I. Frenkel, and José A. Rodriguez. In situ characterization of CuFe<sub>2</sub>O<sub>4</sub> and Cu/Fe<sub>3</sub>O<sub>4</sub> water-gas shift catalysts. *The Journal of Physical Chemistry C*, 113(32):14411–14417, 2009.

- [166] Colin Rhodes and Graham J. Hutchings. Studies of the role of the copper promoter in the iron oxide/chromia high temperature water gas shift catalyst. *Physical Chemistry Chemical Physics*, 5(12):2719–2723, 2003.
- [167] J. Ghijsen, L. H. Tjeng, J. van Elp, H. Eskes, J. Westerink, G. A. Sawatzky, and M. T. Czyzyk. Electronic structure of  $\text{Cu}_2\text{O}$  and  $\text{CuO}$ . *Physical Review B*, 38:11322–11330, 1988.
- [168] Dong Yang, Pinghong Xu, Nigel D. Browning, and Bruce C. Gates. Tracking Rh atoms in zeolite HY: First steps of metal cluster formation and influence of metal nuclearity on catalysis of ethylene hydrogenation and ethylene dimerization. *The Journal of Physical Chemistry Letters*, 7:2537–2543, 2016.
- [169] Roland Bliem, Jessi van der Hoeven, Adam Zavodny, Oscar Gamba, Jiri Pavelec, Petra E. de Jongh, Michael Schmid, Ulrike Diebold, and Gareth S. Parkinson. An atomic-scale view of  $\text{CO}$  and  $\text{H}_2$  oxidation on a  $\text{Pt}/\text{Fe}_3\text{O}_4$  model catalyst. *Angewandte Chemie International Edition*, 54(47):13999–14002, 2015.
- [170] D. Widmann and R. J. Behm. Activation of molecular oxygen and the nature of the active oxygen species for  $\text{CO}$  oxidation on oxide supported Au catalysts. *Accounts of Chemical Research*, 47(3):740–749, 2014.
- [171] R. Dieckmann. Defects and cation diffusion in magnetite (iv): Nonstoichiometry and point defect structure of magnetite ( $\text{Fe}_{3-\delta}\text{O}_4$ ). *Berichte der Bunsengesellschaft für physikalische Chemie*, 86(2):112–118, 1982.
- [172] Gareth S. Parkinson, Zbynek Novotný, Peter Jacobson, Michael Schmid, and Ulrike Diebold. Room temperature water splitting at the surface of magnetite. *Journal of the American Chemical Society*, 133(32):12650–12655, 2011.
- [173] Botao Qiao, Aiqin Wang, Lin Li, Qingquan Lin, Haisheng Wei, Jingyue Liu, and Tao Zhang. Ferric oxide-supported Pt subnano clusters for preferential oxidation of  $\text{CO}$  in  $\text{H}_2$ -rich gas at room temperature. *ACS Catalysis*, 4(7):2113–2117, 2014.
- [174] Wei Tang, Zhenpeng Hu, Miaojun Wang, Galen D. Stucky, Horia Metiu, and Eric W. McFarland. Methane complete and partial oxidation catalyzed by Pt-doped  $\text{CeO}_2$ . *Journal of Catalysis*, 273(2):125–137, 2010.
- [175] Hyun You Kim and Graeme Henkelman.  $\text{CO}$  oxidation at the interface of Au nano-clusters and the stepped- $\text{CeO}_2(111)$  surface by the Mars-van Krevelen mechanism. *The Journal of Physical Chemistry Letters*, 4(1):216–221, 2013.
- [176] Alberto Figueroba, Gabor Kovacs, Albert Bruix, and Konstantin M. Neyman. Towards stable single-atom catalysts: strong binding of atomically dispersed transition metals on the surface of nanostructured ceria. *Catalysis Science & Technology*, 2016. doi:10.1039/C6CY00294C.

## A List of Publications

In this section, the peer-reviewed articles published during my PhD are listed (in chronological order). A short statement following the list of publications provides an outline of my contributions as a co-author of the articles.

1. Z. Wang, X. Hao, S. Gerhold, P. Mares, M. Wagner, R. Bliem, K. Schulte, M. Schmid, C. Franchini, and U. Diebold, **Stabilizing Single Ni Adatoms on a Two-Dimensional Porous Titania Overlayer at the SrTiO<sub>3</sub>(110) Surface**. *The Journal of Physical Chemistry C* 118, 19904-19909 (2014).
2. R. Bliem, R. Kosak, L. Perneczky, Z. Novotny, O. Gamba, D. Fobes, Z. Mao, M. Schmid, P. Blaha, U. Diebold, and G. S. Parkinson, **Cluster Nucleation and Growth from a Highly Supersaturated Adatom Phase: Silver on Magnetite**. *ACS Nano* 8, 7531-7537 (2014).
3. R. Bliem, E. McDermott, P. Ferstl, M. Setvin, O. Gamba, J. Pavelec, M. A. Schneider, M. Schmid, U. Diebold, P. Blaha, L. Hammer, and G. S. Parkinson, **Subsurface Cation Vacancy Stabilization of the Magnetite (001) Surface**. *Science* 346, 1215-1218 (2014).
4. O. Gamba, H. Noei, J. Pavelec, R. Bliem, M. Schmid, U. Diebold, A. Stierle, and G. S. Parkinson, **Adsorption of Formic Acid on the Fe<sub>3</sub>O<sub>4</sub>(001) Surface**. *The Journal of Physical Chemistry C* 119, 20459 (2015).
5. S. Gerhold, M. Riva, Z. Wang, R. Bliem, M. Wagner, J. Osiecki, K. Schulte, M. Schmid, and U. Diebold, **Nickel-Oxide-Modified SrTiO<sub>3</sub>(110)-(4×1) Surfaces and Their Interaction with Water**. *The Journal of Physical Chemistry C* 119, 20481 (2015).
6. R. Bliem, J. Pavelec, O. Gamba, E. McDermott, Z. Wang, S. Gerhold, M. Wagner, J. Osiecki, K. Schulte, M. Schmid, P. Blaha, U. Diebold, and G. S. Parkinson, **Adsorption and Incorporation of Transition Metals at the Magnetite Fe<sub>3</sub>O<sub>4</sub>(001) Surface**. *Physical Review B* 92, 075449 (2015).
7. R. Bliem, J. van der Hoeven, A. Zavodny, O. Gamba, J. Pavelec, P.E. de Jongh, M. Schmid, U. Diebold, and G. S. Parkinson, **An Atomic-Scale View of CO and H<sub>2</sub> Oxidation on a Pt/Fe<sub>3</sub>O<sub>4</sub>(001) Model Catalyst**. *Angewandte Chemie International Edition* 54, 13999 (2015).

8. R. Gargallo-Caballero, L. Martín-García, A. Quesada, C. Granados-Miralles, M. Foerster, L. Aballe, R. Bliem, G. S. Parkinson, P. Blaha, J. F. Marco, and J. de la Figuera, **Co on Fe<sub>3</sub>O<sub>4</sub>(001): towards precise control of surface properties**. *The Journal of Chemical Physics* 144, 094704 (2016).
9. G. S. Parkinson, P. Lackner, O. Gamba, S. Maaß, S. Gerhold, M. Riva, R. Bliem, U. Diebold, and M. Schmid, **Fe<sub>3</sub>O<sub>4</sub>(110)-(1×3) revisited: Periodic (111) nanofacets**. *Surface Science* 649, 120 (2016).
10. L. Martín-García, A. Mascaraque, B. M. Pabón, R. Bliem, G. S. Parkinson, G. Chen, A. K. Schmid, and J. de la Figuera, **Spin reorientation transition of magnetite (001)**. *Physical Review B* 93, 134419 (2016).
11. B. Arndt, R. Bliem, O. Gamba, J. E. S. van der Hoeven, H. Noei, U. Diebold, G. S. Parkinson, and A. Stierle, **Atomic structure and stability of magnetite Fe<sub>3</sub>O<sub>4</sub>(001): an x-ray view**. *Surface Science* 653, 76 (2016).
12. R. Bliem, J. E. S. van der Hoeven, J. Hulva, J. Pavelec, O. Gamba, P. E. de Jongh, M. Schmid, P. Blaha, U. Diebold, and G. S. Parkinson, **The dual role of CO in the stability of sub-nano Pt clusters at the Fe<sub>3</sub>O<sub>4</sub>(001) surface**. *Proceedings of the National Academy of Sciences* (accepted for publication).
13. O. Gamba, J. Hulva, J. Pavelec, R. Bliem, M. Schmid, U. Diebold, and G. S. Parkinson, **The role of surface defects in the adsorption of methanol on Fe<sub>3</sub>O<sub>4</sub>(001)**. *Topics in Catalysis* (accepted for publication).

#### **Contributions to the publications:**

In the publications listed above several authors were involved; most of the articles include collaborations between research groups. Thus, my contributions to the publications shall be briefly outlined here. As a first author of the publications # 2, 3, 6, 7, and 12, I performed the majority of the experimental data acquisition and analysis, and contributed to the DFT calculations (except for 2 and 7). I was also involved in the conception and writing of these manuscripts. The results published in these articles are included in the respective sections of the present thesis.

Considering the remaining articles (# 1, 4, 5, 8-11, and 13), I contributed to specific parts of the research work, such as experimental data acquisition and analysis (publications # 4, 9, and 13), DFT calculations (# 8). The DFT results (publication # 8) are also described in the body of the present thesis (the DFT calculations of the adsorption of Co). The results presented in the publications # 1, 5, 10, and 11 were partially obtained at large research facilities, where I was involved in the experimental preparation and acquisition of data.

## B Further experimental details

### B.1 $\text{Fe}_3\text{O}_4(001)$ single crystals

The experiments in the present thesis have been performed on a broad selection of crystals. The highly stoichiometric synthetic single crystals have been employed preferentially, but commercially available natural crystals have proven equally well-suited for studying the single-atom adsorption properties of magnetite. Each crystal is cleaned and tested for contaminants using XPS and STM before any experiments are performed.

Crystal #	Type	Size	Description
356_1	synthetic	3×8 mm	broken: 2 usable pieces, stoichiometric, freq. used
356_2	synthetic	≈3×6 mm	blue tinge, very steppy
357	synthetic	≈6 mm diam.	broken: 2 similar pieces, stoichiometric, frequently used, 1 piece: screw dislocations
365	natural	≈4×7 mm <sup>3</sup>	used at Maxlab and RTSTM
377	natural	10×10×1.5 mm <sup>3</sup>	used for SXRD and in RTSTM
385	natural	5×5×1 mm <sup>3</sup>	used in RTSTM for Cu

**Table B.1:** Listing of magnetite single crystals used in the course of the present PhD thesis.

## C Additional Figures

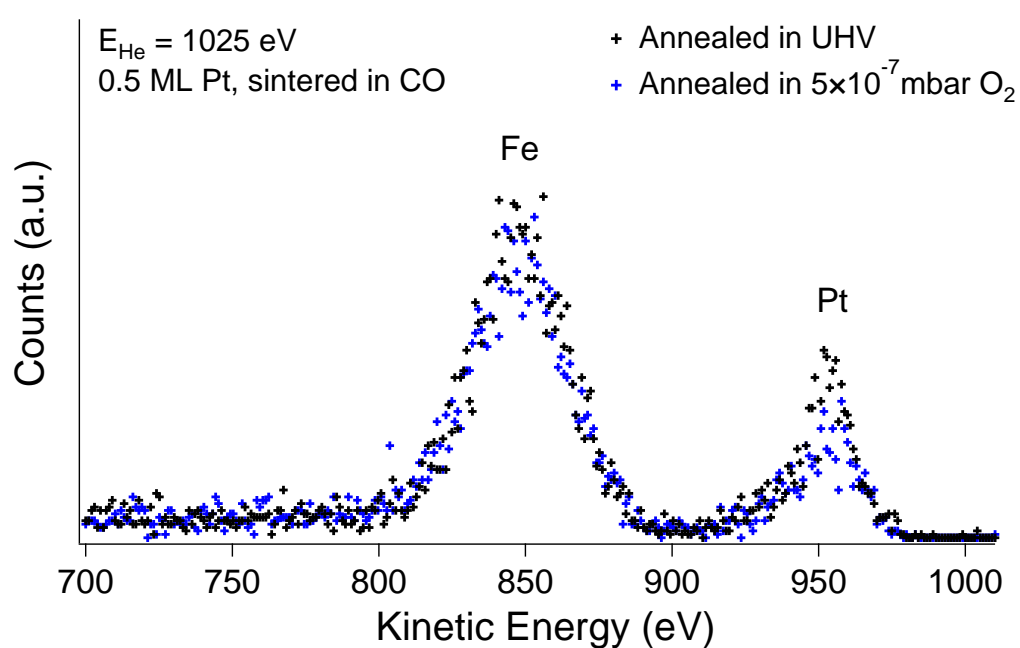


**Figure C.1:** Low-energy ion scattering spectra of Pt clusters after annealing in UHV (a) and  $5 \times 10^{-7}$  mbar  $O_2$  at  $\approx 600$  K, leading to the formation of  $Fe_3O_4(001)$  islands adjacent to all clusters. The presence of a strong Pt peak after annealing in  $O_2$  demonstrates that the Pt clusters are not encapsulated. The small decrease in intensity is attributed to further coarsening.

# Curriculum Vitae

---

## Personal Details

*Name* Roland **Bliem**  
*Address* Siebenbrunnengasse 8/4, 1050 Vienna, Austria  
*Mobile Phone* +43 664 8723433  
*Email* roland.bliem@gmail.com  
*Nationality* Austria

## Education

**PhD Engineering Physics**  
*Dates* March 2013 onwards, expected graduation July 2016  
*University* Vienna University of Technology  
*Principal Subject* Surface science of complex metal oxides  
*Supervisor* Ulrike Diebold  
*Advisors* Gareth S. Parkinson, Michael Schmid, Peter Blaha  
*Description* Graduate research work involving various surface science techniques, such as scanning tunneling microscopy (STM), photoelectron spectroscopy (XPS, UPS), electron diffraction (LEED), ion scattering (LEIS), and electronic structure calculations using density functional theory (DFT)  
*Remarks* Member of the Interdisciplinary Doctoral School Building Solids for Function (Solids4fun)

**Masters Programme Engineering Physics**  
*Dates* October 2010 - December 2012  
*University* Vienna University of Technology  
*Principal Subjects* Solid State Physics  
*Master's thesis* Study of Fe-Ni Invar alloys using density functional theory (DFT) and finite temperature modelling  
*Supervisor* Peter Mohn  
*Remarks* Exchange semester at Universidad de Granada (Spain)  
Graduated with distinction (1.0)

**Bachelors Programme Engineering Physics**  
*Dates* October 2007 - October 2010  
*University* Vienna University of Technology  
*Remark* Graduated with distinction (1.0)

## Language Skills

*Mother Tongue* German  
*Other Languages* English (Fluent), Spanish (Independent), French (Basic)

## Research Stays and Collaborations

<i>Institution</i>	Max Planck Institute Stuttgart, Germany
<i>Description</i>	Electrochemical Measurements on Fe <sub>3</sub> O <sub>4</sub>
<i>Collaborators</i>	Dr. Doris Grumelli, Prof. Klaus Kern
	January 2015 (two weeks)
<i>Institution</i>	European Synchrotron Radiation Facility, Grenoble, France
<i>Description</i>	Surface X-ray Diffraction at high pressures
<i>Collaborators</i>	Dr. Heshmat Noei, Prof. Andreas Stierle
<i>Dates</i>	June 2014 (one week)
<i>Institution</i>	University of Erlangen-Nürnberg, Erlangen, Germany
<i>Description</i>	Quantitative low energy electron diffraction (LEED IV)
<i>Collaborators</i>	Dr. Lutz Hammer, Prof. Alexander Schneider
	January 2014 (one week)
<i>Institution</i>	Max IV Laboratory (Beamline I311), Lund, Sweden
<i>Description</i>	Photoelectron Spectroscopy (UPS, XPS, ARPES) X-ray absorption spectroscopy (XAS)
	October 2013 (two weeks)
<i>Institution</i>	Lawrence Berkeley National Laboratory, Berkeley, USA
<i>Description</i>	(Spin polarized) Low energy electron microscopy ((SP)LEEM)
<i>Collaborators</i>	Prof. Juan de la Figuera, Dr. Andreas K. Schmid
	August 2013 (one week)

## Awards

<i>Type</i>	Christian Doppler Award 2015
<i>Description</i>	Science prize of the Salzburg province awarded biennially by the government (June 2016)
<i>Type</i>	Best Poster Award (Among the 5 best posters of 150)
<i>Occasion</i>	Suncat Summer Institute 2015, Stanford University
<i>Title</i>	Adsorption and Reactivity of Single Metal Adatoms at the Fe <sub>3</sub> O <sub>4</sub> (001) Surface
<i>Type</i>	Academic Excellence Scholarship of the Faculty of Physics
<i>Description</i>	Scholarships for the academic performance in the academic years 2007/08, 2008/09, 2009/10, and 2011/12